Cardiff University

School of Chemistry

A Spectroscopic Investigation of Luminescent Cr(III) Complexes

Thesis submitted for the degree of Doctor of Philosophy by:

Natalia Sawicka

July 2023

Cardiff University

School of Chemistry

ABSTRACT

Natalia Sawicka

Long-lived luminescent compounds are desirable for a range of optoelectronic applications and photoactivated materials. Chromium(III) complexes can be developed to show sharp luminescent bands as a result of relaxation from the spin-forbidden doublet excited states, namely $^2E/^2T_1$, with lifetimes into the microsecond range. In addition, the high natural abundance of chromium in comparison with precious metals such as FTIR(III), Re(I) and Ru(II) makes it a desirable alternative element for the development of luminescent complexes.

This thesis describes three series of Cr(III) complexes which are differentiated by the class of ligand utilised, namely Schiff-bases, polypyridyls and bis-pyridyl isoindolines (BPI). The polypyridyl and BPI series of complexes exhibited emission from doublet excited states. Through correlation of the geometry of the complexes and their emission maxima it was found that BPI ligands provide a more covalent character to the Cr-N bonds leading to emission maxima shifted further into the NIR-II region (> 900 nm, microsecond range lifetimes). This was further supported by EPR measurements at various MW frequencies where complexes which exhibited a significant increase of the covalency of the Cr-N bond (BPI series) led to lower D-values ($\sim$0.1 cm^{-1}) compared to those of the polypyridyl series which possess D-values of $\sim$0.4 cm^{-1}. Having calculated the nephelauxetic effect parameter for the BPI series (0.7-0.75) and compared it with previously reported parameter for [Cr(phen)$_3$]$^{3+}$ (0.85), it was evident that the BPI series presented an increased covalent character of the Cr-N bond introduced via the isoindoline moiety. This led to a conclusion that the decrease in the nephelauxetic effect parameter evidenced a reduced inter-electronic repulsion responsible for an impressive red-shift of the emission maxima and lower D-values.

List of Contents

Acknowledgements

List of Figures

O_h states.

Chapter 2

accounting for diffuse function and (d,p) accounting for polarisation function.

Chapter 3

77 K. y-axis not reported.

Chapter 4

List of Tables

via the indole N atom upon deprotonation

in aerated MeCN.

List of Abbreviations

Photophysics

Abs – Absorbance

BISC – Back Inter-system Crossing

Fl – Fluorescence

FRET – Forster Resonance Energy Transfer

IC – Internal Conversion

ILCT – Intra Ligand Charge transfer

ISC – Inter-system Crossing

LMCT – Ligand-to-Metal Charge Transfer

MLCT – Metal-to-Ligand Charge Transfer

NIR – Near-infrared

OLED – Organic Light-Emitting Devices

Phos – Phosphorescence

Q – Quenching

SOC – Spin-orbit coupling

TCSPC – Total Count Single Photon Counting

UV – Ultraviolet

General Chemistry

CFT – Crystal Field Theory

EtOH – Ethanol

HS – High-Spin

HSAB – Hard and Soft Acid and Base Theory

LS – Low-Spin

MeCN – MeCN

MeOH - Methanol

n-BuOH – n-Butanol

SCO – Spin-Crossover

Solvents

TfOH – Trifluoromethanesulfonic Acid

THF – Tetrahydrofuran

Ligands

en - Ethylenediamine

bpz - Bipyrazine

bathophen – Bathophenanthroline

bpmp - N, N′ -bis (4-pyridylmethyl)piperazine

tpda - Tripyridyldiamine

BPI – Bispyridyl isoindoline

ind – Isoindoline

py – Pyridine

acac – Acetylacetonate

Pho – Phenoxy

tpy – 2,2':6',2''-terpyridine

bpy – 2,2'-bipyridine

Dqp – 2,6-di(quinol-8-yl)pyridyl

Bpmp - 2,6-bis[(bis(2-pyridylmethyl)amino)methyl]-4-methylphenol

Ddpd - N,N'-diMe-N,N'-dipyridine-2-yl-pyridine-2,6-diamine

Dpc - 3,6-di(pyridin-4-yl)-9H-carbazole

Phen – 1,10-phenanthroline

Methods

AUC – Area Under the Curve

DFT – Density Functional Theory

EA – Elemental Analysis

EPR – Electron Paramagnetic Resonance

ESI – Electrospray Ionisation

FTIR – Fourier-Transform Infrared

HPLC – High-Performance Liquid Chromatography

LC-MS – Liquid Chromatography-Mass Spectrometry

MALDI – Matrix Assisted Laser Desorption/Ionisation

MS – Mass Spectrometry

NMR – Nuclear Magnetic Resonance

R_f – Retardation factor

TD-DFT – Time-Dependent Density Functional Theory

TIC – Total Ion Count

TLC – Thin-Layer Chromatography

EPR

CW – Continuous Wave

ZFS – Zero-Field Splitting

Miscellaneous

LCD – Liquid Crystal Device

PKC – Protein Kinase C

WOLED – White Organic Light-Emitting Devices

Chapter 1: Introduction

1.1 Introduction

This thesis describes novel, emissive Cr(III) complexes characterised by various spectroscopic methods, such as photoluminescence and electron paramagnetic resonance (EPR) spectroscopies. It is crucial that the fundamentals of photophysics and EPR techniques are introduced to the reader to facilitate analysis of the experimental results. Therefore, this chapter focuses on providing the theoretical context for these topics and the challenges associated with the design principles of luminescent of Cr(III) complexes.

1.2 The principles of luminescence

Luminescence occurs when a molecule emits light following excitation of its ground state electron, this can happen via several processes including the use of light, chemical or mechanical excitation.[1] An excited electron relaxes back to its ground state with its excess energy released in a form of light which is called a photon.[2]

This thesis only considers photoluminescence and therefore the electrons in their ground states are excited with the use of light of an appropriate wavelength that matches the energy gap between the ground state and the excited state. This is pivotal for observing photoluminescence as the excited states are not thermally accessible. Photoluminescent molecules are known as luminophores.[2]

Furthermore, all electronic transitions are vertical as outlined by the Franck-Condon principle; the femtosecond timescale of an electronic transition does not provide enough time for the nuclei coordinates to respond to the electronic changes such as an electron in its ground state being photoexcited. Therefore, a transition from the ground state is likely to be to a first spin-allowed excited state, namely S_1 as illustrated in a Jablonski diagram (**Figure 1.1**).[3] Spin-allowed transitions occur without the electron changing its spin orientation.[3] Upon absorption of light, an electron is likely to be excited to one of the vibrational levels of the first spin-allowed excited state as indicated by the red arrow to the right in **Figure 1.1**. Excitation to a higher vibrational excited state is not stable and internal conversion (IC) to the lowest excited state occurs from all vibrational levels of higher energy via a loss of heat (Kasha`s rule).[4]

An electron populating the lowest vibrational level of the lowest lying spin allowed excited state (S_1) can either relax back to the ground state via fluorescence (Fl; lifetime < 10 ns) or can undergo intersystem crossing (ISC) during which the electron changes its spin to occupy a triplet excited state (T_1). Intersystem crossing (ISC) is possible for systems for which spin-orbit coupling is observed and occurs on a femtosecond scale. Relaxation from the triplet state is formally forbidden, due to the opposite spin orientation, resulting in emission lifetimes in the range of ns-s.[2,4] ISC results in additional energy loss as the newly populated triplet state lies below the singlet excited state as illustrated in **Figure 1.1**. Emission from the triplet state via a spin-forbidden relaxation pathway is known as phosphorescence (Phos).[3,4,5] Luminescence is characterised by the emission peak maxima, its quantum yield, and a lifetime, all of which are discussed further in this chapter.
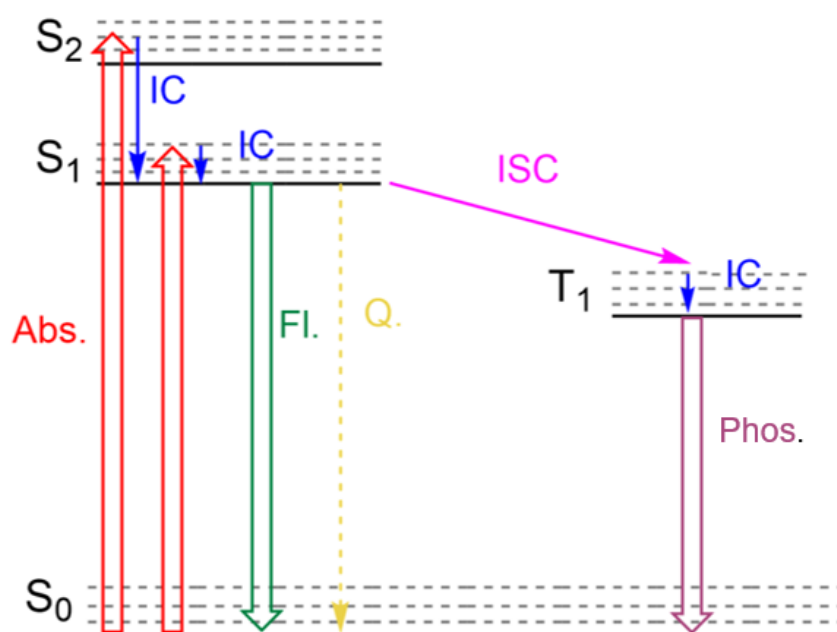
Figure 1.1 Simplified Jablonski diagram. Broken lines signify vibrational levels. Abs - absorption, IC - internal conversion, Fl - fluorescence, Q - quenching, Phos – phosphorescence, ISC – intersystem crossing.

1.2.1 Emission measurement

Emission wavelength can be measured utilising a steady-state method where a constant illumination of the sample using a flash-lamp takes place. This generates a steady excited state resulting in constant emission which can be then detected.[6] Emission can be measured in solution (aerated or deaerated) or in solid state.

1.2.2 Quantum yield (Φ)

Quantum yield, denoted Φ, measures the efficiency of the emission process. It is usually represented by a percentage value or a decimal number, and is a ratio of the rate of radiative decay to the sum of the radiative and non-radiative decay rates. It is also defined as the ratio of photons out (i.e. emission) over the photons in (i.e. absorption), therefore shows that the quantum yield is independent of the energy of the photons and only describes their respective populations. It appears, from **Equation 1.1**, where ϕ is the quantum yield of a luminophore, k_r is the rate of the radiative decay by the luminophore and k_{nr} is the rate of the non-radiative decay, that large contributions from the non-radiative pathways are detrimental to quantum yields.[2] When considering the ligand design of organometallic emitters, it is therefore important to appreciate all potential non-radiative pathways capable of deactivating the excited state and how they can be prevented by the ligand and the resulting geometry.

$$\phi = \frac{k_r}{k_r + k_{nr}} \qquad (1.1)$$

Quantum yield is measured using known standards by integrating the area under the curve (AUC) of the recorded emission band and the corresponding AUC of the known standard whilst also taking into account the relative absorption values for each species and the refractive index of the solvent for the sample and the standard (see **Equation 1.2**), where S is the AUC of the emission spectrum of the sample, A is the sample absorbance at the excitation wavelength and n is the refractive index of the solvent used). Parameter denoted with subscript $_R$ describes the same parameters for the standard.[2]

$$\varphi = \varphi_R \frac{S}{S_R} \frac{A_R}{A} \frac{n^2}{n_R^2} \quad (1.2)$$

Quantum yield can be quenched by many pathways including back-intersystem crossing (BISC), multiphoton relaxation and solvent/oxygen quenching which are discussed in **Section 1.2.5**.[2,3]

1.2.3 Lifetimes

Another method used to measure the efficiency of the emission is a time-resolved measurement of the lifetime, which is the amount of time it takes for the excited electron to relax back to its ground state. For measurements of phosphorescence, a laser flash excites the molecule and after a short delay time (10 ns), the relaxation is recorded as pictured in **Figure 1.2**. The delay time eliminates background fluorescence of which lifetimes are <10 ns. This process is repeated multiple times known as the number of counts (~10 000) and allows to generate a histogram of events against time (also known as multichannel scaling). It is necessary to avoid re-excitation until after the complete decay of the species to ensure that the excited states are allowed to fully relax back to the ground state before the sample can be excited again. The lifetime value is related to the quantum yield and is a reciprocal of the total value of the radiative (k_r) and non-radiative (k_{nr}) decay rate (**Equation 1.3**).[7]
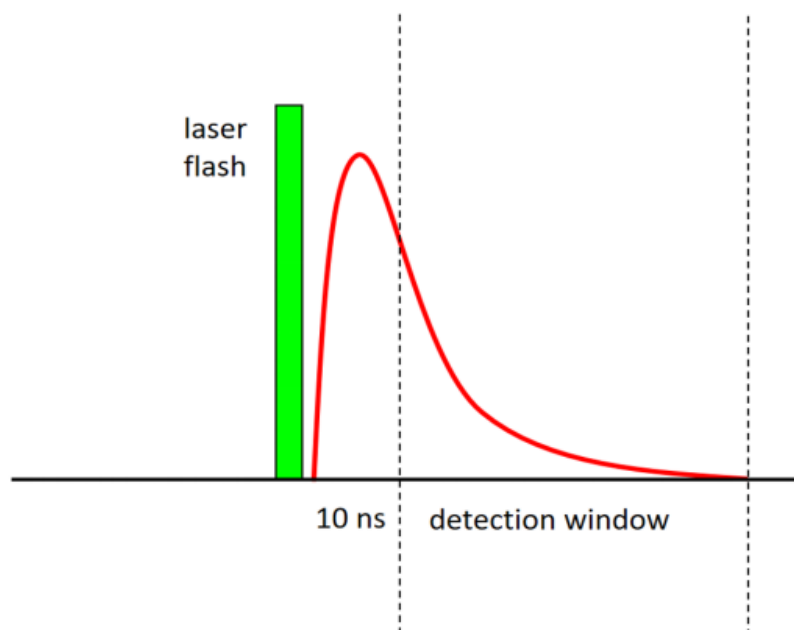
Figure 1.2 Depiction of the lifetime measurement procedure. The flash-lamp excites the sample and after a 10 ns delay, as indicated, the relaxation time of the excited state is measured.

$$\tau \ = \ \frac{1}{k_r + k_{nr}} \qquad (1.3)$$

A definite advantage is that lifetime as an intrinsic molecular property is independent of the sample concentration. Notably, a time-correlated single photon counting method (TCSPC) removes the risk of fluctuations of the intensity of excitation source making this type of measurement easily reproducible.[8] The lifetime values detected are influenced by non-radiative decay pathways in a comparable way to the quantum yield measurement. The more efficient are the non-radiative decay pathways, the shorter the lifetime.

Importantly, organic luminophores often cannot offer lifetimes longer than 10 ns due to the singlet nature of their excited states and therefore spin-allowed relaxations,

however heavy atoms that induce efficient spin-orbit coupling such as transition metal complexes tend to be superior when considering the long-lived luminophores.[2]

1.2.4 Stokes shift

Stokes shift is the difference in energy between the absorption and emission wavelength. Due to the singlet nature of the initially populated excited states and therefore small energy gap between the ground state and the singlet excited state evidenced by a small difference between the absorption and the emission band maxima, organic luminophores often offer very small Stokes shifts and therefore metal complexes are a better choice. Large Stokes shifts can prevent self-quenching; that is when emission of one molecule can excite another molecule for which the energy gap matches the emission of the molecule initiating self-quenching and therefore preventing radiative decay. For luminophores which are used for imaging of biological tissue self-quenching poses an issue. Large Stokes shifts help address this to the point where it becomes irrelevant due to the generous difference between the emission and the absorption bands maxima. [3, 6] This is because of the energy loss resulting from inter-system crossing as described earlier in this section and therefore a smaller energy gap between the ground state and the excited state. Emission/absorption energies are reported in wavenumber (cm^{-1}), therefore naturally smaller energy gaps offer larger differences in wavelength between the absorption and the emission band maxima.
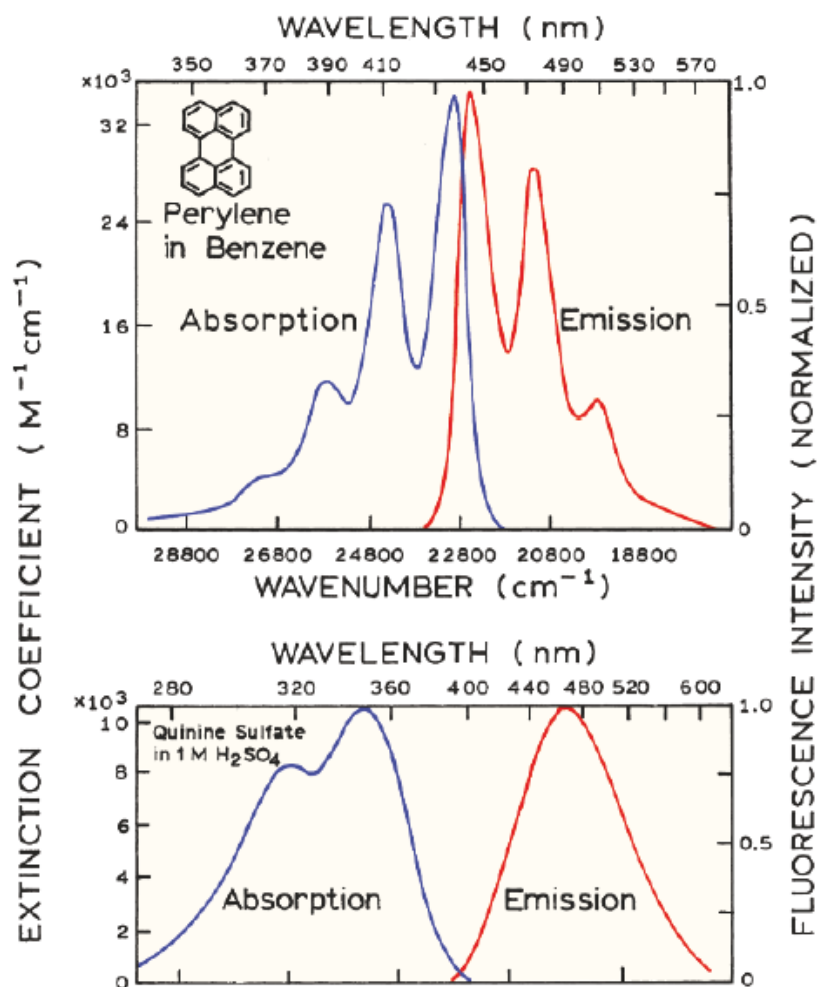
Figure 1.3 A comparison of a small Stokes shift (top) and a large Stokes shift (bottom) [adapted from ref 2].

1.2.5 Quenching

As discussed in **Section 1.2** on the principles of luminescence, the intensity of the emission can be reduced by a process known as quenching, which contributes to the non-radiative decay constant, k_{nr}. It most commonly occurs when in solution known as collisional quenching; it is when the excited state comes into direct contact with another molecule leading to the deactivation of the excited state by energy transfer.[2] Self-quenching discussed in **Section 1.2.4** is also a type of collisional quenching.

1.2.6 Deactivation of the excited state by molecular oxygen

One of the most damaging examples of collisional quenching is that of molecular oxygen. Nearly 21% of the atmospheric air consists of molecular oxygen and it is discernible that its presence within solvents largely affects quantum yield and lifetime values. In its ground triplet state ($^3O_2$) oxygen takes part in energy transfer of the excited state of the luminophore and forms its excited singlet state ($^1O_2$), therefore, leading to a simultaneous non-radiative decay of the luminophore based excited state.[1,2] This is demonstrated with the dashed arrow in **Figure 1.4**.
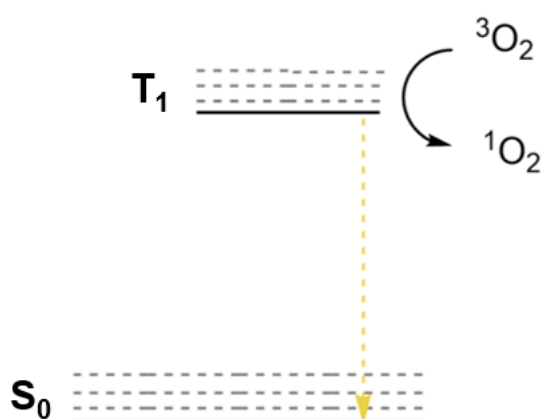
Figure 1.4 Fragment of an energy level diagram depicting deactivation of T_1 excited state by molecular oxygen. The dashed arrow signifies non-radiative decay of an electron simultaneous to scavenging of the energy by the triplet oxygen.

To eliminate the influence of molecular oxygen on photophysical properties, it is common practice to carry out measurements of the quantum yield/lifetime in solvents which have been previously deaerated or at low temperature (77 K) to give a frozen solvent matrix.

1.3 Chromium(III)

Chromium was first discovered in 1797 by treating $PbCrO_4$ (crocoite) with hydrochloric acid to isolate chromium(III) oxide (Cr_2O_3) and was achieved by a French chemist Louis Nicolas Vauquelin.[9,10] He was also able to reduce chromium(III) oxide to elemental chromium with charcoal a year later.[12] A procedure for isolating pure elemental chromium (albeit impure) by combining chromium(III) oxide with elemental aluminium and exposing the mixture to 2100 °C heat was discovered nearly 100 years later by Goldschmidt. This process is known as an aluminothermic reaction.[11, 12]

Today, chromium is known to be available in three forms, namely chromite, crocoite and chromium(III) oxide. The dark grey to black chromite is often contaminated with Mn(II) or Fe(III) and the purest forms found consist of 68% Cr_2O_3 and are very rare to obtain due to natural displacement of Cr(III) by other metals.[13,14] Its abundance in the Earth`s crust is estimated to be nearly 135 ppm as opposed to more expensive metals such as iridium(III) for which the abundance is estimated to be $\sim 3.7 \times 10^{-5}$ ppm.[15,16] This demonstrates chromium as the more sustainable metal in this comparison. Chromite undergoes conversion to dichromite, a known starting material for obtaining chromium salts and elemental chromium.[17]

Initially, chromium compounds such as green chromium(III) oxide (Cr_2O_3), chrome red ($PbCrO_4 \times PbO$) and chrome yellow ($PbCrO_4$) were used as dyes with the latter being a component in the yellow paint used for American school buses.[15, 18, 19] Nowadays, these applications extend to chromising (protecting other metals with an alloy coating) and the production of stainless steel.[20]

Most importantly, the first ruby (Al_2O_3) lasers were produced in 1960 with a Cr(III) dopant of which the spin-forbidden transitions (see **Section 1.4.1**) were responsible for the emission maximum ~700 nm with lifetime in the microsecond range.[21]

1.3.1 Photophysics of Cr(III)

As illustrated in **Figure 1.5**, the ground state of an octahedral chromium(III) centre with an electron configuration of d^3 is $^4A_2$, according to Hund`s rule.[22] Upon excitation, an electron is promoted to one of the three spin-allowed excited states $^4T_2$, $^4T_1$(F), $^4T_1$(P) (F,P – term symbols, not illustrated in **Figure 1.5**. When the transitions are probed via UV-Vis measurements, only the first two transitions ($^4A \rightarrow {}^4T_2$, $^4A \rightarrow {}^4T_1$(F)) are usually observed, with the third transition ($^4A \rightarrow {}^4T_1$(P)) often obscured by charge transfer transitions.[25] The $^4T_1$(F) excited state undergoes a fast non-radiative relaxation to the $^4T_2$ excited state via internal conversion.
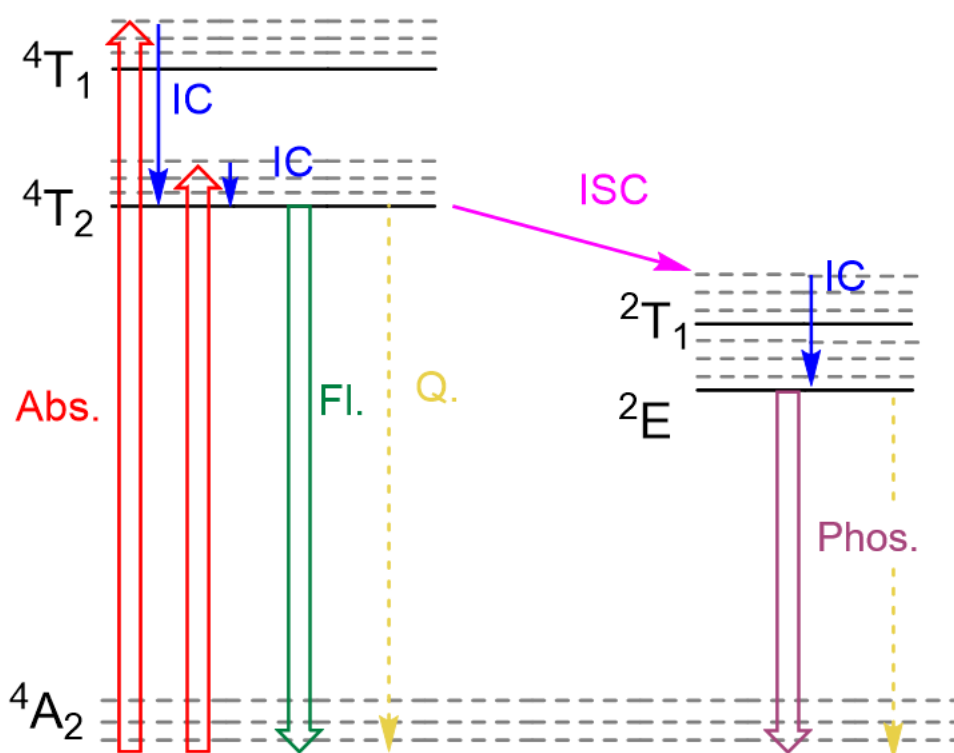
Figure 1.5 Jablonski energy level diagram for octahedral Cr(III) with ground state ($^4A_2$) and two doublet excited states (^2E and $^2T_1$) illustrated to its right. Broken lines signify vibrational levels. Abs - absorption, IC - internal conversion, Fl - fluorescence, Q - quenching, Phos – phosphorescence, ISC -intersystem crossing.

Relaxation back to the ground state ($^4A_2$) from the $^4T_2$ excited state is fast (<10 ns) and not commonly observed in solution at room temperature, however the photoexcited electron that initially occupies the $^4T_2$ can undergo intersystem crossing facilitated by

spin-orbit coupling to promote a population of two doublet excited states illustrated in **Figure 1.5**, namely $^2T_1$ and ^2E. Notably, the multiplicity of the Cr(III) excited states changes from a quartet to a doublet when the spin of the electron changes. Relaxation from the doublet excited states is a spin-forbidden transition, and it takes considerably longer (microsecond range) than that of quartet excited state. This presents to be an important point in the chemistry of luminescence for chromium(III) chemistry systems.

The $^2T_1$ and ^2E doublet excited states are thermally equilibrated at room temperature and the emission bands of octahedral complexes typically present as one sharp band (originating from the ^2E state) with a broad shoulder to its side (assigned to $^2T_1$ emission) at room temperature as illustrated in **Figure 1.6**, whereas two sharp bands can be resolved as the temperature decreases (170 to 130 K). The sharp appearance of the emission band assigned to ^2E relaxation is explained by t_2g^3 configuration of both the ground state $^4A_2$ and ^2E excited state introducing only a very small difference in geometry and vibrational levels of both states, whereas the emission band assigned to $^2T_1$ relaxation is observed as a broad band resulting from a significant difference in the geometry of the ground state ($^4A_2$) in comparison with the excited state ($^2T_1$) (**Figure 1.6**).[23]
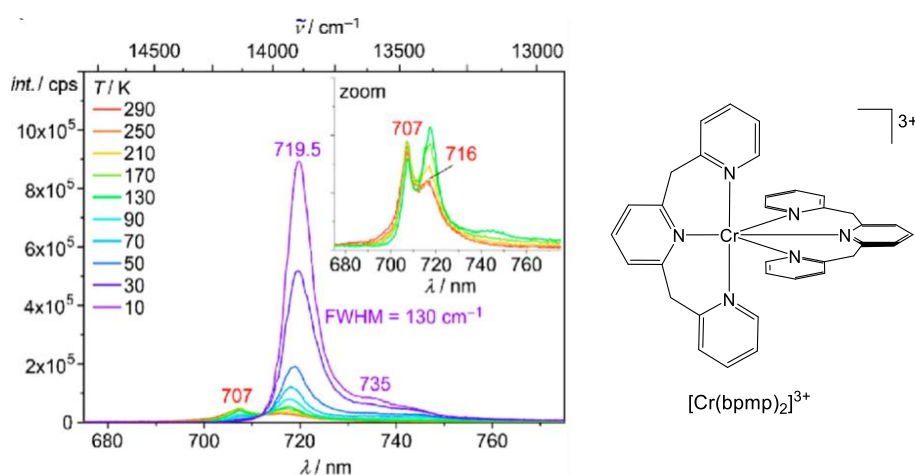
Figure 1.6 A temperature study illustrating the influence of the temperature at which the emission measurement takes place on the appearance of the doublet excited state emission band of [Cr(bpmp)$_2$]$^{3+}$ [Adapted from ref 23].

Broadening of the otherwise sharp doublet excited state emission bands of Cr(III) is observed for complexes with distortion towards D_{4h} symmetry. Splitting of the energy levels is the consequence of this, and is illustrated in **Figure 1.7**. For the ^2E energy level, two new energy levels appear from the split, namely the degenerate $^2A_1$ and $^2B_1$ states. Similarly, the $^2T_1$ state also splits into two upon distortion towards D_{4h} symmetry, creating the new non-degenerate ^2E and $^2A_2$ states. The ^2E state is the lowest lying doublet state. The emission bands resulting from the quadrate splitting are not only broad, but also red-shifted and featureless which directly reflects the changes in geometry for ground and excited states which can lead to state mixing/non-radiative deactivation of the excited states via BISC as the doublet/quartet states start to overlap.[23]
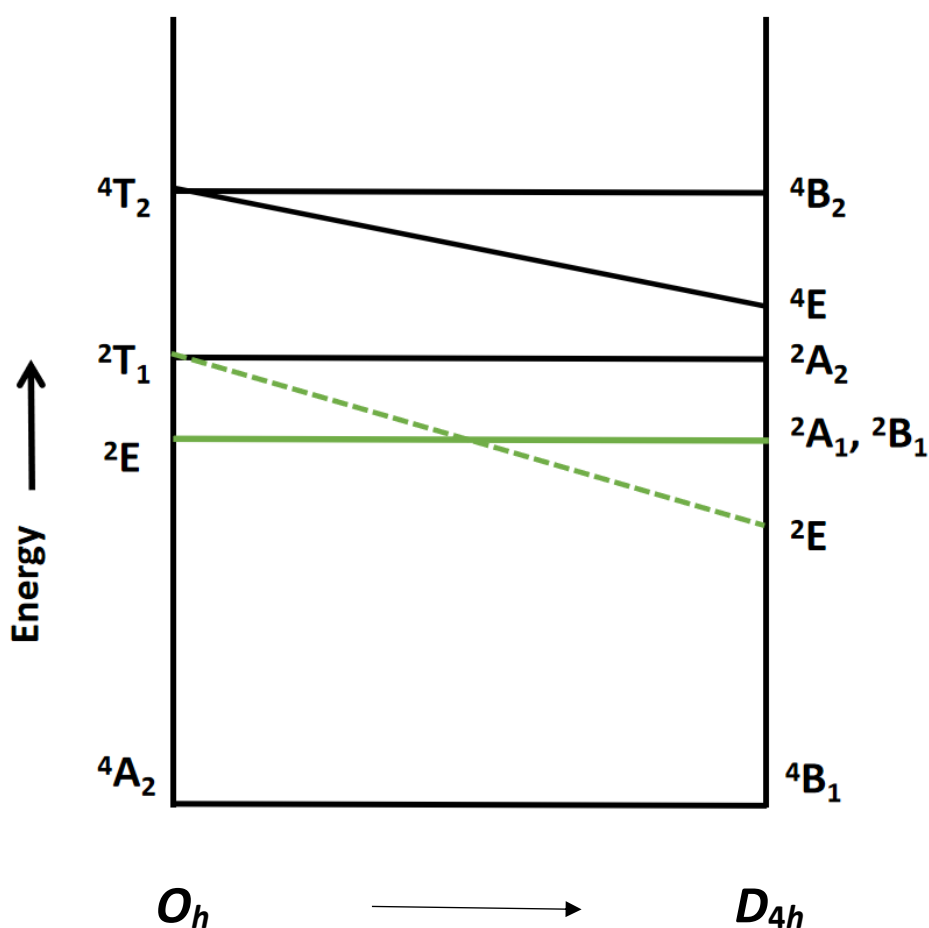
Figure 1.7 An energy level diagram showing the splitting of distorted O_h states.

Upon consideration of the simplified Tanabe-Sugano diagram for a d^3 species **Figure 1.8**, the relative energies of the $^2E/^2T_1$ are not largely dependent on the ligand field splitting energy (Δ_o). As the Δ_o increases, the energy of the $^2E/^2T_1$ remains relatively the same, except for the slight increase between 0 and 10 Δ_o/B. Therefore, most $^2E/^2T_1$ emission bands for Cr(III) complexes are observed around 650-700 nm.
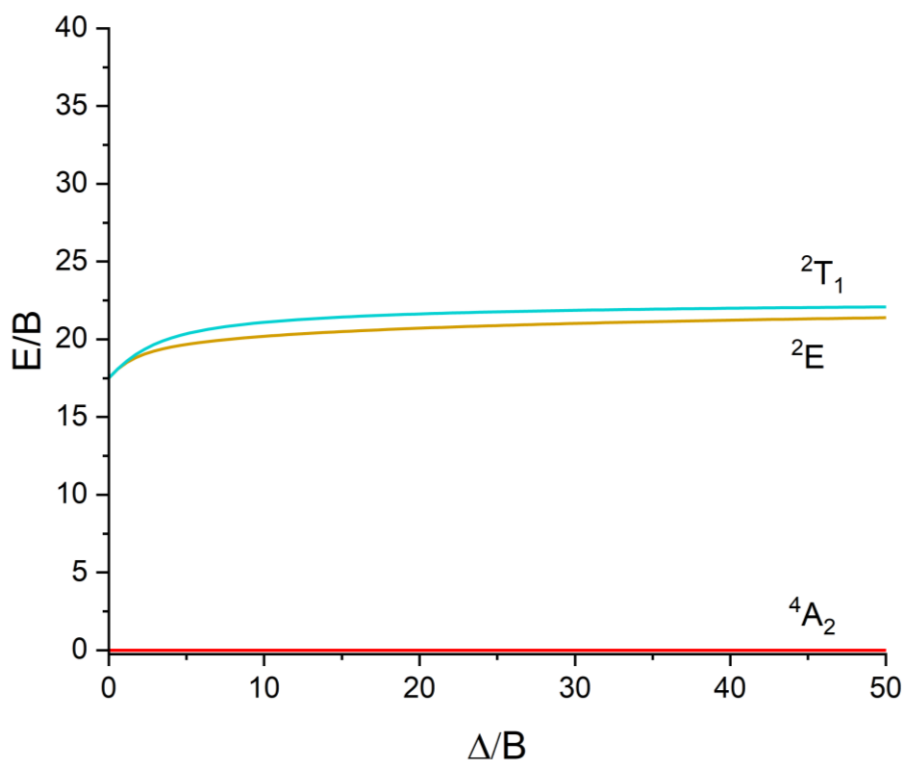
Figure 1.8 Simplified Tanabe-Sugano diagram for a d^3 system, [Reproduced from ref 24]. The ground state $^4A_2$ is not demonstrated, however it resides at $E/B = 0$ across the x-axis. [24]

Nevertheless, tuning of the $^2E/^2T_1$ state emission colour is possible by reducing the inter-electronic repulsion between the three unpaired electrons and is called the nephelauxetic effect. Ligands presenting strong nephelauxetic effects have low-lying π^* anti-bonding orbitals which by accepting the d-electrons cause delocalisation of the d-electron density and reduce in electron repulsion within the metal.[25] Some evidence of the nephelauxetic effect is observed in **Table 1.1**, which is reflected directly in the emission maxima of the complexes which are red-shifted from the 650-700 nm range mentioned earlier. The structures of the complexes can be seen in **Figure 1.9**. Importantly, $[Cr(tpda)_2]^{3+}$ is an example of a six-membered chelate for which a more

significant red-shift is observed than for the two corresponding five-membered chelates, namely $[Cr(bpy)_3]^{3+}$ and $[Cr(tpy)_2]^{3+}$. This is a result of geometry closer to octahedral in comparison with $[Cr(bpy)_3]^{3+}$ and $[Cr(tpy)_2]^{3+}$.

Table 1.1 Literature examples of emission maxima of three Cr(III) complexes. d – deaerated solvent.

	Emission wavelength (nm)	Ref.
$[Cr(bpy)_3]^{3+}$	728	26
$[Cr(tpy)_2]^{3+}$	770	27
$[Cr(tpda)_2]^{3+}$	782	28
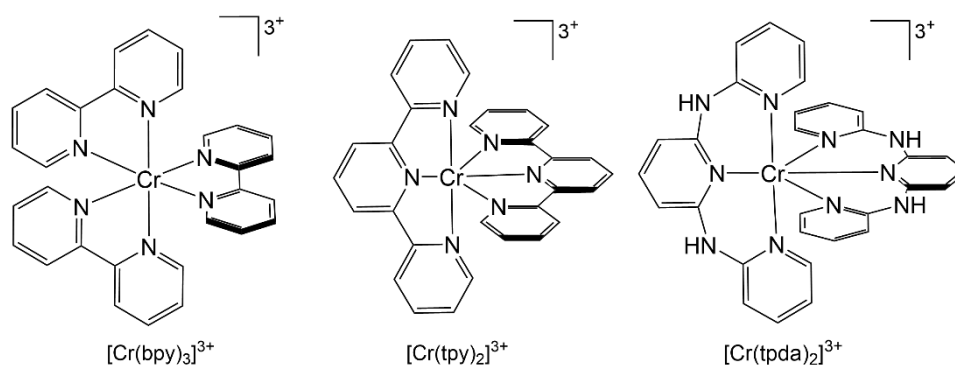
Figure 1.9 Structures of the complexes presented in **Table 1.1**

The nephelauxetic effect can also be induced by incorporating amine type coordination at the metal centre with the cyclam ligand having the strongest effect in the series $NH_3 <$ en $<$ cyclam, although this method seems to have a lesser effect compared to the effect of low-lying π^* antibonding orbitals accepting the d-electrons density.[21]

The nephelauxetic effect can be measured by defining the nephelauxetic effect parameter (ζ). It is defined by the comparison of the Racah parameter (B) of the investigated complex against the magnitude of B for the free Cr(III) ion, which represents the highest level of interelectronic repulsion at the Cr(III) centre in its free state and is defined to be 918 cm^{-1}.[29]

Surface crossing is a known deactivation pathway of the doublet excited state, and it occurs when distortion of the doublet excited state (^2E) leads to its overlap with the ground state ($^4A_2$) leading to a quick non-radiative decay, as the ground state becomes thermally accessible, shown in **Figure 1.10**. Such distortion might be an effect of trigonal twisting, commonly observed for bidentate ligand coordination leading to trigonal prismatic geometry.
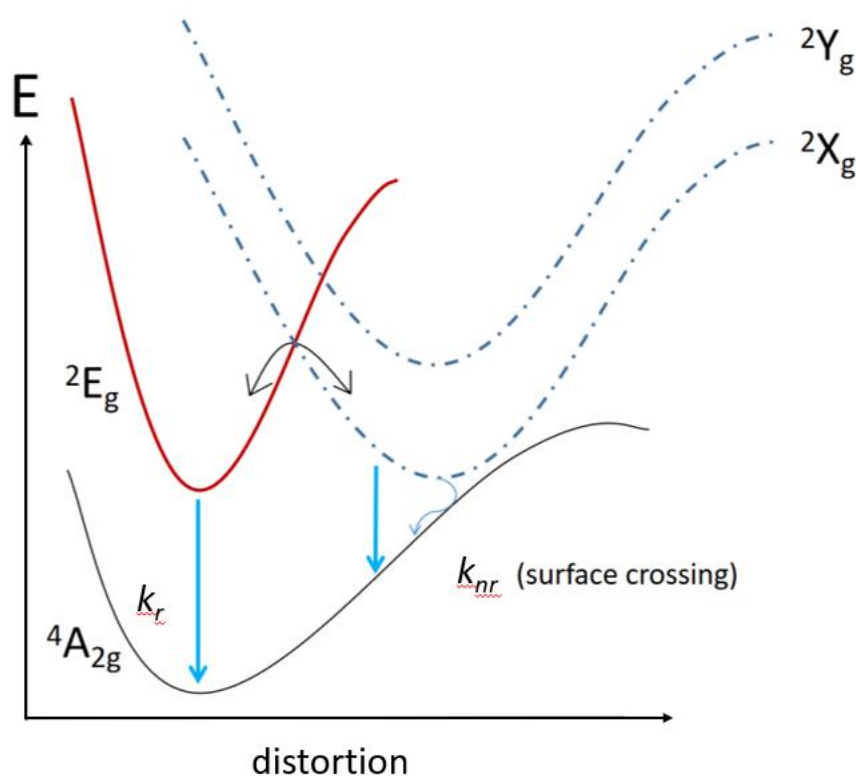
Figure 1.10 Energy diagram of surface crossing in Cr(III) complexes. k_r is radiative decay constant, k_{nr} is non-radiative decay constant.

To prevent surface crossing, it is necessary to assess the potential geometry of the complex during the design process. Previous reports in the literature suggest that ligands with six-membered chelate rings rather than five-membered chelate rings might prove advantageous in sustaining the near perfectly octahedral geometry.[30]

Another common non-radiative decay pathway is an electronic-to-vibrational energy transfer from the doublet excited state to the high-energy oscillators such as N-H, O-H, C-H of the ligand or the surrounding solvent as presented in **Figure 1.11**.
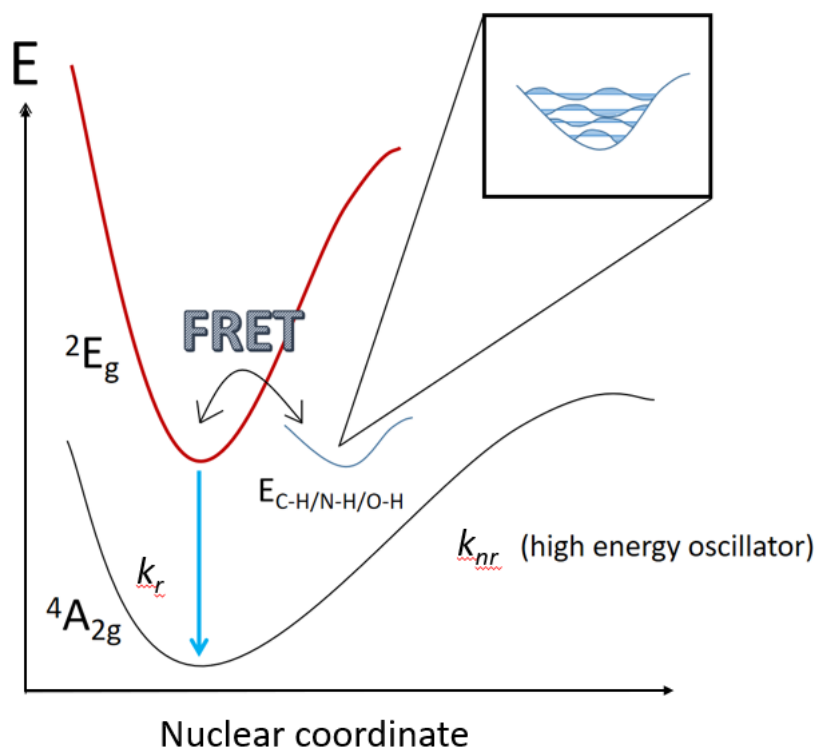
Figure 1.11 Energy level diagram representation of energy transfer between ^2E and high energy oscillators. k_r is radiative decay constant, k_{nr} is non-radiative decay constant, $E_{C-H/N-H/O-H}$ is the energy level of the high-energy oscillator.

All this is possible due to the match in energy between the doublet excited state and overtones of high-energy oscillators within close proximity of the metal centre as pictured in **Figure 1.10**. This energy transfer is analogous to Forster Resonance Energy Transfer (FRET) and is strictly dependent on the distance between the donor (Cr(III)) and the acceptor (C-H/O-H/N-H) with the efficiency being inversely proportional to the sixth power of the donor-acceptor distance.[31] It is therefore a dipole-dipole interaction between the doublet excited state and an anharmonic oscillator.[32] According to the inductive-resonant theory, the rate of non-radiative deactivation is

proportional to the spectral overlap integral (SOI) of the interaction between the doublet excited state and the anharmonic oscillator.[33]

It is common in the literature to suggest deuteration to prevent this particular non-radiative decay pathway. As deuterium is heavier than hydrogen, the frequencies of C-D oscillations are much lower therefore removing the energy gap match between the doublet excited state and the C-D oscillators.[34]

Seitz *et al.*, reported experimentally accessible vibrational overtones of C-H(D) oscillators of pyridines as a basis for understanding the location of the overtones for pyridyl-type ligands. The fourth and fifth overtone (C-H) absorption bands have values of approximately 11250 cm^{-1} (889 nm) and 14050 cm^{-1} (712 nm) showing considerable overlaps with the doublet excited state emission profiles of Cr(III) complexes. Importantly, the fifth and sixth overtones of C-D oscillator show values of approximately 10800 cm^{-1} (925 nm) and 12800 cm^{-1} (781 nm). This example therefore indicates, that deuteration does not necessarily prevent the doublet excited state from deactivation in case of significantly red-shifted Cr(III) emission bands. Chapter 4 will demonstrate Cr(III) complexes emitting in the region ~900 nm and therefore showing good overlap with the fifth overtone of C-D oscillator of pyridine.

1.4 Design of Luminescent Cr(III) complexes

1.4.1 Crystal Field Theory (CFT)

Transition metal complexes consist of a metal ion and a number of ligands coordinated to it via coordinative dative bonds.[35] The lone pair of the ligand is described as a partial charge of an electric dipole or a point negative charge which repels the electrons occupying the d-orbitals of the metal ion. Therefore, ligands coordinate to the metal ion by donating their lone pair of electrons as δ^- or π-donors and by accepting some of the electron density into their anti-bonding orbitals due to their π-acceptor character.[36]

Crystal field theory describes how the nature of the coordinating ligand influences the splitting of d-orbitals of the metal ion which helps the analysis of optical and electronic spectra as well as the magnetic properties of the complexes.[37] For a six-coordinate octahedral complex the d-orbitals split into two non-degenerate groups where three non-bonding orbitals (namely - d_{xy}, d_{xz}, d_{yz}) of t_{2g} symmetry occupy the lower energy regime and the remaining two anti-bonding orbitals of e_g symmetry occupy the higher energy regime and are defined as $d_{x^2-y^2}$ and d_{z^2}.[36]

Crystal field splitting energy (Δ) is dependent on the charge of the metal, the principal quantum number and the field strength of a ligand and is used to rationalise the stability of metal complexes.[37] In octahedral complexes, the crystal field splitting energy is denoted as Δ_o and since it is dependent on the field strength of the coordinated ligand, careful ligand design enables tuning of the photophysical properties. Strong field ligands provide a larger Δ_o, whilst weak field ligands provide a small energy gap. The spectrochemical series which defines the ligand field strength, and the corresponding magnitude of the crystal field splitting can be seen in **Figure 1.12** with Br$^-$ as the weakest field ligand and CO presented as the strongest field ligand in the series.

Br$^-$ < Cl$^-$ < NO$_3^-$ < F$^-$ < H$_2$O < NCS$^-$ < pyr < NH$_3$ < bpy < phen < NO$_2^-$ < PPh$_3$ < CN$^-$ < CO

Poor δ-donor   Good δ-donor
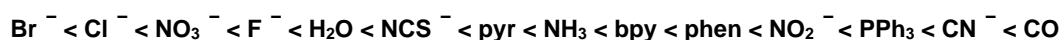
Good π-donor   Good π-acceptor

Weak field   Strong Field

Small Δ$_o$ Large Δ$_o$

Figure 1.12 Spectrochemical series

Polydentate ligands, such as 2,2ʹ-bipyridine or 1,10-phenanthroline, are known to increase the thermodynamic stability of the resulting complex via the chelate effect.[38] The thermodynamic stability can be measured with the Gibbs free energy of a system (ΔG), where low ΔG leads to higher stability (**Equation 1.4**).

$$\Delta G = \Delta H - T\Delta S \quad (1.4)$$

Increased entropy (ΔS) favours polydentate ligands as increasing in the denticity of a ligand also increases the molar equivalents of the reaction product. The enthalpy (ΔH) represents breaking each of the bonds of the polydentate ligand to fully dissociate from the metal ion; the energy required for complete dissociation of a polydentate ligand is greater than the energy required for dissociation of a monodentate ligand.[40] As discussed in **Section 1.4.3**, [Cr(bpy)$_3$]$^{3+}$/[Cr(phen)$_3$]$^{3+}$ complexes present water sensitivity and it is likely that tridentate ligands can provide Cr(III) complexes of increased stability as previously reported for [Cr(ddpd)$_2$]$^{3+}$ which is substitutionally inert.[39]

1.4.2 Hard and Soft Acid and Base Theory (HSAB)

Hard and soft acid and base theory describes what acids and bases are more likely to interact with each other. A central metal ion can accept an electron pair and therefore is defined as a Lewis acid whereas the coordinating ligand acts as a Lewis base based on their ability to donate electrons via dative bonds.[40] In this discussion, ligands will be referred to as hard or soft bases, whilst the metal ion will be described as the acid.

The classification of hard/soft acids and bases depends on three main factors: a) charge-to-size ration, b) polarisability and c) the nature of the interaction (covalent vs. ionic). Based on this information, two HSAB theory categories can be created:

Hard Acids/Bases:

- Hard acids: typically, metal ions with high charge-to-size ratio such as Cr(III).
- Hard bases: small anions/neutral molecules including the second-row heteroatoms such as N, O, F.

Soft Acids/Bases:

- Soft acids: transition metals with a single positive charge such as Cu^+. Soft acids include second and third row metals with single or double positive charge and late transition metals.
- Soft bases: large anion and neutral molecules such as I^- or S^{2-}.

A borderline group between the soft/hard acids/bases includes acids and bases with intermediate character such as Fe^{2+} or Pb^{2+} for intermediate acids, and pyridine/aniline as intermediate bases.[41]

Notably, very subtle differences determine whether species are assigned soft or hard. For instance, N atom is considered hard in an amine group but as mentioned earlier, pyridine resides in the borderline group due to the increased polarisability introduced by the aromatic ring.[42]

Considering the interaction between the acids and the bases, a general rule of thumb is that like binds with like, i.e. hard acids bind with hard bases, and soft acids bind with soft bases. As illustrated in **Table 1.2**, hard acids bind fluoride better than iodide, whereas for soft acids an opposite trend follows. This is based on the value of log K_1 which is an equilibrium constant for the formation of a complex in solution, where a higher value represents a higher yield of complex formation. [42,43,44]

Table 1.2 Representation of the interactions between soft/hard acids and soft/hard bases using log K_1 as a measure of the interaction.

	fluoride	chloride	bromide	iodide	classification
Fe^{3+}	6.0	1.4	0.5	-	hard
Pb^{2+}	1.3	0.9	1.1	1.3	borderline
Ag^+	0.4	3.3	4.7	6.6	soft
Hg^{2+}	1.0	6.7	8.9	12.9	soft

As a metal ion with a high charge-to-size ratio, Cr(III) is a hard acid and therefore is more likely to bind hard/borderline bases such as amines or pyridines. Most common synthetic strategies for the synthesis of Cr(III) complexes are discussed in **Section 1.4.3**.

1.4.3 Synthesis

1.4.2.1 Kinetic lability of CrCl$_2$.

It appears that CrCl$_2$ is a common starting material for obtaining Cr(III) complexes due to its favourable reactivity.[47,48,51,52] As illustrated in **Figure 1.13**, CrCl$_2$ can be stirred at room temperature in the presence of bpy excess under inert conditions to form [Cr(bpy)$_3$]$^{2+}$. The lability of ligands coordinated to the Cr(II) metal centre results in a very rapid ligand exchange and therefore short reaction times. This is due to the differences in energies of the electrons occupying d-orbitals of the Cr(II) as opposed to Cr(III).[45] Additionally, Cr(II) complexes are Jahn-Teller distorted resulting in weaker bonds and therefore lower activation energy of ligand exchange. The resulting [Cr(bpy)$_3$]$^{2+}$ can then be rapidly oxidised to deliver [Cr(bpy)$_3$]$^{3+}$ under aerobic conditions. The ligand field stabilisation energy of Cr(II) is $-0.6\ \Delta_o$ as

compared to $-1.2\,\Delta_o$ for Cr(III) which shows that in the octahedral field, Cr(III) is more stable.[46]
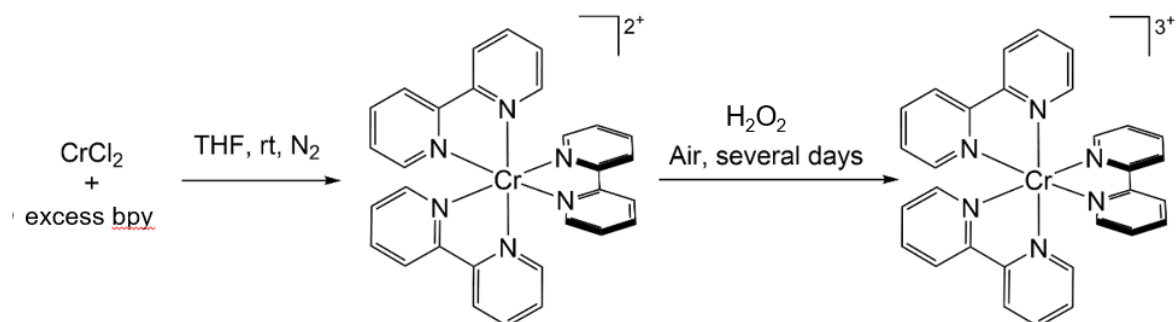
Figure 1.13 Synthetic route for Cr(III) complexes using $CrCl_2$ as the starting material.

$CrCl_3$ possesses three unpaired electrons which occupy three degenerate d-orbitals with its electron configuration described as t_{2g}^3, e_g^0, whereas $CrCl_2$ possesses one additional electron which occupies a d-orbital higher in energy to the three degenerate d-orbitals just described, and its configuration is described as t_{2g}^3, e_g^1. This therefore suggests higher reactivity a of Cr(II) centre when compared with Cr(III). Additionally, the electrostatic attraction between the ligand and the Cr(II) centre is much weaker than that of Cr^{III}-L_n (where n states the equivalents of L coordinated to the metal centre) due to the charge differences and explains the kinetic inertness of Cr(III).[47] This is supported by the water exchange rate constant for the two metal ions. As illustrated in **Figure 1.14**, the rate constant for Cr(II) is determined to be around $10^9\,k_{H_2O}$ / s^{-1} (red hashed bar) representing a very rapid ligand exchange process, whereas for Cr(III) the value sits around $10^{-6}\,k_{H_2O}$ / s^{-1} (red solid bar) and appears very close to the water exchange rate for the Ru(III) metal ion, another example of a kinetically inert transition metal.[48]
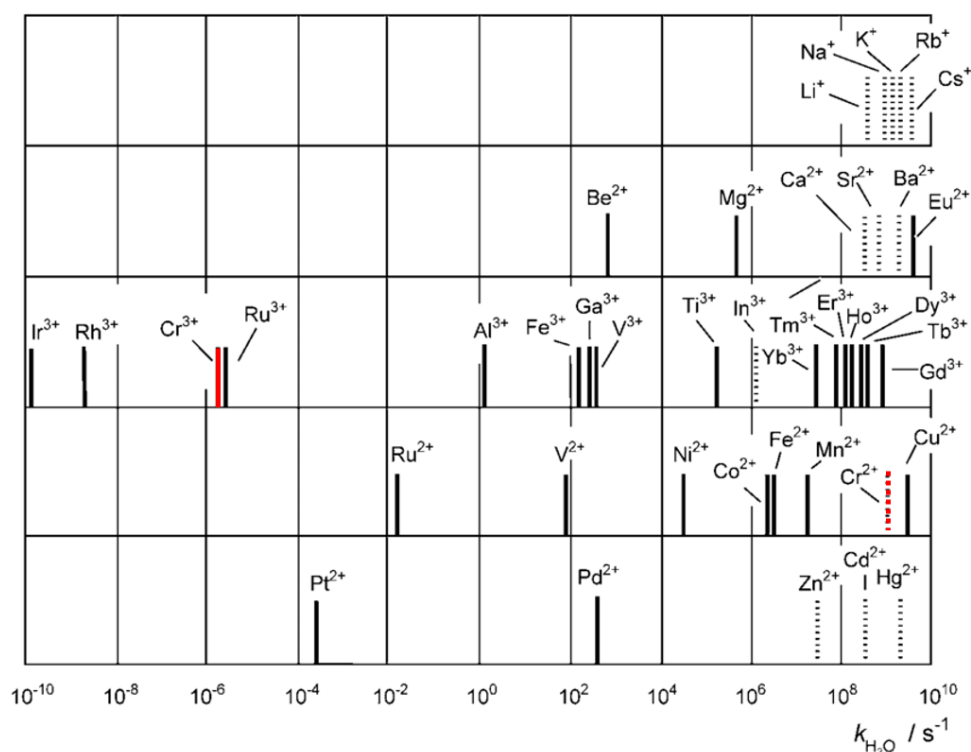
Figure 1.14 Water exchange rate constants for transition metals for the ligand exchange in the first coordination sphere. Bold bars signify values determined experimentally; hashed bars represent estimated values from ligand-substitution studies. Red solid bar indicates the water exchange rate constant for Cr(III), whilst red hashed bar indicates the water exchange rate constant for Cr(II).[52]

When CrCl$_2$ is employed as the starting material and the ligands of interest have been coordinated, the resulting complex requires subsequent oxidation to the +III oxidation state. This can be achieved via two methods. Firstly, the reaction can be allowed to stand in air for several days leading to an oxidation of the metal centre with molecular oxygen and can be observed by the colour change of the solution.[49] The second method uses hydrogen peroxide, if a shorter reaction time is desired, and is therefore a much faster approach. As presented in **Figure 1.15**, the oxygen within hydrogen peroxide scavenges an electron from the Cr(II) centre therefore oxidising it to Cr(III) and generating water along with molecular oxygen.[50]
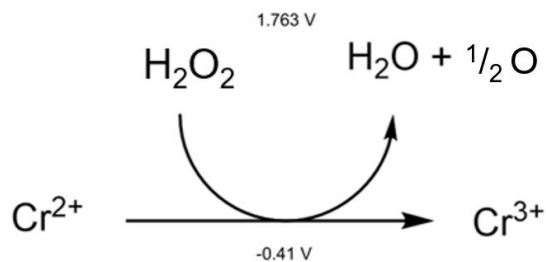
Figure 1.15 Oxidation pathway of Cr(II) when H_2O_2 is utilised. Potentials reported vs standard hydrogen electrode (SHE).

There are several challenges associated with this method. Firstly, $CrCl_2$ is air sensitive, therefore it must be handled in an oxygen free environment to ensure that a complete ligand exchange has taken place, prior to oxidation of the Cr(II) complex, to subsequently take full advantage of the increased reactivity of the Cr(II) centre. This requires dry and degassed solvents, which adds to the overall reaction preparation time. Reactions run in non-dry solvents afford $[Cr(H_2O)_x]^{2+}$ instead.[51] If handled improperly, only partial substitution with the desired ligand occurs and further ligand exchange following the oxidation of the metal centre is more challenging and requires harsh conditions due to the kinetic inertness of the Cr(III) centre.

1.4.2.2 Synthesis via Cr(III) starting materials

Due to the challenges associated with handling such sensitive material as $CrCl_2$, Schönle carried out a study on the applicability of $CrCl_3 \times 3H_2O$ as illustrated in **Figure 1.16**. The primary step was to reduce the Cr(III) centre to Cr(II) with catalytic amounts of Zn.[52] Upon generation of Cr(II) there were two routes that were tested. Firstly, the Cr(II) was further reacted with sodium acetate to improve the solubility and subsequently $[Cr_2(CH_3COO)_4(H_2O)]$ was formed which is an air stable Cr(II) intermediate.
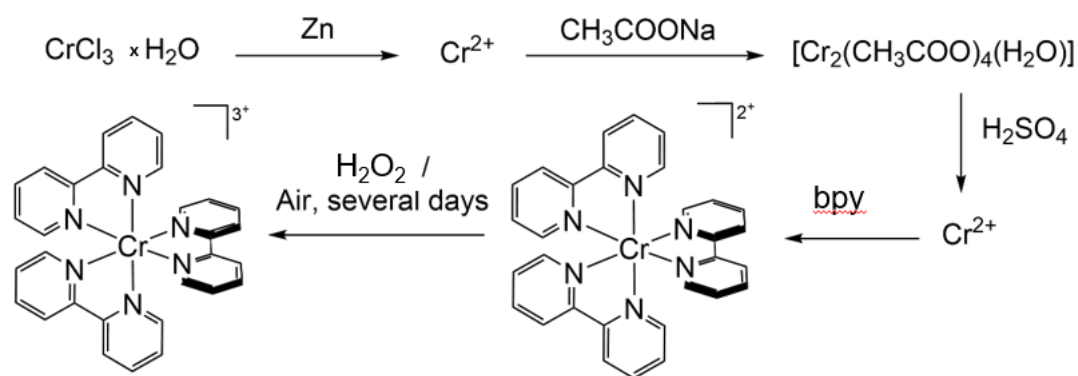
Figure 1.16 Route to Cr(III) complexes synthesis studied by Schönle.

This step was designed to take advantage of the kinetic lability of the Cr(II) by introducing an air stable intermediate and therefore potential for higher yields. The Cr(II) dimer was then treated with sulfuric acid and the free Cr(II) ion was further reacted with three equivalents of bpy. The resulting complex was then oxidised under air or with hydrogen peroxide.[53] Secondly, upon generation of Cr(II) ions with Zn catalyst, three equivalents of bpy were added and the resulting complex was oxidised using the same method as previously mentioned. Complexes obtained using both routes would have undergone counterion exchange to PF_6^- following the oxidation.[54] Unfortunately, none of the methods proved to be reproducible and therefore the Kane-Maguire method is introduced in the next section as a reproducible protocol for obtaining homo- and heteroleptic Cr(III) complexes.[55]

1.4.2.3 The Kane-Maguire procedure

The most popular method to produce Cr(III) polypyridyl complexes is the Kane-Maguire procedure (**Figure 1.17**).[56] The route starts with anhydrous $CrCl_3$ which is stirred along with two equivalents of the desired ligand in dry ethanol. Once the solvent reaches reflux, trace amounts of Zn powder are added. The reaction is almost instantaneous and only requires running under reflux for 1-2 hours. The solution is then cooled to obtain a precipitate which is the desired crude intermediate [Cr(N^N)$_2$Cl$_2$]. In the case of $CrCl_3$ stirred with two equivalents of bpy, the solution turns black/dark green upon reaction with Zn dust.
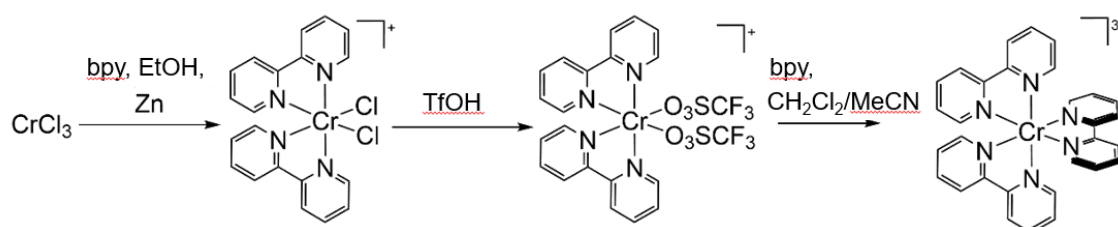
Figure 1.17 Kane-Maguire procedure for Cr(III) synthesis.

This is a crucial step for obtaining heteroleptic Cr(III) diimine complexes. The obtained powder can be recrystallised from H_2O followed by hot filtration where the desired intermediate precipitates out of the hot filtrate. [Cr(L)$_2$Cl$_2$] is then reacted with neat triflic acid (TfOH) to abstract the remaining chloride ions and substitute them with the equal equivalents of triflate ligand ($^-$OTf). Since, triflic acid is considered a superacid, it must be handled with great care; The resulting [Cr(L)$_2$(OTf)$_2$](OTf) can be used as a starting material for the preparation of heteroleptic Cr(III) complexes. It is often reacted with one equivalent of the ligand or alternatively with a slight excess of ligand, in solvents like MeCN or CH_2Cl_2. [56] This method has proven to be the most successful for generating Cr(III) polypyridyl complexes, however it has some challenges that are addressed in **Section 1.5.3**.

1.4.2.4 THF intermediate for tridentate ligands

Another common synthetic route for the synthesis of Cr(III) complexes uses *mer*-CrCl$_3$(thf)$_3$ as a starting material as outlined in **Figure 1.18**. First reported in 1958, it is prepared from CrCl$_3$ in THF with the aid of Zn dust.[57,58,59,60] *mer*-Cr(thf)$_3$Cl$_3$ can be reacted with ligands of interest in various solvents (THF, CH$_2$Cl$_2$, MeCN, EtOH, Toluene) at various temperatures (rt, reflux) to form [Cr(L)$_3$]$^{3+}$ complexes for neutral bidentate ligands and [Cr(L)$_2$]$^{3+}$ for neutral tridentate ligands. [61] Although not as sensitive as CrCl$_2$, *mer*-CrCl$_3$(thf)$_3$ is prone to hydration and therefore must be stored under inert conditions.
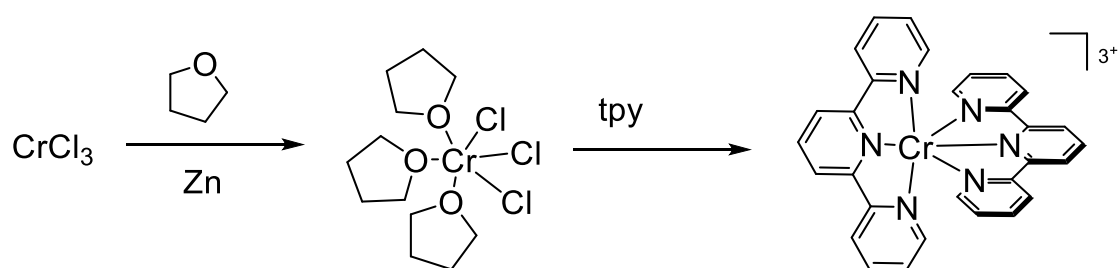
Figure 1.18 *mer*-CrCl$_3$(thf)$_3$ route to Cr(III) complexes.

1.4.3 Synthetic challenges

Polypyridyl complexes have been reported to be substitutionally labile under alkaline conditions resulting in the formation of hydroxido complexes as shown in **Figure 1.19**. The higher concentration of the OH$^-$ ions, the higher concentration of hydroxido species is formed. As indicated in **Figure 1.19**, two equivalents of $^-$OH are required for one hydroxido complex to be formed.
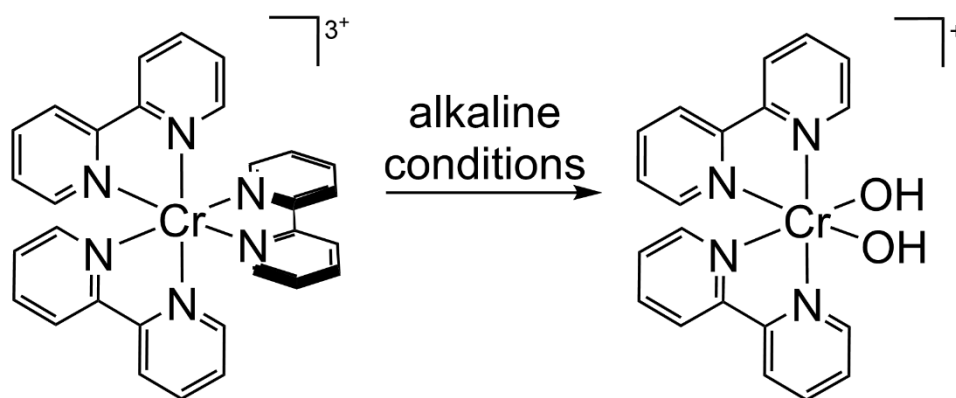
Figure 1.19 Generation of hydroxido species using $[Cr(bpy)_3]^{3+}$ as an example.

Furthermore, in relation to the sensitivity under the alkaline conditions of $[Cr(bpy)_3]^{3+}$ complexes, it was found that water molecules might compete with triflate ions during the substitution reaction in the Kane-Maguire method. Doistau *et al.*, reported that a reaction of $[Cr(phen)_2(OTf)_2]OTf$ with alkylated 1,10-phenanthroline afforded an off-white single crystal of the protonated ligand $[Cr(phen)_2(H_2O)(OH)](OTf)_2$ complex. To avoid hydrolysis, $[Cr(phen)_2Cl_2]Cl$ was dried under vacuum prior to its reaction with TfOH and $[Cr(phen)_2(OTf)_2]OTf$ was used directly after synthesis. In addition, a sacrificial base was used during the last reaction step to trap an excess of TfOH. It was found that pyridine and 2,6-lutidine were the suitable for the purpose. [62] The mechanism has not been investigated although an associative ligand exchange is likely to occur as the trigonally twisted Cr(III) complexes encourage ligand association to the exposed Cr(III) centre.

1.5 Applications of Cr(III) complexes

Studies on using Cr(III) complexes for photo-redox catalysis have been reported. Wenger and co-workers have investigated the efficacy of photoinduced electron transfer performed by $[Cr(dqp)_2]^{3+}$ and found that it showed similar performance to the $[Ru(bpz)]^{2+}$ catalyst which is employed in photo-redox catalysis and therefore $[Cr(dqp)_2]^{3+}$ was reported to be a promising target for light-emitting devices, artificial photosynthesis or photocatalysis (**Figure 1.20**).[63] Another study carried out by the Wenger group analysed the role of oxygen in the Diels-Alder reaction catalysed by $[Cr(bathophen)_3]^{3+}$. As illustrated in **Figure 1.21** below, they found that oxygen acted as an electron shuttle which quenched the photoexcited Cr(III) centre whilst itself becoming singlet oxygen. This is followed by the singlet oxygen returning the reduced catalyst to its ground state forming a superoxide. Next, the superoxide reduces the Diels-Alder cycloadduct radical cation to form the final product and reforms oxygen. [64]
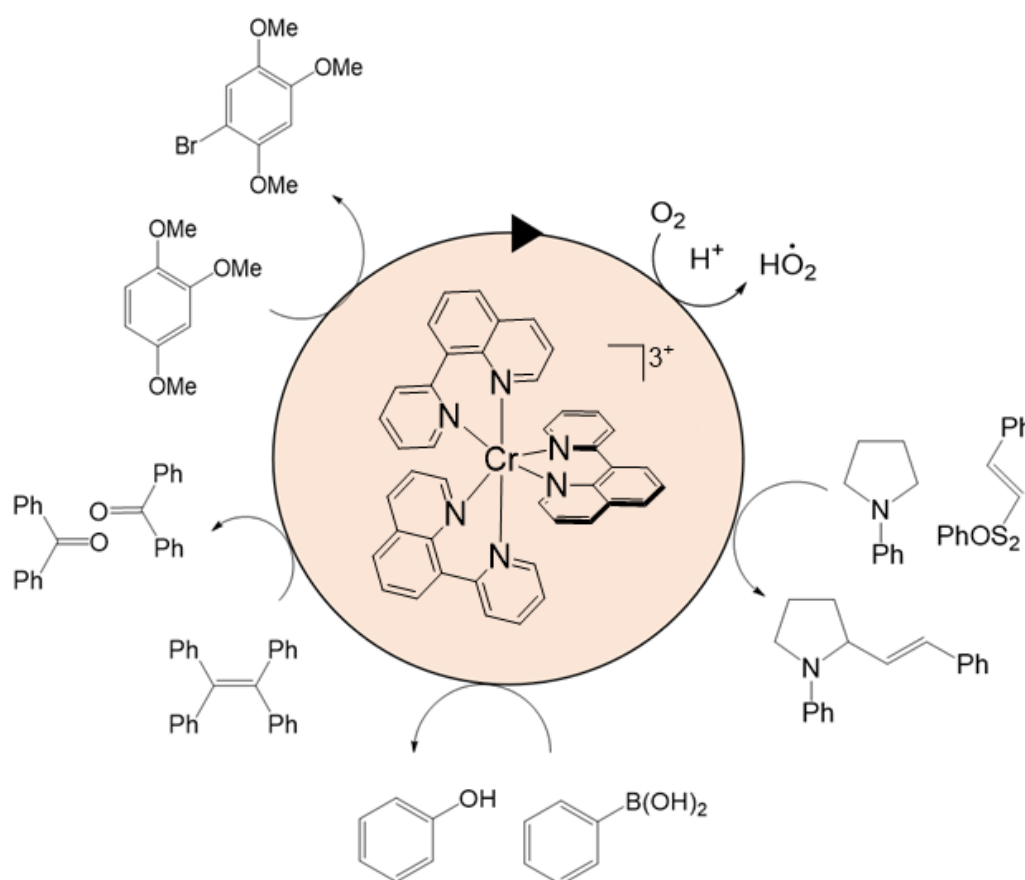
Figure 1.20 Examples of the photoinduced electron transfer of $[Cr(dqp)_2]^{3+}$.[64]
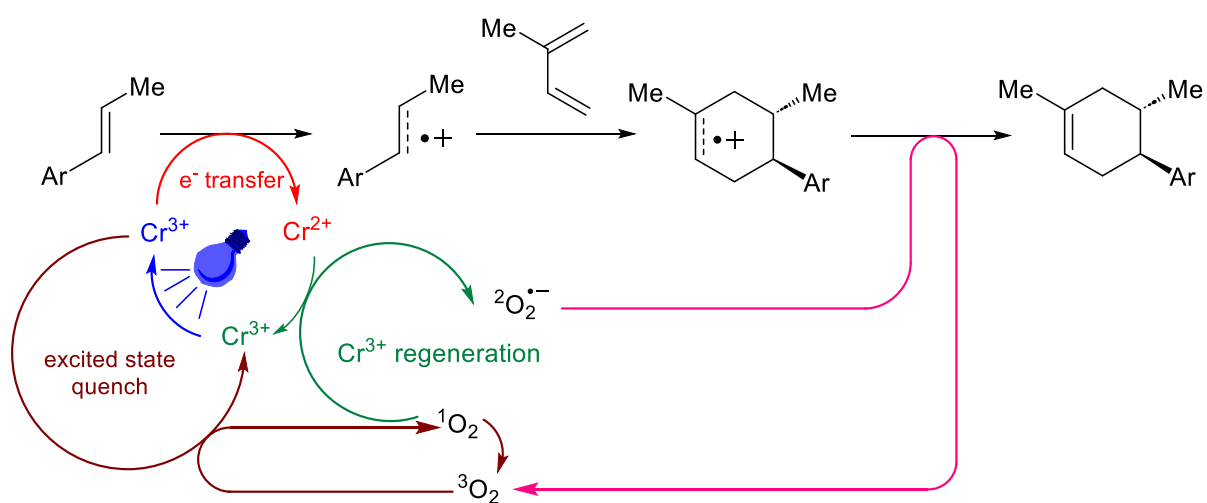
Figure 1.21 Scheme of the Diels-Alder reaction catalysed by [Cr(bathophen)$_3$]$^{3+}$ and the role of oxygen reported by Wenger.[65]

1.6 Principles of EPR

A brief introduction of the theory of EPR will now be given. This concise summary is based on several texts available within the literature.[65,66,67,68] EPR spectroscopy is a technique where microwaves (MW) in combination with an external magnetic field are used to probe paramagnetic species, that is molecules with at least one unpaired electron. The Planck`s law dictates that electromagnetic radiation is absorbed if the energy of the radiation matches the energy gap (ΔE) between the two states investigated.

1.6.1 Angular momentum and magnetic moment of an electron

The history of EPR spectroscopy dates back to 1896 when Zeeman observed the splitting of spectral lines in optical spectra when a static magnetic field was applied. This was later followed with the now famous Stern-Gerlach (**Figure 1.22**) experiment of the 1920`s where a beam of silver atoms was sent through a heterogeneous magnetic field and was split into two distinct beams; the beams represent the + $\frac{1}{2}$ *and* - $\frac{1}{2}$ spin states of an electron respectively, also known as the intrinsic angular momentum (**Figure 1.23**., (**Equation 1.5**); M_s - the total spin, S - the spin quantum number, h - Planck`s constant).
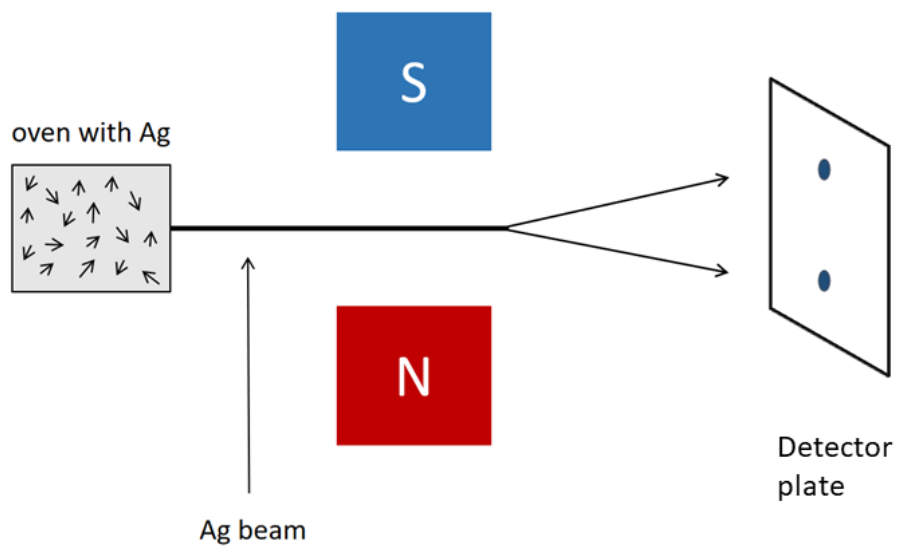
Figure 1.22 Stern-Gerlach experiment.
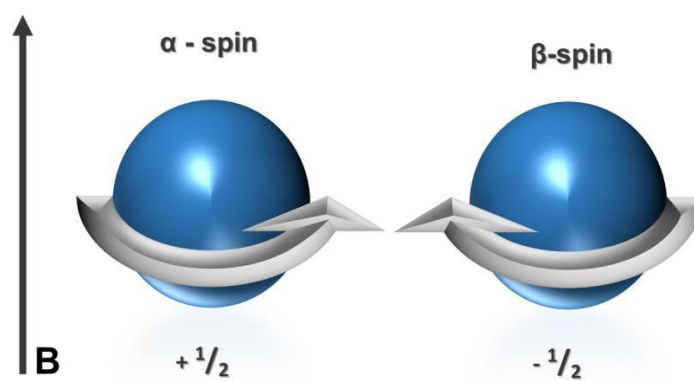
Figure 1.23 Illustration of spin angular momentum of an electron.

$$M_S = \sqrt{S(S+1)} \frac{h}{2\pi} \qquad (1.5)$$

Since an electron is a charged particle, the combination of charge and intrinsic angular momentum creates a magnetic dipole which consists of two magnetic poles of the same magnitude but opposite polarity as illustrated in **Figure 1.23**. The magnetic moment is directly proportional to the spin angular momentum (**Equation 1.6**). The negative value signifies that the angular momentum of an electron is collinear but anti-parallel to the spin of the electron (and originates directly from the negative charge). g_e is the g-factor of an electron and is a proportionality constant value of $g_e = 2.00232$ for a free spin. The g-value for the molecule of interest will vary from the free spin value due to spin-orbit coupling effects where larger spin-orbit coupling (SOC) contributions result in larger deviations of the g-value from the free spin value. In comparison with the more familiar chemical shift values reported in the analogous technique of NMR spectroscopy, the g-factor (or g-value) describes the resonant field position in EPR spectroscopy and therefore can be treated as a chemical fingerprint of the sample of interest. Moreover, the g-factor is sensitive to the environment surrounding the unpaired electron(s) and therefore depends on the electronic configuration of the sample. μ_B is the Bohr magneton and is defined as the unit of electronic magnetic moment, whilst $g_e\mu_B$ represents the gyromagnetic ratio which is the ratio of the electron magnetic moment of an electron to its angular momentum. The Bohr magneton can be defined further (**Equation 1.7**) with e being the charge of an electron and m_e being the mass of an electron.

$$\mu_e = -g_e\mu_B M_S \qquad (1.6)$$

$$\mu_B = \frac{eh}{4\pi m_e} \qquad (1.7)$$

1.6.2 Zeeman effect

The energy differences observed with EPR spectroscopy, for systems where $S = \pm\frac{1}{2}$, are mostly due to the interaction of the unpaired electron within the sample with the applied magnetic field; this is known as the Zeeman effect described by (**Equation 1.8**) and (**Equation 1.9**) for two possible energy states ($\pm\frac{1}{2}$), where g is g-factor, μ_B is Bohr magneton and B is the magnitude of the applied magnetic field:

$$E_{1/2} = \frac{1}{2}g\mu_B B \qquad (1.8)$$

$$E_{-1/2} = -\frac{1}{2}g\mu_B B \qquad (1.9)$$

In the absence of the external magnetic field $\Delta E = 0$ and it is not possible to differentiate between spin states. However, upon application of an external magnetic field, the two spin states become non-degenerate (**Equation 1.10**):

$$\Delta E = hv = g\mu_B B \qquad (1.10)$$

As the strength of the applied magnetic field increases, the energy gap increases until it matches the microwave radiation resulting in absorption of photons. Application of a correct quantum of microwave radiation results in a spin-flip of the electron which is observed as a resonance line in the EPR spectrum. This is governed by the EPR spectroscopy selection rule which states $\Delta m_s = \pm 1$.

1.6.3 Common frequencies of EPR spectrometers

For technical issues relating to the hardware of the instrumentation, EPR spectrometers usually vary the applied external magnetic field and keep the microwave frequency constant. There are several models of commercially available EPR spectrometers that operate at different microwave frequencies which are listed in **Table 1.3** alongside the resonance field for $g = 2$.

Table 1.3 Microwave bands available for EPR spectroscopy.

Microwave band	Frequency (GHz)	B_{res} (mT)
S	3.0	110
X	9.5	348
Q	35	1210
W	95	3350

1.6.4 Zero-Field Splitting (ZFS)

Zero-field splitting is observed for systems with multiple unpaired electrons such that $S > {}^1/_2$. ZFS arises because of SOC which is an interaction between the electron spin angular momentum and its electron orbital angular momentum and spin-spin coupling which is a direct dipolar interaction between at least two unpaired electrons; the observed transitions for ZFS are known as fine structure. In transition metal complexes, the SOC interaction is dominant. For high spin species with $S > {}^1/_2$, the total spin is determined by Hund`s rule, where $2S+1$ determines the multiplicity. For species with multiple unpaired electrons the degeneracy of m_s states is lifted such that it is experienced even without an external magnetic field applied, therefore molecular orbitals are no longer spherically distributed. When spherically distributed, no ZFS is observed and therefore g-value and A-value are the parameters defining the electronic state of the system. For a non-symmetric high-spin system, the spin-Hamiltonian parameters of primary interest are the zero-field splitting parameters labelled D and E, which define the axial distribution and zero-field interaction within the equatorial plane, respectively. The g-value for high-spin systems is typically replaced by a g_{eff} (effective) value which is dependent on the magnitude of ZFS and is discussed later.

For transition metal complexes the D tensor is therefore dominated by SOC and as expected, is sensitive to ligand field effects. Transition metal ions with an odd umber of unpaired electrons such as $S = {}^3/_2$ for Cr(III) are defined as Kramer`s ions. For $S = {}^3/_2$, there are three allowed ($\Delta m_s = \pm 1$) transitions: $|S, m_{s_{initial}} \rangle \rightarrow |S, m_{s_{final}} \rangle = |{}^3/_2, {}^{-3}/_2 \rangle \rightarrow |{}^3/_2, {}^{-1}/_2 \rangle ; |{}^3/_2, {}^{-1}/_2 \rangle \rightarrow |{}^3/_2, {}^{+1}/_2 \rangle ; |{}^3/_2, {}^{+1}/_2 \rangle \rightarrow |{}^3/_2, {}^{+3}/_2 \rangle$ which are

degenerate in the absence of ZFS. In d^3 metal complexes with perfectly octahedral geometry experience a very small magnitude of ZFS. For instance, $[Cr(NH_3)_6]^{3+}$ exhibits only one transition with an isotropic g-value of 1.9857 with a small D-value of 0.019 cm^{-1}.

When no external magnetic field is applied, for an axial system $|S, m_s \rangle = |{}^3/_2, {}^{+1}/_2 \rangle$ state resides at energy representing $-D$ and $|S, m_s \rangle = |{}^3/_2, {}^{+3}/_2 \rangle$ state resides at energy representing $+D$, which makes the energy splitting equal to 2D as illustrated in **Figure 1.24**. For a rhombic system, mixing of the two states is observed, however it occurs at such a small magnitude that it can be omitted and $|S, m_s \rangle = |{}^3/_2, {}^{+1}/_2 \rangle$ and $|S, m_s \rangle = |{}^3/_2, {}^{+3}/_2 \rangle$ still apply. The energy separation is represented by **Equation 1.14**.

$\mp {}^3/_2$

2D

$\mp {}^1/_2$
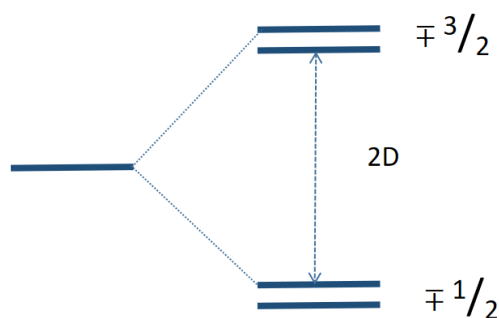
Figure 1.24 Kramers energy level splitting diagram when no external magnetic field is applied for an axial system ($E = 0$).

$$\Delta = 2\sqrt{D^2} + \sqrt{3E^2} \qquad (1.14)$$

Kramers systems allow for the $\pm \frac{1}{2}$ transition to be detected, however the appearance of the spectrum changes drastically with an increase in ZFS. Kramers systems are usually dominated by the central $m_s = -{}^1/_2 \leftrightarrow {}^1/_2$ transition which does not experience ZFS broadening to first-order. However, to second order, ZFS broadening

scales inversely to the magnetic field applied. In addition, *D*- and *E*- strain are often present as a distribution of *D* and *E*-value due to a distribution in the ligand field.

It is important to note that transitions other than $m_s = -\frac{1}{2} \leftrightarrow \frac{1}{2}$ may not be observed due to sample ensemble effects leading to broadening of the signal. The spin Hamiltonian can be described using the equation below where the first three terms describe electron zeeman (EZ), nuclear zeeman (EZ) and hyperfine (HF) interactions meanwhile SDS describes the ZFS interaction and *S* is total spin and *D* is the *D*-value (**Equation 1.15**).[68]

$$E = g_e\, \mu_B B_{ms} - g_N \mu_N B_{mI} + a m_s m_I + SDS \qquad (1.15)$$

In the weak field limit of ZFS (when *D* >> *hv*) only the $-\frac{1}{2} \leftrightarrow \frac{1}{2}$ transition is possible, when *D* ≈ *hv* the transitions observed depend on the magnitude of *D* and *E*, the *g*-anisotropy, and the temperature. When *D* << *hv*, all transitions are possible, and the fine structure is observed.

Additional to that, every sample measured as a neat solid will experience additional interactions as can be seen in **Figure 1.25**, including spin-spin, orbit-orbit, and spin-orbit coupling. Those additional interactions often cause additional broadening effects and therefore generation of magnetically dilute powders is necessary. Magnetically dilute powders consist of a diamagnetic matrix doped with an EPR active material. For Cr(III) complexes an example of magnetically dilute powder can be $[Cr(bpy)_3]^{3+}$ doped into $[Co(bpy)_3]^{3+}$ at 1% level.[69]
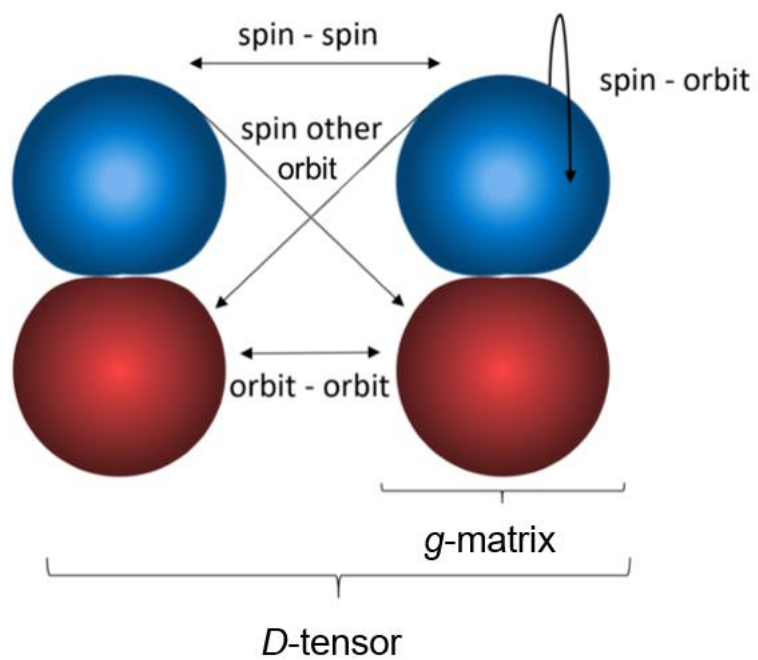
Figure 1.25 Depiction of various interactions between two unpaired electrons. Systems where $D \gg h\nu$ used require higher frequencies to probe their transitions.

1.7 References

[1] K.V.R., Murthy, H. VFTIRk, *Defect and Diffusion Forum*, 2013, 347, 1-34.

[2] J.R. Lakowicz, *Principles of Fluorescence,* Springer, Singapore, 3rd edn., 2006.

[3] V.P. Gupta, *Principles and Applications of Quantum Chemistry*, Academic Press, 2016.

[4] C. Kirmaier, D. Holten, *3 - Electron Transfer and Charge Recombination Reactions in Mild-Type and Mutant Bacterial Reaction Centers*, Academic Press, 1993.

[5] K. G. Fleming, Fluorescence Theory, Encyclopedia of Spectroscopy and Spectrometry, Academic Press, 3rd edn., 2017.

[6] J. Alvarez-Jimenez, I. Cortese, J.A. García, D. Gutiérrez-Ruiz, J.D. Vergara, 2019 *J. Phys.: Conf. Ser.,*12, 47, 012-017.

[7] M. Y. Berezin, S. Achilefu, 2010, *Chem. Rev.,* 110, 5, 2641–2684

[8] *Time resolved fluorescence lifetime measurements*, www.horiba.com, accessed 08/09/2021

[9] N. Eastaugh, V. Walsh, T. Chaplin and R. Siddall, *Pigment Compendium - A Dictionary of Historical Pigments*, Elsevier Butterworth-Heinemann, Oxford, 1st edn., 2004.

[10] G. Schwedt, 2011, *Chem. unserer Zeit*, 45, 294-295.

[11] *High-Purity Chromium Metal: Supply Issues for Gas-Turbine Superalloys*, The National Academies Press, 1995.

[12] L. R. Nelson, *J.Sth. Afr. Inst. Min. Met.,* 1996, 135144.

[13] M. Langa, P. J. Jugo, M. I. Leybourne, D. F. Grobler, J. Adetunji, H. Skogby, 2021, *Min. Dep.,* 56, 31–44.

[14] H. Stobbe, 1962, *R. & min.,* Volume 37, 3-4.

[15] *Iridium - Element information, properties and uses |* Periodic Table (rsc.org), Iridium - *Element information, properties and uses |* Periodic Table (rsc.org), accessed 04/01/2023

[16] Chromium - *Element information, properties and uses |* Periodic Table (rsc.org), Chromium - *Element information, properties and uses |* Periodic Table (rsc.org), accessed 04/01/2023

[17] G. Anger, J. Halstenberger, K. Hochgeschwender, C. Scherhag, U. Korallus, H. Knopf, P. Schmidt and M. Ohlinger, *Ullman's Encyclopedia of Industrial Chemistry*, WILEYVCH, Weinheim, 2012, pp. 157-191.

[18] A. Stwertka, *Guide to the Elements*, Oxford University Press, Oxford, 2nd edn., 2002.

[19] C. Blanford, *Chromium: yellow US school buses, gemstones and shiny chrome car parts (podcast Royal Society of Chemistry),* 2010.

[20] D. A. Herlod and R. L. Fitzgerald, *Handbook on Metals in Clinical and Analytical Chemistry*, ed. H. G. Seiler, A. Siegel and H. Siegel, Marcel Dekker, New York, 1st edn., 1994, ch 25.

[21] L. H. Gade, *Koordinationschemie*, WILEY-VCH, Weinheim, 1st edn., 1998.

[22] C. E. Housecroft and A. G. Sharpe, *Inorganic Chemistry*, Pearson Education Limited, Essex, 2nd edn., 2005.

[23] P. A. Scattergood, *Organomet. Chem.* RSC, 2020.

[24] Tanabe-Sugano diagrams via spreadsheets (uwimona.edu.jm), Tanabe-Sugano diagrams via spreadsheets (uwimona.edu.jm), accessed 20/12/2022.

[25] L. S. Forster, 1990, C*hem. Rev.*, 90, 2, 331–353

[26] C. Wang, S. Otto, M. Dorn, E. Kreidt, J. Lebon, L Srsan, D. Di Martino-Fumo, M. Gerhards, U. Resch-Genger, M. Seitz, K. Heinze., 2018, *Angew. Chem. Int. Ed.,* 1112-1116.

[27] S. Treiling, C. Wang, C. Förster, F. Reichenauer, J. Kalmbach, P. Boden, J. P. Harris, L. M. Carrella, E. Rentschler, U. Resch-Genger, C. Reber, M. Seitz, M. Gerhards, K. Heinze, 2019, *Angew. Chem. Int. Ed.,* 58, 50, 18075-18085.

[28] S. Otto, C. Förster, C. Wang, U. Resch-Genger, K. Heinze, 2018, *Angew. Chem. Int. Ed.,* 24, 48, 12555-12563.

[29] N. Sinha, J. Jiménez, B. Pfund, A. Prescimone, C. Piguet, O. S. Wenger, 2021, *Angew. Chem. Int. Ed.,* 133, 44, 23915-23921.

[30] S. Treiling, C. Wang, C. Förster, F. Reichenauer, J. Kalmbach, P. Boden, J.P. Harris, L.M. Carrella, E. Rentschler, U. Resch-Genger, C. Reber, M. Seitz, M. Gerhards, K. Heinze, 2019, *Angew. Chem. Int. Ed. Engl.,* 58, 50, 18075-18085.

[31] A.Z. Andreou, D. Klostermeier, Methods in Enzymology, 2012, *Ac. Press*, 511,75-109.

[32] M. Götz, P. Wortmann, S. Schmid, T. Hugel, *Methods in Enzymology*, 2016, Ac. Press , 581, 487-516.

[33] S. Otto, M. Dorn, C. Förster, M. Bauer, M. Seitz, K. Heinze,2018, *Coord. Chem. Rev.,* 359, 102-111.

[34] L. Bu, J. E. Straub., 2003, *Biophys J.*, 85, 3, 1429-39.

[35] N. Ashim Nandi, S. Korzuch, 2020, *Chem. A Eur. J.* 26, 4, 759-772.

[36] Robert J. Deeth, *Coord. Chem. Rev.*, 2001, 212, 1, 11-34.

[37] A. K. Bridson, *Inorganic Spectroscopic Methods,* Oxford University Press, New 31 York, 1998.

[38] V. Vallet, U. Wahlgren, I. Grenthe, 2003, *J. Am. Chem. Soc.,* 125, 48, 14941–14950.

[39] S. Otto, M. Dorn, C. Förster, M. Bauer, M. Seitz, K. Heinze, 2018*, Coord. Chem. Rev.,* 359, 102-111.

[40] P. W. Ayers, 2005, *J. Chem. Phys.* 122, 141102.

[41] R. G. PEARSON, *Hard and Soft Acids and Bases*, Elsevier,1969, 5, 1-52.

[42] U. Strahm, R. C. Patel, E. Matijevic, 1979, *J. Phys. Chem., 83,* 13, 1689-1695.

[43] Pearson R. G. *J. Chem. Educ.* 1968, 45, 581.

[44] Pearson R. G. *J. Chem. Educ.* 1968, 45, 643–648.

[45] J. Jiménez, B. Doistau, M. Poncet, C. Piguet, 2021, *Coord. Chem. Rev.,* 434, 213750.

[46] Burrows, Hofman, Parsons, Pilling, *Chemistry ^{3}*, Price, Oxford, 2nd edition.

[47] J. Pérez, L. Riera, 2008, *Chem. Soc. Rev.***,** 37, 2658-2667

[48] S. F. Lincoln 2005, *Helv. Chim. Acta*, 88 , 523 —545.

[49] I. Andrés-Tomé, J. Fyson, F. B. Dias, A. P. Monkman, G. Iacobellis and P. Coppo, 2012, *Dalton Trans.,* 41, 8669-8674.

[50] J. L. Atwood, K. R. Dixon, D. T. Eadie, S. R. Stobart, M. J. Zaworotko, 1983, *Inorg. Chem.*, 22, 5, 779–783.

[51] S. Mustafa, K.H. Shah, A. Naeem, M. Waseem, T. Ahmad, S. Sarfraz, M. Irshad, 2010, *Ch. J. Chem.*, 28, 1, 27-32.

[52] L. R. Ocone and B. Block*,* 1966*, Inorg. Synth.,* 8, 125132

[53] N. Turova, *Inorganic Chemistry in Tables*, Springer, Heidelberg, 1st edn., 2011.

[54] N. Turova, *Inorganic Chemistry in Tables*, Springer, Heidelberg, 1st edn., 2011.

[55] Schoenle, PhD Thesis, 2014

[56] K. D. Barker, K. A. Barnett, S. M. Connell, J. W. Glaeser, A. J. Wallace, J. Wildsmith, B. J. Herbert, J. F. Wheeler and N. A. Kane-Maguire*, 2001, *Inorg. Chim. Acta*, 316, 4149.

[57] J. R. Poncet, M. Doistau, B.Besnard, C. Piguet, 2020, *Dalton Trans.*, *49*, 13528–13532.

[58] T. Song, X. Tao, X. Tong, N. Liu, W. Gao, X. Mu, Y. Mu, 2019, *Dalton Trans.*, *48*, 4912–4920.

[59] O.L Sydora, R.T Hart, N.A. Eckert, E. Martinez Baez, A. E. Clark, C. J. Benmore, 2018, *Dalton Trans.*, *47*, 4790–4793.

[60] C. Förster, M. Dorn, M., T. Reuter, S. Otto, G. Davarci, T. Reich, L. Carrella, E. Rentschler, K. Heinze, 2018, *Inorg.*, *6,* 86.

[61] N. F. Brennan, B. Blom, S. Lotz, P. H. van Rooyen, M. Landman, D. C. Liles, M. J. Green, 2008, *Inorg. Chim, Act.*, 361, 3042-3052. 2

[62] B. Doistau, G. Collet, E. Acuña Bolomey, V. Sadat-Noorbakhsh, C. Besnard, C. Piguet, 2018, *Inorg. Chem.,* 57 , 22, 14362-14373.

[63] T. H. Bürgin, F. Glaser, O. S. Wenger, 2022, *J. Am. Chem. Soc.,* 144, 31, 14181-14194.

[64] R. F. Higgins, S. M. Fatur, S. G. Shepard, S. M. Stevenson, D. J. Boston, E. M. Ferreira, N. H. Damrauer, A. K. Rappé, M. P. Shores, 2016, *J. Am. Chem. Soc.*, 138, 16, 5451–5464.

[65] V. Chechik, E. Carter, D. Murphy. Electron paramagnetic resonance. Oxford chemistry primers. Oxford Univ Press, Oxford, 2016. OCLC: ocn945390515.

[66] J. Telser, *EPR Interactions - Zero-Field Splittings*., eMagRes, 207–234. John Wiley & Sons, Ltd, Chichester, UK, 2017.

[67] P. Gast E.J.J. Groenen. *EPR Interactions - g-Anisotropy*., eMagRes, 1435– 1444. John Wiley & Sons, Ltd, Chichester, UK.

[68] M. Brustolon, E. Giamello, *Electron Paramagnetic Resonance: A Practitioner's Toolkit*, John Wiley & Sons, 2009.

[69] R.P. Bonomo, A.J. Di Bilio, F. Riggi, 1991, *Chem. Phys.*, 151, 3, 323-333.

Chapter 2: Investigation of Schiff-base Ligands to Aid in Populating Doublet Excited State Emission from Cr(III).

2.1 Introduction

This chapter discusses a series of Schiff-base Cr(III) complexes and their photophysical properties. Prior to a detailed discussion of the novel metal complexes, a brief introduction of the history, reactivity and synthesis of Schiff-bases is first provided.

A Schiff-base is an organic compound formed via a condensation reaction of an amine and an aldehyde or ketone to yield an imine.[1,2] The stability of the imine is provided by bonding to at least one electron-withdrawing aromatic partner as opposed to electron-donating alkyl substituents.[3] By withdrawing electron density away from the azomethine nitrogen atom (**Figure 2.1**, shown in bold), the adjacent carbon atom (indicated with an asterisk) is less positively charged (**Figure 2.1** molecule A) than that of alkyl-substituted imines (**Figure 2.1** molecules B and C). The lower partial charge of the imine carbon (*) atom makes it less available for nucleophilic attack. This explains the challenge in obtaining imines in aqueous media where the groups attached are alkyl and/or hydrogen making an imine prone to a nucleophilic attack by water molecules resulting in hydrolysis (see **Section 2.1.4**). Across the series indicated, imine **B** shown in **Figure 2.1** should present a moderate stability in aqueous media.
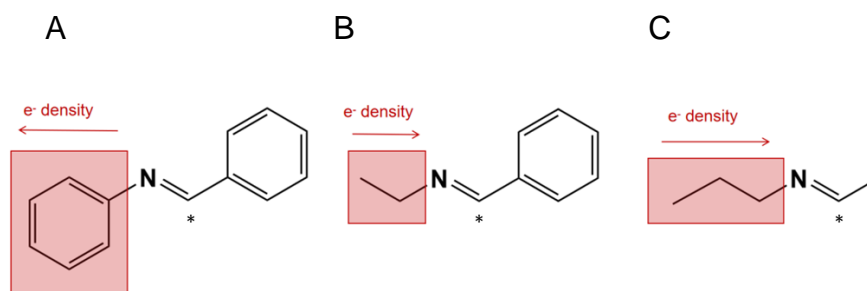
Figure 2.1 Depiction of the direction of electron density distribution depending on the nature of the substituent (indicated by the red frames).

2.1.1 Applications

Schiff-base ligands are widely recognised for their multiple applications, for instance in medicinal chemistry and pharmaceutical industry. They are also known to be employed within dye and materials manufacturing and its due to their kinetic inertness. [4,5,6,7] Moreover, transition metal complexes incorporating Schiff-base ligands have been previously reported to have antibacterial and anticancer activity. [8,9,]

Those complexes are also recognized for their catalytic oxidation activity and their potential in OLED device design.[10,11] Some of these applications are discussed in the sections below.

2.1.2 Biological Applications

Ispir *et al.,* reported TM complexes that exhibit antifungal and antibacterial activities, particularly against bacterial strains such as *E. coli, Staphylococcus aureus* and *Klebsiella pnumoniae.*[12] The group reported coordination complexes of Cr(III) and others such as Co(II), Cu(II), Ni(II) and Mn(II) (**Figure 2.3**).

It was observed that some of the complexes exhibited enhanced antimicrobial activities against the strains in comparison with the free Schiff-bases activities. This was measured by assessing the diameter of the inhibition of the bacterial growth as illustrated in **Figure 2.2** which is known as the disc diffusion method. In regions of the growth dish, where the ligands/complexes were applied, the inhibition diameters were reported to be in the range of 7-12 mm for the complexes and around 10 mm for the ligands, therefore showing a slightly enhanced antimicrobial effect of some of TM complexes.[12]
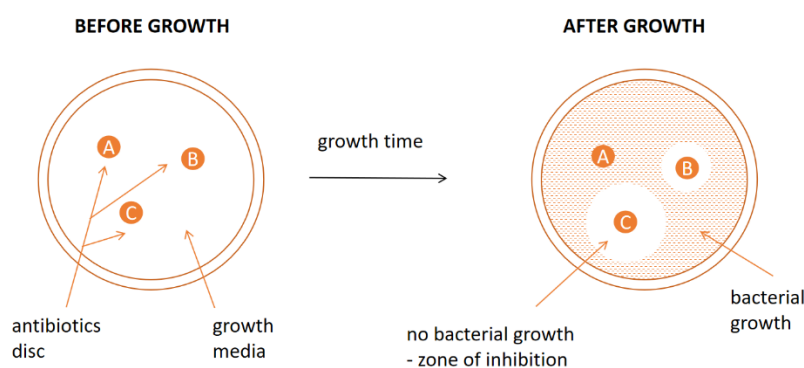
Figure 2.2 Disc diffusion method used to assess antimicrobial activity of potential drugs.
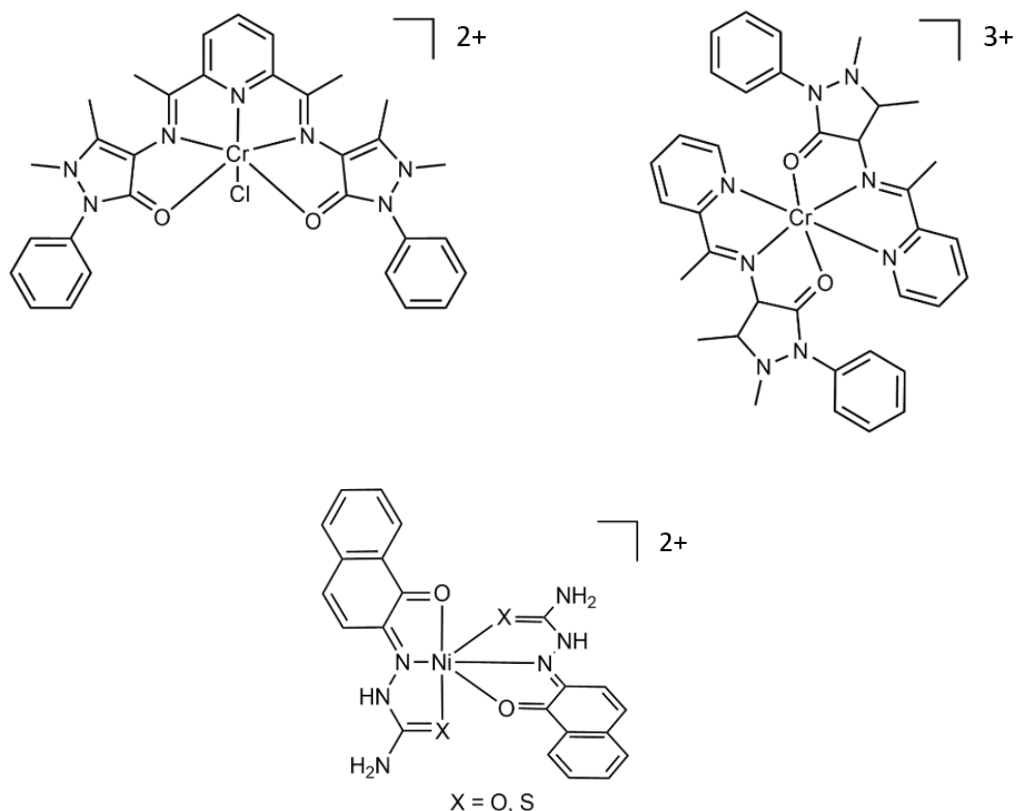
Figure 2.3 Cr(III) and Ni(II) complexes utilised as antimicrobial agents.[7,8,15]

The same enhanced activity effect of metal complexes in comparison to the associated free ligands is also reported in studies of anticancer agents. This is explained through the increase of lipophilicity upon metal complexation which results in increased penetration of the cell membrane followed by a subsequent transportation to the area within the cell where anticancer activity is required. Afrasiabi *et al.,* reported two Ni(II) complexes with thiosemicarbazone and semicarbazone moieties acting as coordinating ligands (**Figure 2.3**). They reported that upon complexation, the anticancer effect is elevated for the complex which showed a stronger inhibition of MCF-7 (human breast cancer cell line) cell proliferation than the free ligand. The semicarbazone moieties were also reported to have lower side effects than thiosemicarbazone moieties.[13]

2.1.3 Catalytic Activity

In 1997 Jacobsen *et al.*, reported a Cr-salen complex employed as a catalyst to effect highly enantioselective ring opening of 1,4-cyclohexadiene monoepoxide with TMSN₃ (**Figure 2.4**).[14] The significance of this discovery lies within the biological

sciences, notably the lack of regulation of an enzyme known as the protein kinase C (PKC) leads to carcinogenesis, inflammation as well as cardiovascular disorders. A PKC-inhibitor (balanol, **Figure 2.4**) can be synthesised owing to the highly enantioselective ring opening catalysed by the chromium catalyst.[14]
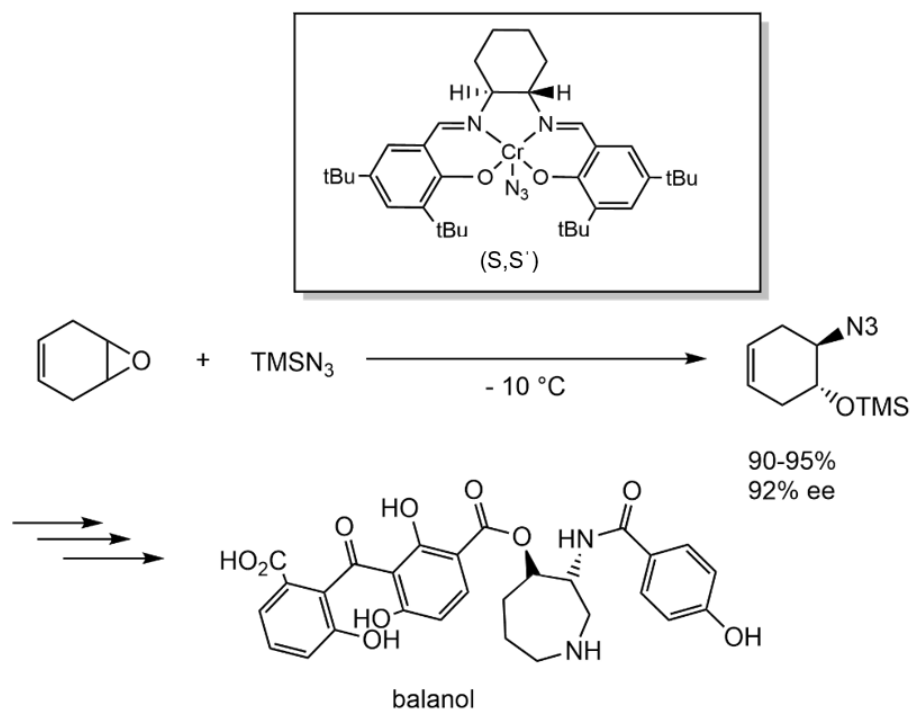
Figure 2.4 Cr-salen catalysed asymmetric ring opening employed in the synthesis of balanol.

The catalyst concentration proved crucial to the enantioselectivity of the reaction. With previously reported conditions (2 mol% catalyst) at room temperature the turnover produced only 81-83% ee within 46 hours. [15] Increasing the catalyst concentration to 7.5 mol% (solvent-free) achieved 92 % ee within 24 hours at -10 °C. This asymmetric ring opening method allowed for the subsequent twelve step synthesis of balanol in 31% overall yield.[16]

2.1.4 Luminescent Activity in Organic Light Emitting Diode (OLED) Devices

OLED devices are a popular choice for the screen industry as compared to the standard liquid crystal display screens (LCD), with richer colours and more realistic image resulting from the red, blue and green (RGB) light combination system. Moreover, they are a more energy-efficient option since they are self-emitting devices and do not need an additional light source.[17] **Figure 2.5** presents various emission

colours that can be harvested from luminophores when used in OLED devices. Nevertheless, the most desired property of the luminophores employed in OLED devices is a narrow emission profile which enables richer combination of colours leading to a more realistic image projection. As discussed in **Section 1.3.1**, Cr(III) complexes exhibit very narrow emission profiles owing to the spin-flip nature of the transition.
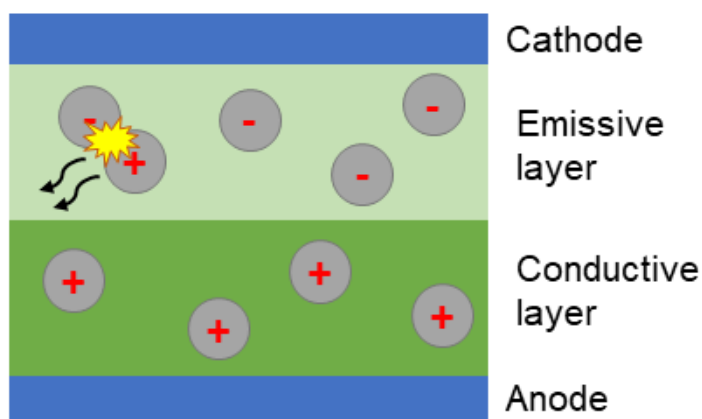
Figure 2.5 Architecture of an OLED device. Indicated with a star icon is the emission of the emissive layer.

OLED devices comprise of a cathode and an anode with a layer of an organic material positioned in between. Once electricity is applied, the luminophores are excited by the energy of the electrons injected by the cathode and the electrode holes (spurious electrons) injected from the anode. The electrostatic forces between the electrons and the holes bring the two together to form an exciton. When excited, the emissive layer relaxes back to its ground state via emission of visible light. The possibility of including several different diodes of narrow emission profiles emitting different shades of the same colour category enables a better image in OLED screens.[18]

Use of metal complexes in the emissive layer of OLED devices carries many benefits such as color-tunable ligands with strong emission, large Stokes shifts and photostability. One of the criteria for high-performance OLEDs is intense luminescence and therefore high quantum yields. These can be achieved with planar extensively conjugated π systems such as Schiff-bases. Pt(II) complexes are quite popular among OLED devices, this is due to their square planar geometry which facilitates aggregation of neighbouring complexes, that suppresses quenching via ligand-

ligand/metal-metal interactions due to the close contact of the adjacent molecules in the emissive layer, leading to enhanced lifetimes. Moreover, their large Stokes shift prevent self-quenching upon aggregation.[19]

Zhang *et al.,* reported Schiff-base complexes emitting blue to orange light with the orange light emitters shown in **Figure 2.6**.[20] With the aid of electron withdrawing (F, Br) and electron donating (t-Bu, NEt$_2$) groups they were able to tune the emission wavelength into the low energy regime (~600 nm) and obtain orange light emitting Pt(II) complexes. Although Pt(II) complexes have shown to be suitable OLED candidates, the literature is not limited to Pt(II) complexes and other transition metal Schiff-base complexes are also known such as the blue light emitting zinc or multinuclear Mn(II)-Fe(III) complexes (**Figure 2.7**). [20, 21, 22, 23, 24]
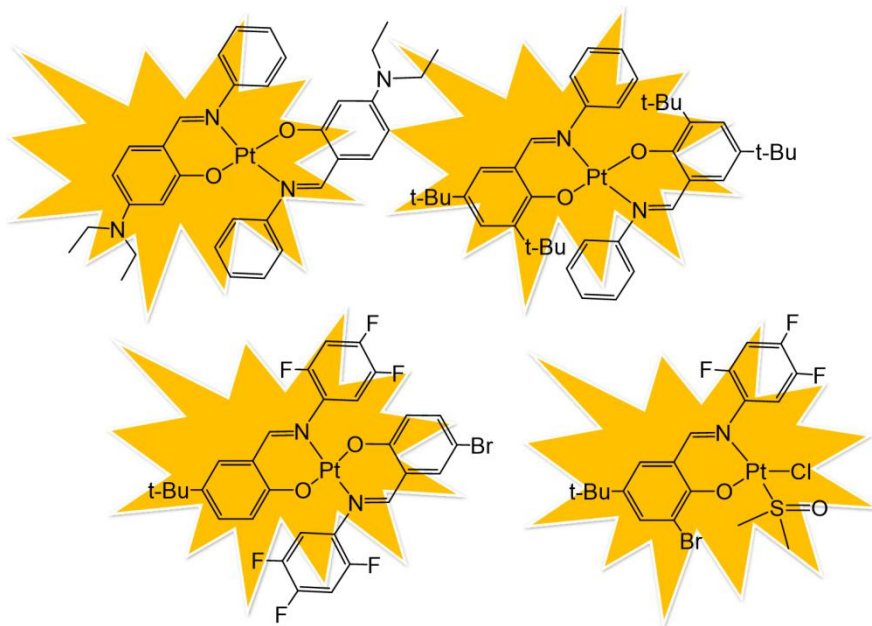
Figure 2.6 Orange light emitting Pt(II) complexes designed for phosphorescent OLEDs.[21]
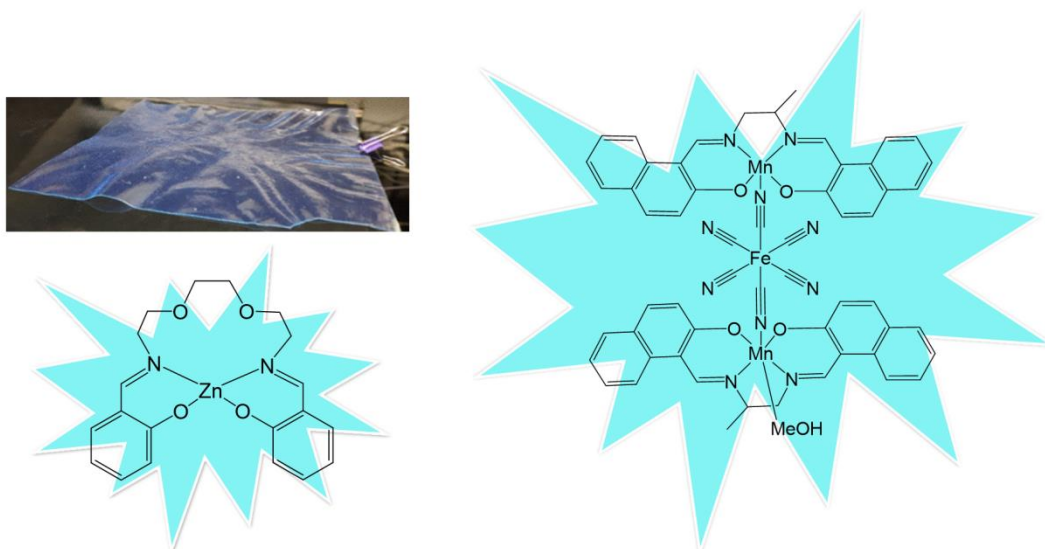
Figure 2.7 Blue light emitting Zn(II) complex (bottom left), a thin film containing the Zn(II) complex (top left) and a trinuclear Mn(II)-Fe(III) complex (right) reported by Donmez *et al.*[20,23]

Moreover, Chan *et al.,* have reported green light emitting tungsten complexes that proceed through thermally activated delayed fluorescence (TADF; **Figure 2.8**). Thin films incorporating the complexes showed quantum yields of up to 84% with excited state lifetimes ~2 μs also making these complexes suitable candidates for OLED devices.[25]
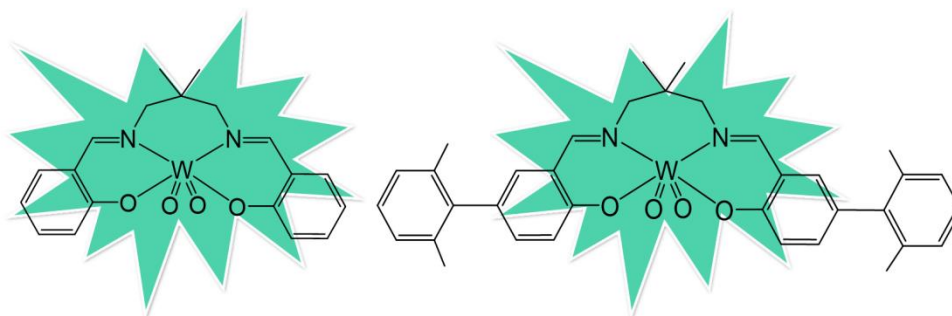
Figure 2.8 TADF tungsten complexes reported by Chan *et al.,* which emit green light.[26]

Other examples of suitable OLED candidates were reported in 2015 by Suresh *et al.*, detailing the emissive properties of Schiff-bases upon complexation to boron. The emission wavelength was directly dependent upon the extent of π conjugation within the ligand system, as shown in **Figure 2.9**.[26]
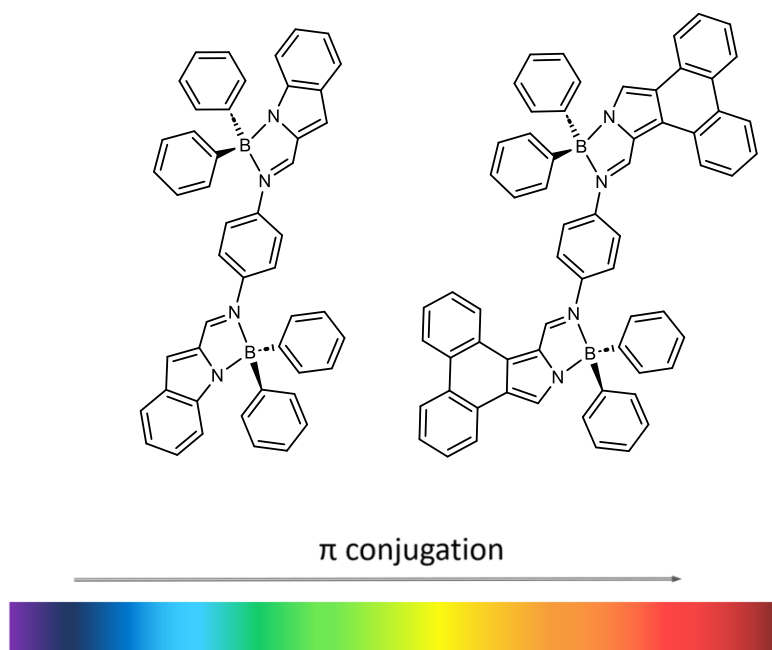
Figure 2.9 Boron complexes synthesised by Suresh presented in an order of increasing conjugation and decreasing HOMO-LUMO gap.[25]

Red light OLED emitters are to-date the most difficult to achieve. This is due to the energy gap law where the red-light emitters are required to have their excited states at very low energies which are considerably closer to the ground state than emitters of other colours and therefore increasing the risk of the non-radiative decay pathway dominating the relaxation process.[27,28] This suggests that the doublet excited state emitting Cr(III) complexes could present potential as red-light phosphorescent OLED emitters if their low quantum yields can be addressed.

Nevertheless, Che *et al.,* reported a red emitting thermally stable Pt(II) complex. It was placed as a guest in a 4,4`-Bis(*N*-carbazolyl)-1,1`-biphenyl (CPB) host layer and organised in a head-to-tail manner owing to the π-π stacking interactions (**Figure 2.10**). This was demonstrated to increase the efficiency of the OLED device when the concentration of the dopant complex decreased (<5.0 wt%). Concentrations higher than 5.0 wt% demonstrated aggregate/excimer formation which lowered the efficiency of the device via light dispersion.[29]
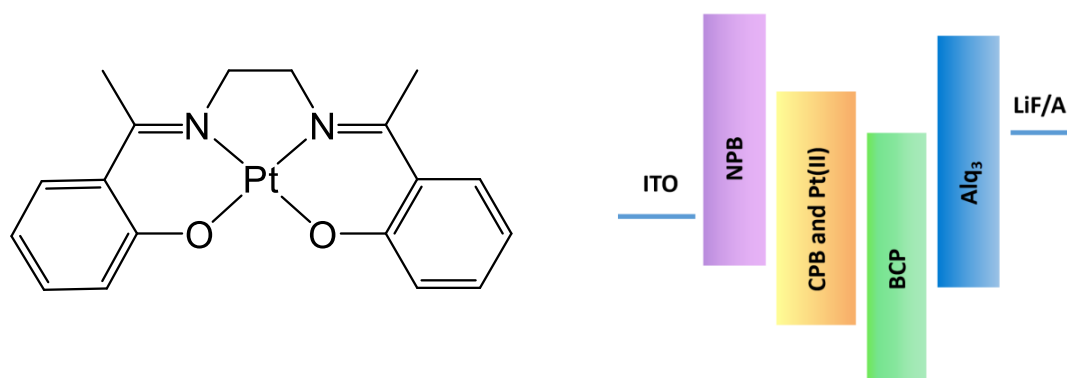
Figure 2.10 Red emitting Pt(II) complex reported by Che *et al.*, alongside the OLED device architecture. ITO (indium tin oxide):(anode; NPB (*N*,*N*`-Di(1-napthyl)-*N*,*N*`-diphenyl-(1,1`-biphenyl)-(1,1`-biphenyl)-4,4`-diamine): hole electrode transporter; CBP (4,4`-Bis(N-carbazolyl)-1,1`-biphenyl):(emissive layer; BCP (bathocuproine): hole electrode blocking layer; Alq$_3$ (tris(8-hydroxyquinoline)aluminium(III)): electron transport material; LiF/Al (lithium fluoride/Aluminium): insulated cathode.

Lastly, white organic light-emitting diodes (WOLED) are also a point of interest which is due to their wide applications such as full-colour screens, backlights for LCD screens and light bulbs. Such OLEDs can be created by combining red, green and blue emitting compounds in poly(*N*-vinylcarbazole). Zn complexes are often the transition metal used owing to their stability, their low cost and tunability of colour.[26] Examples of such Zn complexes can be seen in **Figure 2.11**.

R_1 = H, (CH$_2$)$_4$, (CH$_3$)$_2$
R_2 = H, (CH$_2$)$_4$, H

R = CH$_2$CH$_3$, H

Figure 2.11 Zn complexes utilised in production of WOLEDs.[30]

This brief introduction demonstrates various applications of Schiff-base complexes including biological (antimicrobial and anticancer), catalytic and as photophysical probes in OLED devices. This indicates, given the remarkable photophysical properties of Cr(III) complexes, that if high quantum yields can be obtained, there is a myriad of potential applications employing these complexes.

2.1.5 Electron Paramagnetic Resonance (EPR)

Despite a couple of examples of Cr(III)-Schiff-base complexes being available in the literature, none of these reports refer to the paramagnetic nature of the complexes or any attempt to characterise the spin properties including the zero-field splitting parameters.[31,32] Nevertheless, the evidence of the influence of the Schiff-bases on the electronic behaviour of the metal ion can be observed upon consideration of the copper-pyridoxal-octapamine complex discussed in this section (**Figure 2.12**).

Figure 2.12 Potential species for the copper-pyridoxal-octapamine system at (A) neutraland basic pH (B and C).[33]

54

Sharrock *et al.*, reported a series of X-band EPR spectra of copper-pyridoxal-octapamine recorded at various pH levels (**Figure 2.13**). At pH 2.8 a very broad and featureless spectrum was recorded, assigned to $[Cu(H_2O)_6]^{2+}$ species. As the pH was increased the signal changed to a typical axial-profile with four hyperfine lines visible arising from the nuclear spin of the copper centre ($I(^{63,65}Cu) = {}^3/_2$). This detailed spectrum progressively decreased in intensity as the pH value increased with complete disappearance at neutral pH. The signal intensity was restored at high pH, although showed evidence of changes in the spin-Hamiltonian parameters indicating differences in the structure at the metal centre.[33]
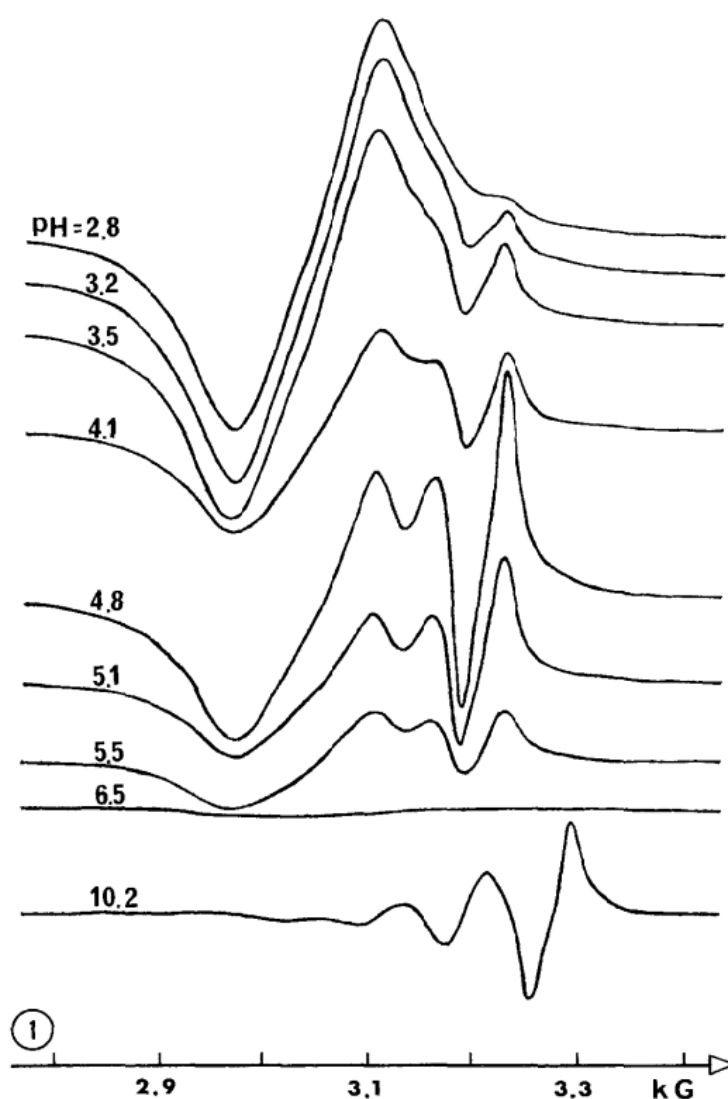
Figure 2.13 X-band EPR spectra of the copper-pyridoxal-octapamine recorded at various pH levels. All spectra are presented as out-of-phase. Reproduced from ref. 30.

The disappearance of the signal at pH 6.5 was assigned to formation of a bimetallic species with bridging OH groups (A in **Figure 2.13**) and restoration of the signal was ascribed to compound B which upon further increase in pH to 10.2 transformed into species C.

2.1.6 Spin-crossover

As spin-crossover (SCO) can only occur when a ligands of borderline field strength coordinates to the metal centre, this can be used to recognise the borderline field strength of a ligand and as this methodological approach is used in this chapter it is imperative that an introduction into the spin-crossover phenomenon is given here. For transition metal complexes where at least one of the spin states is paramagnetic (Kramers ion), EPR spectroscopy can be employed to study the characteristics of SCO behaviour.

It is well recognised that Schiff-base ligands cover a wide range of field strengths depending on the atoms coordinating to the metal centre. As outlined in the introductory chapter (**Section 1.4.1**), ligands where the coordination occurs via an oxygen atom tend to be of weak field nature, whereas coordination via nitrogen atoms shifts the field strength towards the borderline/strong regime. Complexes, with borderline field strength ligands coordinated, can produce both low spin (LS) and high spin (HS) configuration ($3d^4$-$3d^7$) and for those, a spin-crossoverbehaviour between the LS and HS is possible. Spin-crossover occurs when a metal centre can change its spin state once exposed to a stimulus, most commonly temperature and/or pressure, less often light irradiation.[34,35,36]

The literature provides a thorough review of SCO in [Fe(qsal)]$^+$ (qsal = quinolylsalicylaldimine) systems which suggests that the choice of the counterion can influence the degree of completion and the temperature of the SCO transition. Sertphon and co-workers investigated four complexes containing identical cation component and four different anions, namely [Fe(qsal-5-OMe)$_2$]Y, where Y = BF$_4$ (**1**), PF$_6$ (**2**), NCS (**3**) and BPh$_4$ (**4**). Complexes **1** and **4** were reported to be LS and HS only, respectively, whilst complexes **2** and **3** exhibited spin crossover. These results therefore suggest that counterions of intermediate size such as PF$_6^-$ or NCS$^-$ are desirable for SCO to occur. Additionally, in support of this theory, Quesada *et al.,* reported that large counterions (OTf$^-$) can inhibit SCO with the TM complex remaining

in its HS state.[37] Sertphon *et al.,* also investigated the importance of the substituent positioning on the ligand framework. Methoxy substitution at the 4-position, i.e. [Fe(qsal-4-OMe)$_2$]PF$_6$, was reported as to yield a high spin state system, whereas the analogous 5-methoxy complex ([Fe(qsal-5-OMe)$_2$]PF$_6$) was determined to be a low spin system at low temperature with 25% SCO at room temperature and a gradual and almost complete SCO at 350 K.[38] Harding *et al.,* reported [Fe(qsal-5-OMe)$_2$] Cl·2 MeOH to be a mix of HS and LS at 150 K, whereas [Fe(qsal-5-OMe)$_2$]Cl was reported as LS at 100 K. The same compound in solid state was identified as HS at high and low temperature.[39] With reference to the importance of substituent positioning, [Fe(qsal-3-OMe)$_2$]PF$_6$ does not show SCO at all.[40]

Mazur and co-workers reported a variable temperature EPR investigation of an Fe(III) SCO Schiff-base complex at X- and Q- band frequencies.[41] Measurements recorded within the temperature range of 100-300 K showed a clear SCO transformation. Between 200-300 K the dominant species observed was a broad signal at $g_{eff} \approx 4.3$. The same signal was observed at Q-band between 230-300 K with an additional shoulder at $g_{eff} \approx 6.0$. Both of these were assigned to represent the HS state. [42, 43, 44]

In the X-band EPR spectra (**Figure 2.14**), an additional broad shoulder appeared at $g_{eff} \approx 2.0$ at temperatures below 200 K. This same signal was observed in the Q-band spectra at 230 K. At around 190 K, both resonances ($g_{eff} \approx 4.3$ and $g_{eff} \approx 2.0$) were of similar intensity. At 120 K the signal at $g_{eff} \approx 2.0$ was clearly visible at X-band. At Q-band the same trend followed except the signal at $g_{eff} \approx 2.0$ which dominated at 170 K. This signal was assigned to represent the LS state. Importantly, traces of the HS state signals were still present at 100 K.
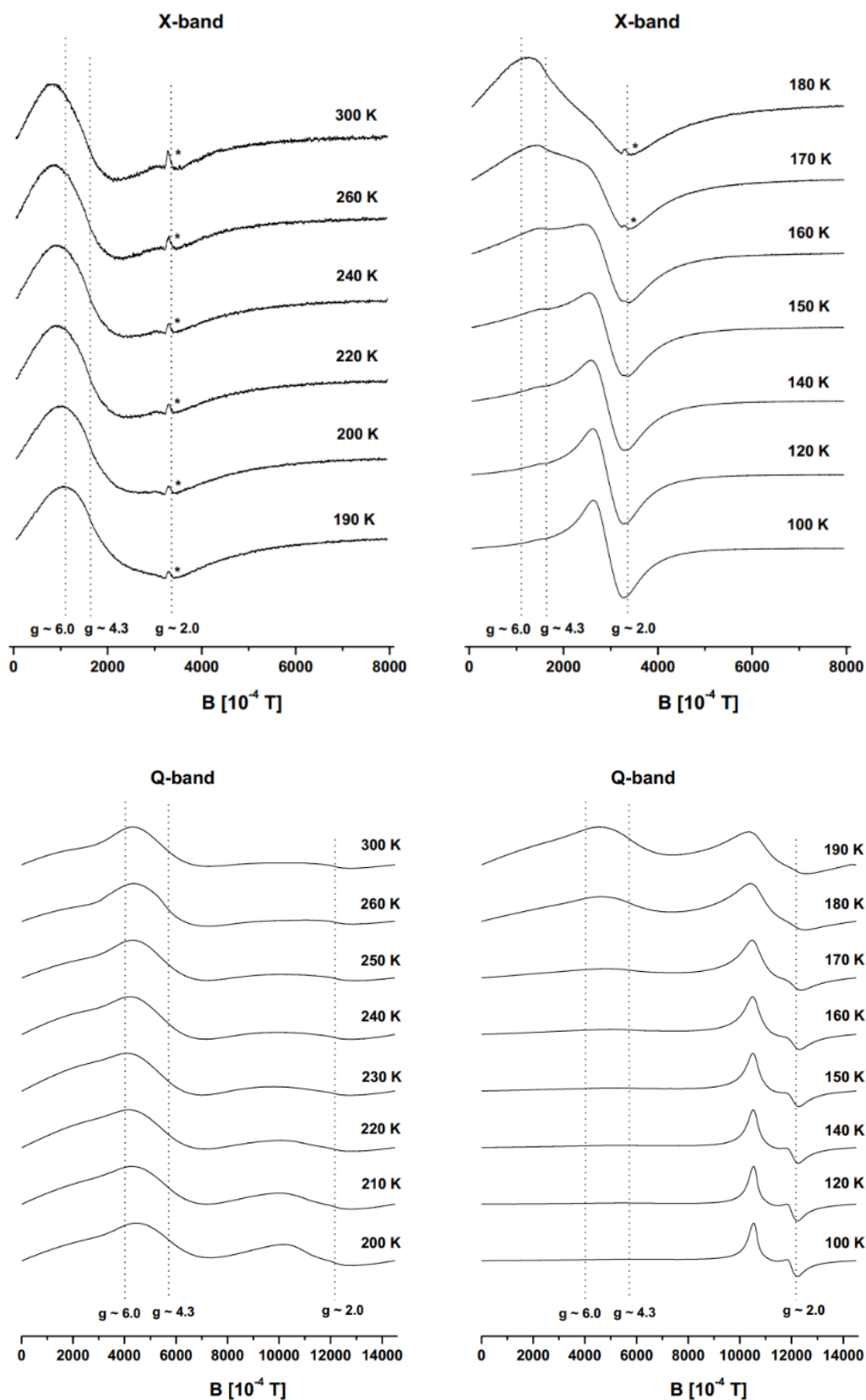
Figure 2.14 Variable temperature X-band (top) and Q-band (bottom) EPR spectra of an Fe(III) complex illustrating SCO behaviour, evidenced by evolution of new signal. Asterisk indicates an impurity in the EPR cavity.[37]

2.1.7 Synthesis of Schiff-base ligands

Having demonstrated the utility of Schiff-base ligands and noted the correlation between ligand design and efficacy in a broad range of applications, the various synthetic protocols for these systems will now be discussed. It is first noted that since imine formation from an aldehyde and amine (a) is a reversible reaction, removing water from the system should drive close to a complete reaction. Water molecules can act as nucleophiles and therefore their presence in the reaction mixture presents a risk of the reverse reaction and therefore hydrolysis of the newly formed imine ((d), **Figure 2.15**). Imines can also react reversibly with amines via transamination (c) and preformed imines via metathesis (b).
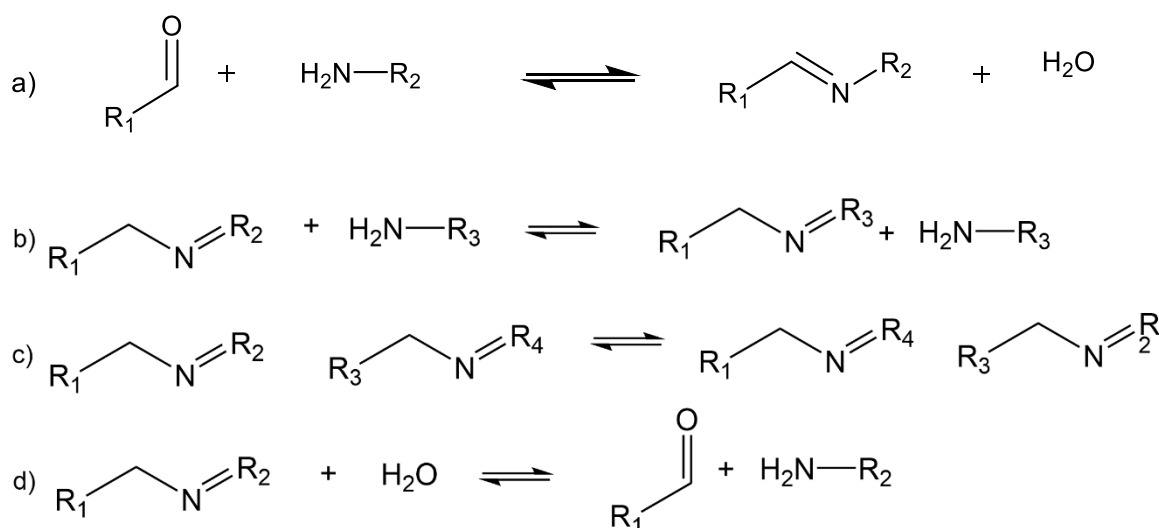
Figure 2.15 Reversible reactions involving imines. a) condensation reaction b) imine-amine transamination; c) imine metathesis; d) hydrolysis.

Generally, imine synthesis occurs in a stepwise manner via the formation of an intermediate carbinolamine, and subsequent water elimination to yield the desired final imine product (**Figure 2.16**). When reactions are performed under aqueous conditions, the rate-determining step is dependent on the pH. For the primary attack of the nitrogen lone pair on the carbonyl carbon, the reaction requires an acidic pH, whereas the subsequent decomposition of the carbinolamine requires alkaline pH. An alternative mechanism is proposed for organic media, where a polar cyclic four-membered transition state is formed in which an amine proton is directly transferred

to the carbonyl oxygen atom, whilst the new C-N bond is simultaneously formed, in a concerted fashion (**Figure 2.16**, schemes a) and b) respectively).[2]

a) aqueous conditions

b) organic media

carbinolamine
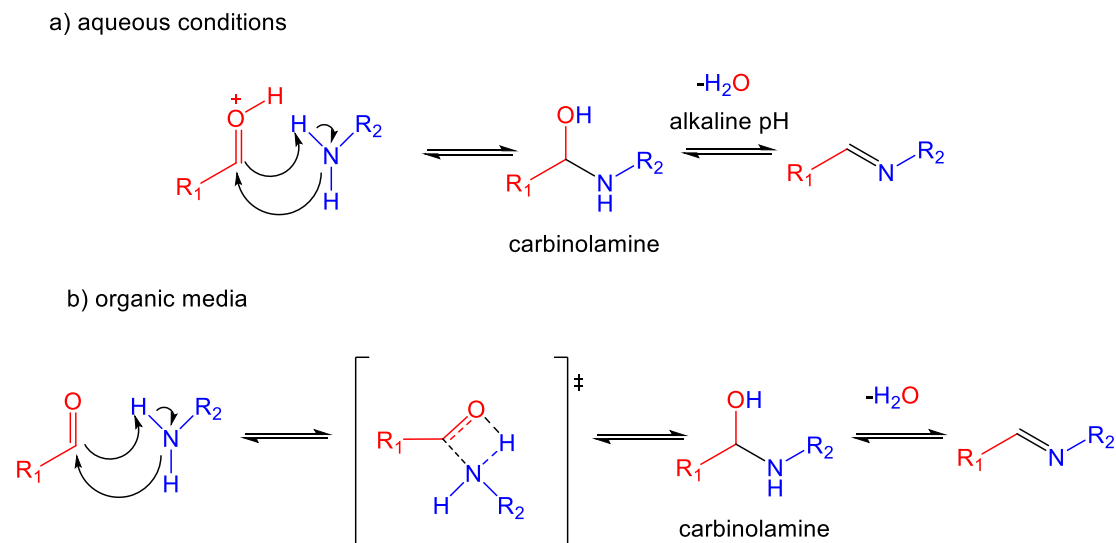
Figure 2.16 Proposed concerted mechanism of imine formation via non cationic intermediate in organic media.

The concerted mechanism is supported by the observation of solvent-dependent rates of reaction (CD$_3$CN, CDCl$_3$, CD$_2$Cl$_2$ or CD$_3$OD). The effect of the chosen solvent is evidenced by reports of an equilibrium being achieved 37 times slower in CDCl$_3$ (dielectric constant = 4.81) than in CD$_3$CN (dielectric constant = 37.5). In a protic solvent (CD$_3$OD, dielectric constant = 32.7), the reaction appears slower than in CD$_3$CN. This therefore rules out the possibility of the solvent acting as a proton shuttle.[45] Rebek and co-workers were able to isolate the carbinolamine and study it by ^{1}H NMR spectroscopy. Their aldehyde of choice, anthracene-1-carboxaldehyde, was attached to a synthetic cavitand (mesitylene) (**Figure 2.17**). Once formed, the carbinolamine intermediate is stabilised in its introverted position by hydrogen bonds between itself and secondary amide groups lining the cavity. Dehydration of the intermediate is retarded by a transition barrier within the cavitand and therefore allowed the Rebek group to carefully study the intermediate.[46]
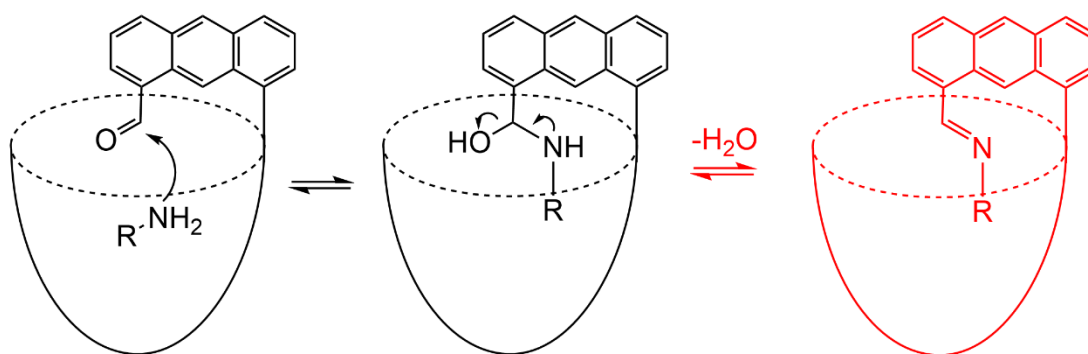
Figure 2.17 Representation of the cavitand function in isolating carbinolamine intermediate. The dehydration step presented for completion, albeit retarded, is shown in red.

2.2 Aims

The aim of research detailed in this chapter was to develop a series of Schiff-base Cr(III) complexes and to investigate their various luminescent properties. Moreover, a series of analogous Fe(III) complexes was targeted in order to probe the field strength of the ligands and utilise this information in the analysis of the photophysical data obtained for Cr(III) complexes. In addition to a characterisation of the photophysical properties of the Cr(III) complexes via UV-Vis and luminescence spectroscopy, EPR spectroscopy was employed to obtain information about the electronic properties of the synthesised complexes.

2.3 Results and discussion

2.3.1 Synthesis

Four Schiff-bases with a variety of functional groups were synthesised and fully characterised. The synthesis of ligands L_{1-4} have been reported before in the literature, hence similar protocols were adopted herein (**Figure 2.18**).[47, 48, 49, 50]

L_1	qsal-2-OH-5	R_1 = OH, R_2 = H, R_3 = H
L_2	qsal-2-OH-5-OMe	R_1 = OH, R_2 = H, R_3 = OMe
L_3	qnal-2-OH *	R_1 = OH, R_2 = H, R_3 = N/A*
L_4	qsal-2,3-OH	R_1 = OH, R_2 = OH, R_3 = H
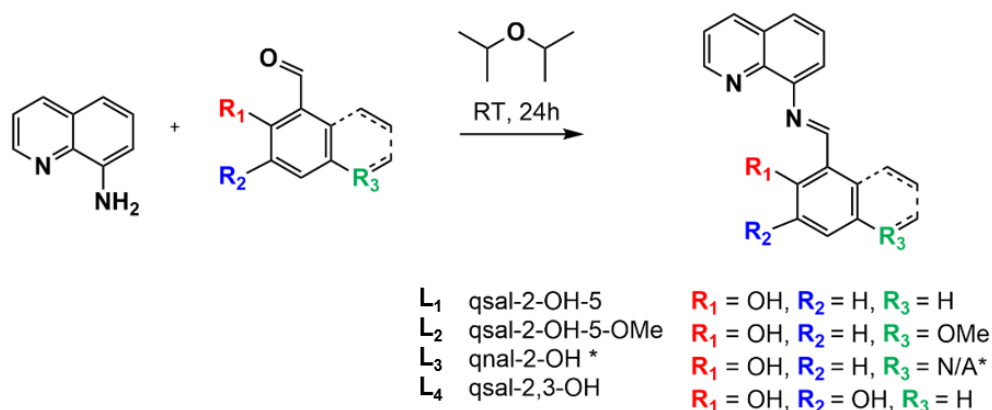
* core is naphthal ring

Figure 2.18 Synthetic protocol for Schiff-base ligands.

The reactions for ligands L_1 to L_4 were stirred in di-isopropyl ether for 24 hours, after which solutions of L_1 to L_3 appeared as bright orange to red in colour, whereas L_4 reaction resulted in formation of a dark red precipitate which was subsequently filtered and washed with small amounts of hexane to remove any remaining impurities trapped within the powder. Slow evaporation of di-isopropyl ether from the reaction solutions of L_1 and L_3, afforded brightly coloured crystals (L_1: red, L_3: orange), which were then filtered under vacuum and washed with small amounts of hexane. Upon evaporation of di-isopropyl ether, the L_2 reaction mixture afforded a brown oil. The addition of a few drops of ethanol allowed for red-orange crystals to form after 20 mins, which were filtered under vacuum and dried in air.

The ligands were obtained via a condensation reaction of an aldehyde and an amine, therefore ^{1}H NMR spectroscopy was used to monitor the reaction by following the presence or absence of distinct signals assigned to reaction substrates and final product. The ^{1}H NMR spectrum of 8-aminoquinoline is expected to show a broad peak ~ 5 ppm which represents the two amine protons. The aldehyde group proton for 2-hydroxybenzaldehyde can be observed ~ 9.8 ppm. A disappearance of the shift around 5 ppm is expected upon formation of the imine product, as this functional group does not bear any protons bonded directly to the nitrogen atom. In contrast, the chemical shift of the aldehyde proton at 9.8 ppm is expected to shift downfield upon imine formation, due to further proton deshielding afforded by the more electronegative (in comparison with carbon atom) nitrogen atom (cf. carbonyl oxygen). As an illustrative example, the imine proton was observed ~ 13.8 ppm for **L-2** (**Figure 2.19**) with the proton shown in red being that represented by the aforementioned shift.
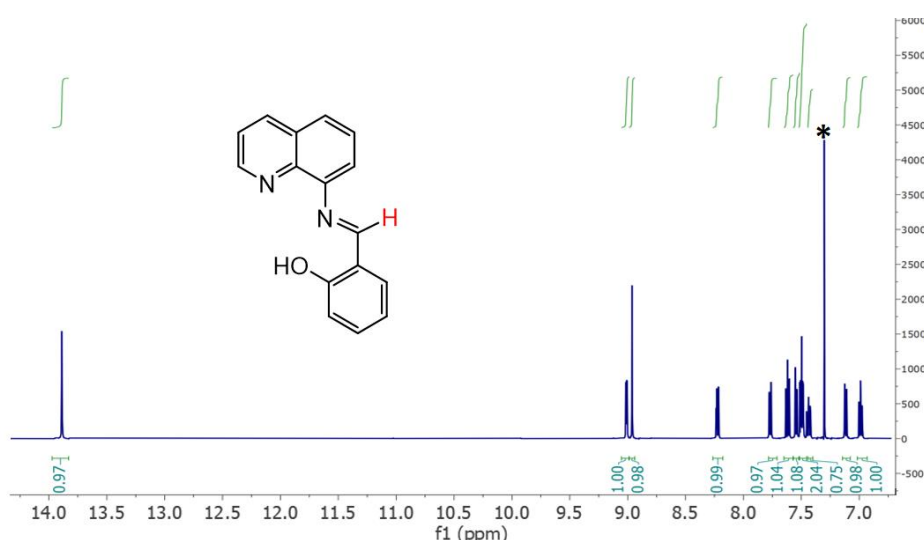
Figure 2.19 ^{1}H NMR spectrum of qsal-2-OH (**L$_2$**) recorded in CDCl$_3$. The proton shown in red represents the shift observed at 13.90 ppm used to identify a successful synthesis of qsal/qnal ligands reported in this chapter. Asterisk signifies residual solvent.

Further to the ligand synthesis, four respective Cr(III) complexes were synthesised (**Figure 2.20**), and their characterisation is discussed below.

(Cr-1) [Cr(qsal-2-OH-5-OMe)$_2$]PF$_6$ R_1 = H R_2 = OMe
(Cr-2) [Cr(qsal-2-OH)$_2$]PF$_6$ R_1 = H R_2 = H
(Cr-3) [Cr(qnal-2-OH)$_2$]PF$_6$ R_1 = N/A* R_2 = N/A*
(Cr-4) [Cr(qsal-2,3-OH)$_2$]PF$_6$ R_1 = OH R_2 = H
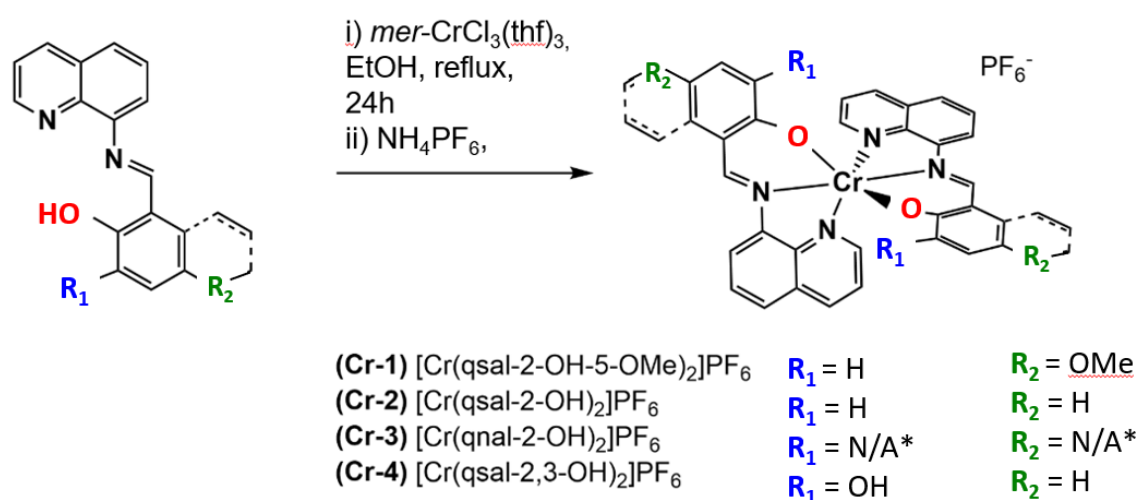
* core is naphthal ring

Figure 2.20 Synthetic scheme for obtaining complexes **Cr-1** to **Cr-4**.

The synthesis of the complexes included an overnight reaction of *mer*-CrCl$_3$(thf)$_3$ which was added to a dry ethanol solution of the ligand at reflux. Upon cooling, the resulting precipitate was filtered and recrystallised from hot acetone which allowed for removal of unreacted starting materials and/or any potential impurities. This was enabled due to the Cl$^-$ salt of the complex having only partial solubility in acetone. Once filtered, the resulting powder was redissolved in small amount of methanol and NH$_4$PF$_6$ was added in excess to induce counterion exchange. This final step improves the solubility of the Cr-based complexes, and acts to remove any potential impurities remaining soluble in methanol. In the case of poor precipitation of the final complex, a few drops of distilled water were added. Red to brown precipitates were obtained for complexes **Cr-1** to **Cr-4**, which were subsequently filtered and dried on air. The purity was assessed by thin layer chromatography (TLC) using MeCN/H$_2$O (7:1) solvent system. All complexes were run through an alumina column plug in MeCN solvent system to remove trace NH$_4$PF$_6$ prior to characterisation.

Elemental analysis results for all complexes provided inconclusive data and therefore LC-MS was used to analyse the sample purity. An exemplary mass spectrum of complex **Cr-1** is shown in **Figure 2.21** clearly indicating the expected molecular ion peak at 606.1371 *m/z* (all other spectra are given in **Appendix 2**).
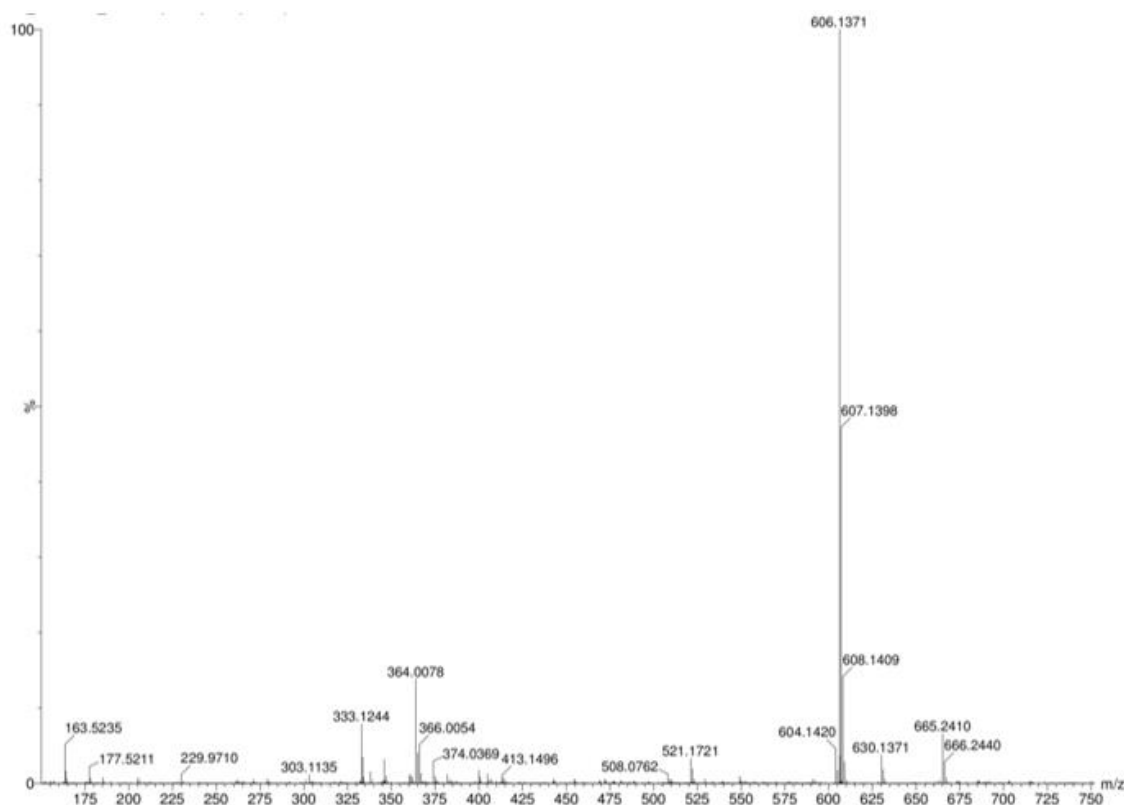
Figure 2.21 Mass spectrum for **Cr-4** ran using electrospray ionisation in MeCN.

All complexes were characterised by LC-MS (**Appendix 2**), although a good quality chromatogram of **Cr-3** could not be obtained, nevertheless TLC analysis showed only one spot. Due to the increased lipophilicity of the **Cr-3** complex (due to the additional phenyl ring in the ligand framework) it is possible that this sample would stick to the C-18 column used for the LC-MS measurements, thereby generating only a very low signal detectable amongst other background impurities.

Following on, four Iron (**Fe-1** to **Fe-4**) analogues of complexes **Cr-1** to **Cr-4** were synthesised to investigate the effects of ligand field strength on the SCO character of formed complexes. Ligands **L-1** to **L-4** were stirred with $FeCl_3$ in MeOH under reflux for 3 hours. Upon cooling, dark brown to black precipitates were obtained which were recrystallised from acetone followed by counterion exchange to form PF_6^- salts as described for the synthesis of Cr(III) complexes.

2.3.2. Photophysical Properties

The room temperature UV-Vis measurements of L_1 to L_4 were recorded in MeCN (**Figure 2.22**). All ligands presented strong π-π^* transitions within the 200-250 nm region. L_1 to L_4 show n-π^* transitions of the imine within the 300-400 nm region, L_1 showed a transition around 470 nm that is likely of π-π^* or CT character based on the molar extinction coefficient value of ~5000 M^{-1} cm^{-1}. Further to this, L_3 shows two additional overlapping bands at 449 and 476 nm, likely to be charge transfer in character such as that of L_4 observed around 355 nm (ε > 10000 M^{-1} cm^{-1}). [48, 49, 50, 51]
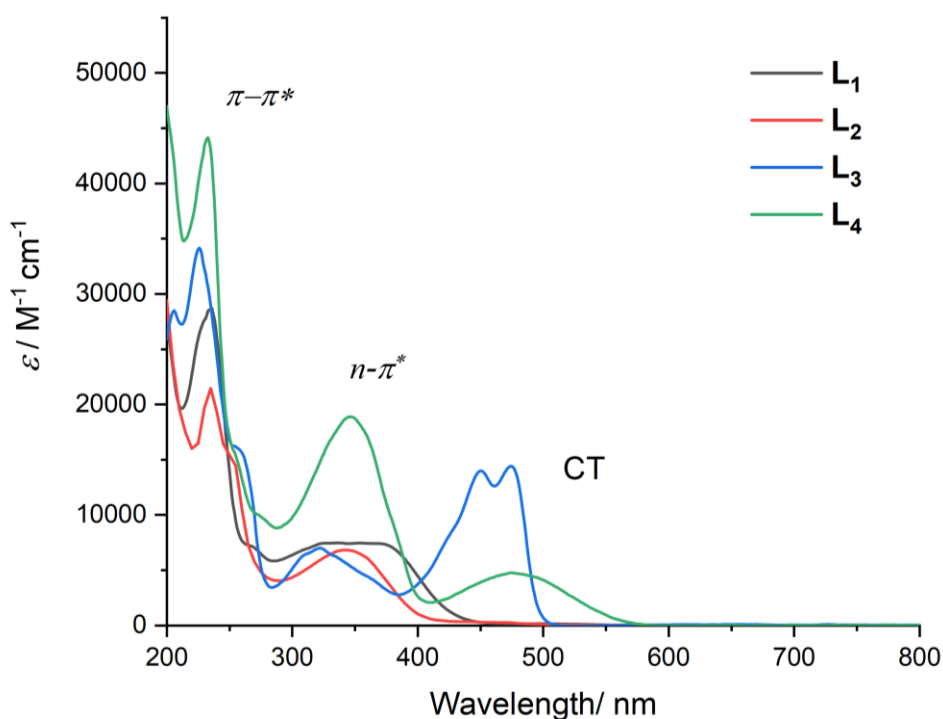
Figure 2.22 Overlay of the UV-Vis spectra for **L-1** to **L-4** in MeCN at room temperature.

The UV-Vis spectra of complexes **Cr-1** to **Cr-4** were also recorded in aerated MeCN (**Figure 2.23**). The bands around 250-350 nm are most likely of π-π^* character, whereas the intense bands ($\varepsilon \sim 10\ 000\ M^{-1}\ cm^{-1}$) around 400-600 nm were assigned to CT-type transitions. These spectral features are consistent with the literature reported on similar complexes (see **Table 2.1**).[52,53,54]
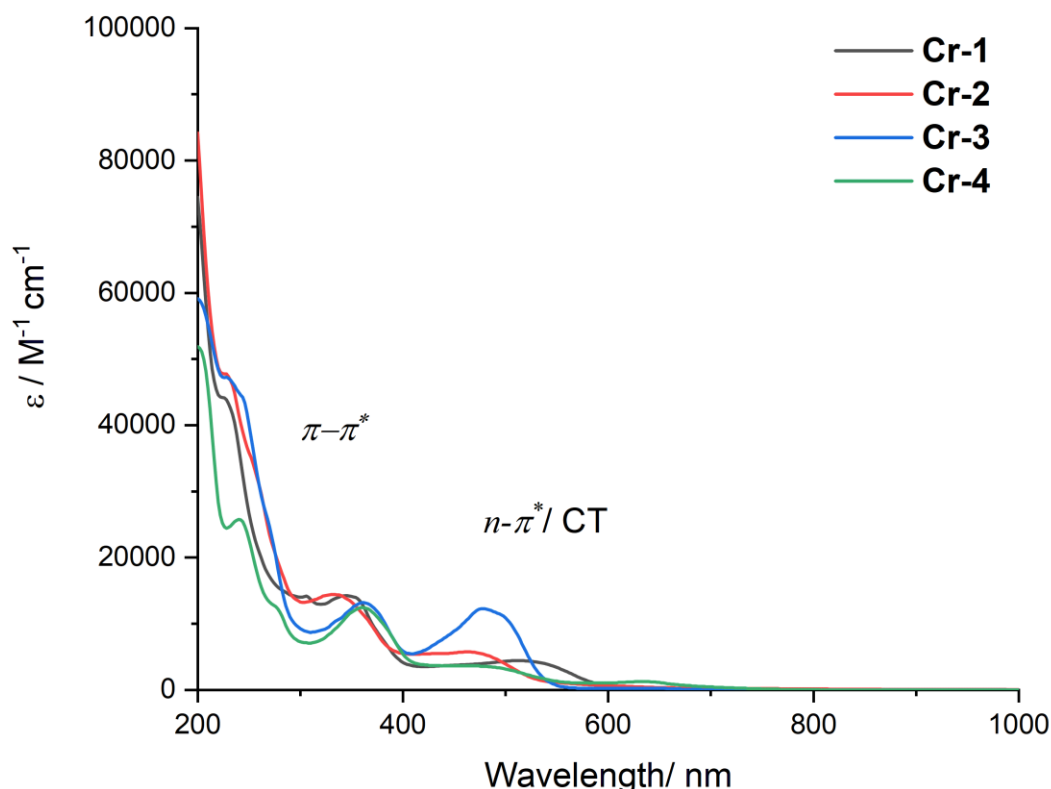
Figure 2.23 UV-Vis spectra recorded for complexes **Cr-1** to **Cr-4** in aerated MeCN.

UV-Vis measurements recorded at higher concentration (10^{-2} M) did not show distinguishable spin-forbidden *d-d* bands for any complexes within the region 600-800 nm. However, due to the highly concentrated solutions and obvious issues with solubility the baseline appeared broader than expected, therefore likely obscuring these signals.

Values for spin-forbidden d-d transitions reported in the literature for polypyridyl chromium(III) complexes such as $[Cr(dqp)(tpy)]^{3+}$, $[Cr(ddpd)(dqp)]^{3+}$ and $[Cr(dqp)(dqpOMe)]^{3+}$ (**Figure 2.24**) are reported within 670-800 nm.[55] All of these reports assign the bands at higher energy to the $^4A_2 \rightarrow {}^2T_1$ transition and the bands at

lower energy to the $^4A_2 \rightarrow {}^2E$ transition. These assignments arise directly from the associated Tanabe-Sugano diagram for d^3 systems where the ^2E state lies below the doublet state $^2T_1$ at all times (**Figure 1.8**). This shows that the $^4A_2 \rightarrow {}^2T_1$ transition is of higher energy than $^4A_2 \rightarrow {}^2E$ and therefore is seen at a shorter wavelength in the UV-Vis spectrum.
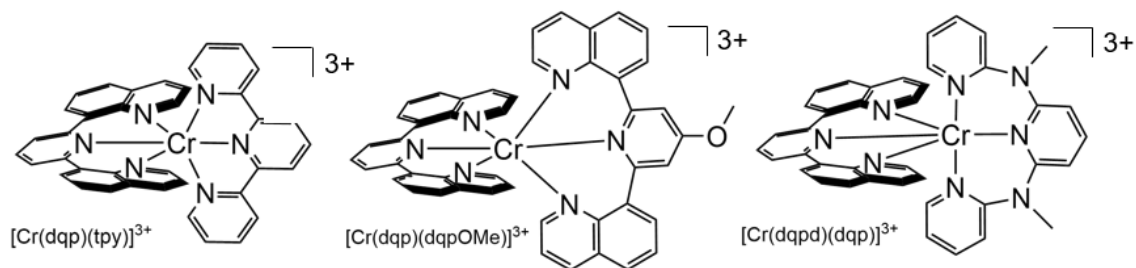
Figure 2.24 Cr(III) complexes with tridentate ligands coordinated for which d-d bands of spin-forbidden nature were measured in the 600-800 nm region.

Table 2.1 Representation of UV-Vis data for Cr-1 to Cr-4 and similar metal complexes reported.

Compound	UV-Vis data/ nm (cm^{-1})
Cr-1	229 (44284), 306 (13893), 350 (14119), 516 (4584)
Cr-2	231 (47623), 259 sh (31635), 339 (14572), 473 (5461), 569 (820).
Cr-3	236 (46491), 273 sh (24533), 363 (12790), 480 (12110).
Cr-4	206 (50707), 241 (25664), 278 (11686), 361 (11912), 489 (3904), 636 (1245).
[Zn(L$_1$)$_2$]	350 (10 150), 466 (781)
[Ni(L$_1$)$_2$]	330 (sh, 16 600), 338 (17 760), 353 (sh, 12 640), 465 (15 960)
[Ni(L$_2$)$_2$]	341 (10 760), 371 (sh, 6560), 520 (11 800)
[Al(L$_3$)]$^+$	330, 440, 480

The room temperature emission spectra for **L-1** to **L-4** were recorded in MeCN solvent using 320 nm excitation wavelength. The emission bands observed for **L-1** to **L-4** are listed in **Table 2.2**. There are multiple emission bands observed for each ligand with **L-4** showing four emission bands. In instances in which the conjugation within the ligand systems is disrupted, the quinoline moiety is expected to emit at a longer wavelength compared to the phenolate/naphtholate moieties. This is deducted from a direct correlation between the extent of the conjugation present within a molecule and its effect on the HOMO-LUMO gap.[56] From the results listed in **Table 2.2**, it is shown that the first emission band for **L-1** appears at higher energy of 23530 cm^{-1} than **L-2** and **L-3**, which are comparable with one another (18510 and 18690 cm^{-1} respectively). Since there are no substitutions on the quinoline part of the ligand, this would suggest that the substituents on the phenol ring influence the electronics of the quinoline moiety since all four ligands present the first emission band at different wavelengths (375, 425, 360 and 280 nm).

A similar effect is observed for L_4 for which the second emission band was observed at 440 nm. Ligand L_1 experiences destabilising effects from one of the two substituents, namely OH and OMe groups, both of which donate lone pairs of electrons into the phenyl ring by resonance therefore increasing the energy of the emission. This becomes clear when the phenolate emission band (375 nm) is compared to L_2 (425 nm), suggesting that since both ligands experience the influence of the OH group, it is unlikely that this functional group is the cause of higher energy of the singlet excited state in L_1. This is also true for L_4 (280 nm) which experiences electron donating effects from two OH groups. L_3 is expected to show a red-shifted emission due to its extensive conjugated system, however the OH group might have a destabilising effect and therefore causes a blue-shift in the emission (535 nm) with respect to the first emission band of L_2. No reasonable explanation for the resulting four emission bands for L_4 was found.

It is possible that the second emission band for ligands L_1 to L_3 originates from a triplet excited state and therefore represents a spin-forbidden relaxation, however since the UV-Vis bands observed are all ϵ >10 000 M^{-1} cm^{-1} it is difficult to confirm any potential spin-forbidden transitions in the region of the excitation wavelength used for the measurements (350 nm) as those would be expected to have low molar extinction coefficient values.

Table 2.2 Emission properties of L_1 to L_4 at 350 nm excitation.

	Emission/ nm (cm^{-1}))
L_1	375 (26660), 425 (23530)
L_2	425 (23530), 540 (18520)
L_3	360 (27780), 535 (18690)
L_4	280 (35710), 370 (27030), 440 (22730), 630 (15870)

The room temperature emission spectra for **Cr-1** to **Cr-4** were recorded in MeCN solvent using 350 nm excitation wavelength (**Figure 2.25**). All of the chromium complexes presented bands in the 400-550 nm range, possibly arising from a ligand based transition. Complexes **Cr-1** to **Cr-3** show two bands compared to complex **Cr-4** which presents only one emission band. The first emission band for all complexes is centred at ~425 nm; in contrast, the second emission band presents some variability across the series. For **Cr-1** the second band is observed at 510 nm, whereas this is red-shifted to 525 and 550 nm for complexes **Cr-2** and **Cr-3**, respectively. Since all the ligands contain OH substitution in the ligand framework, the emission band at 525 nm for complex **Cr-2** is treated as the benchmark in this analysis. In complex **Cr-4,** it is possible that the second emission band is buried within the broad emission band observed over the range of 400-500 nm.

No sharp emission bands in the NIR region were observed. As discussed in the introductory chapter (see **Section 1.3.1**), doublet excited emission bands appear as one intense sharp band (^2E) with a weaker shoulder to its left ($^2T_1$). Therefore, no doublet excited state emission was observed for complexes **Cr-1** to **Cr-4** at room temperature.
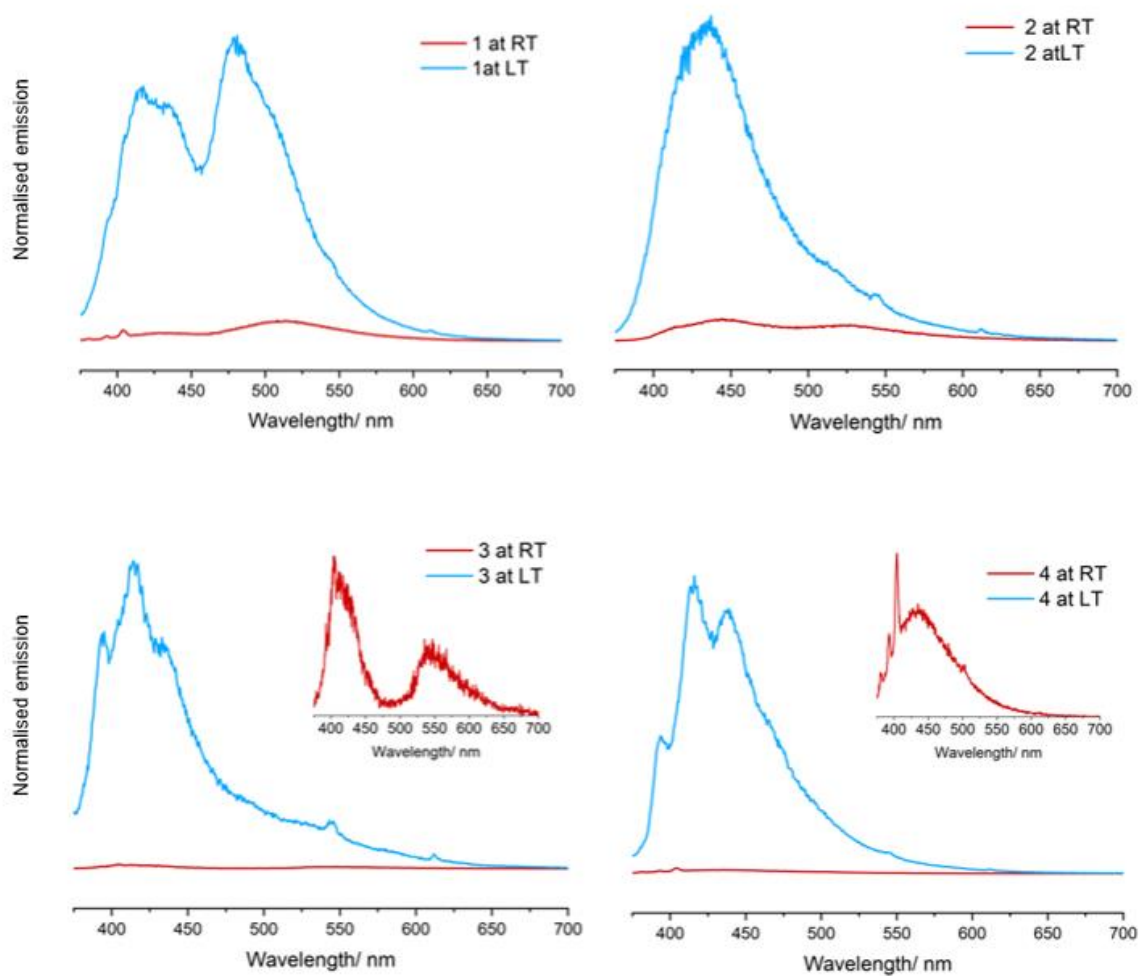
Figure 2.25 Emission spectra of complexes **Cr-1** to **Cr-4** recorded in aerated MeCN at 298 and 77 K; excited with 350 nm. Insets show expansion of the room temperature spectrum.

As discussed in **Section 1.2.6**, performing emission spectroscopy at low temperature (77 K) eliminates oxygen quenching as one of the deactivating pathways. This should lead to enhanced emission and longer excited state lifetimes. Naturally, all four Cr-based complexes show increased intensity at low temperature as shown in blue (**Figure 2.25**). However, despite increased emission intensity, the spectra recorded at low temperatures still contained unresolved peak regions. These may be a result of a poor-quality glass of the frozen solutions which can cause scattering of the emitted light and/or the presence of multiple overlapping vibronic bands showing, which are sharp and are normally buried within the broad emission bands caused by the broadening effects of the solvent environment.[57,58] At low temperatures, all complexes show similar features to the spectra recorded at room temperature. Complex **Cr-1** shows two emission bands, whilst complexes **Cr-2** to **Cr-4** show only one emission band with a slight red-shifted shoulder at low temperature. It is possible that the non-substituted phenolate ring moiety for both ligands of complexes **Cr-2** and **Cr-3** experiences a higher level of C-H deactivation (see **Section 1.4.2**). Since vibrations are possible at low temperatures, this seems feasible.[59] More importantly, no evidence of sharp doublet excited state emission bands was observed at 77 K.

2.3.3. DFT geometry optimisation and TD-DFT UV-Vis simulation

As discussed in **Chapter 1**, the spin-forbidden emission from the doublet excited state of Cr(III) is largely governed by the geometry of the complexes. Since no doublet excited state emission was observed (**Section 2.3.2**) for **Cr-1** to **Cr-4**, it is rational to investigate the geometry of the complexes.

No crystal structures were obtained for the complexes synthesised in this chapter (despite numerous attempts) and therefore supporting DFT studies were performed to analyse the geometry of the complexes (see **Section 2.5.2** for experimental details). This section will explore the bond angles and bond lengths for **Cr-1** to **Cr-4** to investigate whether distortion from the octahedral geometry is responsible for doublet state deactivation. To do this, trans angles and bond lengths are investigated. **Tables 2.3** and **2.4** list Cr-N-N/ Cr-N-O angles and Cr-N/Cr-O bond lengths, respectively, with the shortest bond lengths shown in green. **Figure 2.26** illustrates the relevant atom numberings.
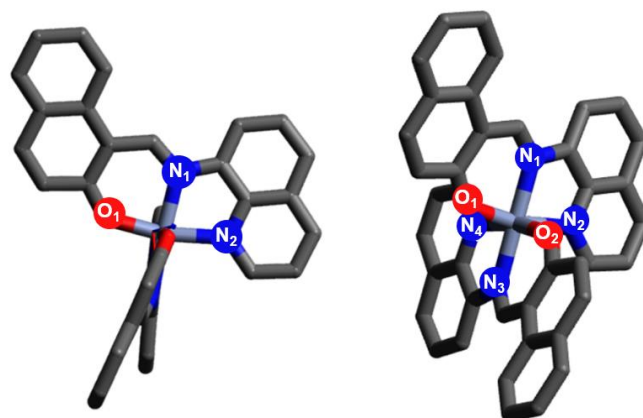
Figure 2.26 Geometry optimized structure for **Cr-3** showing the distortion across the N_2-Cr-O_1 trans angle. The alternative angle showcases all remaining atoms, namely O_2, N_3 and N_4.

Table 2.3 Cr-N-O and Cr-N-N angles from DFT geometry optimisation of the ground state.

	Cr-1	Cr-2	Cr-3	Cr-4	[Ni(qsal-5-Cl)$_2$]	[Ni(qsal-5-Me)$_2$]
N_2-Cr-O_1 (°)	170.93	170.19	168.71	170.99	161.49	161.04
N_1-Cr-N_3 (°)	175.57	175.43	176.28	176.28	172.17	171.46
N_4-Cr-O_2 (°)	169.58	170.19	168.71	170.91	161.53	161.02

Table 2.4 Cr-N/Cr-O bond lengths extracted from geometry optimisation DFT calculations.

	Cr-1	Cr-2	Cr-3	Cr-4	[Ni(qsal-5-Cl)$_2$]	[Ni(qsal-5-Me)$_2$]
Cr-N_1 (Å)	2.109	2.103	2.100	2.084	2.226	2.234
Cr-N_2 (Å)	2.057	2.056	2.039	2.051	2.200	2.193
Cr-N_3 (Å)	2.112	2.103	2.100	2.082	2.226	2.234
Cr-N_4 (Å)	2.052	2.056	2.039	2.063	2.200	2.193
Cr-O_1 (Å)	**1.940**	**1.937**	**1.933**	**1.940**	**2.071**	**2.2067**
Cr-O_2 (Å)	**1.927**	**1.937**	**1.933**	**1.926**	**2.069**	**2.2067**

Upon consideration of the trans angles across the complexes, it becomes clear that distortion away from octahedral is the case for all four complexes with the trans angles observed for **Cr-1** to **Cr-4** within the range 169-175°, where angles of 180° are expected for complexes with octahedral geometry. Similar results were observed for a series of [Ni(qsal-R)] complexes.[53] This therefore suggests that deactivation of the doublet excited state proceeds through quadrate splitting (O_h to D_{4h} symmetry reduction) as discussed in **Section 1.4.2**. This results directly from the nature of the

complexation of qsal/qnal ligands to the Cr(III) centre, where five- and six-membered chelate rings are formed upon coordination that introduce significant strain on the system. From these observations it is therefore suggested that a ligand system that contains two five-membered rings or two six-membered rings (as opposed to a combination) would be more beneficial for obtaining doublet excited state emission. Detailed discussion of such systems is provided in **Chapter 3** and **Chapter 4**. As previously described in **Section 1.3.1**., quadrate splitting has its consequences in the electronic structure and therefore the observed electronic transitions of the Cr(III) complexes. One of the results is that the former $^2T_1$ state becomes the lowest lying excited state and therefore the emission of this doublet excited state can only be observed when the separation between the ground and excited states is large enough for the radiative decay to be able to compete with non-radiative decay. Its broad appearance is due to the differences in the geometry of the ground and excited state which is not the case for octahedral Cr(III) complexes where the ^2E state is the lowest lying excited state with little difference in the geometry between the ground and excited states (see **Figure 2.27**)

Ground state

Lowest lying excited state

Ground state

Lowest lying excited state

O_h

D_{4h}
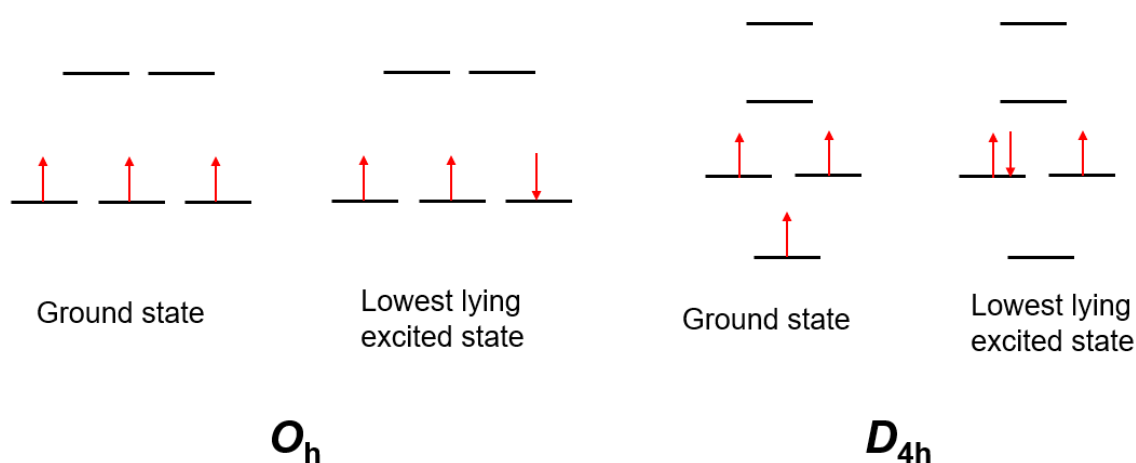
Figure 2.27 Partial MO diagrams showing frontier orbitals for octahedral and quadrate geometries with ground state and lowest lying excited state shown.

Considering that the emission of the complexes is assumed to be ligand-based, the UV-Vis transitions of the complexes were simulated using TD-DFT to support this assignment and the detailed discussion of the results follows in this section.

The calculated geometries were used to proceed with time-dependent density functional theory (TD-DFT) calculations to obtain information on the expected

absorption transitions and the possibility to simulate the UV-Vis for all four complexes. A diffuse function was applied in the calculations in order to afford a higher level of accuracy and closer representation of the experimental results. Polarisation functions were also applied to allow for consideration of the charge polarisation away from the atomic distribution to occur which minimises electron-electron repulsion and to ensure correct computation of the molecular orbitals/chemical bonds.[60,61]

The calculated and experimental UV-Vis spectra for **Cr-1** to **Cr-4** are shown in **Figure 2.28**. The TD-DFT calculations are in good agreement for complexes Cr-3 and Cr-4 in particular whilst lacking for the remaining two complexes with the experimental data within the 300-600 nm range for all complexes. The TD-DFT calculations also predict a series of metal centred transitions around 600 nm but as mentioned previously these were not detected experimentally, even at high concentrations (10^{-2} M; **Section 2.3.2**).
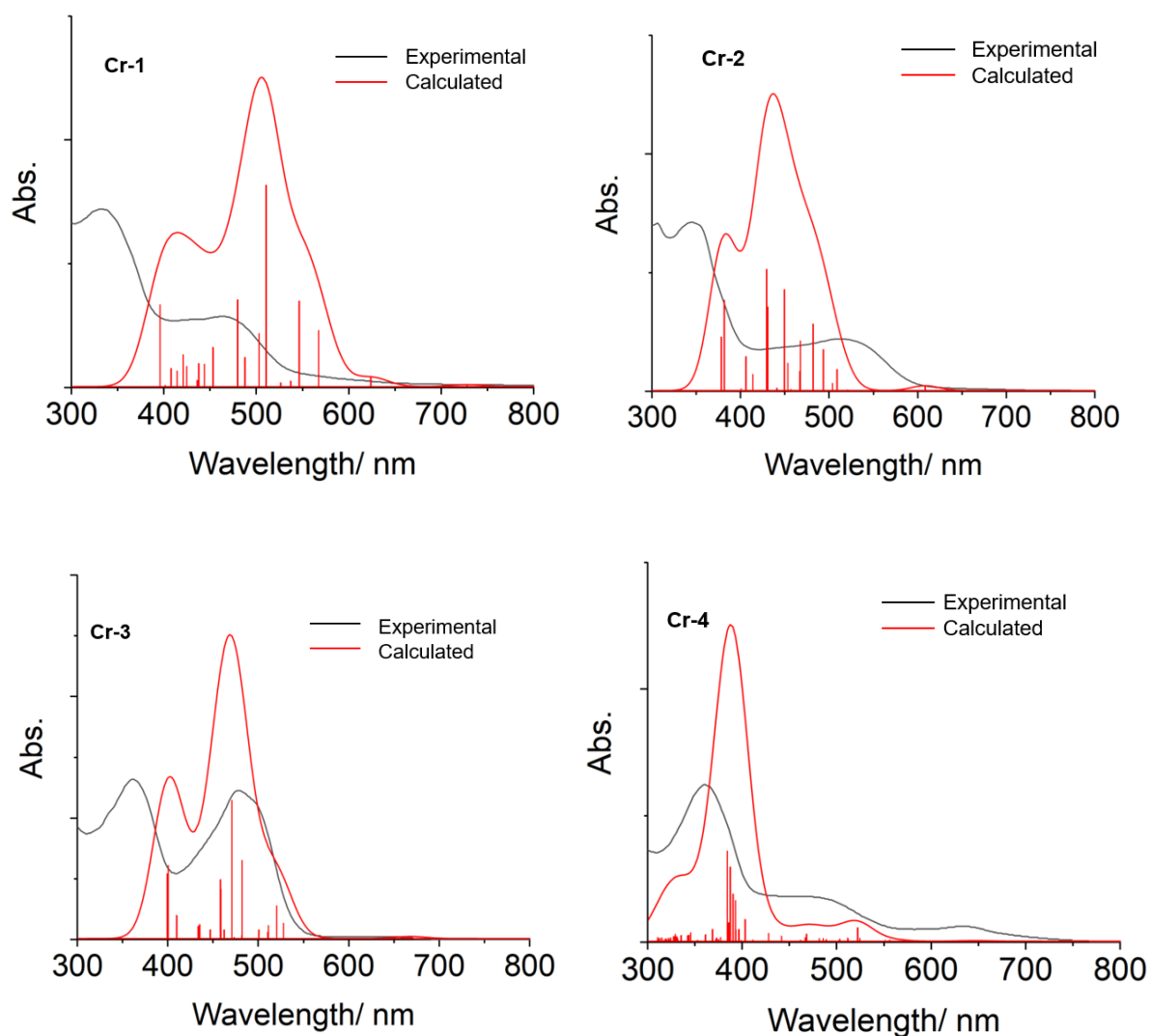
Figure 2.28 TD-DFT calculated UV-Vis spectra plotted against the experimental data for **Cr-1** to **Cr-4**.

An investigation into the HOMO-LUMO orbitals for these transitions reveal their charge transfer character. As illustrated in **Figure 2.29**, the HOMO orbitals for 399 and 470 nm transitions of **Cr-3** indicate that the electron density is predominantly localised around the ligands, particularly around the phenolate moiety for the transition around 400 nm. The LUMO orbitals seem to occupy an entire ligand with the more intense regions around the naptholate moiety for the second ligand, therefore intraligand (IL) and ligand-to-ligand (LL) charge transfer transitions are possible. Importantly, some contribution from the metal ion is also observed for both HOMO and LUMO orbitals. These transitions are likely of spin-allowed quartet character ($^4A_2 \rightarrow \,^4T_1/^4T_2$) as spin-forbidden spin-flip transitions cannot be calculated for d^3 system using this method.[62]

The HOMO-LUMO models of the remaining complexes presented similar results and the visualisation of those orbitals for all complexes can be viewed in **Appendix 2**.
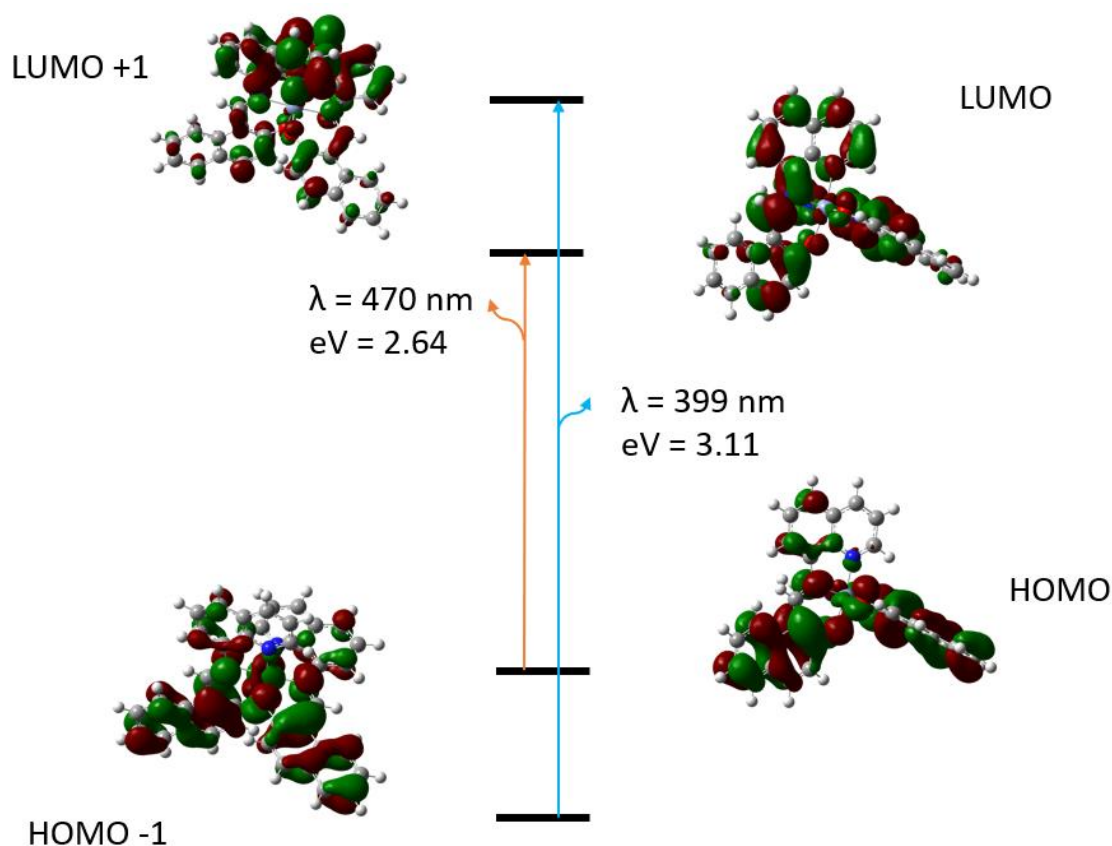
Figure 2.29 Frontier MO's orbitals calculated with TD-DFT for **Cr-3** for two transitions, namely 399 and 470 nm showing LLCT/ILCT/LMCT character. Calculated using previously geometry optimized structures (B3LYP/6-311G(d,p)). TD-DFT calculations were computed using B3LYP functional and def2-SVP basis set with diffusion function accounting for diffuse function and (d,p) accounting for polarisation function.

Therefore, careful analysis of the photophysical properties of complexes **Cr-1** to **Cr-4** obtained experimentally and their comparison with the HOMO-LUMO models calculated with DFT delivered a conclusion that all complexes exhibit ligand based emission with no evidence of doublet excited state radiative relaxation, neither at room temperature, nor 77 K. The geometry analysis (DFT) showed that all complexes show significant distortion away from octahedral geometry introduced by the phenolate/naphtholate coordination evidenced by significantly shorter bond lengths for Cr-O bonds (~1.9 Å) in comparison with Cr-N bond lengths (2.05-2.11 Å). It is

anticipated that the doublet excited state is deactivated due to reduction in geometry (O_h to D_{4h}).

2.3.4 EPR spectroscopy results

In order to determine more information about the electronic structure of the high-spin Cr(III) complexes, EPR spectroscopy was utilised. The EPR spectra of solid samples and dilute solutions of **Cr-1** to **Cr-4** were recorded at room temperature (solid) and 120 K (frozen solutions) using X-band frequency but unfortunately all presented as broad featureless spectra which prevented further analysis and determination of spin-Hamiltonian parameters. The broadening effects in solid state measurements were caused by direct dipole-dipole interactions between the neighbouring Cr(III) centres, meanwhile the frozen solution broadening observed was thought to be due to partial precipitation upon freezing. Several solvent systems were employed to aid this issue, including 9:1 EtOH/MeOH, 1:1 CH_2Cl_2/Toluene and 1:1 MeCN/Toluene. Unfortunately, no significant improvement in the quality of the spectra was observed as seen in the representative example of **Cr-1** (**Figure 2.30**). Analogous measurements at Q-band frequency also generated very broad spectra which are available to view in **Appendix 2**.
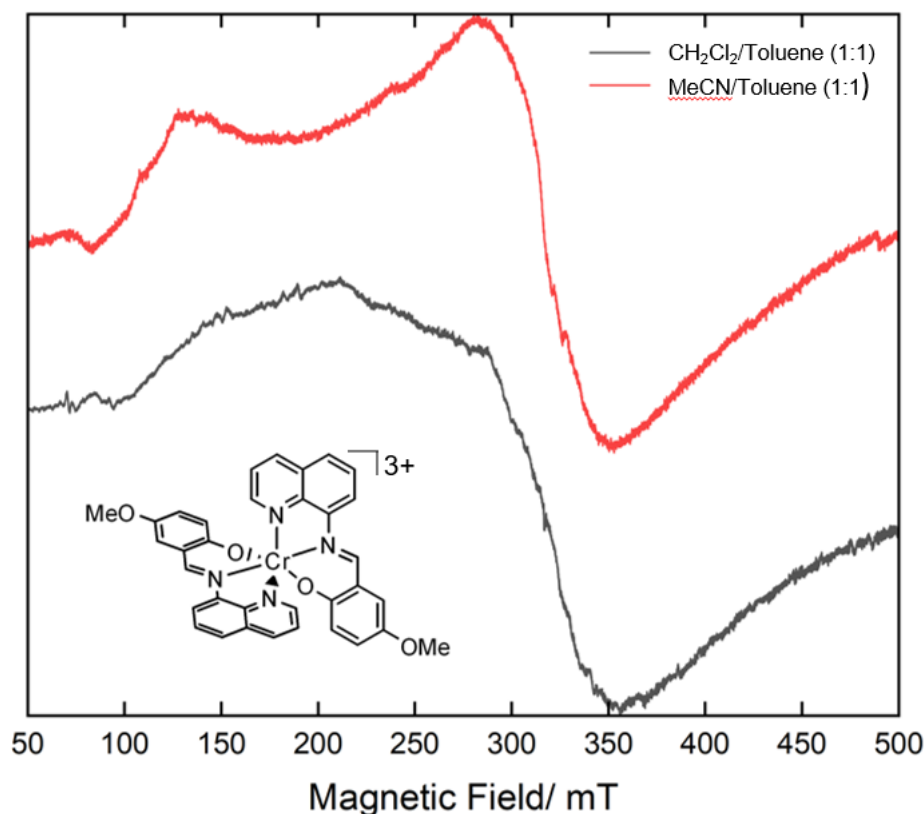
Figure 2.30 X-band EPR spectra (T = 140 K) of **Cr-1** recorded in a) MeCN/Toluene (1:1) and b) DCM/Toluene (1:1) solvent systems.

Following on from the challenging spectra for **Cr-1** to **Cr-4** recorded in solution at 140 K (as exemplified by **Figure 2.30**), solid state measurements were employed. This was motivated by the difficulties with the determination of the correct solvent system for the samples. It was considered that solubility difficulties could have lead to aggregates forming in solution further complicating the signal observed. As discussed in **Section 1.3.1**, complexes with multiple unpaired electrons experience additional interactions which originate from the ZFS and occur between the unpaired electrons which can lead to significant broadening of the resulting EPR spectra. Additionally, interactions between two or more neighbouring Cr(III) spin centres can also lead to spin-spin interactions and result in additional broadening effects. In order to limit the impact of the latter broadening effect on the quality of the EPR spectra, it is good practice to generate magnetically dilute powders which consist of an diamagnetic matrix and the EPR active dopant. Ideally, the matrix should be an EPR silent analogue of the complex which is investigated. For the Cr(III) complexes studied

herein, Co(III) complexes provide ideal host. The magnetically dilute powder effectively isolates the EPR-active species reducing the interaction between neighbouring Cr(III) centres.

Attempts at using 1% doped **Cr-1** in the corresponding Co-matrix generated one weak signal in the X-band EPR spectrum around 330 mT (**Figure 2.32**) with additional broad signals across a wide magnetic field range (50-550 mT, Appendix 2). Unfortunately, a satisfactory simulation of the full experimental results could not be achieved ($+D = 0.082$ cm^{-1}, $E/D = 0.015$, $g_{iso} = 1.99$) used to simulate the spectrum in **Figure 2.31**). Therefore, no other doped powders were generated.
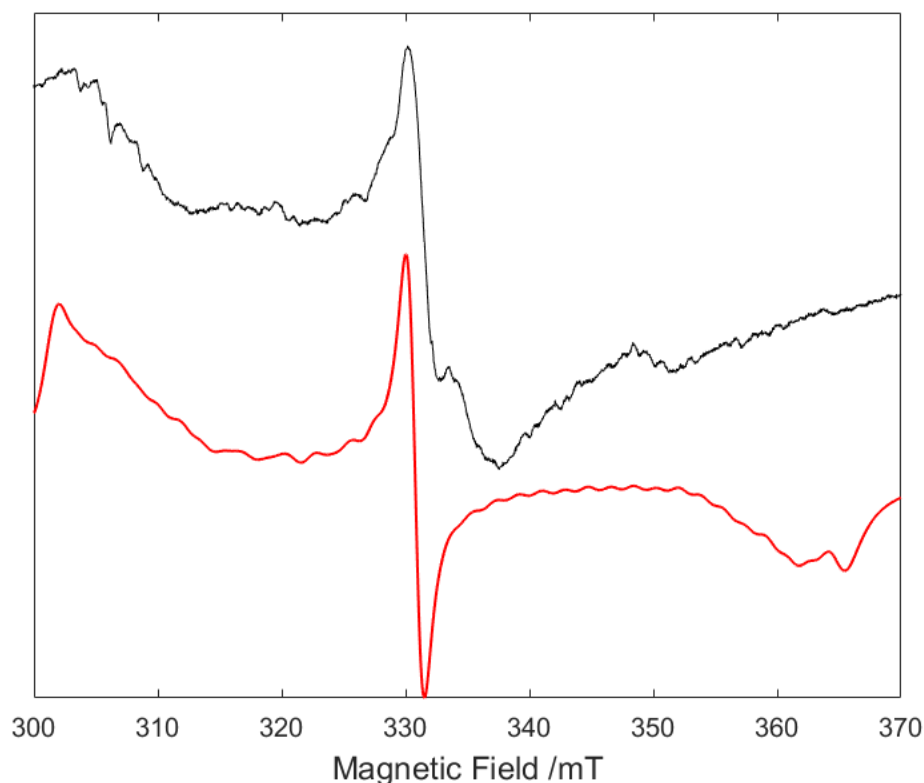
Figure 2.31 X-band EPR spectrum (T = 298 K) of 1% doped solid of **Cr-1** in the equivalent Co(III) matrix. Red = simulation, black = signal. $D = 0.082$ cm^{-1} (2485 MHz), $E/D = 0.015$, g_{iso} = 1.99.

To assist in analysis of the experimental EPR result, the zero-field parameter contributions to the spin Hamiltonian were determined from ORCA calculations on the geometry-optimized ground states for **Cr-1** to **Cr-4** and are listed in **Table 2.5** alongside values for other Cr(III) systems reported in the literature.

Table 2.5 ZFS parameters from ORCA calculations for complexes **Cr-1 to Cr-4**.

Complex	E/D	D (cm^{-1})	g-value		
Cr-1	0.17	0.3	1.99	1.99	1.99
Cr-2	0.14	0.29	1.99	1.99	1.99
Cr-3	0.24	0.31	1.99	1.99	1.99
Cr-4	0.22	0.2	1.99	1.99	1.99
$[Cr(H_2O)_6]^{3+}$ [20]	~ 0	0.1	1.99	1.99	1.99
$[Cr(acac)_3]$ [21]	0.089	0.592	1.99	1.99	1.99

The D-values for all complexes are calculated to be higher than that for $[Cr(H_2O)_6]^{3+}$ (0.1 cm^{-1}) which manifests near-perfect octahedral geometry.[63,64,65] These spin-Hamiltonian results reflect that complexes **Cr-1** to **Cr-4** have distorted octahedral geometry, which is also supported by the DFT geometry optimisation. The E/D values calculated for the complexes are all determined to be much higher than that of $[Cr(acac)_3]$ (0.089) suggesting an increased ZFS interaction localised around the equatorial (xy) plane of **Cr-1** to **Cr-4**, which is consistent with the coordination sphere of two negatively charged oxygen atoms coordinated in the equatorial plane as the coordination of the oxygen occurs via pointing negative charge towards the Cr(III) centre.[66,67] As described in the introductory chapter **Section 3.1**, the E value describes the ZFS interaction in the equatorial plane and therefore an increased E value suggests a distortion away from the octahedral geometry across the equatorial plane which is consistent with the O_h geometry of $[Cr(acac)_3]$ as compared to D_{4h} geometry of complexes **Cr-1** to **Cr-4**.

2.3.5 Effect of Ligand Field on Spin-crossover

As mentioned in **Section 2.1.3**, spin-crossover can only occur when the ligands coordinated are of intermediate field strength. Since no doublet excited state emission was observed from all four chromium(III) complexes and no d-d bands could be detected, four Fe(III) analogues of complexes **Cr-1** to **Cr-4** were synthesised to investigate the ligand field strength of **L₁** to **L₄**. The complexes were expected to demonstrate geometry analogous to their Cr(III) predecessors, that is distorted octahedral across the equatorial plane via shorter Fe-O bonds.

For a high spin system, the expected g_{eff} values depend on the magnitude of the ZFS parameters. For octahedral systems in the Fe(III) oxidation state, two possible

spin states are commonly observed, namely high-spin S = $^5/_2$ low spin S = $^1/_2$ (**Figure 2.32**).

$$S = {}^5/_2 \qquad\qquad S = {}^1/_2$$

Figure 2.32 MO diagram of both spin states observed for octahedral Fe(III) complexes, namely $S = {}^5/_2$ and $S = ½$.

Therefore, at X-band if the two states were to co-exist the EPR spectrum should present a mixture of a low-spin $S = {}^1/_2$ signal, characterised by g(Fe)/A(N) values and additional features arising from the $S = {}^5/_2$ spin state that could be dominated by ZFS, characterised by the D and E values. The spin state observed can be rationalised with the concept of entropy which is associated with the level of disorder in a system and provides insight into the direction of spontaneous change. With increasing disorder, there is a decrease in energy available within the system for conversion, here spin-crossover. As entropy increases alongside temperature, more disordered states (here high-spin state) are expected to prevail at higher temperatures and only reducing the temperature of the system can induce the conversion into a less disordered state (here low-spin state). Therefore, at low temperatures LS states are expected to be observed which spin crossover to the HS as the temperature increases. As entropy is a function of temperature, it is therefore possible for a mixture of spin states to co-exist at borderline temperatures specific to each system.[68] For strong field ligands, Fe(III) is expected to exist in its low-spin state at room temperature as only borderline field strength ligands facilitate SCO.

The X-band EPR spectra of complexes **Fe-2** to **Fe-4** showed signals at $g_{eff} = 2$ (**Figure 2.33**), with the signal around $g_{eff} = 4.3$ are likely to be of background noise origine (dust). As the expected g_{eff} values for octahedral geometry with $S = {}^5/_2$ are ~ 6 and ~ 2, whilst for $S = {}^1/_2$ g is expected to fall around 2. For rhombic geometry, HS g_{eff} values complicate leading to several expected values (~ 10, ~4, ~1), therefore it is likely that these signals are a representation of LS states at room temperature.[69] Given

that hexafluorophosphate counterion was determined to allow for spin-crossover (see **Section 2.1.6**) it is concluded that the Schiff-base ligands present strong field and therefore rules out BISC deactivation (**Section 1.2.2**).
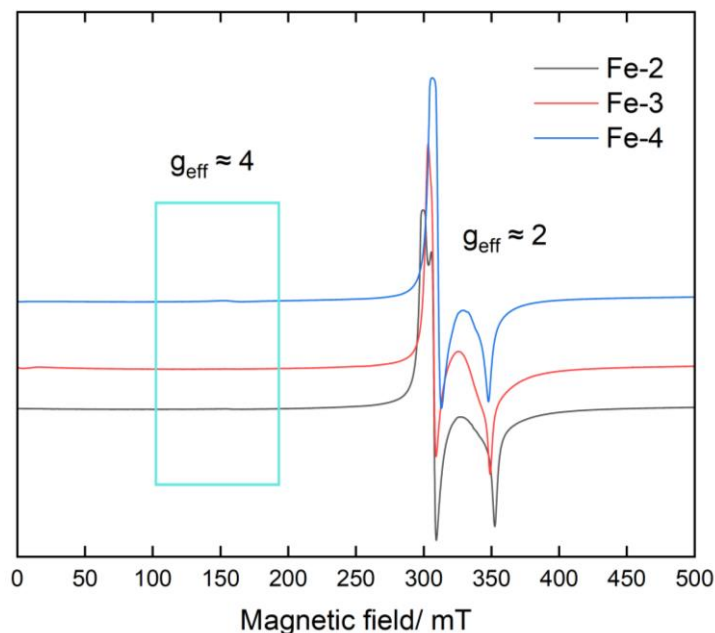
Figure 2.33 X-band EPR spectrum of complexes **Fe-2, Fe-4** and **Fe-4** recorded in MeCN/toluene (1:1). Recorded at 140 K.

2.4 Conclusion

To sum up, four Schiff-base ligands and four corresponding homoleptic Cr(III) complexes were synthesised. All the complexes have shown ligand-based emission which is likely to be of charge transfer character (LL/IL/LM). Unfortunately, no doublet excited state emission was observed at any temperature investigated. Further analysis of the complexes indicated significant distortion from the octahedral geometry (trans angles: 169-175°) with Cr-O bonds of significantly shorter length (~1.9 Å) than the Cr-N bonds (2.05-2.1 Å). This suggested the possibility of doublet excited state deactivation via reduction of the O_h geometry to D_{4h}. Upon consideration of the fact that only strong field ligands can facilitate the population and continuance of the desired doublet excited state of the Cr(III) metal centre, we performed an investigation into the field strength of **L-2** to **L-4** with the Cr(III) complexes and their corresponding Fe(III) analogues. The spin-crossover behaviour for the Fe(III) complexes indicated that all ligands synthesised in this chapter are strong field ligands and therefore rules out BISC deactivation. Moreover, the strain imposed upon the coordination of the

ligands introduced the possibility of the D_{4h} doublet excited states non-radiative relaxation as a deactivation pathway for the emission from the doublet excited state.

Additionally, calculations suggested that the coordination via the phenolate anion introduced electron density around the equatorial plane of the Cr(III) centre therefore potentially increasing the electron repulsion at the metal centre via the coordination of the negatively charged oxygen atoms donating electron density to the Cr(III) centre. Whether this had a positive or negative effect on the emission from the doublet excited state is not fully understood from the results presented in this chapter. Since no information could be obtained on the spin-forbidden d-d transitions, the effect of the additional electron density in the equatorial plane on the electronic repulsion could not be proved. However, it is anticipated that increased electronic repulsion could induce a blue-shift of the emission maxima from the doublet excited state, if observed. Overall, it is suggested that ligands which, upon coordination, form a combination of five- and six-membered chelates are not the optimal ligand system for creating near-perfect octahedral geometry and therefore preserving of the doublet excited state of Cr(III) complexes. It is advised that complexes with only five- or six-membered chelates should be considered as a design principle for potential future candidates.

2.5 Experimental

All reactions were performed with the use of vacuum line and Schlenk techniques. Reagents were commercial grade and were used without further purification. ^{1}H and ^{13}C {H} NMR spectra were recorded on a Bruker Avance dpx 400, or Bruker Avance dpx 500 MHz spectrometer and were recorded in CDCl$_3$. ^{1}H and ^{13}C{^{1}H} NMR chemical shifts (δ) were determined relative to internal tetraMesilane, Si(CH$_3$)$_4$ and are given in ppm. Low- and high-resolution mass spectra were obtained by the staff at Cardiff University. All photophysical data was obtained on a JobinYvon-Horiba Fluorolog-3 spectrometer fitted with a Hamamatsu R5509-73 detector. FTIR spectra were recorded on an ATR equipped Shimadzu IRAffinity-1 spectrophotometer. UV-Vis data were recorded as solutions on a Perkin Elmer Lamda20 spectrophotometer. LC-MS analysis was conducted using a Waters Synapt G2 SI using a water/MeCN solvent gradient.

2.5.1 EPR Spectroscopy

Samples for EPR measurements were prepared as solids or in solvents, as listed in the discussion section, under atmospheric conditions. The X-band EPR measurements were performed on a Bruker EMX spectrometer utilising an ER4119HS resonator, 100 kHz field modulation and 0.4 mT modulation depth at 140 K. The Q-band EPR measurements were performed on a Bruker E500 spectrometer utilising an ER5106 QT-E resonator, 5 kHz field modulation and 0.4 mT modulation depth at room temperature. EPR simulations were performed using the *Easyspin* toolbox within *Matlab.* [70]

2.5.2 DFT studies

Non-relativistic calculations of the fully relaxed geometries in the ground state and optimized excited state were performed on the Gaussian 09 program, and calculations of the spin Hamiltonian parameters were performed using ORCA (version 4.0.0.1).[71,72] Geometry optimisation calculations were computed using B3LYP functional and 6-311G(d, p) basis set for all atoms except Cr which was computed using LANL2DZ.[73] The chosen solvent was MeCN for all complexes.[74] TD-DFT calculations were computed using B3LYP functional and def2-SVP basis set with diffuse function and (d,p) accounting for polarisation function.[75,76] ORCA calulations were computed using

EPR-II with BLYP functional and QZVP basis sets produce results of ZFS parameters estimation using quasi-restricted orbitals (qro) method for calculating the spin-orbit coupling contributions.[74,77,78]

2.5.3 Synthesis

General procedure for formation of the ligands

To a solution of 8-aminoquinoline dissolved in di-isopropyl ether, an aldehyde of choice was added. The reaction was stirred for 24 hrs at room temperature. In case of a resulting precipitate, it was filtered and dried on air. In case of a solution obtained, slow evaporation afforded crystals coloured red to yellow, which were washed with minimal amount of hexanes. Where upon slow evaporation an oily substance was obtained, a few drops of EtOH aided affording crystals.

L-1

8-aminoquinoline (0.150 g, 1.06 mmol) stirred with 2-hydroxy-5-methoxybenzaladehyde (0.130 mL, 1.04 mmol) red crystals were obtained (0.300 g, 98%). ^{1}H NMR (500 MHz, CDCl$_3$): δ_H 13.42 (1 H, s), 8.98 (dd, $^3J_{HH}$ = 4.2, $^4J_{HH}$ = 1.8, 1H), 8.90 (1 H, s), 8.19 (dd, $^3J_{HH}$ = 8.3, $^3J_{HH}$ = 1.7, 1H), 7.73 (dd, $^3J_{HH}$ = 8.1, $^4J_{HH}$ = 1.4, 1H), 7.58 – 7.46 (3 H, m), 7.02 (2 H, m), 6.95 (1 H, m) and 3.82 (3 H, s). FTIR (solid, V_{max})/ cm^{-1}: 2997, 2979, 2943, 2835, 1577, 1558, 1485, 1423, 1384, 1338, 1330, 1269, 1246, 1219, 1192, 1157, 1087, 1056, 1026, 968, 887, 848, 825, 817, 798, 783, 756, 717, 655, 594, 563, 551, 474, 466, 455 and 424; UV/Vis (MeCN): λ_{max} / nm ($\mathcal{E}$ / M^{-1}cm^{-1}): 234 (29000), 343 (9300) and 494 (2400) nm.

L-2

8-aminoquinoline (0.58 g, 4.03 mmol) stirred with salicylaldehyde (0.441 mL, 4.23 mmol), yellow-brown crystals were obtained (0.80 mg, 80%). Prepared according to the literature procedure.[79] ^{1}H NMR (500 MHz, CDCl$_3$): δ_H 13.90 (1 H, s), 8.98 (dd, $^3J_{HH}$ = 4.3, $^4J_{HH}$ = 1.8 Hz, 1H), 8.93 (1 H, s), 8.19 (dd, $^3J_{HH}$ = 8.3, $^4J_{HH}$ = 1.8 Hz, 1H), 7.73 (dd, $^3J_{HH}$ = 8.2, $^4J_{HH}$ = 1.4 Hz, 1H), 7.58 (t, $^3J_{HH}$ = 7.8 Hz, 1H), 7.51 (dd, $^3J_{HH}$ = 7.3, $^4J_{HH}$ = 1.5 Hz, 1H), 7.46 (2 H, m), 7.40 (1 H, m), 7.07 (ddt, $^3J_{HH}$ = 8.3, $^4J_{HH}$ = 1.1, 0.5 Hz, 1H) and 6.94 (td, $^3J_{HH}$ = 7.5, $^4J_{HH}$ = 1.2 Hz, 1H). FTIR (solid, V_{max})/ cm^{-1}: 2987, 2977, 2942, 1577, 1560, 1485, 1413, 1386, 1330, 1270, 1219, 1180, 1157, 1056, 1026, 969, 887, 849, 824, 798, 783,777, 756, 715, 655, 594, 562, 551, 473, 467, 454

and 423. UV/Vis (MeCN): λ_{max} / nm ($\mathcal{E}$/ M^{-1} cm^{-1}): 234 (23400), 267 (15000)sh, 345 (7500), 482 (500) nm.

L-3

8-aminoquinoline (0.49 g, 3.33 mmol) stirred with 2-hydroxynapthaldehyde (0.59 g, 3.43 mmol), orange solid was obtained (0.76 g, 76%). ^{1}H NMR (500 MHz, CDCl$_3$): δ_H 9.30 (1 H, s), 9.09 (dd, $^3J_{HH}$ = 4.2, $^4J_{HH}$ = 1.7, 1H), 8.20 (dd, $^3J_{HH}$ = 8.3, $^4J_{HH}$ = 1.7, 1H), 8.01 (d, $^3J_{HH}$ = 8.3, 1H), 7.77 (dd, $^3J_{HH}$ = 7.5, $^4J_{HH}$ = 1.3, 1H), 7.69 (2 H, m), 7.61 (3 H, m), 7.52 (q, $^3J_{HH}$ = 4.2, 1H), 7.48 (1 H, m), 7.28 (1 H, m) and 6.92 (d, $^3J_{HH}$ = 9.5, 1H).) FTIR (solid, V$_{max}$)/ cm^{-1}: 1624, 1608, 1589, 1566, 1535, 1489, 29 1469, 1396, 1353, 1334, 1296, 1246, 1203, 1161, 1134, 1080, 1037, 956, 852, 817, 786, 744, 702, 644, 594, 574, 551, 528, 478, 462 and 428 cm-1; UV/Vis (MeCN): λ_{max} / nm ($\mathcal{E}$/ M^{-1} cm^{-1}): 228 (53000), 257 sh (25000), 339 (9000), 454 (27000) and 478 (29000) nm.

L-4

8-aminoquinoline (0.55 g, 3.82 mmol) stirred with dihydroxybenzaldehyde (0.55 g, 3.99 mmol), red solid was obtained (0.23 g, 23%). ^{1}H NMR (400 MHz, CDCl$_3$): δ_H 9.08 (1 H, m), 8.76 (1 H, s), 8.22 (d, $^3J_{HH}$ = 8.2, 1H), 7.76 (d, $^3J_{HH}$ = 7.8, 1H), 7.67 (d, $^3J_{HH}$ = 7.2, 1H), 7.61 (t, $^3J_{HH}$ = 7.8, 1H), 7.52 (q, $^3J_{HH}$ = 4.2, 1H) 6.96 (d, $^3J_{HH}$ = 7.7, 2H), 6.88 (1 H, d, $^3J_{HH}$ = 8.1), 6.62 (t, $^3J_{HH}$ = 7.9, 1H) and 6.47 (1 H, s).) FTIR (solid, V$_{max}$)/ cm^{-1}: 3232, 3035, 3028, 1624, 1608, 1543, 1508, 1473, 1446, 1381, 1361, 1346, 1327, 1267, 1195, 1157, 1134, 1076, 1010, 914, 867, 821, 740, 644, 624, 586, 555, 547, 528, 505, 486 and 470 cm-1; UV/Vis (MeCN): λ_{max} / nm ($\mathcal{E}$ / M^{-1} cm^{-1}): 238 (38000), 276 (10000), 346 (15000) and 468 (2500) nm.

Ligand of choice was dissolved in EtOH and brought to reflux for 30 min, followed by addition of Cr(Cl)$_3$(THF)$_3$. The reaction was refluxed overnight. Upon cooling, the resulting precipitate was filtered and recrystallised from acetone. The solid was filtered and redissolved in MeOH, followed by addition of NH$_4$PF$_6$, a precipitate occurred which was subsequently filtered and dried on air.

Cr-1

L-1 (0.270 g, 0.97 mmol) stirred with *mer*-CrCl$_3$(thf)$_3$ (0.170 g, 0.46 mmol), red powder obtained (0.200 g, 71 %). FTIR (solid, V$_{max}$)/ cm^{-1}: 2828, 1586, 1546, 1513, 1465, 1376, 1312, 1247, 1214, 1166,1086, 1021, 836 (PF$_6$$^-$), 763, 569, 512, 432 cm^{-1}.

UV/Vis (MeCN): λ_{max} / nm (ε / M^{-1} cm^{-1}): 229 (44000), 306 (14000), 350 (14000), 516 (4600). HRMS [M+H]$^+$ m/z found 607.1329, m/z calculated 606.1359 for $C_{36}H_{30}CrN_4O_2^+$.

Cr-2

L-2 (0.107 g, 0.44 mmol) stirred with mer-CrCl$_3$(thf)$_3$ (0.077 g, 0.21 mmol). Brown solid obtained (0.120 g, 75 %). FTIR (solid, V_{max})/ cm^{-1}: 2966, 1602, 1537, 1505, 1456, 1433, 1384, 1327, 1255, 1222, 1166, 1101, 1037, 836 (PF$_6^-$), 755, 561, 521, 408 cm^{-1}. UV/Vis (MeCN): λ_{max} / nm (ε / M^{-1} cm^{-1}): 231 (48000), 259 sh (32000), 339 (15000), 473 (5400), 569 (800). HRMS [M+H]$^+$ m/z found 547.1181 , m/z calculated 645.1158 for $C_{32}H_{22}CrN_4O_2^+$.

Cr-3

L-3 (0.345 g, 1.16 mmol) stirred with mer-CrCl$_3$(thf)$_3$ (0.21 g, 0.55 mmol). Orange solid obtained (0.250 g, 70 %). FTIR (solid, V_{max})/ cm^{-1}: 2973, 2918, 2841, 1603, 1526, 1461, 1433, 1386, 1255, 1199, 1110, 1029, 836 (PF$_6^-$), 803, 746, 569, 504, 424 cm^{-1}. UV/Vis (MeCN): λ_{max} / nm (ε/ M^{-1} cm^{-1}): 236 (47000), 273 sh (25000), 363 (13000), 480 (12000). HRMS [M+] m/z found 646.1460, m/z calculated 646.1461 for $C_{40}H_{26}CrN_4O_2^+$.

Cr-4

L-4 (0.28 g, 1.05 mmol) stirred with mer-CrCl$_3$(thf)$_3$ (0.19 g, 0.50 mmol). Red solid obtained (0.20 g, 69 %). FTIR (solid, V_{max})/ cm^{-1}: 3054, 2933, 2845, 1602, 1554, 1497, 1448, 1400, 1384, 1320, 1264, 1206, 1166, 1101, 1037, 836 (PF$_6^-$), 723, 561, 521, 456, 416 cm^{-1}. UV/Vis (MeCN): λ_{max} / nm (ε / M^{-1} cm^{-1}): 206 (51000), 241 (26000), 278 (12000), 361 (12000), 489 (3900), 636 (1200). HRMS [M+H]$^+$ m/z found 579.1079, m/z calculated 578.1046 for $C_{32}H_{22}CrN_4O_4^+$.

Ligand of choice and anhydrous FeCl$_3$ were added to methanol and stirred for 3 hours. Followed with cooling down of the solution and filtering of the resulting precipitate which was recrystallised in acetone and then dried in vacuo. The precipitate was filtered, redissolved in MeOH and upon addition of aqueous NH$_4$PF$_6$, a precipitate was

obtained, then subsequently filtered and washed with diethyl ether. Resulting precipitates were dried on air.

Fe-1

Iron (III) chloride (0.055 g, 0.34 mmol) was added to the solution of L_1 (0.28 g, 0.74 mmol) in methanol (20 mL) and stirred for 3 h. Following the purification process, a red-brown powder was obtained. (0.210 g, 99%). FTIR (solid, V_{max})/ cm^{-1}: 3321, 1597, 1531, 1504, 1454, 1415, 1365, 1292, 1222, 1199, 1157, 1087, 1029, 813, 551 and 466 cm-1; UV/Vis (MeOH): λ_{max} / nm ($\mathcal{E}$/ M^{-1} cm $^{-1}$): 231 (14000), 263 sh (7000), 337 (5000) and 473 (2700) nm. HRMS [M+] *m/z* found 610.1303, *m/z* calculated 610.1298 for $C_{36}H_{30}FeN_4O_2^+$.

Fe-2

Iron (III) chloride (0.055 g, 0.34 mmol) was added to the solution of **L_2** (0.25 g, 1.02 mmol) in methanol (20 mL) and stirred for 3 h. Following the purification process, a brown solid was obtained. (0.030 g, 15%). FTIR (solid, V_{max})/ cm^{-1}: 1600, 1577, 1527, 1504, 1462, 1423, 1404, 1381, 1303, 1211, 1149, 1087, 825, 748 and 555 cm-1; UV/Vis (MeOH): λ_{max} / nm ($\mathcal{E}$/ M^{-1} cm $^{-1}$): 228 (23000), 333 (9800) and 418 (5000) nm. HRMS [M+] *m/z* found 550.1159, *m/z* calculated 550.1086 for $C_{32}H_{22}FeN_4O_2^+$.

Fe-3

Iron (III) chloride (0.055 g, 0.34 mmol) was added to the solution of L_3 (0.210 g, 0.72 mmol) in methanol (20 mL) and was stirred for 3 h. Following the purification process, a brown powder was obtained (0.120 g, 60 %). FTIR (solid, V_{max})/ cm^{-1}: 1693, 1597, 1573, 1531, 1504, 1454, 1427, 1373, 1338, 1319, 1296, 1249, 1199, 1165, 1149, 1087, 1041, 975, 821, 786, 748, 555 and 493 cm-1; UV/Vis (MeOH): λ_{max} / nm ($\mathcal{E}$ / M^{-1} cm $^{-1}$): 220 sh (36518), 256 (23000), 340 (12000) and 452 (12000) nm. HRMS [M+] *m/z* found 650.1404, *m/z* calculated 650.1399 for $C_{40}H_{26}FeN_4O_2^+$.

Fe-4

Iron(III) chloride (0.055 g, 0.34 mmol) was added to the solution of L_4 (0.23 g, 0.88 mmol) in methanol (20 mL) and was stirred for 3 h. Following the purification process, a black powder obtained (0.080 g, 45 %). FTIR (solid, V_{max})/ cm^{-1}: 1600, 1581, 1554, 1508, 1438, 1404, 1381, 1315, 1269, 1203, 1165, 1087, 1026, 829, 779, 740, 732, 30

636, 555, 513 and 412 cm^{-1}; UV/Vis (MeOH): λ_{max} / nm ($\mathcal{E}$ / M^{-1} cm $^{-1}$): 237 (36000), 290 sh (14000) and 352 (20000) nm. HRMS [M+] *m/z* found 582.0991, *m/z* calculated 582.0985 for C$_{32}$H$_{22}$FeN$_4$O$_4^+$.

2.6 References

[1] H. Schiff, Ann. Suppl. 3, 1864, 343.

[2] M. Ciaccia, S. Di Stefano**,** Org. Biomol. Chem.**,** 2015,13**,** 646-654

[3] E. V. Anslyn and D. D. Dougherty, Modern physical organic chemistry, Sausalito, CA, USA, 2006, 597.

[4] S. Gaur, Asian J. Chem. 15, 1, 2003, 250

[5] M.J. Gemi, C. Biles, B.J. Keiser, S.M. Poppe, S.M. Swaney, W.G. Tarapley, D.L. Romeso, Y. Yage, J. Med. Chem. 43, 2000, 1034.

[6] C.T. Supuran, M. Barboiu, C. Luca, E. Pop, M.E. Brewster, A. Dinculescu, Eur. J. Med. Chem. 31, 1996, 597.

[7] W.A. Zoubi, Int. J. Org. Chem. 3, 2013, 73-95.

[8] C.-M. Che, S.-C. Chan, H.-F. Xiang, M.C.W. Chan, Y. Liu, Y. Wang, Chem. Commun., 2004, 1484-1485

[9] C.M. Liu, R.G. Xiong, X.Z. You, Y.J. Liu, K.K. Cheung, Polyhed., 15, 1996, 4565.

[10] S.I. Al-Saeedi, L.H. Abdel-Rahman, A.M. Abu-Dief, S.M. Abdel-Fatah, T.M. Alotaibi, Ali M. Alsalme, A. Nafady, Cat., 2018, 8, 452, 1-14.

[11] D.E. De Vos, P.P. Knops-Gerrits, D.L. Vanoppen, P.A. Jacobs, Supramol. Chem., 1995, 6, ½, 49-57.

[12] İspir, E., Toroğlu, S. & Kayraldız, A. Trans. Met. Chem, 2008, 33, 953–960.

[13] Z. Afrasiabi, Ekk K. Sinn, Weisheng Lin, Yinfa Ma, Charles Campana, Subhash Padhye, J. Inorg. Biochem., 2005, 99, 1526-1531.

[14] Bradshaw, D.; Hill, C. H.; Nixon, J. S.; Wilkinson, S. E. Agents Actions 1993, 38, 135.

[15] Martinez, L. E.; Leighton, J. L.; Carsten, D. H.; Jacobsen, E. N. J. Am. Chem. Soc., 1995, 117, 5897.

[16] M. H. Wu, .N. Jacobsen, Tet. Lett., 1997, 38, 10, 693-1696.

[17] A. M. Ijeaku, M. H. Chidubem, E. K. Chukwunonyerem, N. U. Obioma, 2015, AJER 4,9, 153-159.

[18] S.-J. Zou , Y. Shen , F.-M. Xie , J.-D. Chen , Y.-Q. Li and J.-X. Tang , Mater. Chem. Front., 2020, 4 , 788 —820.

[19] J.S. Wilson, N. Chawdhury, M.R.A. Al-mandhary, M. Younus, M.S. Khan, P.R. Raithby, A. Ko, and R.H. Friend, 2001, J. Am. Chem. Soc 123, 9412.

[20] J. Zhang, X. Zhu, A. Zhong, W. Jia, F. Wu, D. Li, H. Tong, C. Wu, W. Tang, P. Zhang, L. Wang, D. Han, Org. Electr., 2007, 42, 153-162.

[21] . A.N. Gusev, M.A. Kiskin, E.V. Braga, M. Chapran, G. WiosnaSalyga, G.V. Baryshnikov, V.A. Minaeva, B.F. Minaev, K. Ivaniuk, P. StakhFTIRa, H. Ågren, and W. Linert, J. Phys. Chem., 2019, 123, 118-150.

[22] .S. Kang, J.G. Kang, Y. Sohn, and K.T. Leung, ACS Appl. Mater. Interfaces, 2018, 10, 447-468.

[23] N.K. Gondia, J. Priya, and S.K. Sharma, AIP Conf. Proc., 2018, 1, 19-53.

[24] A. Donmez, M.B. Coban, and H. Kara, J. Clust. Sci., 2018, 29, 951.

[25] K.T. Chan, T.L. Lam, D. Yu, L. Du, D.L. Phillips, C.L. Kwong, G.S.M. Tong, G. Cheng, and C.M. Che, Angew. Chemie - Int. Ed., 2019, 58, 42, 14896-14900.

[26] D. Suresh, C.S.B. Gomes, P.S. Lopes, C.A. FigueFTIRa, B. FerreFTIRa, P.T. Gomes, R.E.D. Paolo, A.L. MaçAnita, M.T. Duarte, A. Charas, J. Morgado, D. Vila-Viçosa, and M.J. Calhorda, Chem. - A Eur. J., 2015, 21, 9133-9149.

[27] O. Lavastre, I. Illitchev, G. Jegou, and P.H. Dixneuf, J. Am. Chem. Soc., 2002, 124, 5278-5279.

[28] B. Blondel, F. Delarue, M. Lopes, S. LadeFTIRa-Mallet, F. Alary, C. Renaud, and I. Sasaki, Synth. Met., 2017, 227,106-116.

[29] C.M. Che, C. Kwok, S.W. Lai, A.F. Rausch, W.J. Finkenzeller, N. Zhu, and H. Yersin, Chem. - A Eur. J. 2010, 16, 233-247.

[30] F. Dumur, L. Beouch, M.A. Tehfe, E. Contal, M. Lepeltier, G. Wantz, B. Graf, F. Goubard, C.R. Mayer, J. Lalevée, and D. Gigmes, 2014, Thin Solid Films, 564, 351-360.

[31] S. Chandra, P. Pipil, J. Inorg. Chem., 2014, 4, 30-40.

[32] S.P. Kumar, R. Suresh, K. GFTIRibabu, R. Manigandan, S. Munusamy, S. Muthamizh, V. Narayanan. Spectrochim. Acta A Mol. Biomol. Spectrosc,. 2015,15, 139, 431-441.

[33] P. Sharrockl, F. Nepveu-Juras, M. Massol and R. Haran, Biochem. Biophys. Res. Comm.,1979, 86, 2, 428-433.

[34] P. Gutlich, H.A. Goodwin, Spin crossover in transition metal compounds., 233. Springer, Berlin, 2004.

[35] M. Nihei, T. Shiga, Y. Maeda, H. Oshio, Coord Chem Rev., 2007, 251, 2606–2621.

[36] M. A. Halcrow, Chem. Soc. Rev., 2011, 40, 4119–4142.

[37] M. Quesada, F. Prins, E. Bill, H. Kooijman, P. Gamez,O. Roubeau, A. L. Spek, J. G. Haasnoot, J. Reedijk, Chem.A Europ. J., 2008, 14, 28, 8486-8499.

[38] D. Sertphon, D. J. Harding, P. Harding, K. S. Murray, B. Moubaraki, H. Adams, A. Alkaş , S. G. Telfer, Eur. J. Inorg. Chem., 2016, 432-438.

[39] D. J. Harding, D. Sertphon, P. Harding, K. S. Murray, B. Moubaraki, J. D. Cashion, H. Adams, Chem. A Eur. J., 2013, 19, 1082-1090.

[40] D. Sertphon, D. J. Harding, P. Harding, K. S. Murray, B. Moubaraki, J. D. Cashion, H. Adams, Chem. A Eur. J., 2013, 788-795.

[41] M. Mazúr, L. Pogány, B. Brachňaková, I. Šalitroš, 2019, Chem. Pap., 1-10.

[42] H. H. Wickman, P. M. Klein, D. A. Shirley, J Chem Phys, 1965, 42, 2113– 2117.

[43] R. Aasa, J Phys Chem, 1970, 52, 3919–3930.

[44] W. R. Hagen, Biomolecular EPR spectroscopy. CRC Press, Taylor & Francis Group, Boca Raton, 1970.

[45] M. Ciaccia , R. Cacciapaglia , P. Mencarelli , L. Mandolini and S. Di Stefano , Chem. Sci., 2013, 4 , 2253 —2261.

[46] T. Iwasawa, R. J. Hooley and J. Rebek Jr., Science, 2007, 317, 493–496.

[47] R.C. Dickinson Jr., W.A. Baker, R.L. Collins J. Inorg. Nucl. Chem., 1977, 39, 1531.

[48] A. M. Donia, H. A. El-Boraey, Trans. Met. Chem., 1993, 18, 315–318.

[49] M. Takahashi, T. Fukushima,   , M. Takezaki,   , T. Tominaga,   , H. Akashi,   , H. Takagi,   , T. Shibahara,   2012, 85, 11, 1210-1221.

[50] N. S. Kozlov, G. V. Vorob'eva,Khimiya Geterotsiklicheskikh Soedinenii, 981, 10, 1379-1381.

[51] N. Ahmad, E. H. Anouar, A. M. Tajuddin, K. Ramasamy, B. M. Yamin, H. Bahron, PLoS One., 2020, 14, 15, 4.

[52] A. Çapan, S. Uruş, M. Sönmez, J. Sau. Chem. Soc., 2018, 22, 6, 757-766.

[53] A. Hens, P. Mondal and K. K. Rajak, Dalton Trans., 2013, 42, 14905-14915

[54] P. Insiti, P. Jitthiang, P. Harding, K. Chainok, R. Chotima, J. SFTIRFTIRak, S. Blackwood, A. Alkaş, S. G. Telfer, D. J. Harding, 2014, Polyh., 114, 242-248.

[55] J.-R. Jiménez , M. Poncet , B. Doi , C. Besnard and C. Piguet , Dalton Trans., 2020, 49, 13528.

[56] A. Shimizu, Y. Ishizaki, S. Horiuchi, T. HFTIRose, K. Matsuda, H. Sato, J. Yoshida J. Org. Chem., 2021, 86, 1, 770-781.

[57] P. Mohammad-Jafarieh, A. Akbarzadeh, R. Salamat-Ahangari, M. Pourhassan-Moghaddam, K. Jamshidi-Ghaleh BMC Chemistry, 2021, 15, 53.

[58] F. José Avila Ferrer, J. Cerezo, J. Soto, R. Improta, F. Santoro, Comp. Theo. Chem., 2014, 1040–1041, 328-337.

[59] N. Deb, PhD Thesis, 2014

[60] T. Clark, J. Chandrasekhar, G. W. Spitznagel, P. Von Ragué Schleyer, J. Comp. Chem., 1983, 4, 3, 294-301.

[61] E. Papajak, J. Zheng, X. Xu, H. R. Leverentz, D. G. Truhlar, J. Chem. Theory and Comput., 2011, 7, 10, 3027-3034.

[62] F. Vlahović, M. Perić, M. Gruden-Pavlović, M. Zlatar,. *J Chem Phys.,* 2015, 7, 142, 21, 214111-214114.

[63] D. G. Liakos, D. Ganyushin, F. Neese, Inorg. Chem., 2009 48, 22, 10572-10580.

[64] G. P. Vishnevskaya and B. M. Kozyrev Kazan, Zhu. Strukt. Kh., 6, 5, 667-678.

[65] Manoogian, A. and Leclerc, A. J. Chem. Phys. 1976, 64, 4504-4508.

[66] L. S. Singer, J. Chem. Phys., 1955, 23 , 379-388.

[67] K. Sugisaki , K. Toyota , K. Sato , D. Shiomi and T. Takui , Phys. Chem. Chem. Phys., 2017, 19 , 30128 —30138.

[68] A. Nicolaides, T. Soulimane, C. Varotsis, RSC Adv. 2019, 9, 4776– 4780.

[69] D. Sertphon, D. J. Harding, P. Harding, K. S. Murray, B. Moubaraki, H. Adams, A. Alkaş , S. G. Telfer, Eur. J. Inorg. Chem., 2016, 432-438.

[70] S. Stoll, A. Schweiger, J. Magn. Reson. 2006, 178, 1, 42-55.

[71] Gaussian 16, Revision C.01, Frisch, M. J.; Trucks, G. W.; Schlegel, H. B.; Scuseria, G. E.; Robb, M. A.; Cheeseman, J. R.; Scalmani, G.; Barone, V.; Petersson, G. A.; Nakatsuji, H.; Li, X.; Caricato, M.; Marenich, A. V.; Bloino, J.; Janesko, B. G.; Gomperts, R.; Mennucci, B.; Hratchian, H. P.; Ortiz, J. V.; Izmaylov, A. F.; Sonnenberg, J. L.; Williams-Young, D.; Ding, F.; Lipparini, F.; Egidi, F.; Goings, J.; Peng, B.; Petrone, A.; Henderson, T.; Ranasinghe, D.; Zakrzewski, V. G.; Gao, J.; Rega, N.; Zheng, G.; Liang, W.; Hada, M.; Ehara, M.; Toyota, K.; Fukuda, R.; Hasegawa, J.; Ishida, M.; Nakajima, T.; Honda, Y.; Kitao, O.; Nakai, H.; Vreven, T.; Throssell, K.; Montgomery, J. A., Jr.; Peralta, J. E.; Ogliaro, F.; Bearpark, M. J.; Heyd, J. J.; Brothers, E. N.; Kudin, K. N.; Staroverov, V. N.; Keith, T. A.; Kobayashi, R.; Normand, J.; Raghavachari, K.; Rendell, A. P.; Burant, J. C.; Iyengar, S. S.; Tomasi, J.; Cossi, M.; Millam, J. M.; Klene, M.; Adamo, C.; Cammi, R.; Ochterski, J.

W.; Martin, R. L.; Morokuma, K.; Farkas, O.; Foresman, J. B.; Fox, D. J. Gaussian, Inc., Wallingford CT, 2016.

[72] F. Neese, Software Update: The ORCA Program System—Version 5.0. Wiley Interdiscip. Rev. Comput. Mol. Sci. 2022, 12, e1606.

[73] P. J. Hay and W. R. Wadt, J. Chem. Phys., 1985, 82, 299-310.

[74] J. Tomasi, B. Mennucci, and R. Cammi, Chem. Rev., 2005, 105, 2999-3093.

[75] A.D. Becke, , Phys. Rev., 1988, 38, 3098.

[76] F. Weigend, R. Ahlrichs, Phys. Chem. Chem. Phys., 2005, 7, 3297.

[77] F. Weigend and R. Ahlrichs, Phys. Chem. Chem. Phys., 2005, 7, 3297-305.

[78] F. Neese, JACS, 2006, 128, 10213-10222.

[79] B. M. Dahl and O. Dahl. Acta Chem. Scand., 1969, 23, 1503-1513.

Chapter 3 - Investigation into Luminescent Polypyridyl Cr(III) Complexes and Their Electronic Characteristics as an Informative Tool for Future Ligand Design.

3.1 Introduction

This chapter focuses on a series of luminescent Cr(III) complexes in which polypyridyl ligands such as 2,2ˈ-bipyridine and 1,10-phenanthroline are employed. Furthermore, a thorough investigation of the relationship between the ligand design, doublet excited state population and the electronic properties of Cr(III) complexes was carried out. EPR spectroscopy was employed to investigate the ground state electronic structure of the paramagnetic Cr(III) systems including the influence of the ligands on the interelectronic repulsion at the metal centre. Despite many reports on luminescent polypyridyl Cr(III) complexes within the literature, no in-depth EPR analysis has been reported to date on these systems. Therefore, this chapter provides a detailed characterisation of the NIR emission and ZFS parameters for these high spin paramagnetic complexes.

Polypyridyl Cr(III) complexes are an example as to why strong field ligands with values larger than 20 Δ/B are required for emission from the lowest lying doublet excited state (^{2}E) (**Figure 3.1,** red circle), specifically, to overcome deactivation of doublet excited states (^{2}T/^{2}E) via back intersystem crossing (BISC) such as it is observed for systems with weaker ligand field strength. BISC leads to deactivation of the doublet excited state and therefore reverse generation of the quartet excited state (^{2}E/^{2}T$_1$ to ^{4}T$_2$) followed by its spin-allowed relaxation back to the quartet ground state (^{4}A$_2$). This is also the case for ligand field strengths around 30 Δ/B, where the ^{2}T$_2$ state overlaps with ^{4}T$_2$ as indicated in **Figure 3.1** with red circle.[1]
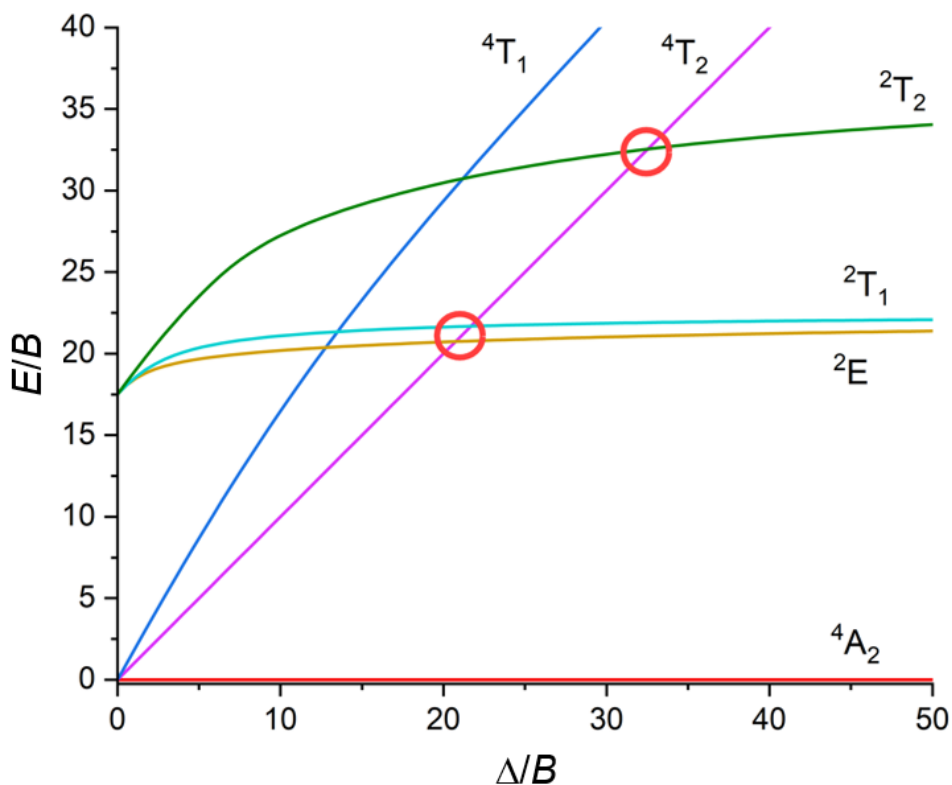
Figure 3.1 Tanabe-Sugano diagram for a d^3 system. Red circles indicate the critical points where both doublet ($^2T_2$, $^2T_1$ and ^2E) and quartet ($^4T_2$) excited states are degenerate which facilitates BISC deactivation.

The strong ligand field of bipyridine/phenanthroline type ligands is evidenced by the large prevalence of metals of d^4 to d^7 electron configuration forming low spin complexes upon coordination with bpy or phen as shown in **Figure 3.2** representing d^6 complexes, all of which are low spin. [2, 3, 4] The ligands induce an energy gap larger than that of electron pairing energy leading to the formation of low-spin complexes which is consistent with crystal field theory (see **Chapter 1.4.1**).[5]
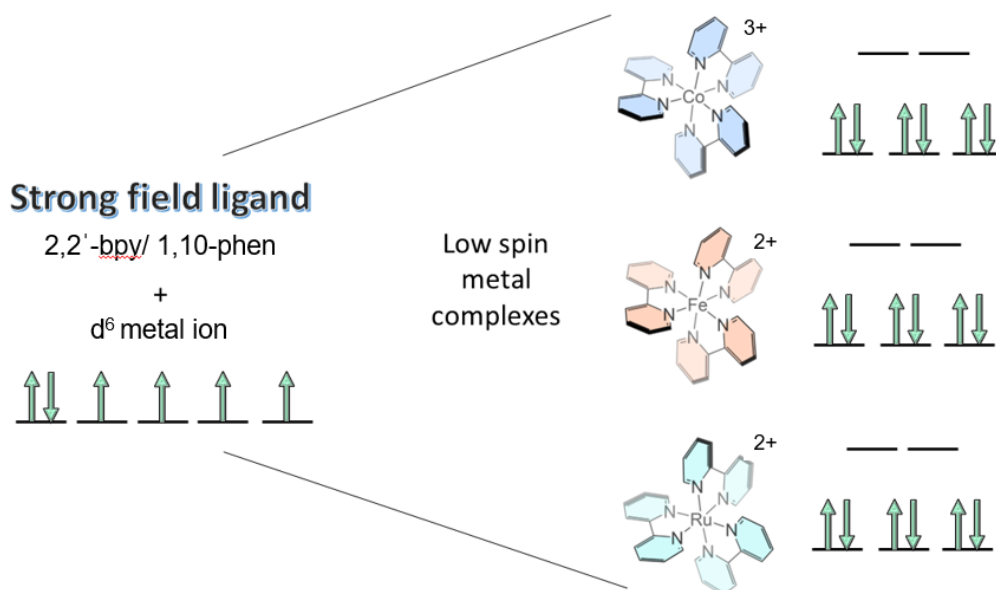
Figure 3.2 The influence of strong field ligands on the d-orbital splitting of the resulting d^6 transition metal complexes $[M(bpy)_3^{n+}]$ reported in the literature. Different colours signify the varying metal ions (Co(III), Fe(II) and Ru(II)). [2, 3, 4]

3.1.1 Luminescent properties of homoleptic Cr(III) properties

Emission properties of a range of previously reported Cr(III) homoleptic complexes (see **Figure 3.3**) are listed in **Table 3.1**. The sharp emission bands were determined to occur from the doublet excited state and the wavelength range reported was 720-800 nm depending upon the coordinated ligand and its field strength.
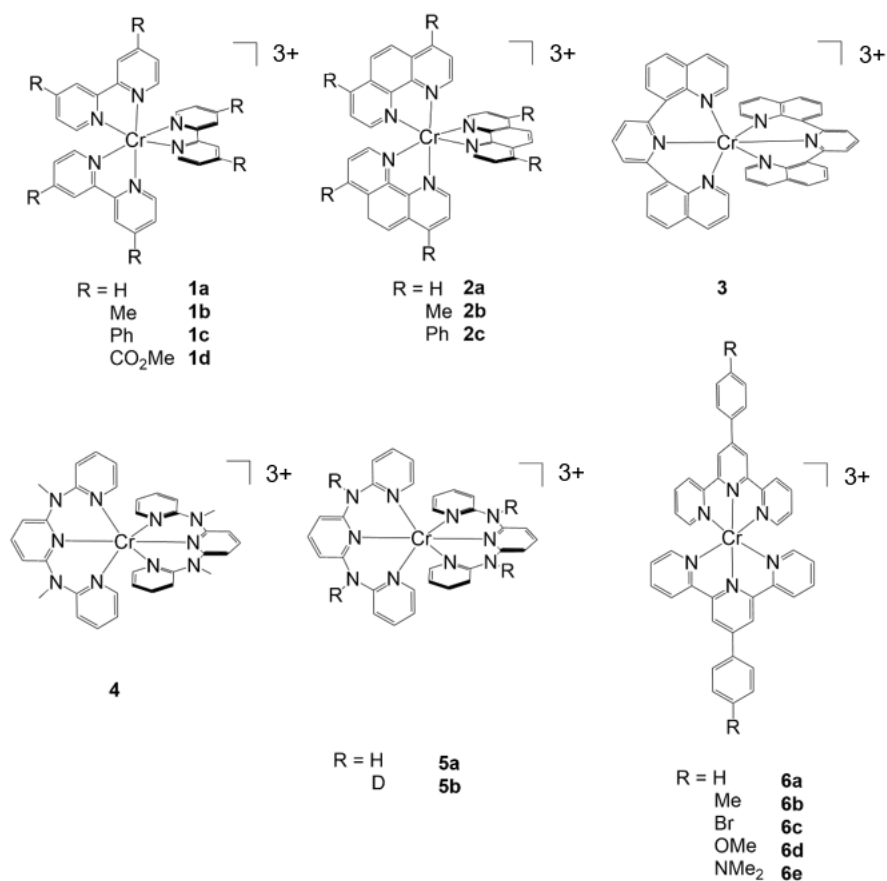
Figure 3.3 Cr(III) compounds reported in the literature. [6, 7, 8, 9, 10, 11, 12]

Table 3.1 Photophysical properties of various polypyridyl Cr(III) complexes reported.

Complex	Emission/ nm	$\tau/\mu s$	Φ	Ref.
1a	728[a]	63[a]	8.9×10^{-4}	
1b	731[a]	230[a]	1.5×10^{-6}	6
1c	742[a]	140[a]	4.2×10^{-4}	
1d	733[a]	7.7[a]	1.8×10^{-5}	7
2a	728[a]	270[a]	1.5×10^{-3}	
2b	734[a]	340[a]	8.9×10^{-4}	8
2c	743[a]	370[a]	8.1×10^{-6}	
3	747[c]	1200[c]	5.2×10^{-2}	9
4	775[b]	899[b]		10
5a	782[b]	770[b]	6.3×10^{-2}	
5b	782[b]	1100[b]	1.5×10^{-1}	11
6a	785[b]	0.3[b]		
6b	788[b]	0.4[b]		
6c	785[b]	0.28[b]		12
6d	797[b]	0.6[b]		
6e	Not observed	Not observed		

[a] deaerated 1 M HCl, [b] deaerated MeCN, [c] deaerated H_2O.

In homoleptic complexes, red-shifted emission is commonly observed which is relative to initial reports of 650-700 nm emission range for Cr(III) complexes such as $[Cr(NH_3)_6]^{3+}$, $[Cr(NH_5)Cl]^{3+}$, *trans*-$[Cr(NH_3)_4Cl_2]^{3+}$, *cis*-$[Cr(NH_3)_4Cl_2]^{3+}$ (see **Figure 3.4**).[13,14] The NH_3 ligand is known to be weaker than bpy and phen (see **Section 1.4.1**) therefore it is likely that the splitting between the ^4T and ^2T states is smaller, therefore producing emission bands at a shorter wavelength than tris-chelate complexes.
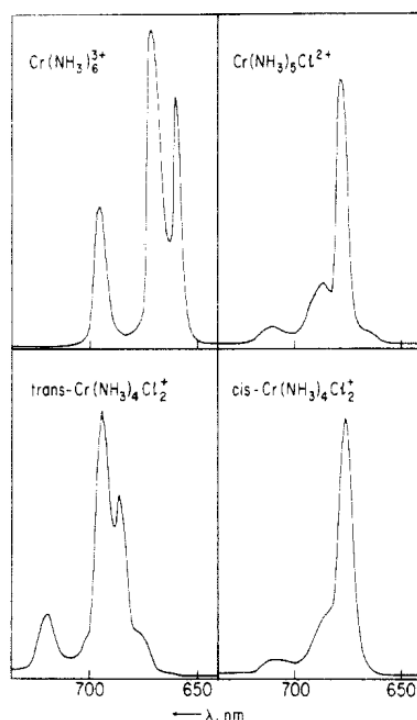
Figure 3.4 An example of Cr(III) emission from ^2E excited state within the range 650-700 nm reported in ethylene glycol/H_2O (2:1)) at 77 K. y-axis not reported. [13, 14]

Unsubstituted complexes such as [Cr(bpy)$_3$]$^{3+}$ are reported to display emission maxima of ~ 730 nm, whereas 4,4´-Ph substitution on the bpy ligand leads to a red-shift of ~ 12 nm for [Cr(4,4-Ph-bpy)$_3$]$^{3+}$ and a 13-15 nm red-shift for [Cr(4,4-Ph-phen)$_3$]$^{3+}$.[6,7] It should be noted that the phenyl substitution on the ligand framework results in enhanced conjugation in comparison to the unsubstituted ligand and this likely is responsible for the largest red-shifts observed across this series (66-68 nm) for [Cr(4-OMe-9-Ph-tpy)$_2$]$^{3+}$.[12] These ligands also provide far more rigidity resulting from the increasing denticity and therefore stronger ligand field. Finally, [Cr(N,N-H-dpd)$_2$]$^{3+}$, [Cr(N,N-D-dpd)$_2$]$^{3+}$ and [Cr(dqp)$_2$]$^{3+}$ are all examples of six-membered chelate rings that impart lower strain on the octahedral system resulting in lower energy of the $^2T/^2E$ excited states which is consistent with emission maxima within the range of 747-782 nm.

Excited state lifetimes near the millisecond range are reported for all six-membered chelate ring complexes. In those systems, surface crossing

deactivation pathways are reduced which is dependent on the final geometry of the complex as discussed in **Chapter 1.3.1**. In the case of five-membered chelates, longer lifetimes are often associated with Me substitution as substitution of C-H oscillators with heavier C-C bonds within the close vicinity of the metal centre reduces the deactivation via multiphoton relaxation. Moreover, the quantum yield data reported in the literature (see **Table 3.1**), suggests that bulkier ligands produce higher quantum yields such as complex **3** (5.2%), this is likely because of the physical shielding from the oxygen quenching that bulkier ligands offer to the metal centre. It is also worth noting that deuteration of the ligand can also result in increased quantum yield, e.g. **5b** (15 %), as a result of a decreased multiphoton relaxation (see **Chapter 1.2.2**).

3.1.2 Heteroleptic Cr(III) complexes

The same pattern was observed for heteroleptic Cr(III) complexes where substitution on the bpy/phen facilitated red-shifted emission (**Figure 3.5**). For direct comparison, it is useful to compare complexes **8** and **9** as the additional Me groups on the bpy framework resulted in a 7 nm red-shift of the emission maxima and more than tripled the excited state lifetime with 450 ms for complex **9** and only 112 ms for complex **8**. Importantly, the excited state lifetime measurements for these two complexes were recorded in two different solvent systems which may impact on absolute values. Moreover, utilising phen ligands over bpy ligands is reported to increase the excited state lifetime values as evidenced by the results for complexes **8** (112 ms), **7** (200 ms) and **13** (317 ms), for which an increase in the excited state lifetime is reported with an increasing number of equivalents of the phen ligand utilised.

Additionally, a series of heteroleptic Cr(III) complexes utilising strongly electron-withdrawing nitrile groups was reported which exhibited red shifts of 30-63 nm suggesting that the electron withdrawing capabilities of the CN groups is able to lower the interelectronic repulsion at the metal centre.[5,17,18]
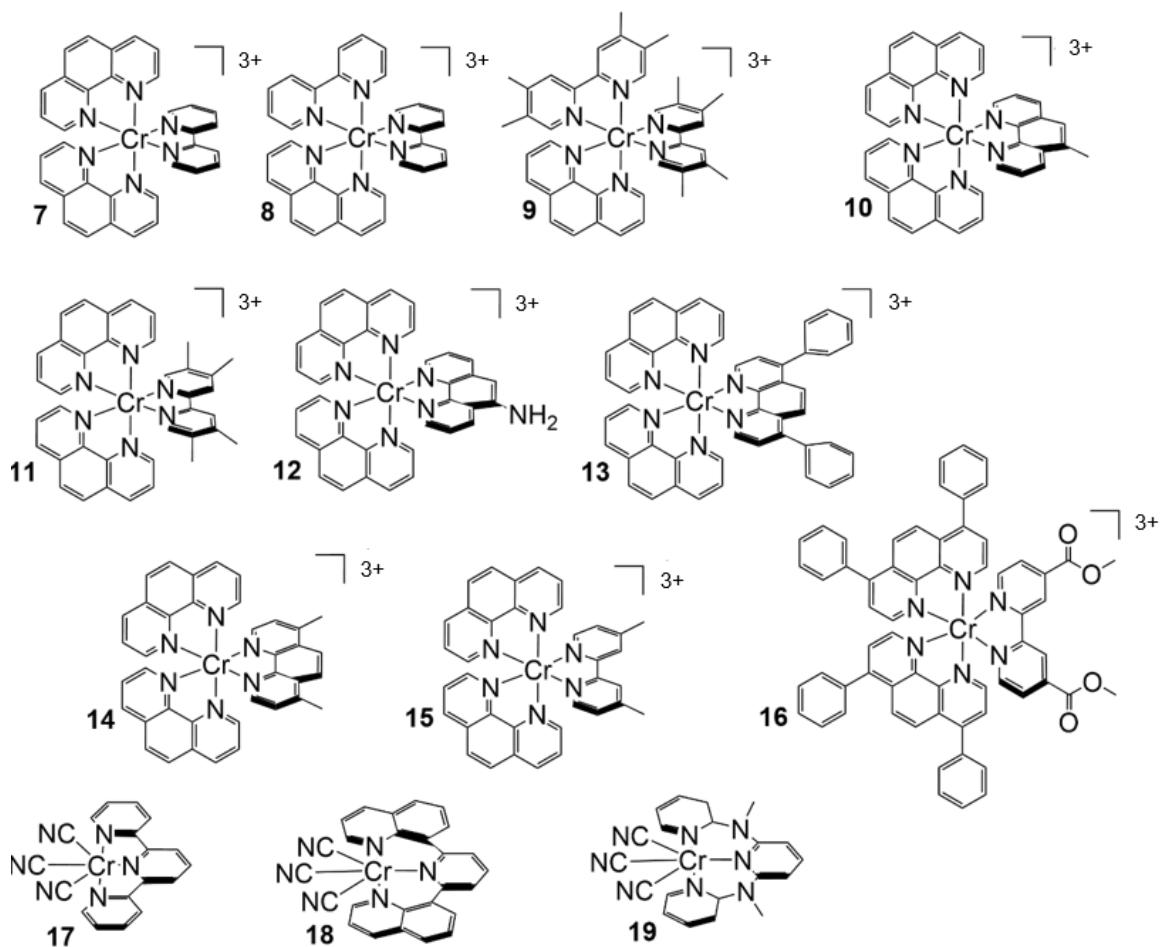
Figure 3.5 Previously reported heteroleptic complexes.[5, 15, 16, 17, 18]

Table 3.2 Photophysical properties of previously reported heteroleptic polypyridyl Cr(III) complexes.

Complex	Emission/ nm	τ/ ms	Ref.
7	730[a]	200[a]	
8	730[a]	112[a]	15
9	737[b]	450[b]	
10	729[b]	208[b]	16
11	734[b]	280[b]	15
12	730[b]	0.21[b]	
13	732[b]	317[b]	
14	730[b]	91[b]	16
15	730[b]	259[b]	
16	742[b]	108[b]	
17	793[a]	0.00312[a]	17
18	764[a]	79[a]	5
19	758[a]	13[a]	18

[a] deaerated 1 M HCl, [b] deaerated MeCN, [c] deaerated H_2O.

3.1.3 EPR characterisation

In 2014, Schönle attempted characterisation of neat and magnetically diluted powders of $[Cr(tpy)_2](PF_6)_3$ and $[Cr(tpy)(5,5'-Me_2tpy)](PF_6)_3$ utilising EPR which showed spectra with considerable line broadening causing difficulties with spectral simulations and the extraction of zero-field splitting parameters (D and E/D). Schönle reported broad spectra of neat powders with finer resolution upon 2% doping into Co(III) analogues with unsuccessful simulations due to the suspected impurity of the samples and therefore no ZFS parameters were given (**Figure 3.6**).[19]

However a well resolved spectrum of $[Cr(tpy)_2]^{3+}$, doped into its diamagnetic host, was reported by Casellato *et al*, with isotropic *g*-values suggesting octahedral geometry and *E/D* value < 0.2 suggesting rhombic distortion. The *D*-value was reported to be 0.16 cm^{-1} (**Figure 3.7**). [20] This falls closely to the *D*-value of +0.18 cm^{-1} reported for $[Cr(ddpd)_2]^{3+}$, of which *E/D* value of 0.33(3) suggests a fully rhombicity meanwhile the geometry of the complex was determined to be octahedral via X-ray crystallography.[21]
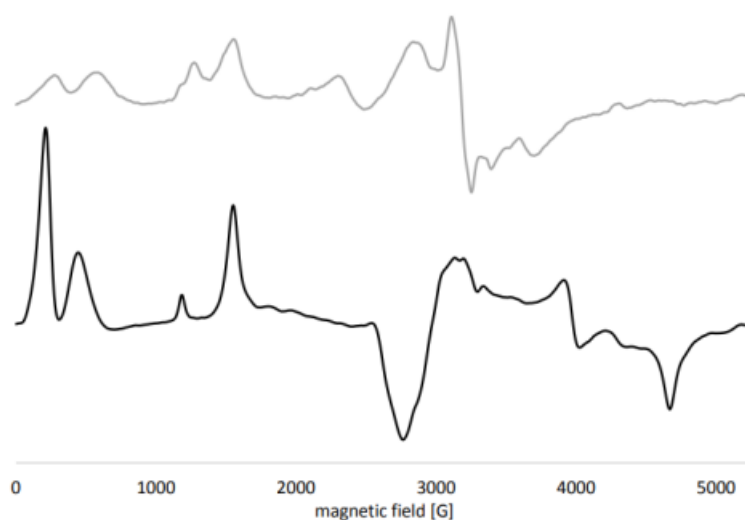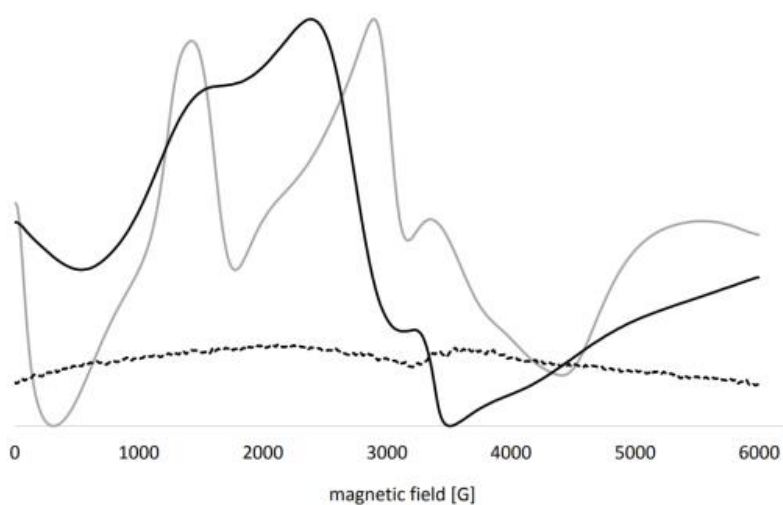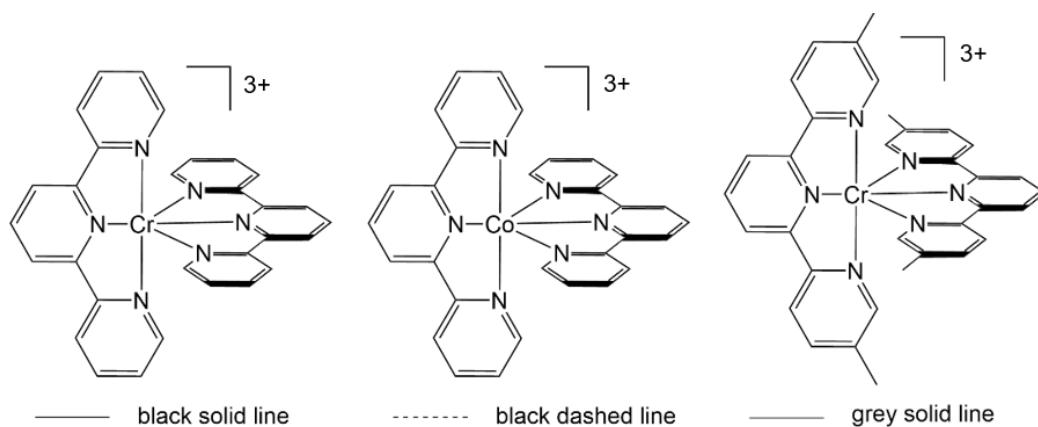
Figure 3.6 Top: neat solid EPR recorded at 295 K of $[Cr(tpy)_2](PF_6)]_3$ (black solid line), $[Cr(tpy)(5,5`-Me_2tpy](PF_6)]_3$ (grey solid line) and $[Co(tpy)_2](PF_6)]_3$ (black dashed line). Bottom: 2 % $[Cr(tpy)_2](PF_6)]_3$ in $[Co(tpy)_2](PF_6)]_3$ (black line) and 2 % $[Cr(tpy)(5-Me_2tpy)](PF_6)]_3$ in $[Co(tpy)_2](PF_6)]_3$ (grey line). [Reproduced from ref 19].
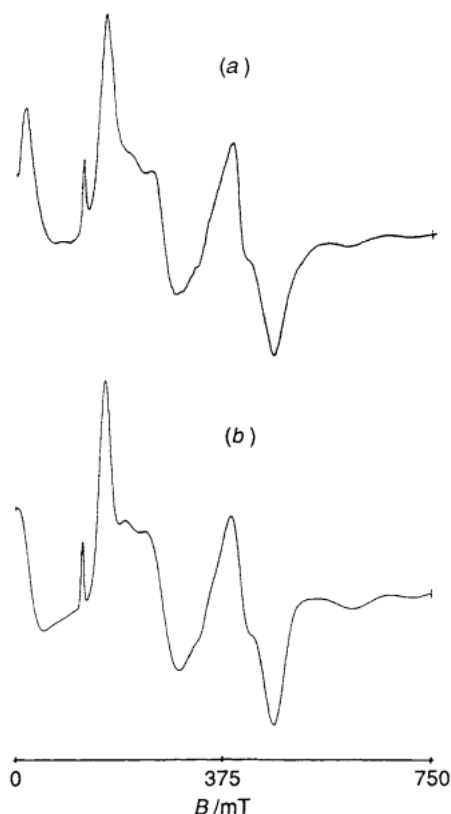
Figure 3.7 Experimental (a) and simulated (b) X-band spectra of $[Cr(tpy)_2]^{3+}$.[20]

Since there are no other EPR studies reported on $[Cr(bpy/phen)_3]^{3+}$ systems, it is worth noting other simpler examples available in the literature such as the Q-band study of $[Cr(acac)_3]$ single crystal measured at room temperature and $[Cr(H_2O)_6]^{3+}$ (**Figure 3.8**). An experimental *D*-value for $[Cr(H_2O)_6]^{3+}$ was reported to be 0.1 cm^{-1} in solution and solid state (single crystal) across a range of temperatures, namely 4.2, 77, 195, and 297 K at X-band frequency.[22] The $[Cr(acac)_3]$ *D*-value was approximated to be 0.592 cm^{-1} at room temperature using X- and K- band frequencies.[23]

As illustrated in **Figure 3.9**, two of the d-orbitals for octahedral metal complexes are localised directly on the *x*, *y* and *z* axes providing on optimal orbital overlap between the d-orbitals and the bonding orbitals of the coordinating ligands which results in covalent bonding and its direct effect is observed in decreased interelectronic repulsion (nephelauxetic effect) between these d-electrons. Distortions to the octahedral geometry result in poorer overlap of the d-orbitals and the bonding ligand orbitals leading to a smaller

nephelauxetic effect. The extent of the nephelauxetic effect can be measured by calculating the nephelauxetic effect parameter ζ (**Equation 3.1**), where the Racah parameter (**B**) for the metal complex of interest is divided by the Racah parameter ($B_{\text{free ion}}$) for the free ion. [24]

$$\zeta \ = \ \frac{B_{complex}}{B_{free\,ion}} \qquad\qquad (3.1)$$

$$D \ = \ \left(\frac{2\lambda}{10Dq}\right)^2 (\Delta_z - \Delta_x) \qquad\qquad (3.2)$$

$$\lambda \ = \ 0.11\,(B + 1.08)^2 + 0.0062 \qquad\qquad (3.3)$$

Moreover, the *B* is directly proportional to the *D*-value of the paramagnetic system as indicated in **equations 3.2** and **3.3**, therefore lower Racah parameter results in lower *D*-values. Moreover, **equation 3.2** suggests a correlation between the geometry of the metal complex and the *D*-value of the system, where perfectly octahedral geometry (cubic geometry, therefore $\Delta_z - \Delta_x = 0$) results in $D = 0$.[25,26,27]

Trans angles
179.24
177.48
179.01

Trans angles
180.00
180.00
180.00
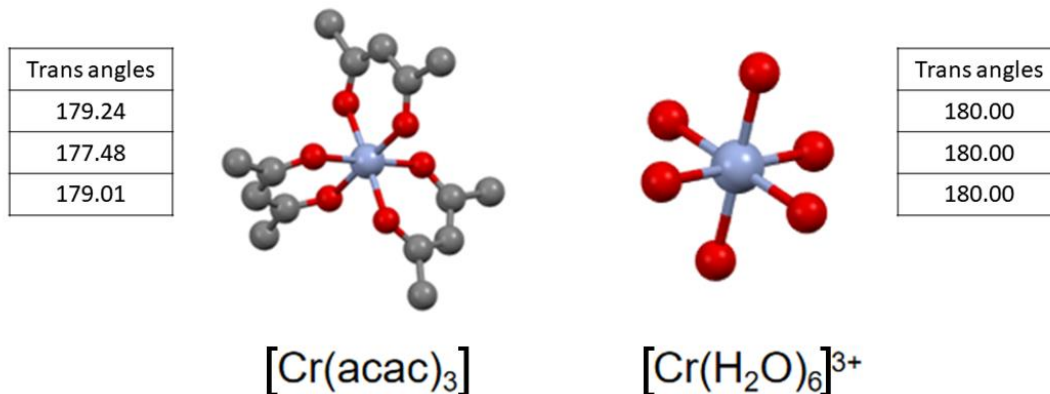
$[Cr(acac)_3]$ $[Cr(H_2O)_6]^{3+}$

Figure 3.8 Crystal structures of $[Cr(acac)_3]$ and $[Cr(H_2O)_6]^{3+}$ and their trans angles.[28,29]

$d_{x^2-y^2}$ d_{z^2}
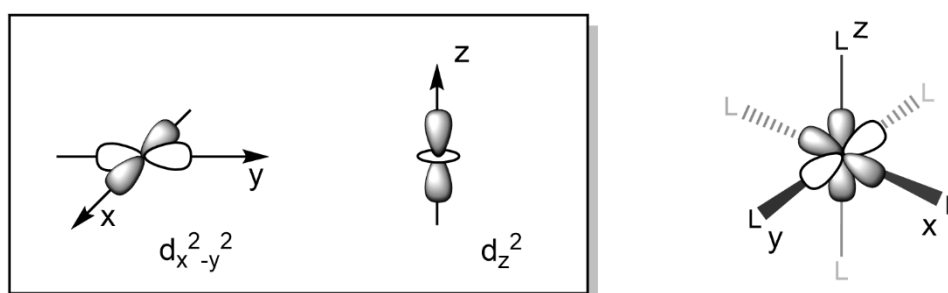
Figure 3.9 Representation of the d-orbitals involved in metal-ligand bonding.

It is therefore useful at this stage to note that a benchmark computational study reported in the literature on $[Cr(acac)_3]$, determined that the combination of the BLYP functional with a QZVP basis set were the only combination tested that produced ZFS spin Hamiltonian parameters that were within 0.01 cm^{-1} error of experimentally determined results (D_{calc} = 0.58 cm^{-1}, E_{calc}/D_{calc} = not given, D_{exp} = 0.59 cm^{-1}, E_{exp}/D_{exp} = 0.085), and therefore those parameters are used for all ORCA calculations in this chapter.[30] This includes the quasi-restricted orbitals (qro) method for calculating the spin-orbit coupling contributions.[30]

3.2 Aim

Considering the thorough literature introduction on the polypyridyl Cr(III) complexes given, it is somewhat disappointing that no reports of EPR spectroscopy characterisation exists for these paramagnetic systems. The aim of this chapter was to deepen the understanding of electronic properties of a newly synthesised series of Cr(III) polypyridyl complexes upon full characterisation of the series, and to investigate the potential relationship between their photophysical properties and the zero-field splitting parameters using EPR and emission spectroscopy. The ultimate goal was to provide a comprehensive electronic picture of the complexes, as reflected in spin Hamiltonian parameters, that could serve as an additional tool in future ligand design.

3.3 Results and Discussion

3.3.1 Synthesis

All complexes were synthesised via the Kane-Maguire method (**Section 1.4.2.3**) where anhydrous $CrCl_3$ was reacted with two equivalents of 2,2'-bipyridine or 1,10-phenanthroline in dry ethanol with catalytic amounts of Zn powder (**Figure 3.10**). Two-hour reflux gave green precipitates which were recrystallised from H_2O and hot filtered to obtain beige/brown crystals for bpy complexes and silver for 1,10-phen complexes upon cooling down of the filtrate.
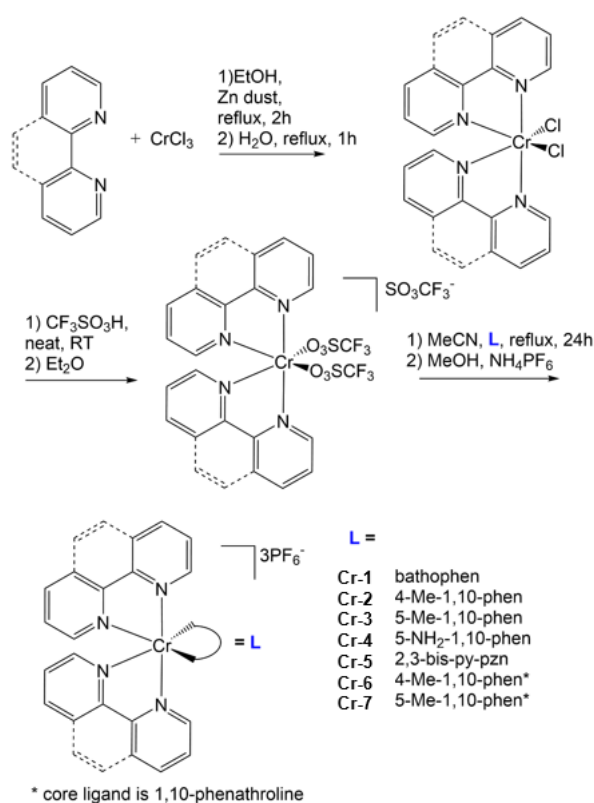
Figure 3.10 Kane-Maguire synthetic route towards polypyridyl Cr(III) complexes.

3.3.2 Liquid Chromatography-Mass spectrometry (LC-MS)

Due to very low yields for complexes **Cr-1** and **Cr-4** to **Cr-7** elemental analysis was only performed for complexes **Cr-2** and **Cr-3**. Both complexes returned results suggesting good purity and were therefore used as standards for determining purity via LC-MS (H_2O/MeCN gradient) for the remaining complexes. All complexes undergo some degree of hydrolysis in contact with water, therefore all LC-MS chromatograms contain three peaks - the expected complex, its hydrolysis product and the dissociated ligand as illustrated in **Figure 3.11**. Upon initial review of the LC-MS results, it was thought that the two peaks (final compound and hydrolysed by-product) were inseparable and coexisted within the mixture. However, upon LC-MS analysis of complexes **Cr-2** and **Cr-3** (purity determined by EA), it became clear that the pure complexes generated two peaks which represented the final product and its hydrolysis by-product and a third peak which represented the dissociated ligand (**Figure 3.12**).
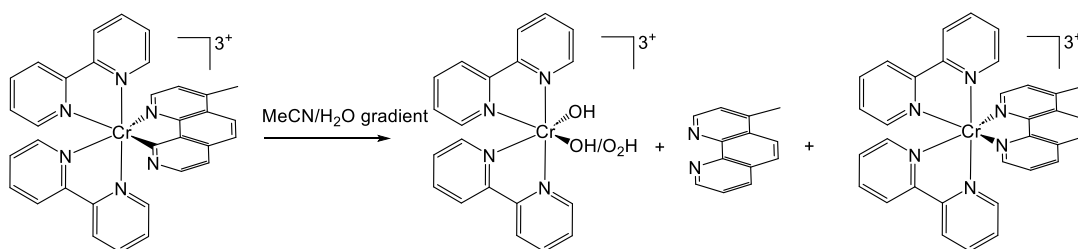
Figure 3.11 Potential by-products generated during LC-MS data acquisition of complex **Cr-2**.

Moreover, it should be noted that our LC-MS chromatograms were recorded in Total Ion Count (TIC) mode, therefore direct integration of the Area Under the Curve (AUC) does not lead to direct purity analysis. Each peak in the chromatogram can be assumed to have different fragmentation characteristics and therefore larger/more labile molecules might fragment more easily in contact with electrospray ionisation (ESI) than smaller molecules. This reinstates the significance of an LC-MS standard (complexes **Cr-2** and **Cr-3**).
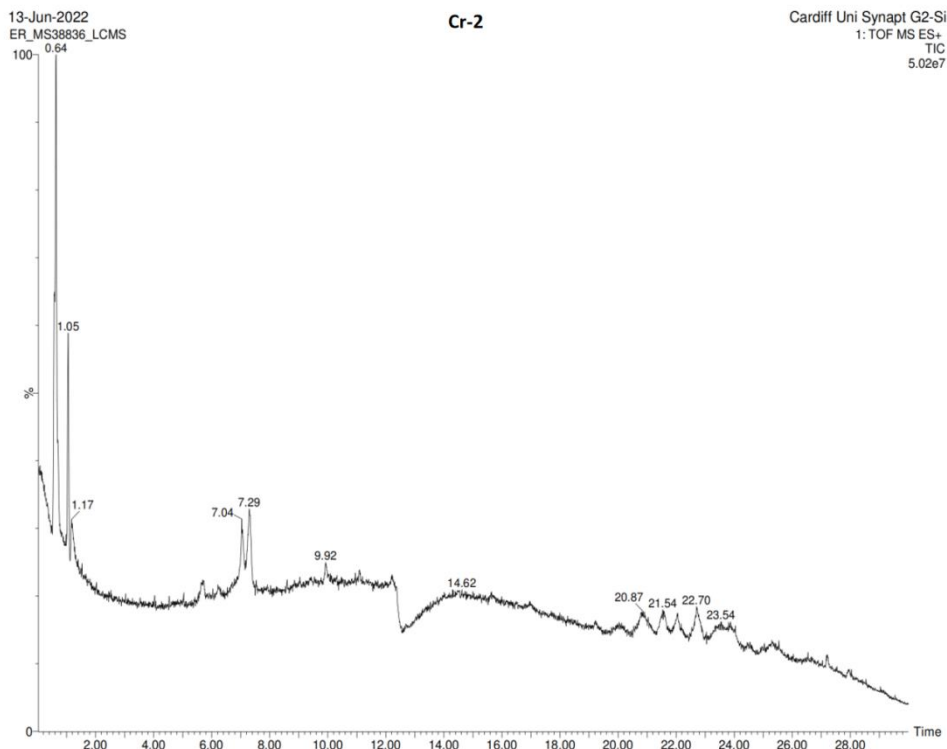
Figure 3.12 LC-MS chromatogram (TIC) of complex **Cr-2** used as a standard for purity in the LC-MS study. Peak at 0.64 min represents the hydrolysis product, whilst the peak at 1.05 min signifies the complex of interest. Smaller peaks around 7 min represent the dissociated ligand (here: 4-Me-phen).

To provide more experimental evidence of the purity of the samples, all complexes were analysed via thin layer chromatography (TLC) prior to LC-MS analysis. All complexes except **Cr-5** showed only one bright yellow spot by TLC.

Following the LC-MS analysis, all complexes were also characterized using positive mode electrospray ionisation mass spectrometry to investigate whether any hydrolysis products could be detected in fresh samples. All measurements were run using only LC-MS grade organic solvents (MeCN or MeOH; ≥ 99.9 %) to eliminate the possibility of hydrolysis during the sample preparation process. For all complexes that showed one yellow spot by TLC, no hydrolysis product was identified in the ESI-MS data.

3.3.3 Stability analysis

As discussed in **Chapter 1.4.3**, the polypyridyl Cr(III) complexes are known to respond to an alkaline environment resulting in dissociation of the ancillary ligand and substitution by H_2O and/or ^-OH groups. Therefore, complex **Cr-2** (due to high yields achieved) was investigated to analyse its stability in alkaline and acidic conditions by UV-Vis measurements. The anticipated mechanism for $H_2O/^-OH$ is via dissociation of the ancillary ligand.[31,32] As indicated in **Figure 3.13**, complex **Cr-2** shows a decrease in intensity for bands at ~260 and 310 nm, with a new band at around 275 nm increasing in intensity under alkaline conditions. This is thought to be due to the 4-Me-phen dissociating from the Cr(III) metal centre which is in line with the absorbance data presented in the UV region as the new band appears at higher energy (275 nm) than that of the complex at 310 nm. The second band expected for the phen ligand at 260 nm is most likely buried within the newly formed band at 275 nm. The observed colour change was from yellow to colourless.
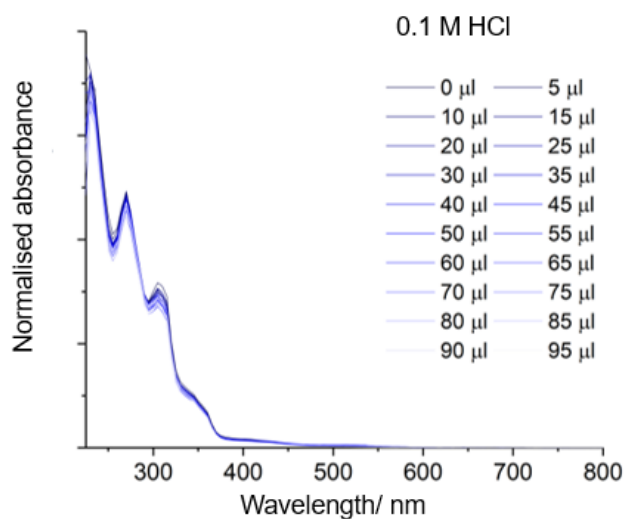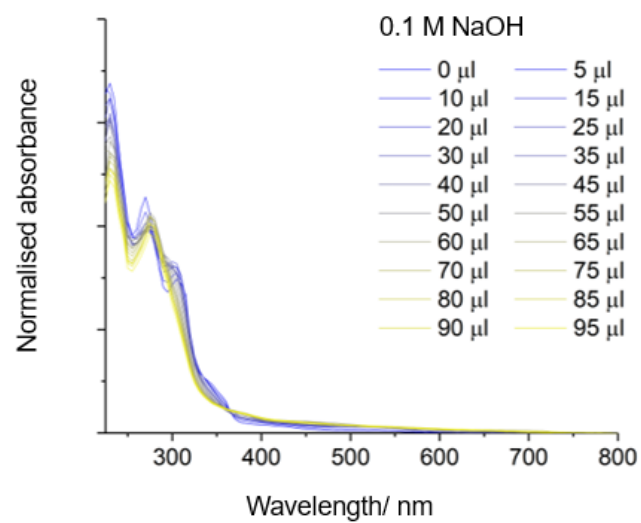
Figure 3.13 UV-Vis spectra of complex **Cr-2**. Top: in an alkaline environment; 0.1 M NaOH. Bottom: in an acidic environment; 0.1 M HCl. Starting concentration was 10^{-5} M (3 mL, aerated MeCN).

In the acidic medium, no meaningful change in the appearance of the UV-Vis spectrum was observed. As expected, the absorbance intensity is slightly decreased due to the dilution effect of additional aliquots of $HCl_{(aq)}$ reducing the effective concentration of complex **Cr-2**. No colour change was observed under acidic conditions.

3.3.4 Synthetic challenges - Ligand scrambling

The literature reports the synthesis of heteroleptic Cr(III) complexes to be challenging, with ligand scrambling often creating difficulties in isolating the desired product. It is not uncommon for $[Cr(bpy)_x]^{n+}$ complexes to undergo ligand dissociation and subsequent substitution in the presence of another ligand, for example in the case of the polypyridyl Cr(III) complexes described herein, a more stable 1,10-phenanthroline derivative. As expected, the same occurred during the synthesis of the target compound $[Cr(bpy)_2(bathophen)](PF_6)_3$ (**Cr-1**) and a range of side products were identified by MS due to ligand scrambling as illustrated in **Figure 3.14**. As a result, the yield for this reaction was very low (0.065%).

Cr-1a   **Cr-1b**   **Cr-1c**   **Cr-1d**
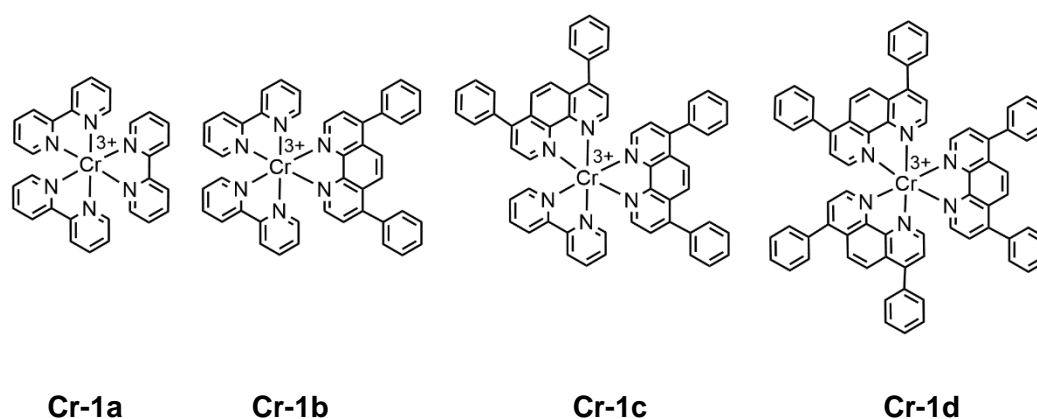
Figure 3.14 Ligand scrambling observed during the synthesis of $[Cr(bpy)_2(bathophen)](PF_6)_3$.

Determination of the extent of ligand scrambling was possible via TLC and mass spectrometry. It was determined that longer reaction times resulted in higher level of ligand dissociation which yielded by-products with higher equivalents of the substituted (bathophen) ligand. Whilst characterisation via

mass spectrometry appeared to be a straightforward process, the choice of the stationary phase proved crucial when chromatography techniques were considered.

TLC performed using alumina coated aluminium plates in MeCN/H$_2$O/KNO$_{3(sat)}$ (14:2:1) showed a pink spot on the baseline and a brightly coloured yellow spot on the solvent front, whilst silica coated plates showed five spots - the pink spot representing the hydrolysed product on the baseline and four yellow spots, respectively in an order of decreasing, **Cr-1a**, **Cr-1b**, **Cr-1c**, **Cr-1d** as depicted in the **Figure 3.15**.
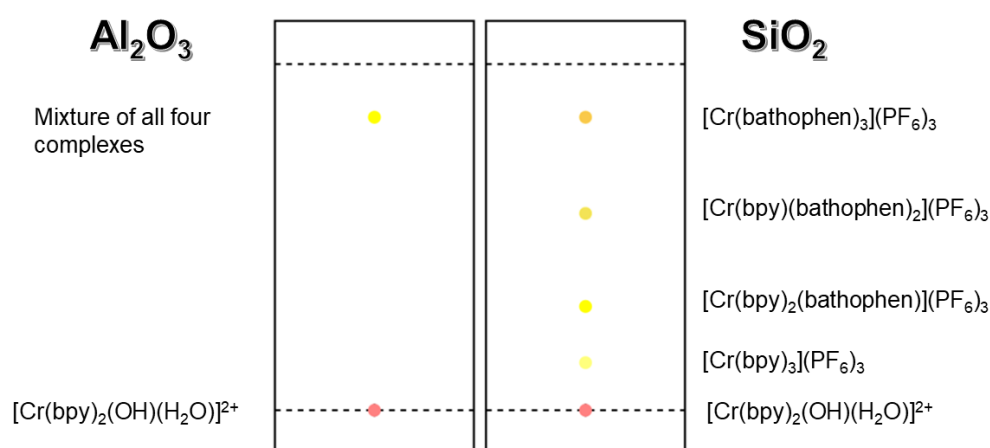
Figure 3.15 Representation of the TLC plates of the [Cr(bpy)$_2$(bathophen)](PF$_6$)$_3$ (**Cr-1**) reaction mixture with complexes in an order of decreasing polarity: **Cr-1a**, **Cr-1b**, **Cr-1c**, **Cr-1d**. Pink spot represents hydrolysis product. Left: Al$_2$O$_3$ coated aluminium plate. Right: SiO$_2$ coated aluminium plate.

The separation observed on the SiO$_2$ coated plate could be due to the changes in polarity across the series of by-products, nevertheless the overall size of each by-product complex is also significant as it increases alongside the molecular weight. As illustrated in **Figure 3.16** which represents the space fill simulation of all identified products, as the number of bathophenanthroline equivalents increases across the series, the overall size of the complex also increases; Based on this, the differences of the separation between SiO$_2$ and Al$_2$O$_3$ coated TLC plates as opposed to the column chromatography separation, discussed below depend on the pore size of the TLC plate material itself where

the SiO_2 offers pore sizes between 10-12 Å and Al_2O_3 offers 60 Å pore size. Naturally, larger pores present higher tolerance for the size of the particle that can pass through, where smaller pore size provides more selectivity and therefore better separation.
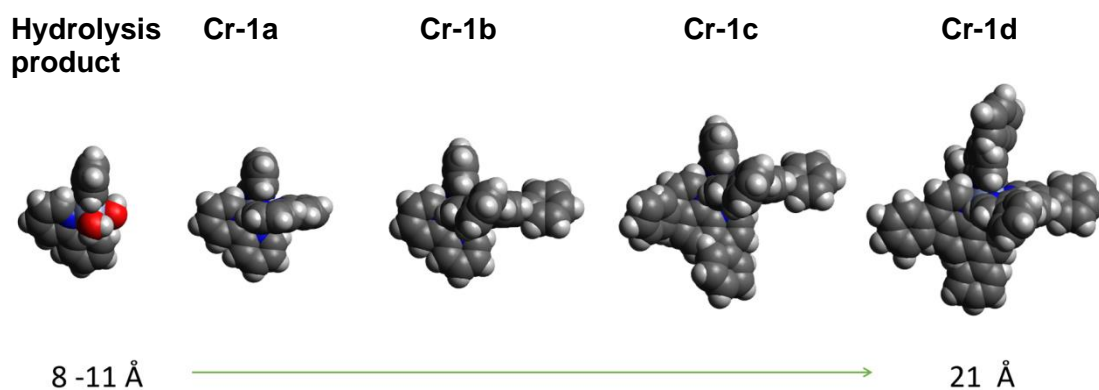
Figure 3.16 Space-fill models of ligand scrambling series of $[Cr(bpy)_2(bathophen)]^{3+}$. Complex on the far left represents the hydrolysis product.

Further purification was attempted with the aid of flash column chromatography as illustrated in **Figure 3.17**. However, once the mixture was loaded onto a freshly packed SiO_2 column and $MeCN/H_2O/KNO_{3(sat)}$ (14:2:1) was added, one broad yellow band appeared to elute rather than the expected four yellow bands as predicted by the silica TLC results. To no avail, MeOH was added to remove the band completely. The conclusion was that due to the acidic nature of silica, all complexes could have formed hydrogen bonds and/or dipole-dipole interactions with the OH group on the silica surface resulting in all of the products sticking to the silica column. Further attempts included deactivating silica with triethylamine (TEA) prior to loading the compound mixture onto the column with no success, unless small portions of the crude were used (ca. 20 mg), however upon elution in $MeCN/H_2O/KNO_{3(sat)}$ (14:2:1), further hydrolysis was observed during the concentration of the solvent under reduced pressure. This was followed with a gravity column chromatography using neutral alumina which resulted in all four complexes eluting together, however the hydrolysed product was observed to be stuck to the top of the alumina column with no motion at any point of the procedure. Therefore, Al_2O_3 column successfully

removed the hydrolysed product. The crystal structure of an analogue $[Cr(phen)_2(L)]^{3+}$ hydrolysis product $[Cr(phen)_2(OH)(H_2O)]^{2+}$ was reported before by Piguet.[33] This method was used for all complexes to remove the hydrolysed product.
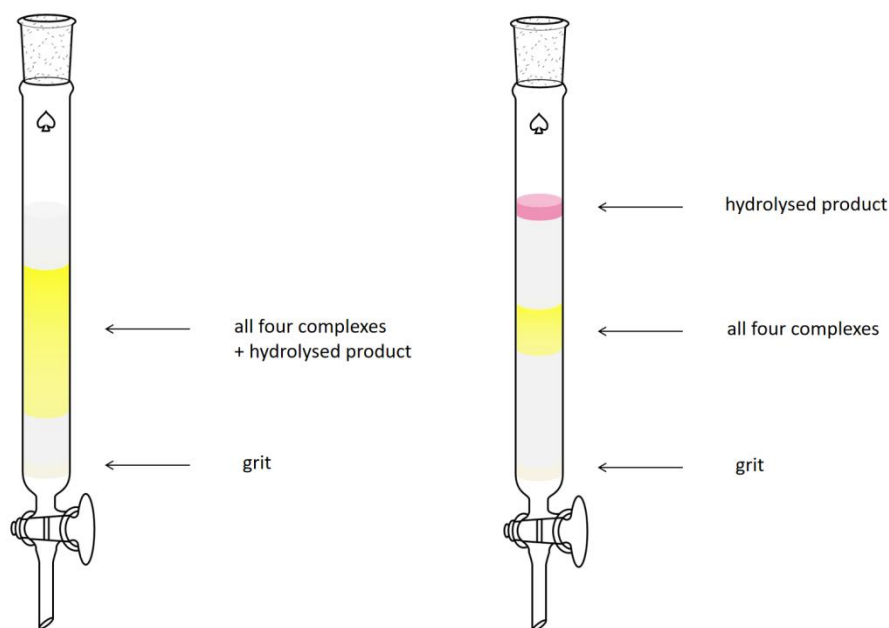
Figure 3.17 Representation of the difference in elution between SiO_2 packed column and neutral Al_2O_3 column.

As mentioned earlier in this section, an additional challenge was associated with the post-column chromatography work-up. Since the fraction of all complexes were obtained in $MeCN/H_2O/KNO_{3(sat)}$ (14:2:1), removing the solvent under reduced pressure at temperatures higher than 20 °C resulted in further hydrolysis of the complex as was noted using TLC. Therefore, the fractions were diluted with substantial amounts of water (1:10 ratio) and the same amount of CH_2Cl_2, followed by NH_4PF_6 addition and a standard solvent extraction with the combined organic layers dried over Na_2SO_4 instead of $MgSO_4$ which had shown to absorb the product. Thereafter, preparatory TLC was performed as the only feasible method of separating the four complexes involving minimal contact with water. Preparatory TLC obtained fractions were then characterised using LC-MS (**Figure 3.18**).
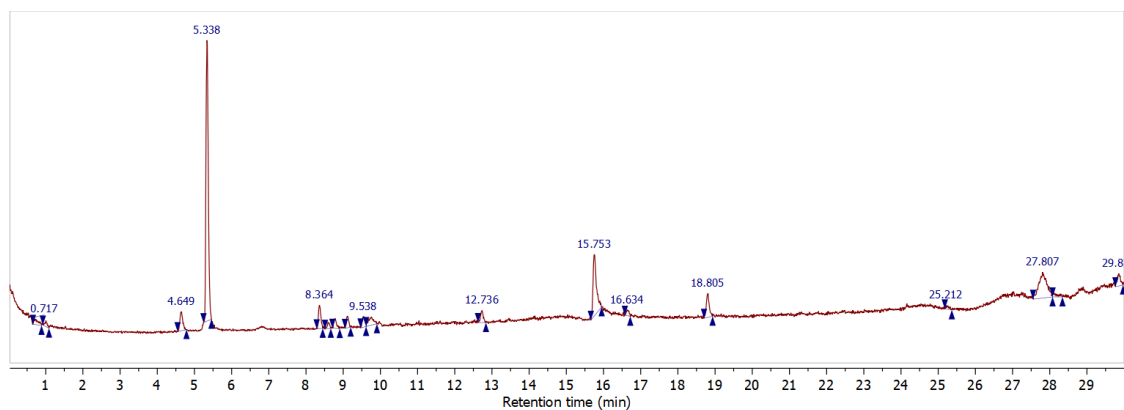
Figure 3.18 TIC chromatogram of complex **Cr-1** measured in MeCN/H_2O gradient.

The peak at 0.717 min represents a metal ion adduct of the hydrolysed complex $[Cr(bpy)_2(OH)(H_2O)]^{2+}$. Peaks at 4.649 and 15.753 min represent 2,2ʹ-bpy and bathophen ligand, respectively. The only distinguishable complex observed was $[Cr(bpy)_2(bathophen)]^{3+}$ as evidenced by the peak at 5.338 min. All the remaining peaks represent metal ion adducts of the desired complex. Although, the exact metal ion adducts could not be determined, the isotope pattern suggest an adduct of Cr and another ion as commonly observed in MS, therefore confirming the origin of the peaks being the complex of interest. Common metal adducts such as Na^+ and K^+ were trialled, however those adducts did not match the *m*/*z* value observed. The isotope patterns are given in **Appendix 3**.

3.3.5 Synthetic challenges - Hydrolysis of complex Cr-5

It should be noted that whilst all of the polypyridyl complexes discussed in this chapter were prone to hydrolysis, complex **Cr-5** presented a distinct sensitivity to water which became apparent during its purification. For instance, precipitation of the complex out of MeOH with saturated aqueous solution of NH_4PF_6 resulted in a colour change from bright yellow solution to orange solution. This is assumed to be due to the hydrolysis of the complex affording a pinkish by-product as mentioned previously. A low yield was obtained for this complex (0.5%) and purification with minimal water content was necessary to retain as much of the complex as possible. Unfortunately, **Cr-5** presented a very low Rf value and overlapped with hydrolysed product and was therefore difficult to purify with the Al_2O_3 column. Sticking of the compound to the column

120

proved to complicate the purification and attempts at using MeCN to elute the compound were not successful; therefore MeCN/H$_2$O/KNO$_{3(sat)}$ (14:7:1) had to be used. Unfortunately, due to the high water content of this solvent system, the fraction was observed to hydrolyse post-column. An MS spectrum of a partially hydrolysed complex **Cr-5** is shown in **Figure 3.19**; the peak at 191.54 *m*/*z* represents a [M-OH$_2$+H]$^+$ fragment of the hydrolysed species.
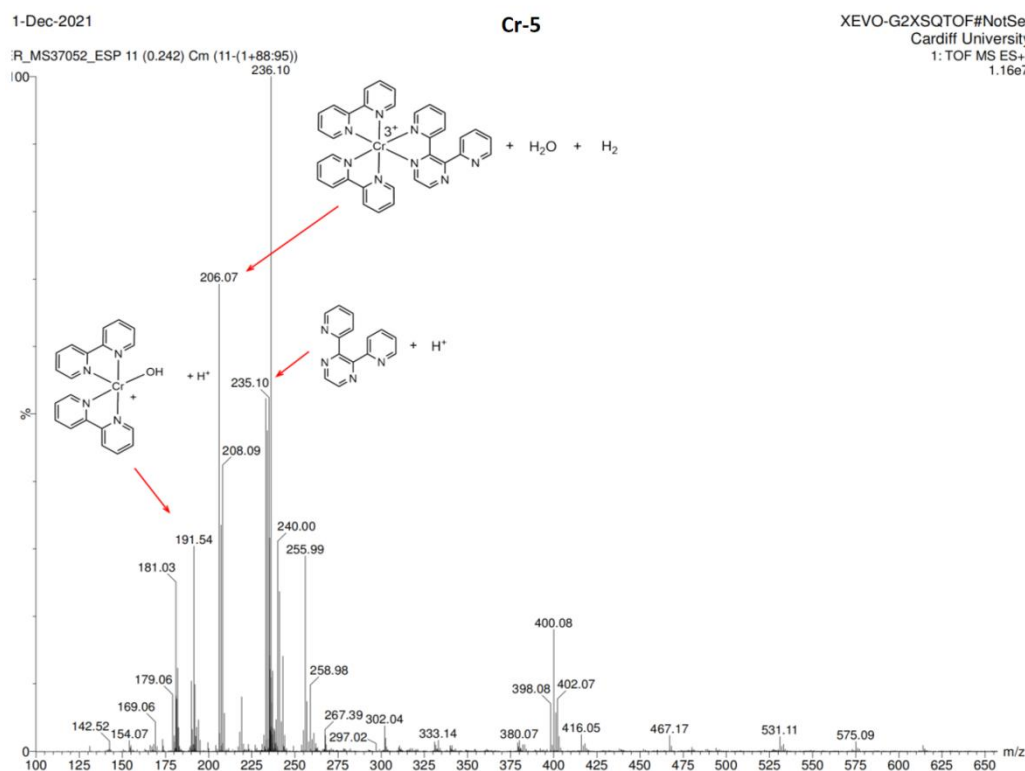
Figure 3.19 Mass spectrum showing Cr-5 and its hydrolysis by-product after initial column chromatography purification.

Therefore, the next steps in the purification process were to dissolve complex **Cr-5** in a minimal amount of MeCN/H$_2$O/KNO$_{3(sat)}$ (14:7:1) and dilute further with MeCN (approximate ratio 1:10). This was then filtered using a thin, but tall Al$_2$O$_3$ plug leaving the hydrolysed product on the top of the plug with the overly diluted complex running through with ease. The co-existence of complex **Cr-5** and its hydrolysed by-product could be noticed in FTIR measurements (**Figure 3.20**). The overall broad appearance of all recorded signals suggests extensive hydrogen bonding throughout the whole molecule, possibly originating from the OH$_2$ and OH ligands of the hydrolysed complex **Cr-5**. Additionally, signals at

3314 and 3636 cm^{-1} can both be attributed to O-H stretching and C-H vibrations, the latter weaker overtone vibrations entirely masked by the O-H signals. The reduced level of broadening of these signals when compared to pure water FTIR spectra suggests that the overall level of vibrations is reduced for OH$_2$ and OH ligands, as expected, upon coordination and formation of a near perfectly octahedral complex. It is important to note, that **Cr-5** was oven dried prior to FTIR measurements.
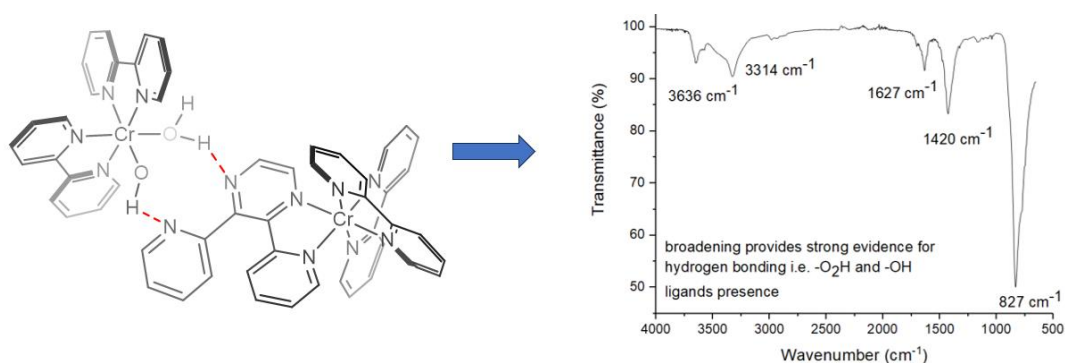
Figure 3.20 FTIR spectrum of complex **Cr-5** and the hydrogen bonding between the hydrolysed compound and **Cr-5** demonstrated as a possible origin of signal broadening.

This was followed up by a hydrolysis test on the complex. A freshly synthesised yellowish solid of complex **Cr-5** was suspended in water and left to stand overnight. Red crystals were found the following morning suggesting complete hydrolysis under room temperature conditions. This is in accordance with the reduced basicity of pyrazine in comparison to pyridine with pK_b values predicted to be 13.12 and 8.88 respectively (simulated with *MarvinSketch*).[34]

The hydrolysis was confirmed with ESI-MS (**Figure 3.21**), where the molecular peak (190.54 *m/z*) represents hydrolysed complex **Cr-5** upon a loss of water, which is a common fragmentation when electrospray ionisation method is employed. No signal attributed to **Cr-5** could be determined, whilst both ligands were still clearly present in the reaction mixture. This is not uncommon, where the complex and ligands co-crystallise together out of the solution. Therefore, a complete hydrolysis of complex **Cr-5** under ambient conditions when suspended in water was assumed.
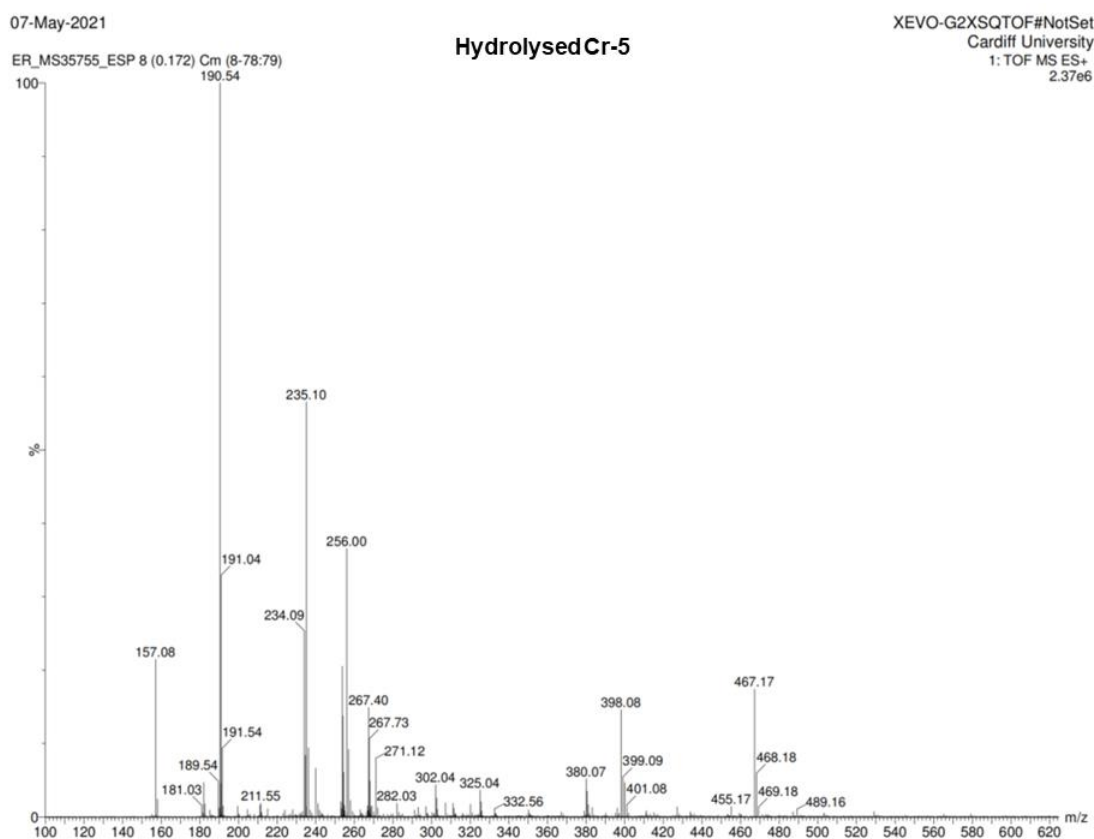
Figure 3.21 ESI MS of hydrolysed complex **Cr-5**.

3.3.6 Spectroscopic analysis

UV-Vis spectra were measured in aerated MeCN at room temperature and are illustrated in **Figure 3.22**. The spectra of the full series are consistent with closely related examples previously reported in the literature.[35] In particular, two sets of singlet intra-ligand charge transfers are observed at 250 and 300-350 nm for 2,2'-bipyridine and 1,10-phenanthroline derivatives, respectively, which is consistent with increased conjugation. Relatively high concentration measurements (10^{-3} M) revealed weak bands in the 400-550 nm region with $\varepsilon < 100$ M^{-1} cm^{-1} values. Heinze has previously assigned these absorption bands to the $^4A_2 \rightarrow {}^4T_2$ transition, however ^{3}ILCT transitions have also been reported to occur within the region according to others.[36,37]
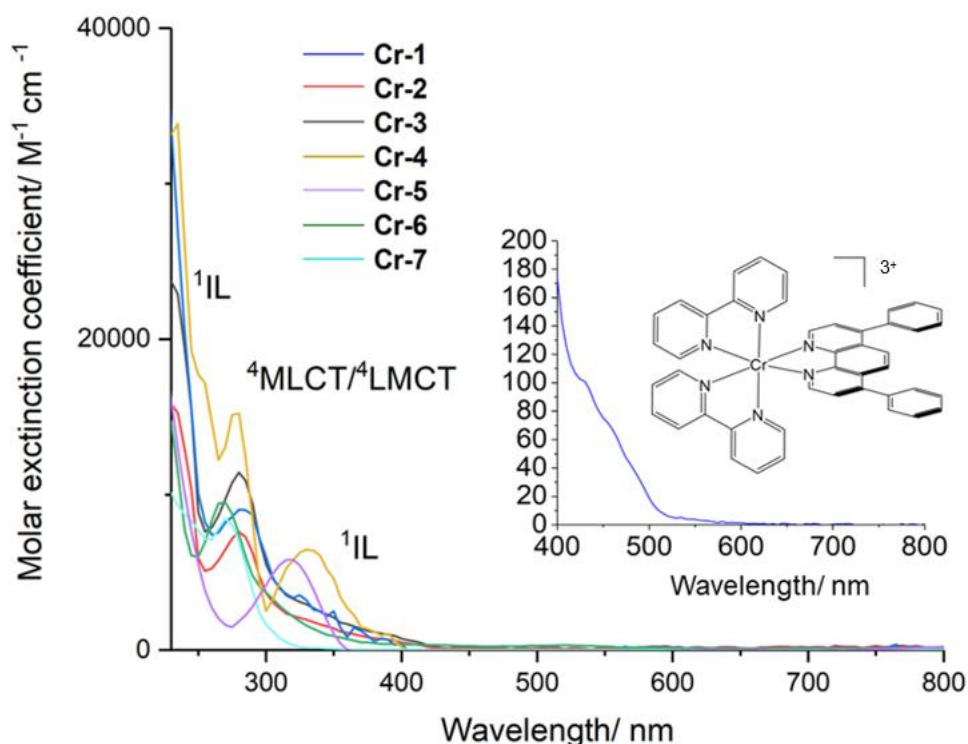
Figure 3.21 UV-Vis spectrum of complexes **Cr-1** to **Cr-7**. Measured in aerated MeCN solutions at 10^{-5} M. Inset UV-Vis was measured at 10^{-3} M in the same solvent.

Nevertheless, as discussed in **Chapter 2.3.2**, spin-forbidden d-d bands for Cr(III) polypyridyl complexes are expected within 670-800 nm for tridentate ligands and 650-710 nm for bidentate ligands. Good agreement with the reported values of the weak bands observed within 400-550 nm suggests that

the spin-forbidden bands for this series should be expected within a similar range to that reported in the literature.
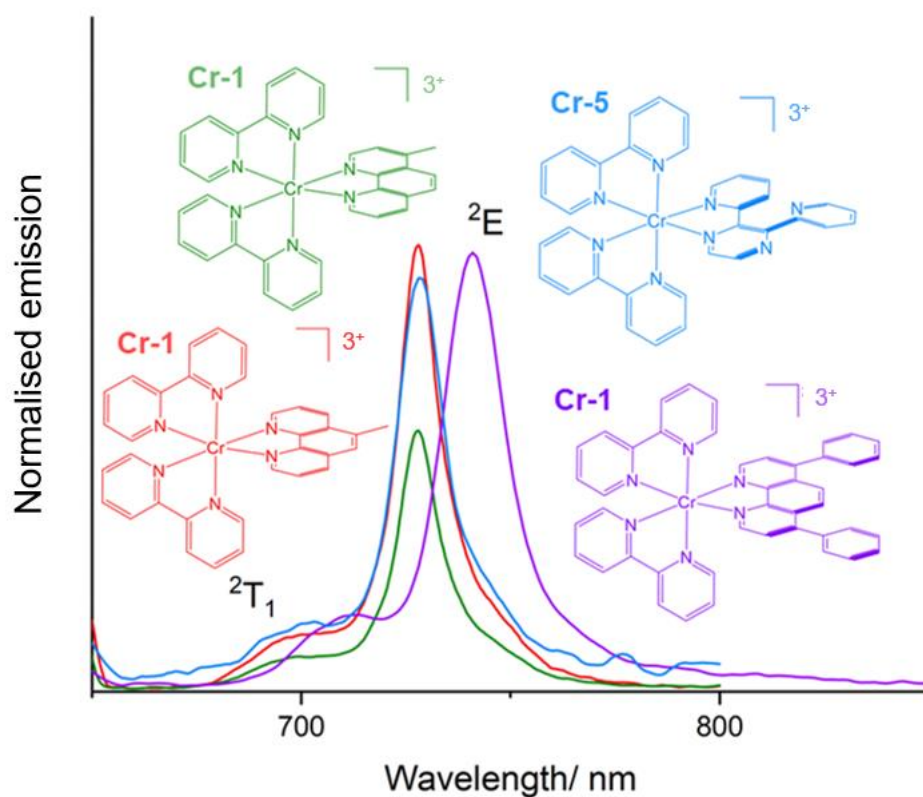
Figure 3.23 Emission profile of **Cr-1** to **Cr-3** and **Cr-5** recorded in aerated MeCN at room temperature (concentration 10^{-5} M).

Table 3.3 Emission bands of **Cr-1** to **Cr-7** measured in aerated MeCN at room temperature (concentration 10^{-5} M) using excitation wavelength of 320 nm.

Complex	Emission/ nm	Φ %	Error	Lifetime (µs)
Cr-1	740	0.0477	0.0627	N/A
Cr-2	727	0.0131	0.00151	23.3
Cr-3	728	0.0357	0.00256	27.9
Cr-4	760, 570	0.0613, 2.4	0.00436, 0.00755	N/A
Cr-5	726	0.0746	0.00265	N/A
Cr-6	729	0.0902	0.00543	23.0
Cr-7	738	0.0698	0.00326	N/A
[Cr(bpy)$_3$]$^{3+}$	728[a]	0.089[a]		63[a]
[Cr(phen)$_3$]$^{3+}$	728[a]	0.15[a]		270[a]

[a] - measured in deaerated HCl (ref 41).

The emission spectra of all complexes (**Cr-1** to **Cr-7**) were recorded at room temperature in aerated MeCN solutions, using 320 nm excitation. The results for selected examples are shown in **Figure 3.23**, all of which exemplify the typical emission spectrum expected for a Cr(III) complex, represented by the bands within the 720-760 nm region. The emission properties, including lifetimes and quantum yields are listed in **Table 3.3**. The emission bands for all of the complexes are very sharp, which is directly related to the nature of the spin-flip transition. As illustrated in **Figure 3.24**, since the excited electron experiences a spin-flip from quartet to doublet excited state occupying the same orbital, there is little to no change in the overall geometry of the excited state complex.[38] This means that the bond lengths and bite angles remain unchanged. Therefore, the line broadening that is characteristic of transitions in which the electron changes orbital character upon excitation, leading to a mismatch in vibrational levels of the excited and the ground state, is not observed. Instead, the differences between the maxima of the vibrational levels of the excited state and the ground state are minimal and give rise to a very sharp band for the ^2E state in addition to a small shoulder on the high energy side representative of the $^2T_1$ state (**Figure 3.23**) typical for Cr(III) complexes.

This leads to a conclusion that the emission maxima from Cr(III)-based doublet states are likely to be influenced by the electron withdrawing/donating properties of ligand substituents and the resulting ligand field strength. Therefore, strong field ligands allow for generation of the doublet excited state and its spin-forbidden relaxation back to the ground state rather than deactivation via BISC (see **Section 3.1**). Fine tuning of the emission wavelength for Cr(III) complexes, in particular to create a red-shift beyond the commonly reported 650-700 nm range, can therefore be achieved through judicious selection of the ligand substituents. The presence of three unpaired electrons results in significant interelectronic repulsion and any decrease in the magnitude of this interaction acts to lower the ^2E state energy, therefore red-shifting the emission maxima as discussed in **Chapter 1.3.1**.
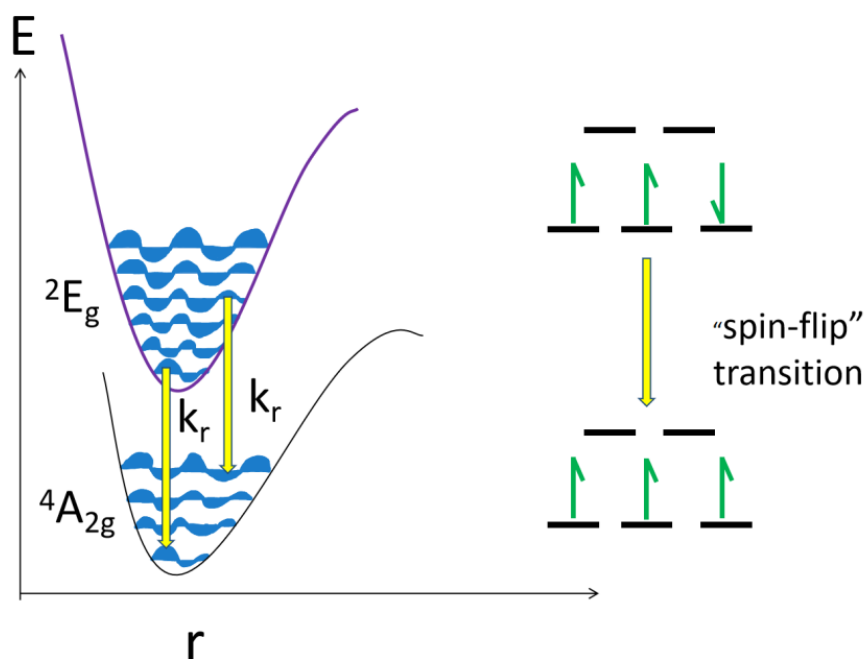
Figure 3.24 Depiction of the "spin-flip" nature of $^2E \rightarrow {}^4A_2$ transition and the overlap of associated vibrational levels.

The emission window for Cr(III) complexes is usually reported to be 660-700 nm (see **Section 3.1.1**). These results indicate that all complexes in the polypyridyl series presented herein show some reduction in interelectronic repulsion, as is expected for both the bpy and phen ligands with low lying anti-bonding orbitals.[39] It is interesting to note that complexes **Cr-1**, **Cr-4** and **Cr-7** all show a particularly substantial shift of the emission maxima. For complex **Cr-1** (bathophenanthroline ancillary ligand), it is reasonable to assume that the extensive conjugation further lowers the energy of the ^2E state resulting in 760 nm emission maxima.

For complexes **Cr-4** and **Cr-7**, it is possible that the inductive effect of the peripheral substituents (NH_2 and CH_3, respectively) leads to an increased nephelauxetic effect wherein the metal-centred electron density is delocalised into the anti-bonding orbitals of the surrounding ligands.

Due to very low yields, the lifetime data could only be collected for complexes **Cr-2** (23.3 µs), **Cr-3** (27.9 µs) and **Cr-6** (23.0 µs) which are also listed in **Table 3.3**. As outlined in **Section 3.1.2**, it is not possible to make direct comparison of lifetime data measured in aerated solvents. However, it is worth noting that these three complexes show consistency with other polypyridyl Cr(III) complexes reported in the literature for which lifetimes in the microsecond range are (see **Sections 3.1.1** and **3.1.2**). [6-18]

Quantum yield analysis can be challenging considering there is little information on quantum yields for Cr(III) complexes available in the literature. Due to the close energy gap between the low-lying doublet excited state and the ground state, non-radiative decay competes with NIR emission. Across the polypyridyl Cr(III) complexes reported in the literature, $[Cr(phen)_3]^{3+}$ shows the highest quantum yield reported with Φ = 0.15% measured in aerated aqueous solutions. $[Cr(tpy)_2]^{3+}$ shows the lowest reported quantum yield of < 8.9×10^{-6}, also in aerated aqueous solution.[40] When studying the quantum yields of Cr(III) complexes, direct comparison becomes more complex when aerated solutions are considered. This is because of collisional quenching via triplet oxygen and solvent quenching as discussed in **Section 1.2.5**. That means, each complex might have a specific sensitivity to such quenching mechanisms, and it might be difficult to draw direct conclusions based on the substituents present. The quantum yield values determined from our experimental data on complexes **Cr-2** and **Cr-3** are lower (0.0131 and 0.0357%, respectively) than that of $[Cr(bpy)_3]^{3+}$ (0.089%) reported previously in deaerated 1 M HCl. The same is true for complex **Cr-1** (0.0477%), although the error associated with the measurement (0.0627) makes it fundamentally inaccurate. This is likely to be a result of the very weak signal and difficulties with defining the AUC values for the series of concentrations used to determine the quantum yield value for **Cr-1**. However, the Φ of complex **Cr-4** (0.0613%) is approximately 0.028% lower than for $[Cr(bpy)_3]^{3+}$, which is due to the potential multiphoton relaxation deactivation pathway via N-H oscillations resulting from the NH_2 substituent of the phenanthroline ligand. Complex **Cr-5** (0.0746%) shows to have a quantum yield of remarkably similar value to $[Cr(bpy)_3]^{3+}$,[41] this could be due to the additional pyridine ring exposing the molecule to higher level of collisional

quenching by molecular oxygen as well as attracting the solvent molecules via hydrogen bonding and therefore inducing collisional quenching via solvent. The quantum yields of complexes **Cr-6** and **Cr-7** are significantly higher (0.0902 and 0.0698%, respectively) than those of complexes **Cr-2** and **Cr-3**, which is consistent with the additional rings reducing the level of multiphoton relaxation and is consistent with literature in which $[Cr(phen)_3]^{3+}$ is reported to have a higher quantum yield (0.15%) than that of $[Cr(bpy)_3]^{3+}$.[41]

It is commonly observed that paramagnetic metal centres tend to significantly quench the ligand-based emission upon coordination, due to either Ligand to Metal Charge Transfer (LMCT) or Metal-to-Ligand-Charge-Transfer (MLCT) processes. [42,43,44] Those processes describe a charge transfer occurring between the excited electron originating from the ligand being transferred over to the metal centre or the metal centre donating an excited electron to the excited ligand-based orbital, eg π^*. This is facilitated by close proximity of the ligand-centred and metal-centred energy levels. For LMCT, the ligand excited state must lie above the metal centred energy level for the transfer to be energetically favourable. In the case of MLCT, the opposite occurs. Therefore, it is not common to observe fluorescent paramagnetic complexes, although an example of Ni^{2+} has been reported.[45]

As illustrated in **Figure 3.25**, complex **Cr-4** proves to be an outstanding example of dual emission. As expected, the complex emits from its doublet excited state around 760 nm with very low quantum yield of ~0.06%. However, the same excitation wavelength also triggers a high quantum yield emission at ~500 nm (2.4%). This newly observed emission band can be assigned to ligand-based emission of 5-amino-1,10-phenanthroline and is assigned to an ILCT modulated upon aggregation due to its concentration dependent behaviour.
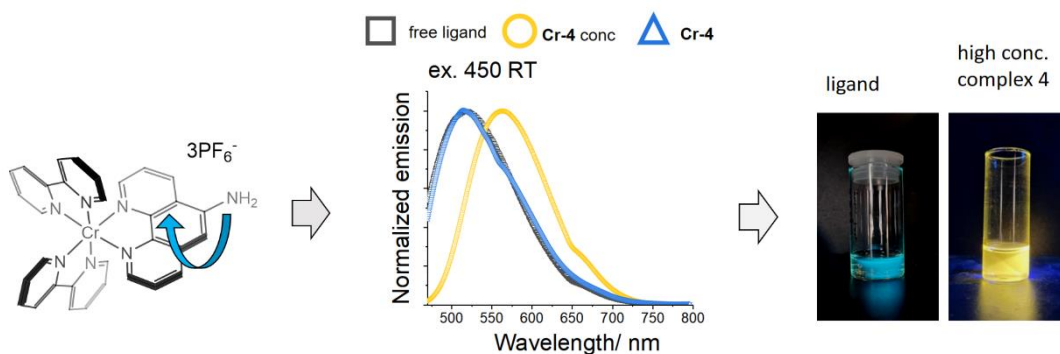
Figure 3.25 Emission spectra of **Cr-4** (yellow = 10^{-3} M, blue = 10^{-5} M) and free ligand (10^{-5} M) and the corresponding emission colours (right). Excitation wavelength = 450 nm.

Furthermore, a slight shoulder in the red part of the spectrum with respect to the 500 nm emission band is observed for **Cr-4** when excited at 375 nm (**Figure 3.25**). This becomes even more apparent at high concentration, where two strong bands are observed to co-exist within 450-650 nm range. At low temperature, the two bands seem to merge at high concentration, whereas the low concentration sample shows no difference to the room temperature data. Stark differences are observed upon excitation at 450 nm between the spectra recorded in different concentration regimes. At both temperatures, the low concentration spectrum shows emission at 500 nm with a slight shoulder in the red part of the spectrum, whereas the high concentration sample shows a red-shifted emission band at 570 nm. A comparison between the two excitation wavelengths and temperature conditions is illustrated in **Figure 3.26**.
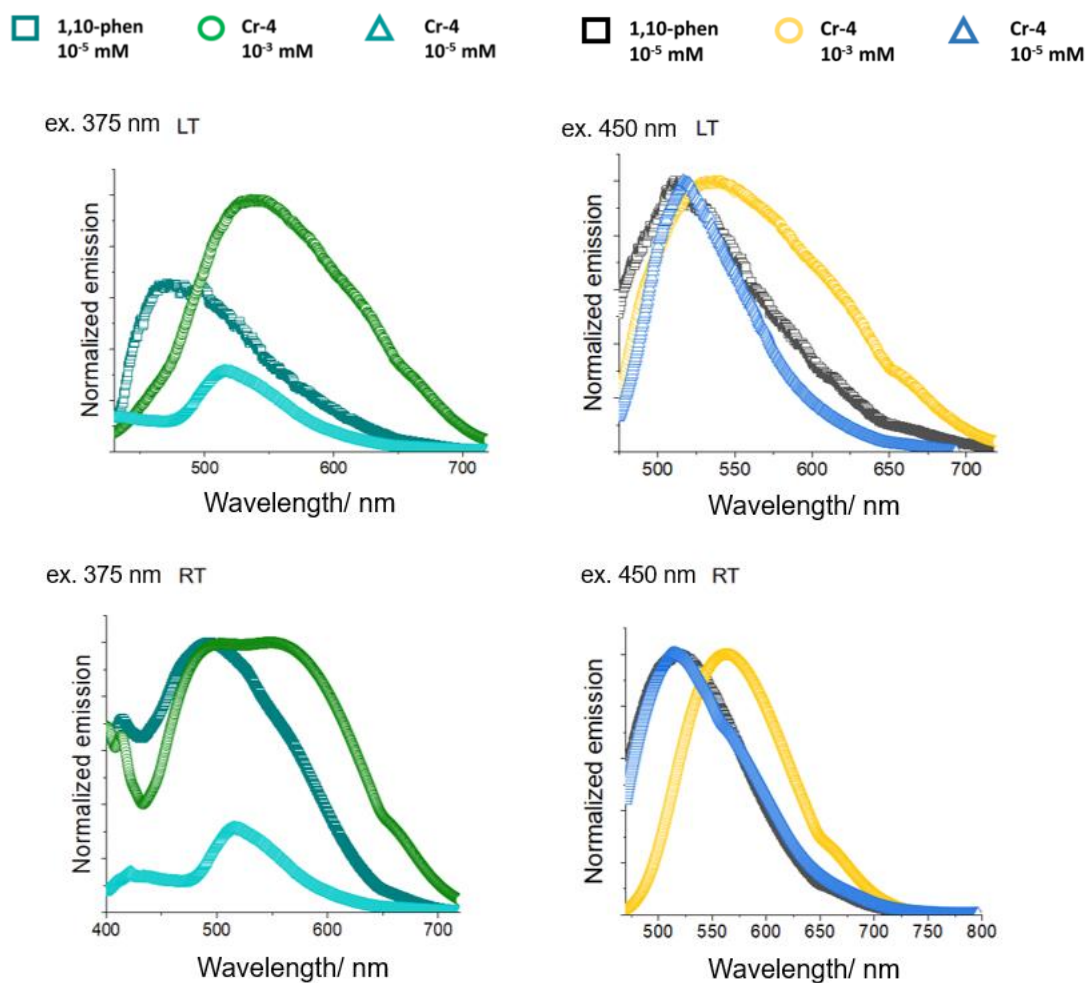
Figure 3.26 Comparison of low temperature and room temperature luminescence measurements of complex **Cr-4** at (top) 375 nm and (bottom) 450 nm excitation wavelength.

Possible explanation for this type of emissionare triplet ligand-based emission, ligand to ligand charge transfer or quartet emission from Cr(III) centre. It is not possible to distinguish between the ^{4}A → ^{4}T$_1$ transition and the ligand-based transition in the UV-Vis spectra, as most probably the intra-ligand transition overlaps with the much weaker d-d transition.[46,47] This is consistent with the literature on 5-amino-1,10-phenanthroline.[48]

Lifetime measurements could offer some insight into the origin of the emission bands. Standard singlet emission lifetimes for organic molecules are typically within the 1-10 ns range, whereas emission originating from quartet excited states are calculated to have lifetimes not longer than 1 µs, however it is rare to observe Cr(III) complexes for which the ^{4}T$_2$ excited state is the lowest lying state.[34,49,50,51] It should be noted that emission originating from triplet states of organic molecules can result in quantum yields and lifetimes that are similar to those reported for the emission originating from the quartet excited state such as that of Nap-IBDP (Bisnapthalene- 2,6-diiodoBODIPY) with a lifetime of 1.4 µs reported in aerated 2-Metetrahydrofuran (**Figure 3.27**). Therefore lifetime measurements can only serve as a tool for distinguishing the emission origin between the singlet-triplet excited state of 5-amino-1,10-phenanthroline or the quartet excited state of complex **Cr-4**.[52,53] Nevertheless, the low yield for **Cr-4** did not provide enough material for additional lifetime measurements to be performed.
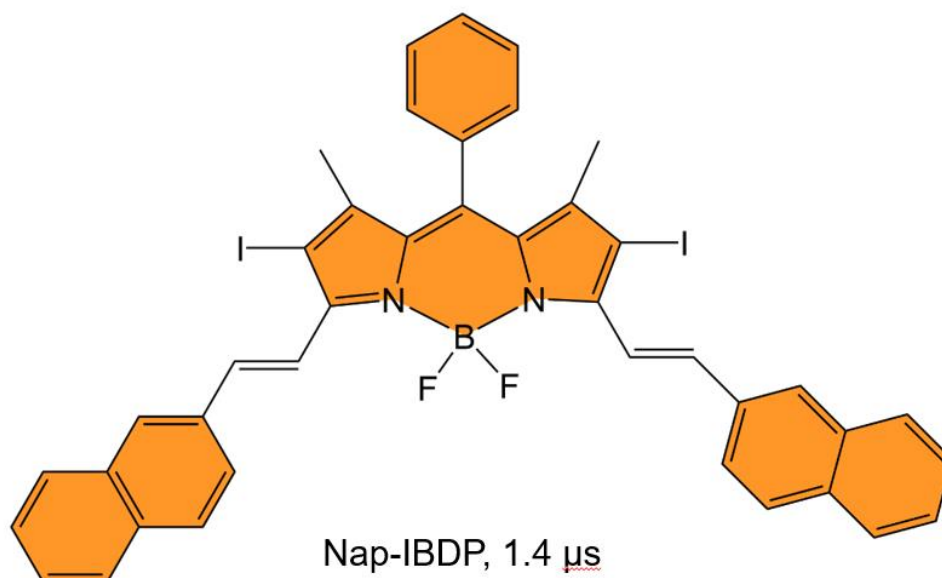
Figure 3.27 Nap-IBDP reported by Wang *et al.*, with a lifetime in the microsecond range in aerated 2-Metetrahydrofuran.[52]

Interestingly, comparison of the UV-Vis spectra recorded at different concentration regimes for **Cr-4** can provide additional insight into the nature of this emission (**Figure 3.28**). At 10^{-5} M, the highest energy band resolved is ∼ 350 nm, which is assigned to the singlet intra-ligand charge transfer of 5-amino-1,10-phenanthroline. However, another band emerges at ∼ 434 nm at higher concentration (10^{-3} M). This feature is assigned to triplet intra-ligand charge transfer, consistent with the fact that this peak could not be resolved at low concentrations.
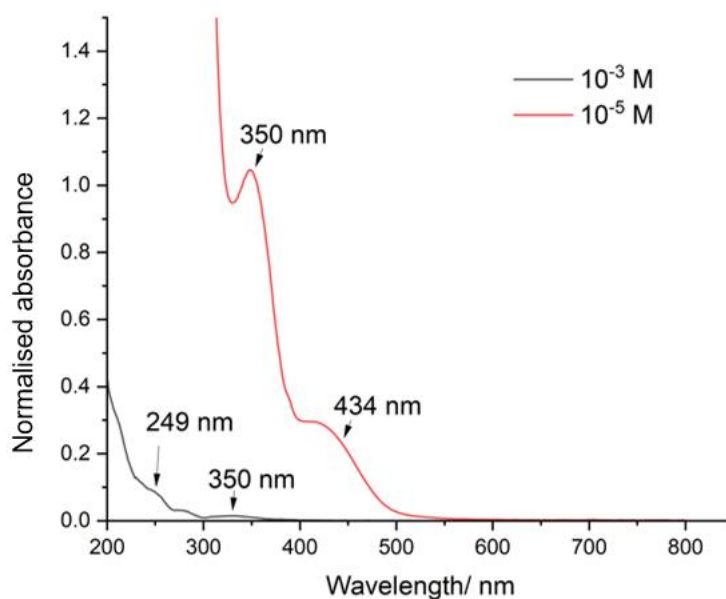
Figure 3.28 Features of the UV-Vis spectra (298 K) of 10^{-3} M vs 10^{-5} M concentrations of **Cr-4** in deaerated MeCN.

3.3.7 Crystal Structure Analysis

As the emission properties of Cr(III) complexes are strongly correlated with coordination geometry, we sought to grow crystals of each sample. Low temperature crystallisation was attempted in which the complexes were first dissolved in the minimal amount of a CH_2Cl_2/MeCN mixture, followed by addition of Et_2O/Toluene ensuring that the complexes remained well dissolved. The vials were placed in a freezer stored at $-18°C$ for a week. This process resulted in good quality light yellow block of **Cr-2**. Data collection, refinement and structure solution was conducted by Dr Peter Horton at the UK National Crystallography Service, Southampton and the analysis indicated that a single molecule occupies the asymmetric unit (**Figure 3.29**). Experimental details are available in **Table 3.4**.
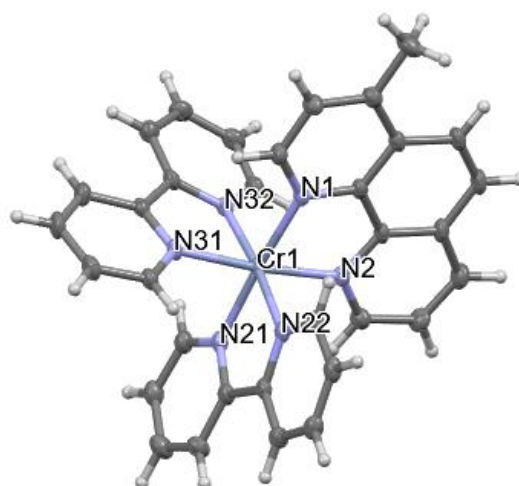
Figure 3.29 Crystal structure obtained for [Cr(bpy)$_2$(4-Me-phen)](PF$_6$)$_3$ (**Cr-2**). Ellipsoids shown at 50% probability. Solvent and counterion were removed for clarity.

Table 3.4 Crystal data for **Cr-2**.

Compound	Cr-2
Formula	$C_{37}CrF_{18}H_{32}N_8P_3$
$D_{calc.}$/ g cm^{-3}	1.697
m/mm^{-1}	0.507
Formula Weight	1075.61
Colour	light yellow
Shape	block
Size/mm^3	0.120×0.100×0.040
T/K	100(2)
Crystal System	triclinic
Space Group	P-1
a/Å	9.3849(2)
b/Å	11.9112(3)
c/Å	20.2877(4)
a/°	84.587(2)
b/°	84.293(2)
g/°	69.152(2)
V/Å^3	2104.64(9)
Z	2
Z`	1
Wavelength/Å	0.71075
Radiation type	Mo K$_a$
Q_{min}/°	2.022
Q_{max}/°	28.700
Measured Refl`s.	32750
Indep`t Refl`s	10789
Refl`s I≥2 s(I)	8546
R_{int}	0.0281
Parameters	551
Restraints	0
Largest Peak	0.665
Deepest Hole	-0.784
GooF	1.050
wR_2 (all data)	0.1188
wR_2	0.1127
R_1 (all data)	0.0575
R_1	0.0435

$R_1 = \Sigma \ ||F_o| - |F_c|| \ / \ \Sigma \ |F_o|$, $wR_2 = \{\Sigma \ [\ w(F_o{}^2 - F_c{}^2)^2] \ / \ \Sigma \ [w(F_o{}^2)^2] \ \}^{1/2}$,

$GooF = S = \{ \ \Sigma \ [w(F_o{}^2 - F_c{}^2 \ )^2] \ / \ (n-p) \ \}^{1/2}$

Fo – experimental model, Fc – calculated model, w -weighting scheme

The analysis of trans and bite angles (172-173° and 78-80°) suggests a slightly distorted octahedral geometry which implies that some level of surface crossing is to be expected as a deactivating pathway towards the doublet excited state emission.[18] Since only one crystal structure was obtained, a detailed DFT analysis was performed on the remaining complexes to create a full picture of the geometry across the series reported herein. DFT geometry optimisation

was utilised to obtain information about the trans and bite angles of all the other complexes. To ensure accuracy of the computational results, a comparison of the trans angles extracted from the crystal structure of complex **Cr-2** was performed. Pleasingly, only a very small error of ~2-4 ° was determined, demonstrating the validity of the computational approach. Crystal structure extracted trans angles for **Cr-2** are 176.20(7)°, 174.05(6)° and 174.49(6)° (**Table 3.5**) whilst the calculated trans angles are 173.10°, 172.62°, 172.62°, therefore both methods reveal a distorted octahedral geometry, which may give rise to possible surface crossing deactivation of the doublet excited state emission as discussed previously by Heinze (**Table 3.6**).[54] Moreover, the bite angles extracted from the crystal structure were 80.30(6)°, 79.68(6)° and 80.23(6)°, while the calculated bite angles are 78.92°, 79.81° and 78.81° further supporting distorted octahedral geometry. Representation of atom numbering for appropriate understanding of trans and bite angles listed in **Table 3.6** is available in **Figure 3.30**.

Table 3.5 Experimental trans angles in **Cr-2**.

	Cr-2
N_1-Cr-N_4	176.20(7)
N_2-Cr-N_5	174.49(6)
N_3-Cr-N_6	174.05(6)

Table 3.6 Trans and bite angles obtained from geometry optimized structures for **Cr-1** to **Cr-7**.

Name	Cr-N-Cr Trans angles (°)			Cr-N-N Bite angles (°)		
	N₁-Cr-N₄	**N₂-Cr-N₅**	**N₃-Cr-N₆**			
Cr-1	173.60	172.62	172.62	79.11	79.71	79.11
Cr-2	173.10	172.89	172.95	78.92	79.81	78.81
Cr-2$_{exp}$	176.20(7)	174.49(6)	174.05(6)	80.30(6)	79.68(6)	80.23(6)
Cr-3	173.15	172.83	172.53	78.83	79.79	78.91
Cr-4	173.47	172.98	172.72	78.74	79.94	78.92
Cr-5	172.34	172.92	172.63	78.72	78.09	78.92
Cr-6	172.62	173.13	173.09	79.95	80.03	80.04
Cr-7	172.95	173.34	173.53	79.98	80.00	80.10

Trans angles:

1)   **2)**   **3)**

Bite angles:

1)   **2)**   **3)**
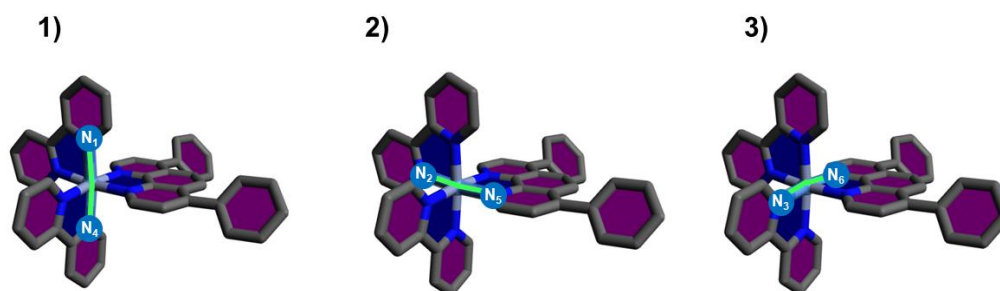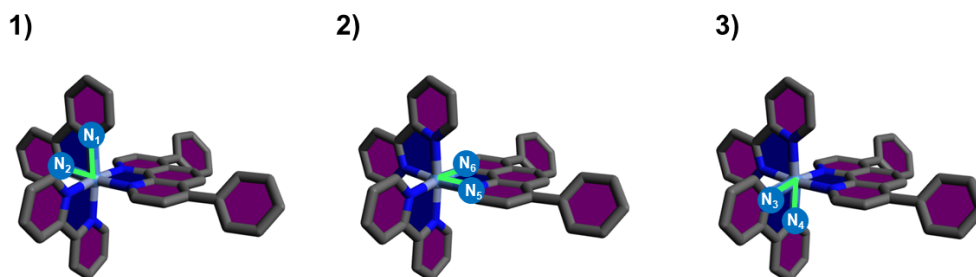
Figure 3.30 Representation of trans and bite angles listed in **Table 3.6**.

All geometries were optimized using the B3LYP functional and 6-311G (d,p) basis set, and were performed using Gaussian 09. Similarly, to the calculated Cr-N-N trans angles, all the complexes display very similar Cr-N-N bite angles (79-80°). However, comparison between the trans and bite angles only provides an insight into the relative geometry of the complexes and further analysis is needed where the trans and bite angles remain so similar. In addition to the close similarity of trans and bite angles calculated across the series of the complexes, despite the range of substitutions made at peripheral groups, it is worth noting that all complexes show substantial distortion away from the octahedral geometry which attributes to significant strain induced by the rigid five-membered ring chelates. Therefore, the low quantum yields and relatively short lifetimes of these complexes, in comparison to their six-membered analogues, can be understood. Whilst the bond lengths and trans angles for **Cr-1** to **Cr-7** were almost identical, it was noted that the complexes displayed a twist angle between the two ligand planes (**Table 3.7**) which is consistent with trigonal twisting leading to surface crossing as discussed by Heinze.[18] Furthermore, this showed more variation across the series than the trans/bite angles previously discussed. As can be seen in **Table 3.7**, all of the complexes displayed different absolute geometry, that was closely correlated with the overall bulk of each ligand coordinated to the metal centre. A comparison between the angles of the mean planes is illustrated in **Figure 3.31** for **Cr-2** and **Cr-6.** As can be seen, the increased steric bulk of the phenanthroline ligand leads to an increase in the trigonal twist angle in comparison to the smaller bipyridine analogue.
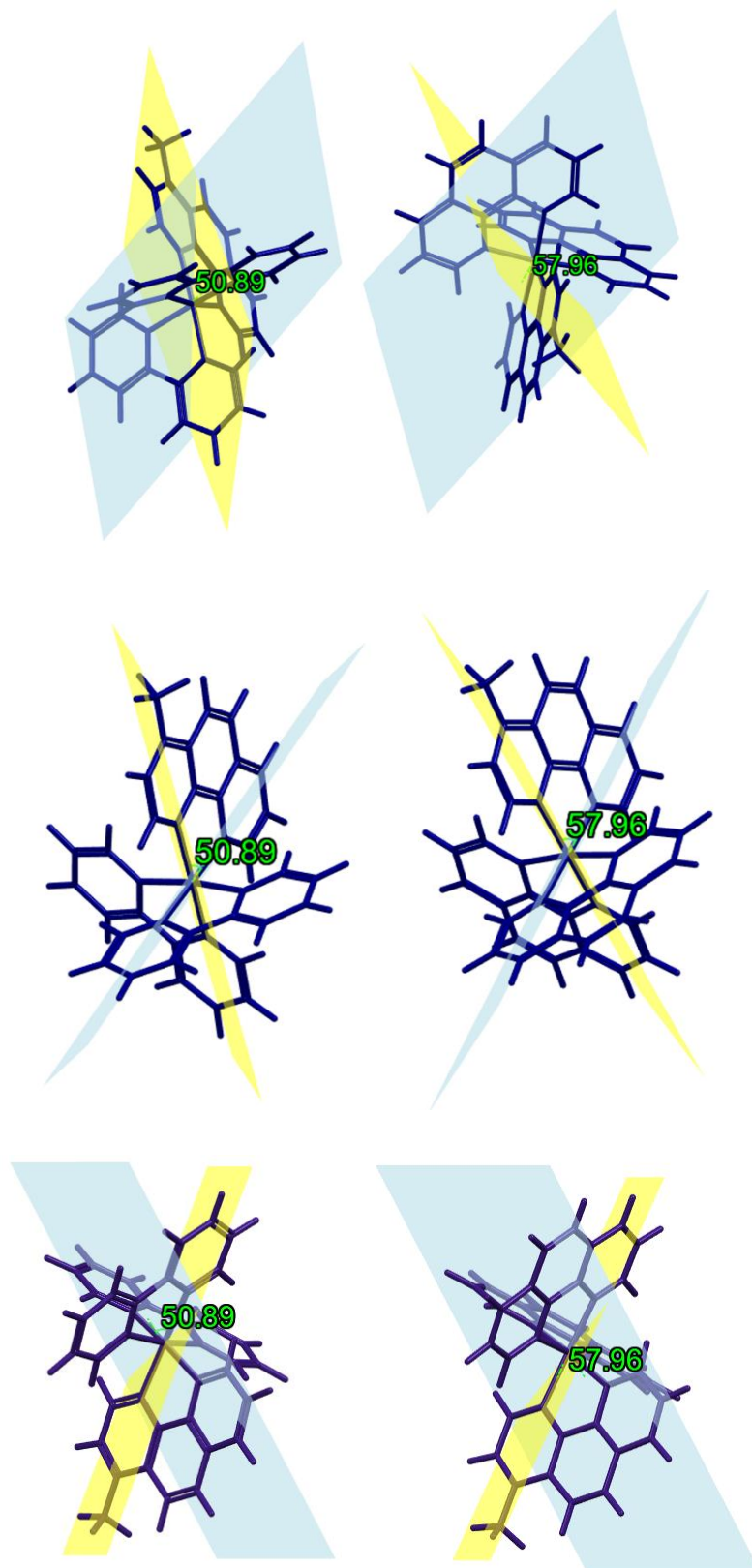
Figure 3.31 Mean plane representation for complexes **Cr-2** (left) and **Cr-6** (right). For simplicity, only planes across X (blue) and Y (yellow) axes are shown with the angle between the planes shown in green.

Table 3.7 Representation of the mean plane analysis obtained from DFT optimized structures for complexes **Cr-1** to **Cr-7**.

Name	X-Y (°)	X-Z (°)	Y-Z (°)
Cr-1	55.54	52.30	52.28
Cr-2	50.89	54.25	54.25
Cr-2$_{exp}$	53.48	56.81	48.08
Cr-3	51.52	54.80	53.52
Cr-4	52.55	51.40	55.44
Cr-5	49.90	54.41	54.88
Cr-6	57.96	52.66	51.88
Cr-7	55.70	52.17	53.94

In the $[Cr(bpy)_2(L)]^{3+}$ series, the angles of X-Y axes mean planes decrease with the decreasing bulk of the ligand, as the angles of X-Z and Y-Z increase. For instance, the bulkiest bathophenanthroline ligand imposes the largest angle between X-Y mean planes for complex **Cr-1** of 55.54°, with the least bulky bis-pyridyl-pyrazine ligand (**Cr-5**) generating an angle of 49.90°.

To sum up, the results obtained from the DFT and crystal structure analysis clearly point to a correlation between the emission of the complexes from the doublet excited state and the geometry of the complexes. As previously indicated by Heinze, the distorted octahedral geometry of polypyridyl Cr(III) complexes via trigonal twisting as observed herein, leads to surface crossing and therefore deactivation of the doublet excited state to a degree which is somewhat reflected in the low quantum yields of the complexes.[46]

3.3.8 EPR Spectroscopy results

The X-band EPR spectra for all complexes were recorded (neat solids, see **Section 3.5** for further experimental details) with individual spectra available in Appendix 2. To support the analysis of the experimental results, complementary DFT calculations of the spin Hamiltonian ZFS parameters were performed on the ground state systems. **Figure 3.32** shows simulated experimental spectra of **Cr-1** and **Cr-2** recorded at room temperature. Spectra for **Cr-3** to **Cr-7** are available in **Appendix 3**.
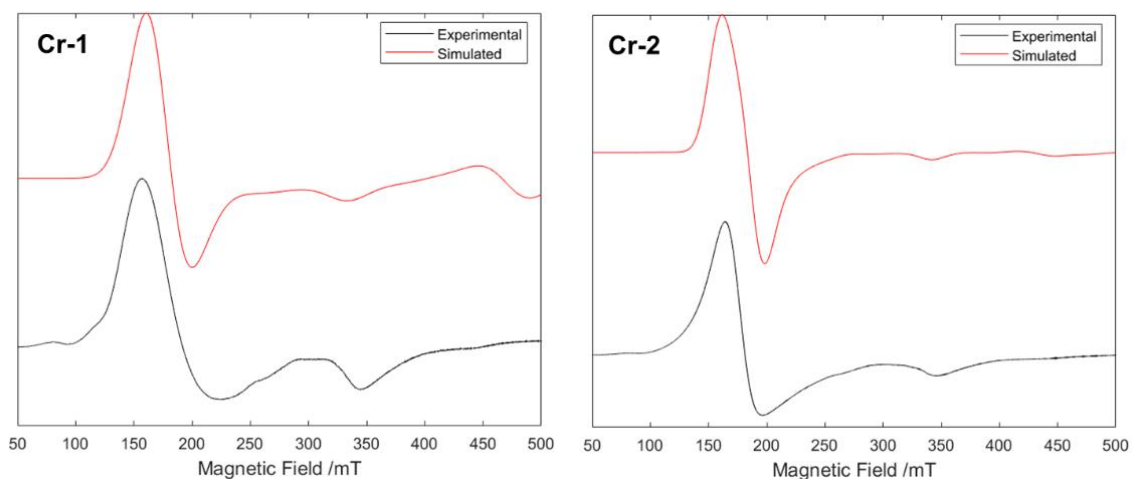
Figure 3.32 Experimental (black) and simulated (orange) spectra for **Cr-1** and **Cr-2**. The measurement was carried out at X-band at room temperature using neat solid.

All measurements showed broad axial spectra with at least two clearly visible lines.[55] The experimental and calculated g-value and zero-field parameters are listed in **Table 3.5**. Although, the g-value for Cr-2, Cr-3 and Cr-5 was simulated to be isotropic the appearance of the EPR spectra suggest axial geometry for those complexes which is consistent with the geometry observed by X-ray crystallography (**Section 3.3.7**). This is also supported by single crystal measurements recorded at different angles which prove that the g-value is anisotropic and therefore the spectrum appearance is dependent on the position of the crystal with respect to the magnetic field. Nevertheless, such measurements should be carried out for **Cr-3** and **Cr-5**. The small negative shift from $g_e \approx 2.0023$ for the two complexes is to be expected as a result of the less than half-filled d-orbitals, and the relatively small spin-orbit coupling parameter of the central chromium ion (for Cr(III) = 275 cm^{-1}).[56] The results indicate a clear correlation between the ligand field strength and the magnitude of the ZFS parameters, as exemplified by the *D*-values of complexes **Cr-1** to **Cr-5** (bpy, 0.37-0.54 cm^{-1}) and **Cr-6** and **Cr-7** (9,10-phen, 0.30-0.31 cm^{-1}). The stronger π-acceptor character of 9,10-phen lowers the electron density at the metal centre and therefore reduces the ZFS effect which results in lower *D*-values for [Cr(phen)$_2$(L)]$^{3+}$ complexes in comparison with [Cr(bpy)$_2$(L)]$^{3+}$ analogues. It can also be noted across the [Cr(bpy)$_2$(L)]$^{3+}$ series where the *D*-value decreases across the series as the ligand field strength of L increases.

The individual experimental and simulated spectra for Complexes **Cr-2** to **Cr-7** are shown in **Appendix 3**. These results clearly reflect the sensitivity of the zero-field parameters with the ligand environment at the metal centre. For example, **Cr-1** is characterised by a D-value of +0.37 cm^{-1}, whereas complex **Cr-5**, is characterised by D = +0.54 cm^{-1}, a result of the much weaker field ligand bis-pyridyl-pyrazine. A decrease in the magnitude of the zero-field splitting parameter D is indicative of a reduced ZFS interaction in the axial plane.

Table 3.8 Experimental and calculated EPR parameters for complexes **Cr-1** to **Cr-7**, complemented with values of the ordering parameter utilised in EPR simulations of the experimental ZFS parameters.

Complex	Calculated					Experimental				
	g-value			D (cm^{-1})	E/D	g-value			D (cm^{-1})	E/D
Cr-1	1.99	1.99	1.99	0.37	0.0009	2.05	1.99	1.99	0.37	0.013
Cr-2	1.99	1.99	1.99	0.40	0.049	1.99	1.99	1.99	0.42	0.096
Cr-2[a]	1.99	1.99	1.99	0.41	0.048					
Cr-3	1.99	1.99	1.99	0.40	0.120	1.99	1.99	1.99	0.4	0.058
Cr-4	1.99	1.99	1.99	0.42	0.111	1.90	1.90	1.95	0.42	0.071
Cr-5	1.99	1.99	1.99	0.54	0.016	1.99	1.99	1.99	0.54	0.016
Cr-6	1.99	1.99	1.99	0.30	0.057	1.9	1.99	1.9	0.31	0.060
Cr-7	1.99	1.99	1.99	0.31	0.014	1.99	1.99	1.9	0.3	0.007

[a] 1 cm^{-1} = 29,979 MHz

The bathophenanthroline ligand of Complex **Cr-1** shows substantial π-acceptor character, which is confirmed by the lowest experimental and simulated D-value across the bpy series. Therefore, a decrease in the electron density at the Cr(III) centre through increased delocalisation onto the ligand framework results in a decrease in the D-value and a corresponding red-shift of the emission band to 740 nm (**Section 3.3.6**). Furthermore, the E/D (and hence E-value) is much lower for **Cr-1** than those of other complexes in the series, therefore the lower spin density in the equatorial plane due to higher level of π-acceptor character also influences the red-shift of the emission peak. **Cr-5** shows one of the lowest luminescence emission peaks (726 nm) suggesting that the bis-pyridyl-pyrazine does not demonstrate significant π-acceptor, which is consistent with

the highest D-value (0.54 cm^{-1}) in the series. The D-value for Complex **Cr-7** was determined to be 0.1 cm^{-1} lower than that of its direct analogue **Cr-3** where the two core ligands are bpy instead of phen. Noticeably, its E/D value (0.007) is much lower than that of complex **Cr-3** E/D (0.058) and therefore suggests that a delocalisation of the electron density from the metal centre to the non-bonding orbitals of the ligands in the equatorial plane (xy molecular plane) facilitates that red-shift. This is consistent with a substantial red-shift of the luminescence of **Cr-7** (738 nm) compared to its analogue complex **Cr-3** (728 nm).

The very slight differences in the experimental D-values between the matched pairs of **Cr-2** and **Cr-3** complexes and **Cr-6** and **Cr-7** complexes are the result of the versatile differences in partial charge distribution which depend on the positioning of the Me group. As illustrated in **Figure 3.33**, which depicts partial charge distributions for 1,10-phenanthroline, 5-Me-1,10-phenanthroline and 4-Me-1,10-phenanthroline, the electron donating character of the Me group in position 5 is only reflected in a decrease of the partial charge of only one of the N atoms, whereas substitution in position 4 results in a decrease of the partial charges of both N atoms of the core 1,10-phenanthroline ligand. This decrease of the partial charges of N atoms result in an increase in the electron density contributing to the coordination of the N atoms to the Cr(III) centre, therefore increasing the electronic repulsion at the metal centre which is observed in higher D-values for complexes **Cr-2** and **Cr-6**. It is important to note that both complexes exhibit blue-shifted emission with respect to their matched pairs (727 and 728 nm for **Cr-2/3** and 729 and 738 nm for **Cr-6/7**) further agreeing the very subtle increase in interelectronic repulsion.
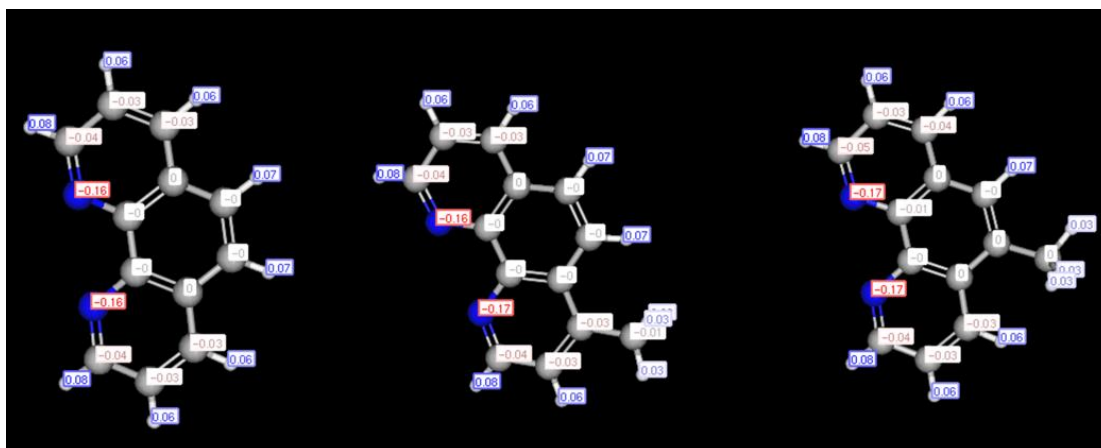
Figure 3.33 *MarvinSketch* simulated partial charge distribution using the Mulliken method of (from left): 1,10-phenanthroline, 5-Me-1,10-phenanthroline and 4-Me-1,10-phenanthroline.[57]

To further test the accuracy of the computational results, a comparison of the spin-Hamiltonian parameters obtained using the atomic coordinated directly from the crystal structure and those calculated from the geometry optimized structure was undertaken. The *D*-value was found to be in very close agreement for the two calculations, differing by only 0.01 cm^{-1}. The *E*/*D* values differed by 0.001 cm^{-1} as listed in **Table 3.7**.

Importantly, *E*/*D* values and therefore *E*-value nearing zero suggest axial geometry.[58]

A definite assignment of experimental values is not possible due to a myriad of broadening effects, in particular the potential for dipole-dipole interaction between neighbouring Cr(III) centres in the neat solids (see **Section 1.6.5**). This could be avoided by performing the measurements on solids doped into EPR silent matrices (see **Section 1.6.5**), however disappointingly all synthetic attempts at generating Co(II) analogues in order to generate EPR silent Co(III) analogues of the Cr(III) series demonstrated in this chapter failed and no Co(III) complex formation was observed.

For some crystal lattices the ordering might be absolute where the metal complex shows only one possible orientation, whereas for others it might be a combination of two orientations such as that for **Cr-2** (see **Figure 3.34**), where the crystal lattice shows two orientations of the complex which are point symmetrical mirror images of each other.[59] Given the axial symmetry of the g-

value, this ordering might further complicate the spectra observed recorded at different angles. The EPR spectra of a single crystal of **Cr-2** recorded at multiple orientations with respect to the external magnetic field are shown in **Figure 3.35**. Crystal was aligned with the *x*-axis and rotation occurred around the same axis whilst the *z*-axis was aligned with the direction of the magnetic field. As can be seen, the results clearly indicate that there are different signal intensities observed at fixed positions upon sample rotation (e.g. at 180 mT) which correlate with the roadmap plot in the 0-200 mT range (**Figure 3.36**) and suggest some level of ordering within the system.
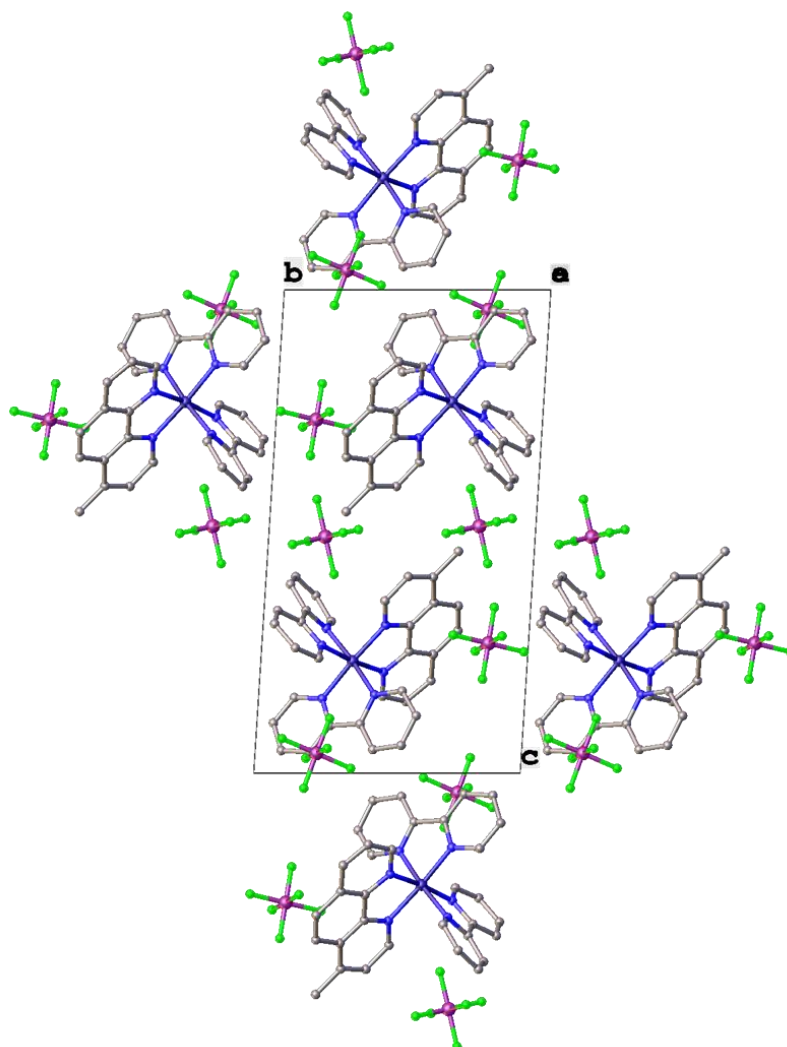
Figure 3.34 Crystal lattice of **Cr-2** representing the two solved orientations of the complex.
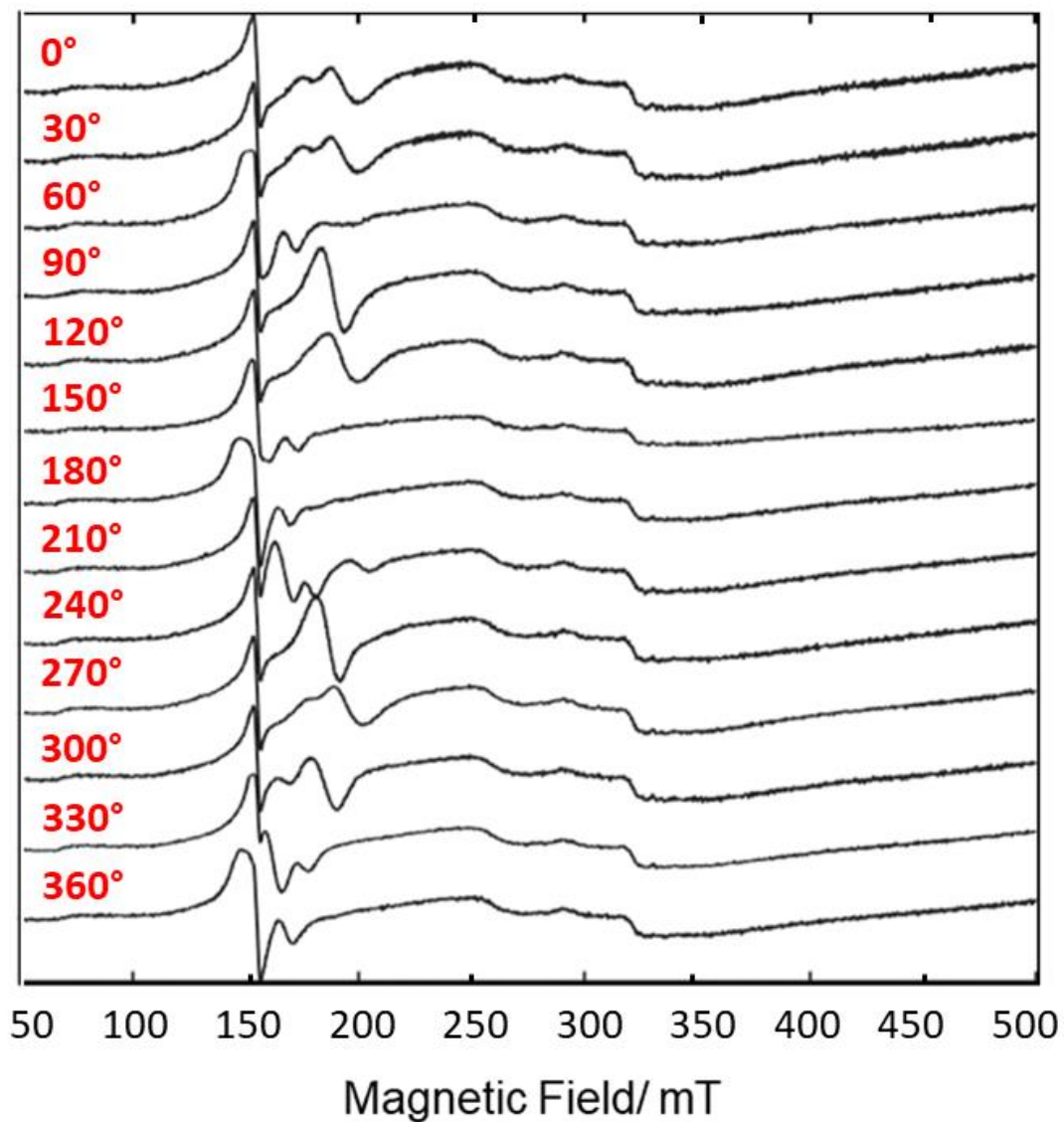
Figure 3.35 X-band EPR spectra (T=298 K) of a single crystal of complex **Cr-2** measured at 12 orientations.
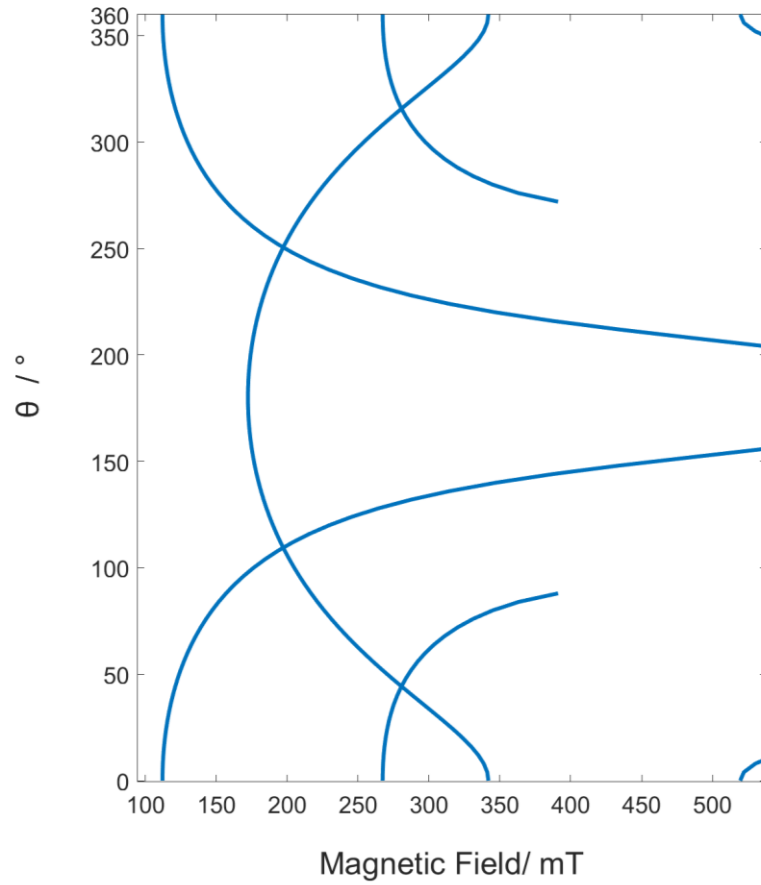
Figure 3.36 The crystal orientation roadmap plot simulated for **Cr-2**, representing the expected signal positions based on the angle of the sample with respect to the external magnetic field.

3.4 Conclusion

This chapter investigated the electronic characteristics of a series of synthesised polypyridyl Cr(III) complexes analysed by UV-Vis, emission and EPR spectroscopies with the ambition of using this analysis as an informative tool for future ligand design of long-lived NIR emitters. The synthesis, although successful, proved challenging in some instances such as that for **Cr-1** which revealed several by-products and therefore complicated the purification process resulting in a very low yield of 0.065%. Furthermore, as previously reported in the literature for polypyridyl Cr(III) complexes of $[Cr(bpy)_3]^{3+}$ type, sensitivity to OH^- ions was identified for **Cr-2** and **Cr-3**.

All of the complexes showed far red to NIR emission in the range of 730-760 nm with lifetimes in the millisecond range obtained for **Cr-2**, **Cr-3,** and **Cr-6** as previously reported for similar polypyridyl Cr(III) complexes.[60] Detailed analysis of the spin Hamiltonian ZFS parameters revealed a correlation between inter-electronic repulsion and the ligand field strength. In particular, we report that the two complexes with the strongest field ligands coordinated to the Cr(III) centre (**Cr-6** and **Cr-7**, comprising two unsubstituted phen ligands and one substituted phen ligand) resulted in the lowest *D*-values reported across the series. Nevertheless, as suggested future work for this chapter, measurements at multiple orientations within the cavity ought to be performed for complexes **Cr-1** and **Cr-3** to **Cr-7** to support the simulated local ordering. Despite the clear correlation between the ligand field and resulting spin Hamiltonian parameters, no trend was observed in the ZFS parameters that could explain the versatile tunability of the NIR luminescence of the Cr(III) complexes. Nevertheless, the X-ray crystallography results for **Cr-2** and EPR data obtained for the whole series suggest that for near-perfect octahedral Cr(III) complexes with emission in the NIR region (> 700 nm), low *D*-values (<0.4) are desired. This might be achieved with tris-chelate complexes if six membered chelates are formed upon coordination of the ligands. Alternatively, tris-dentate ligands might also be employed and are discussed in **Chapter 4**.

3.5 Experimental

All reactions were performed with the use of vacuum line and Schlenk techniques. Reagents were commercial grade and were used without further purification. ^{1}H and ^{13}C{H} NMR spectra were recorded on a Bruker Avance dpx 400, or Bruker Avance dpx 500 MHz spectrometer and were recorded in CDCl$_3$. ^{1}H and ^{13}C {^{1}H} NMR chemical shifts (δ) were determined relative to internal tetramethylsilane, Si(CH$_3$)$_4$ and are given in ppm. Low- and high-resolution mass spectra were obtained by the staff at Cardiff University. All photophysical data was obtained on a JobinYvon-Horiba Fluorolog-3 spectrometer fitted with a Hamamatsu R5509-73 detector. FTIR spectra were recorded using ATR equipped Shimadzu IRAffinity-1 spectrophotometer. UV-Vis data were recorded as solutions on a Perkin Elmer Lamda20 spectrophotometer. LC-MS analysis was conducted using a Waters Synapt G2 SI using a water/MeCN solvent gradient.

3.5.1 EPR Spectroscopy

Samples for EPR measurements were prepared in solvents, as listed in the discussion Section, under atmospheric conditions. The X-band EPR measurements were performed on a Bruker EMX spectrometer utilising an ER4119HS resonator, 100 kHz field modulation and 0.4 mT modulation depth at 140 K. EPR simulations were performed using the *Easyspin* toolbox within *Matlab*. [61]

3.5.2 DFT studies

Non-relativistic calculations of the fully relaxed geometries in the ground state and optimized excited state were performed on the Gaussian 09 program, and calculations of the spin Hamiltonian parameters were performed using ORCA (version 4.0.0.1).[62,63] Geometry optimisation calculations were computed using B3LYP functional and 6-311G(d, p) basis set for all atoms except Cr which was computed using LANL2DZ.[64] The chosen solvent was MeCN for all complexes.[65] TD-DFT calculations were computed using B3LYP functional and def2-SVP basis set with diffuse function and (d,p) accounting for polarisation

function.[66,67] ORCA calculations were computed using BLYP functional and QZVP basis sets produce results of ZFS parameters estimation using quasi-restricted orbitals (qro) method for calculating the spin-orbit coupling contributions.[74,68,69]

3.5.1 Synthesis

Preparation of [Cr(bpy)$_2$]Cl$_2$

To a suspension of CrCl$_3$ (1.46 g, 9.19 mmol) in EtOH (50 mL), 2,2`-bipyridine (8.00 g, 18.38 mmol) was added and the reaction was brought to reflux for 10 mins. This was followed by an addition of trace amounts of Zn powder. Shortly after that, the reaction mixture turned dark, almost black, colour and was allowed to reflux for 2 hr. Upon cooling, green precipitate was observed, filtered, and dried on air. The precipitate was redissolved in water, refluxed and hot filtered. The filtrate was cooled to 0°C and after 30 mins, brown/cream crystals were observed in a dark red solution. The crystals were filtered, washed with cold water and dried on air. 5.57 g, 50%). FTIR (solid, V_{max})/ cm^{-1}: 554 (br), 645 (w), 650 (w), 662 (w), 666 (w), 729(s), 754 (w), 764 (s), 771 (s), 809 (w), 905 (m), 1019 (s), 1033 (s), 1047 (w), 1065 (w), 1077 (w), 1107 (w), 1156 (m), 1166 (w), 1227 (w), 1246 (w), 1287 (w), 1314 (m), 1322 (m), 1444 (m), 1472 (m), 1499 (m), 1603 (m), 1608 (m), 3050 (w), 3344 (w).

Preparation of [Cr(bpy)$_2$(SO$_3$CF$_3$)$_2$]SO$_3$CF$_3$

[Cr(bpy)]Cl$_2$ (5.57 g, 12.80 mmol) was dissolved in excess trifluoromethanesulfonic acid (10 mL), whilst on ice, giving a dark red coloured solution and stirred at room temperature for 24 hrs. The reaction was then cooled down to 0°C and Et$_2$O was added dropwise until orange precipitate appeared, which was subsequently filtered and washed with 250 ml of Et$_2$O and dried on air. Then subsequently redissolved in MeCN and run through an alumina plug leaving a red coloured band within alumina, an orange solution eluted and was concentrated. The product was used in subsequent reactions without further purification (8.12 g, 50%).

Preparation of complexes Cr-1*, Cr-2 and Cr-3

Ligand of choice was dissolved in DCM and [Cr(bpy)$_2$(OTf)$_2$]OTf was added. The reaction was stirred for 2-4 hrs at reflux, until the point a colour change was reached and/or yellow precipitate appeared or orange precipitate ([Cr(bpy)$_2$(OTf)$_2$]OTf) has dissolved completely. In case of a resulting precipitate, it was filtered, washed with Et$_2$O, and recrystallised from MeCN using Et$_2$O. Followed by counterion exchange with NH$_4$PF$_{6(aq)}$. In case of no precipitate, the solution was concentrated, and the remaining oily substance was dried on air until crystal like material formed. 2 ml of water was added and sonicated for 50 min. Undissolved material was filtered off and an aqueous solution of NH$_4$PF$_6$ was added to the resulting yellow filtrate causing yellow precipitate to occur. Precipitation with NH$_4$PF$_{6(aq)}$ was carried out in a fractional manner to achieve the product as pure as possible. This was then filtered, washed with water and Et$_2$O and dried on air.

* **Cr-1** was prepared in a pressure tube.

The complex was dissolved in minimal amount of MeCN/H$_2$O/KNO$_{3\,(sat)}$ (14:2:1) and loaded onto Al$_2$O$_3$ column, followed by three portions of acetone (3x10mL). Upon elution of the last impurity (monitored by TLC), a portion of MeCN/H$_2$O/KNO$_{3\,(sat)}$ (14:2:1) caused a bright yellow band to elute leaving a pink band at the top of Al$_2$O$_3$ column. The yellow fraction was combined, and DCM (200 mL) was added followed by addition of H$_2$O with slight excess of NH$_4$PF$_6$. Solvent extraction resulted in combined DCM layers dried over Na$_2$CO$_3$ and concentrated to obtain pure product.

Cr-1

Due to extensive ligand scrambling, a pressure tube was used for a 10 min reaction (reflux). Starting materials: bathophenanthroline (0.034 g, 0.1 mmol), [Cr(bpy)$_2$(OTf)$_2$]OTf (0.070 g, 0.1 mmol). Bright yellow powder was obtained, 0.005 g, 0.065 %. FTIR (solid, V$_{max}$)/ cm^{-1}: 652 (w), 667 (w), 702 (w), 730 (w), 737 (w), 767(w), 842 (s, PF$_6^-$), 1017 (w), 1035 (w), 1230 (w), 1319 (w), 1447 (w), 1521 (w), 1604 (w), 3095 (w), 3116 (w). UV-Vis (MeCN) λmax (ε, M^{-1}cm^{-1}): 230 (30000), 290 (9000), 375 (4000) sh nm. HRMS (ESI+, MeCN) [M+] m/z found 232.0785, calculated m/z 232.0693 for for C$_{44}$H$_{32}$CrN$_6^{3+}$.

Cr-2

Starting materials: 4-Me-1,10-phenanthroline (0.027 g, 0.14 mmol), [Cr(bpy)$_2$(OTf)$_2$]OTf (0.095 g, 0.14 mmol). Bright yellow powder was obtained, (0.057 g, 73 %). FTIR (solid, V$_{max}$)/ cm^{-1}: 652 (w), 721 (w), 729 (w), 760(m), 828 (s, PF$_6^-$), 1034 (w), 1443 (w), 1604 (w), 3579 (w), 3649 (w). UV-Vis (MeCN) λmax (ε, M^{-1}cm^{-1}): 235 (1600), 280 (7800), 325 (1800) sh nm. Anal. Cald for C$_{33}$H$_{26}$CrF$_{18}$N$_6$P$_3$: C, 39.90; H, 2.64; N, 8.46. Found: C, 39.91; H, 2.47; N, 8.30. HRMS (ESI+, MeCN) [M+] m/z found 186.0625, calculated m/z 186.0536 for C$_{33}$H$_{26}$CrN$_6{}^{3+}$.

Cr-3

Starting materials: 5-Me-1,10-phenanthroline (0.027 g, 0.14 mmol), [Cr(bpy)$_2$(OTf)$_2$]OTf (0.095 g, 0.14 mmol). Bright yellow powder was obtained, (0.032 g, 41 %). FTIR (solid, V$_{max}$)/ cm^{-1}: 668 (w), 723 (w), 738 (w), 762 (m), 831 (s, PF$_6^-$), 1036 (w), 1427 (w), 1448 (w), 1606 (w), 3581 (w), 3653 (w). UV-Vis (MeCN) λmax (ε, M^{-1}cm^{-1}): 235 (24800), 275 (12000), 325 (2500) sh nm. Anal. Calcd for C$_{33}$H$_{26}$CrF$_{18}$N$_6$P$_3$: C, 39.90; H, 2.64; N, 8.46. Found: C, 40.11; H, 2.36; N, 8.27. HRMS (ESI+, MeCN) [M+] m/z found 186.0542, calculated m/z 186.0536 for C$_{33}$H$_{26}$CrN$_6{}^{3+}$.

Preparation of complexes Cr-4 to Cr-7

Ligand was dissolved in MeCN and [Cr(bpy)$_2$(OTf)$_2$]OTf was added. The reaction was stirred at reflux 24 hrs. Upon cooling, MeCN was concentrated, and the crude was redissolved in MeOH, the sonicated for 10-30 min. Undissolved material was filtered off and NH$_4$PF$_6$ was added to the filtrate causing a formation of a precipitate, which was subsequently filtered and dried on air and subsequently purified using column chromatography using Al$_2$O$_3$. The complex was dissolved in minimal amount of MeCN/H$_2$O/KNO$_3$ (sat) (14:2:1) and loaded onto Al$_2$O$_3$ column, followed by three portions of acetone. Upon elution of the last impurity (monitored by TLC), a portion of MeCN caused a bright yellow band to elute leaving a pink band at the top of Al$_2$O$_3$ column. The yellow fraction was concentrated, and DCM (100 mL) was added followed by addition of H$_2$O with slight excess of NH$_4$PF$_6$. Solvent extraction resulted in

combined DCM layers dried over Na_2CO_3 and concentrated to obtain pure product.

Cr-4

5-amino-1,10-phenanthroline (0.02 g, 0.11 mmol), [Cr(bpy)$_2$(OTf)$_2$]OTf (0.07 g, 0.11 mmol). Bright yellow powder was obtained (0.014 g, 23 %). FTIR (solid, V$_{max}$)/ cm^{-1}: 670 (w), 716(w), 736 (w), 795 (m), 835 (s, PF$_6^-$), 1034 (w), 1064 (w), 1091 (w), 1260 (w), 1418 (w), 1510 (w), 1645 (w), 2838 (w), 2921 (w), 2957 (w). UV-Vis (MeCN) λmax (ε, M^{-1}cm^{-1}): 235 (33000), 255 (18000), 260 (15300), 340 (6260) nm. LRMS (ESI+, MeCN) [M+] found m/z 186.39 m/z, calculated m/z 186.3853 for $C_{32}H_{25}CrN_7^{3+}$.

Cr-5

2,3-bispyridyl-pyrazine (0.047 g, 0.2 mmol), [Cr(bpy)$_2$(OTf)$_2$]OTf (0.088 g, 0.13 mmol). Orange powder was obtained which contained a mix of the product and the hydrolyzed by-product (0.040 g, 34 %). FTIR (solid, V$_{max}$)/ cm^{-1}: 764 (m), 827 (s, PF$_6^-$), 1021 (w), 1153 (w), 1420 (m), 1627(w),2923 (w), 2972 (w), 3314 (w), 3636(w). UV-Vis (MeCN) λmax (ε, M^{-1}cm^{-1}): 230 (15100), 325 (5000) nm. LC-MS (ESI+, MeCN) [M+] found m/z 199.3895, calculated m/z 199.3890 for $C_{34}H_{26}CrN_8^{3+}$.

Cr-6

Me-1,10-phenanthroline (0.019 g, 0.1 mmol), Cr(bpy)$_2$(OTf)$_2$]OTf (0.07 g, 0.1 mmol). Yellow powder was obtained, (0.010 g, 17 %). FTIR (solid, V$_{max}$)/ cm^{-1}: 651 (w), 669 (w), 723 (w), 739 (w), 764 (m), 831 (s, PF$_6^-$), 1036 (w), 1428 (w), 1448 (w), 1606 (w), 3099 (w). UV-Vis (MeCN) λmax (ε, M^{-1}cm^{-1}): 230 (15100), 255 (10000), 315 (1500) sh nm. LC-MS (ESI+, MeCN) [M+] found m/z 202.05, calculated m/z 202.0536 for $C_{37}H_{26}CrN_6^{3+}$.

Cr-7

5-Me-5-amino-1,10-phenanthroline (0.090 g, 0.13 mmol), [Cr(bpy)$_2$(OTf)$_2$]OTf (0.024 g, 0.12 mmol). Yellow powder was obtained (0.020 g, 27 %). FTIR (solid, V$_{max}$)/ cm^{-1}: 656 (w), 668 (w), 721 (w), 739 (w), 840 (s, PF$_6^-$), 1003 (w), 1103 (w), 1150 (w), 1156 (w), 1424 (w), 1520 (w), 3092 (w). UV-Vis (MeCN) λmax (ε,

M^{-1}cm^{-1}): 230 (10000), 258 (9000) nm. LC-MS (ESI+, MeCN) [M+] found m/z 202.0542, calculated m/z 202.0536 for C$_{37}$H$_{26}$CrN$_6^{3+}$.

3.6 References

[1] C. Wegeberg, O. S. Wenger, *J. Am. Chem. Soc. Au.* 2021, 1, 11, 1860–1876.

[2] S. S. N. Lalthambika, R. Golnak, B. Winter, K. Atak, *Inorg. Chem.* 2019, 58, 8, 4731–4740.

[3] K. M. Omberg, J. R. Schoonover, J. A. Treadway, R. M. Leasure, R. Brian Dyer, and T. J. Meyer, *J. Am. Chem. Soc.* 1997, 119, 30, 7013–7018.

[4] L. M. Lawson Daku and A. Hauser *J. Phys. Chem. Lett.* 2010, 1, 12, 1830–1835.

[5] R. J. Deeth, *Coord. Chem. Rev.* 2001,212,1,11-34.

[6] N. Serpone, M. A. Jamieson, M. S. Henry, M. Z. Hoffman, F. Bolletta and M. Maestri, *J. Am. Chem. Soc.,* 1979, 101, 2907–2916

[7] A. M. McDaniel, H.-W. Tseng, N. H. Damrauer and M. P. Shores, *Inorg. Chem.,* 2010, 49, 7981–7991.

[8] J. C. Barbour, A. J. I. Kim, E. deVries, S. E. Shaner and B. M. Lovaasen, *Inorg. Chem.,* 2017, 56, 8212–8222.

[9] J.-R. Jimenez, B. Doistau, C. M. Cruz, C. Besnard, J. M. Cuerva, A. G. Campan͂a and C. Piguet, *J. Am. Chem. Soc.,* 2019, 141, 13244–13252.

[10] J. C. Barbour, A. J. I. Kim, E. deVries, S. E. Shaner and B. M. Lovaasen, *Inorg. Chem.,* 2017, 56, 8212–8222.

[11] S. Otto, C. Fo̎rster, C. Wang, U. Resch-Genger and K. Heinze, *Chem. Eur. J.,* 2018, 24, 12555–12563.

[12] J. C. Barbour, A. J. I. Kim, E. deVries, S. E. Shaner and B. M. Lovaasen, *Inorg. Chem.,* 2017, 56, 8212–8222.

[13] Forster, L. S.; Rund, J. V.; Fucaloro, A. F. *J. Phys. Chem.* 1984, 88, 5012

[14] Flint, C. D.; Greenough, P. *J. Chem. Soc., Faraday Trans.* 2 1972, 68, 897.

[15] K. D. Barker, K. A. Barnett, S. M. Connell, J. W. Glaeser, A. J. Wallace, J. Wildsmith, B. J. Herbert, J. F. Wheeler and N. A. P. Kane-Maguire, *Inorg. Chim. Acta, 2001*, 316, 41–49.

[16] M. Isaacs, A. G. Sykes and S. Ronco, *Inorg. Chim. Acta*, 2006, 359, 3847–3854.

[17] S. Otto, C. Fo̎rster, C. Wang, U. Resch-Genger and K. Heinze, *Chem. Eur. J.,* 2018, 24, 12555–12563.

[18] J.-R. Jimenez, B. Doistau, C. Besnard and C. Piguet, *Chem. Comm.,* 2018, 54, 13228–13231.

[19] J. Schonle, PhD thesis, 2014, University of Bern.

[20] U. Casellato, R. Graziani, R. P. Bonomo, A. J. Di Bilio, *Dalton. Trans.*, 1991, 23-31.

[21] W. R. Kitzmann and K. Heinze , *Angew. Chem., Int. Ed.*, 2022, 17 , 955.

[22] A. Manoogian, A. J. Leclerc, *Chem. Phys.* 1976, 64, 4504-4508.

[23] L. S. Singer, *J. Chem. Phys.*, 1955, 23 , 379-388.

[24] M. Dalal, A Textbook of Physical Chemistry, *Dalal Institute*, ISBN: 8193872002, 9788193872000 (Paperback).

[25] S. Lakshmi, T. Endo, G. Siva, Advanced Aspects of Spectroscopy*, InTech,* 2012*.*

[26] K. Sugisaki, K. Toyota, K. Sato, D. Shiomi, T. Takui*, Phys. Chem. Chem. Phys.***,** 2017,19**,** 30128-30138.

[27] D. G. Liakos, D. Ganyushin, and F. Neese, *Inorg. Chem.,* 2009, 48*,* 22, 10572-10580.

[28] R.E.Marsh, F.H.Herbstein, *Acta. Crystallogr. B. Struct. Sci.*, 1983, 39, 280.

[29] B.Morosin, *Acta Crystallogr.*, 1965, 19, 131.

[30] S. Bennie, PhD Thesis, 2013, Manchester University.

[31] M. Maestri, F. Bolletta, N. Serpone, L. Moggi, and V. Balzani, *Inorg. Chem.,* 1976, 15, 9.

[32] M. Maestri, F. Bolletta, L. Moggila V. Balzani, M. S. Henry,,b and . Z. Hoffman, *J. Am. Chem. Soc.,*1978, 100, 9.

[33] B. Doistau, G. Collet, E. A. Bolomey, V. Sadat-Noorbakhsh, C. Besnard, and C. Piguet, *Inorg. Chem.,* 2018, 57, 22, 14362-14373.

[34] B. Cherinka, B. Andrews, J. Sanchez-Gallego, J. Brownstein, M. Argudo-Fernández, M. Blanton, K. Bundy, A. Jones, K. Masters, D. Law, K. Rowlands, A.M. Weijmans, K. Westfall, R. Yan, 2019, Marvin: A Tool Kit for Streamlined Access and Visualisation of the SDSS-IV MaNGA Data Set. *\aj, 158(2), 74.*

[35] S. J. Milder, J. S. Gold and D. S. Kliger, *Inorg. Chem.,* 1990, 29, 2506-2511.

[36] J. Jiménez, B. Doistau, C. M. Cruz, C. Besnard, J. M. Cuerva, A. G. Campaña, and C. Piguet, *J. Am. Chem. Soc.,* 2019, 141, 33, 13244-13252.

[32] W. R. Kitzmann, C. Ramanan, R. Naumann, K. Heinze., *Dalton Trans.*, 2022,51, 6519-6525.

[33] S. Otto, N. Scholz, T. Behnke, U. Resch-Genger, K. Heinze, *Chem. A Eu. J.*, 23, 50,12131-12135.

[39] L. S. Forster, C*hem. Rev.* 1990, 90, 2, 331–353.

[40] *Chem. Soc. Rev.*, 2013,42, 6128-6185.

[41] L. A. Büldt, O. S. Wenger OS. *Chem Sci.* 2017 Nov 1, 11, 7359-7367.

[42] W. Yang, X. Chen, H Su, W. Fang, Y. Zhang, *Chem. Comm.,* 2015, 51, 47, 9616-9619.

[43] H. Huang, Y. Bu, *J. Phys. Chem.* 2019, 123, 46, 28327–28335.

[44] *Chem. Sci.*, 2021, 12, 12391-12399.

[45] C. Lochenie, K. G. Wagner, M. Karg, B. Weber, *J. Mater. Chem. C*, 2015,3, 7925-7935.

[46] N. Sawicka, C. J. Craze, P. N. Horton, S. J. Coles, E. Richards, S. J. A. Pope, *Chem. Comm.*, 2022, 58, 5733-5736.

[47] J. Lee, Y. Kim, Y. Son, H. Kim, Y. Nam Choi, D. D'Alessandro, P. Chandra Rao, . Dr. Y. Yoon, *Chem.*, 2021, 27, 60, 14899–14910.

[48] M.T. Ramírez-Silva, M. Gómez-Hernández, M. de Lourdes Pacheco-Hernández, A. Rojas-Hernández, L. Galicia, *Spectr. Act. Part A Mol. Biomol. Spectr., 2004,* 60, 4, 781-789.

[49] R. Reisfeld, C.K. Jorgénsen, *Struct. Bonding, 1988,* 69, 63.

[50] J. R. Lakowicz, Principles of Fluorescence Spectroscopy, Springer, Singapore, 3rd edn., 2006.

[51] Arthur W. Adamson*, J. Phys. Chem.* 1967, 71, 4, 798–808.

[52] F. Gotardo, L. H.Z. Cocca, T. V. Acunha, A. Longoni, J. Toldo, P. F.B. Gonçalves, B. A. Iglesias, L. De Boni, *Chem. Phys. Lett.,*2017, 674, 48-57.

[53] Z. Wang, A. Toffoletti, Y. Hou, J. Zhao, A. Barbon, B. Dick, *Chem. Sci.,* 2021, 12, 2829.

[54] S. Treiling, C. Wang, C. Förster, F. Reichenauer, J. Kalmbach, P. Boden, J. P. Harris, L. M. Carrella, E. Rentschler, U. Resch-Genger, C. Reber, M. Seitz, M. Gerhards, K. Heinze *Angew. Chem. Int. Ed. Engl.* 2019, 58, 50, 18075-18085.

[55] B.V. Padlyak, M. Grinberg, T. Łukasiewicz, J. Kisielewski, M. Świrkowicz, J. *All. and Comp.*, 361, 1–2, 2003, 6-12.

[56] G. M. Cole Jr. and B. B. Garrett , *Inorg. Chem.*, 1970, 9 , 1898-1902.

[57] Mulliken, R.S.,J. Chem. Phys., 1934, 2, 782.

[58] P. H. Rieger, Electron Spin Resonance: analysis and interpretation, RSC, Cambridge, 2007.

[59] Huebener, R.P., 2019. Well Ordered Lattice Structures in Crystals. In: Conductors, Semiconductors, Superconductors. Undergraduate Lecture Notes in Physics. Springer, Cham.

[60] T. H. Bürgin, F. Glaser, O. S. Wenger, 2022, *J. Am. Chem. Soc.*, 10, 144, 31, 14181–14194.

[61] S. Stoll, A. Schweiger, *J. Magn. Reson.* 2006, 178, 1, 42-55.

[62] Gaussian 16, Revision C.01, Frisch, M. J.; Trucks, G. W.; Schlegel, H. B.; Scuseria, G. E.; Robb, M. A.; Cheeseman, J. R.; Scalmani, G.; Barone, V.; Petersson, G. A.; Nakatsuji, H.; Li, X.; Caricato, M.; Marenich, A. V.; Bloino, J.; Janesko, B. G.; Gomperts, R.; Mennucci, B.; Hratchian, H. P.; Ortiz, J. V.; Izmaylov, A. F.; Sonnenberg, J. L.; Williams-Young, D.; Ding, F.; Lipparini, F.; Egidi, F.; Goings, J.; Peng, B.; Petrone, A.; Henderson, T.; Ranasinghe, D.; Zakrzewski, V. G.; Gao, J.; Rega, N.; Zheng, G.; Liang, W.; Hada, M.; Ehara, M.; Toyota, K.; Fukuda, R.; Hasegawa, J.; Ishida, M.; Nakajima, T.; Honda, Y.; Kitao, O.; Nakai, H.; Vreven, T.; Throssell, K.; Montgomery, J. A., Jr.; Peralta, J. E.; Ogliaro, F.; Bearpark, M. J.; Heyd, J. J.; Brothers, E. N.; Kudin, K. N.; Staroverov, V. N.; Keith, T. A.; Kobayashi, R.; Normand, J.; Raghavachari, K.; Rendell, A. P.; Burant, J. C.; Iyengar, S. S.; Tomasi, J.; Cossi, M.; Millam, J. M.; Klene, M.; Adamo, C.; Cammi, R.; Ochterski, J. W.; Martin, R. L.; Morokuma, K.; Farkas, O.; Foresman, J. B.; Fox, D. J. Gaussian, Inc., Wallingford CT, 2016.

[63] F. Neese, Software Update: The ORCA Program System—Version 5.0. Wiley Interdiscip. *Rev. Comput. Mol. Sci.* 2022, 12, e1606.

[64] P. J. Hay and W. R. Wadt, *J. Chem. Phys.,* 1985, 82, 299-310.

[65] J. Tomasi, B. Mennucci, and R. Cammi, *Chem. Rev.*, 2005, 105, 2999-3093.

[66] A.D. Becke, , *Phys. Rev.,* 1988, 38, 3098.

[67] F. Weigend, R. Ahlrichs, *Phys. Chem. Chem. Phys.,* 2005, 7, 3297.

[68] F. Weigend and R. Ahlrichs, *Phys. Chem. Chem. Phys.*, 2005, 7, 3297-305.

[69] F. Neese, *J. Am. Chem. Soc.*, 2006, 128, 10213-10222.

Chapter 4 -NIR Emitting 1,3-Bis(pyridin-2-ylimino)isoindolin-2-ide Chromium(III) Complexes and Their Electronic Behaviour

4.1 Introduction

Chapter 3 described a series of polypyridyl Cr(III) complexes which showed doublet excited state emission in the range of 726-740 nm with lifetimes in the microsecond range. Unfortunately, all reported quantum yields were low (0.09-0.01%) which was linked to trigonal twists in the five membered chelates formed upon coordination with bidentate ligands of bpy/phen type – distorting the octahedral geometry away from octahedral with trans angles in the range of 172-173°. This chapter therefore discusses a series of Cr(III) complexes with ligands which form six membered chelates, and investigates whether this subtle change and the resulting geometry can improve the photophysical properties of Cr(III) complexes.

4.1.1 Six-membered chelates

The literature provides several examples of Cr(III) six-membered chelates upon coordination, some of which will now be discussed. Most of the complexes discussed in this section show improved photophysical properties such as longer lifetimes and higher quantum yields in comparison with [Cr(bpy/phen)$_3$]$^{3+}$ type complexes; however as pointed out later, some challenges remain.

In 2017, the Heinze group presented deuteration of the ligand/solvent as a strategy to increase the quantum yields for Cr(III) complexes.[1-4] For example, a quantum yield of 11% was reported for [Cr(ddpd)$_2$]$^{3+}$, with a a lifetime of 898 μs in degassed H$_2$O that decreased significantly to 177 μs in aerated H$_2$O. The authors reported sensitivity of the lifetime parameters upon changes in the solvent system. Upon deuteration of the solvent, the lifetime increased to 1164 μs in degassed D$_2$O, however it decreased to 150 μs in aerated D$_2$O (which is notably lower than that measured in aerated H$_2$O). Full deuteration of the pyridine moieties and Me groups (**Figure 4.1**) resulted in record high quantum yield of 30% and a lifetime of 1200 μs in degassed H$_2$O.[1]

[D14]-ddpd
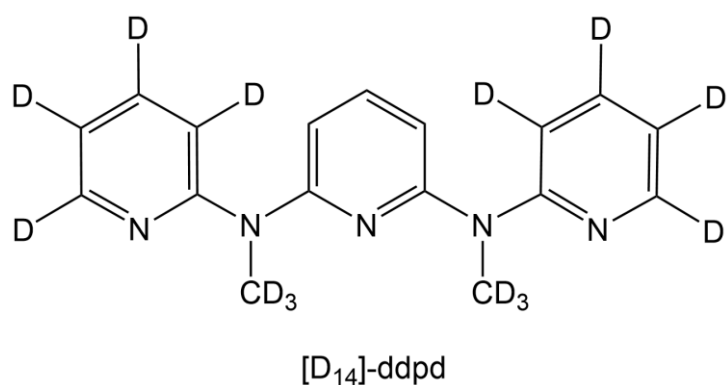
Figure 4.1 Deuterated ligand reported by Heinze *et al.* [1]

In 2018 Heinze then reported a NIR emissive $[Cr(H_2tpda)_2]^{3+}$ (**Figure 4.2**) which demonstrated a quantum yield of 6.3% in H_2O. When D_2O was used, the same complex exhibited a quantum yield of 15% showing the significant influence of solvent quenching processes. [2] In 2021, the same group showed that $[Cr(bpmp)_2]^{3+}$ can exhibit a quantum yield of up to 20% in acidified D_2O. Partial deuteration of bpmp increased the quantum yield further to 25 % under the same conditions.[3] All complexes were synthesised utilising $CrCl_2$ as the source of chromium.[2-4]
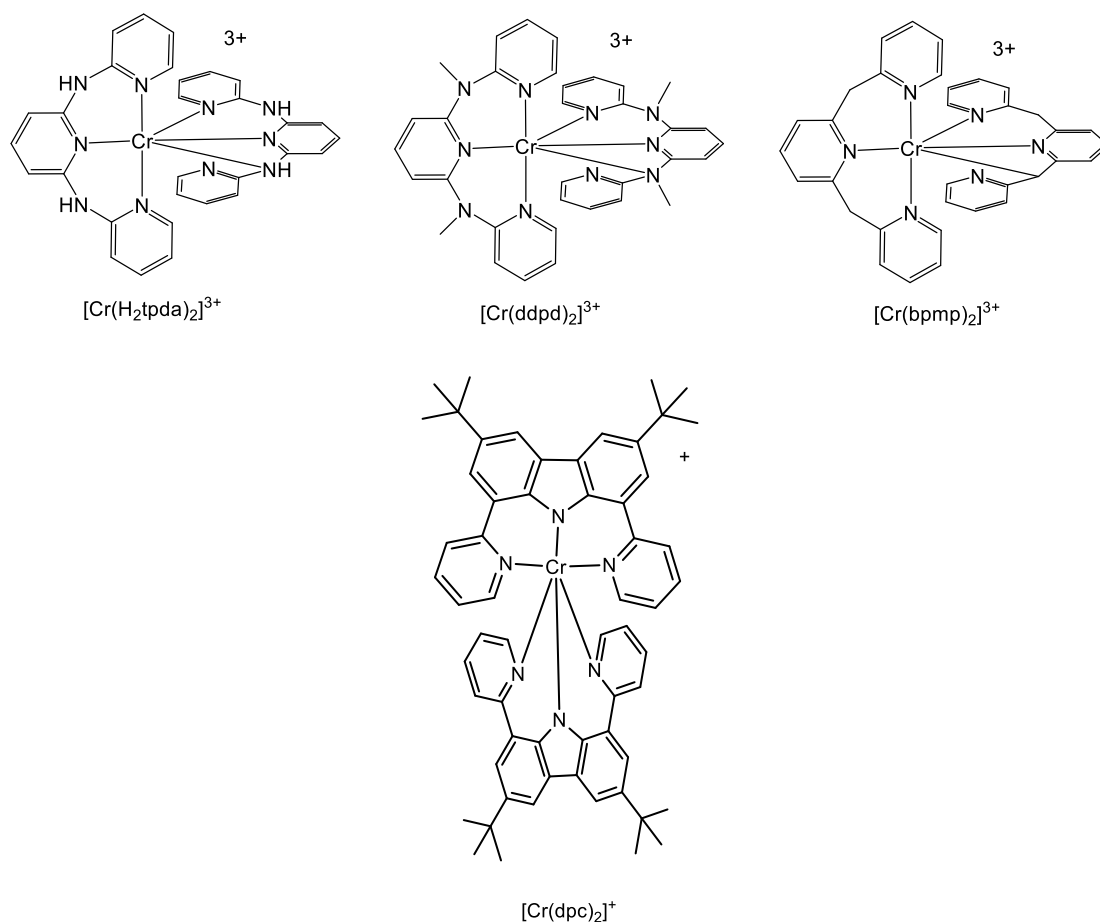
Figure 4.2 Complexes reported by Heinze (top) in and Wenger (bottom) 2021.[2-5]

Another adept suggestion from the Heinze group was to place bulky groups in close proximity the Cr(III) centre. In 2022, the group showed that placing Me/Ar groups close to the Cr(III) ion can protect the doublet excited state from oxygen quenching. Complexes with bulky groups in position 5 of the pyridine moiety within a ddpd ligand showed quantum yields of up to 5.1% and 518 μs in air saturated MeCN. The unsubstituted scaffold of ddpd ligand is shown in **Figure 4.2**. Heinze also attempted utilising Me/Ar group in position 6 of the pyridyl ring of ddpd, however the group reported all attempts as unsuccessful.[4]

In 2021, Wenger reported the first Cr(III) system to emit in the NIR-II region with the emission peak at 1067 nm at 77 K.[5] Significantly, the excitation wavelength

shifted from the 300-350 nm range for $[Cr(bpy)_3]^{3+}$ analogues to 450 nm for the complex reported by Wenger. This significant red-shift was explained to have occurred due to the nephelauxetic effect of the dpc ligand. The nephelauxetic effect was introduced via the negatively charged nitrogen atom forming a Cr-$N_{carbazole}$ bond of increased covalency compared to the Cr-N_{py} bond present in the $[Cr(bpy)_3]^{3+}$ analogues. To support this theory, Wenger investigated the Racah (B) parameter of the $[Cr(dpc)_2]^{3+}$ complex and determined it to be in the range of 470-570 cm^{-1} , which is much lower than that of $[Cr(phen)_3]^{3+}$ (780 cm^{-1}).[11] This was followed up with determining a nephelauxetic effect parameter reporting a range of 0.5-0.6 and therefore proving an increased covalency if the Cr-$N_{carbazole}$ bond. [5] The discovery raised interest towards *in vivo* applications of Cr(III) luminescent complexes. The NIR-II range provides deep tissue penetration and high signal-to-noise ratio, both very beneficial for bio-imaging agents as explicitly discussed in **Section 1.3**. Considering the abundance of chromium in the Earth`s crust, this provides a very economical alternative to FTIR(III), Re(I) or Ru(II) bio-imaging agents given that the NIR-II emission can be observed at room temperature with good quantum yields such as those reported by Heinze. [5]

4.1.2 Bis(pyridyl) isoindoline ligands

Bis-pyridyl isoindoline (abbreviated as BPI) ligands were first reported in the 1950`s and were later recognized for their antiproliferative activity.[6] Although their potential as multidentate ligands forming six-membered chelates was identified instantly, the first BPI coordinated metal complexes were reported in the late 1970`s.[7,9]

There are two common synthetic methods for the preparation of BPI, namely the Linstead method and the Siegl method.[8,9] As illustrated in **Figure 4.3**, the first method is a two-step synthetic process where phthalonitrile is reacted with ammonia in MeOH resulting in a 1,3-diiminoisoindoline intermediate which is then reacted with two equivalents of an amine in EtOH over 24 h at reflux. Siegl method involves a one pot reaction where the phthalonitrile is reacted directly with two equivalents of an amine in the presence of CaCl$_2$ stirred over 48 h in n-BuOH.
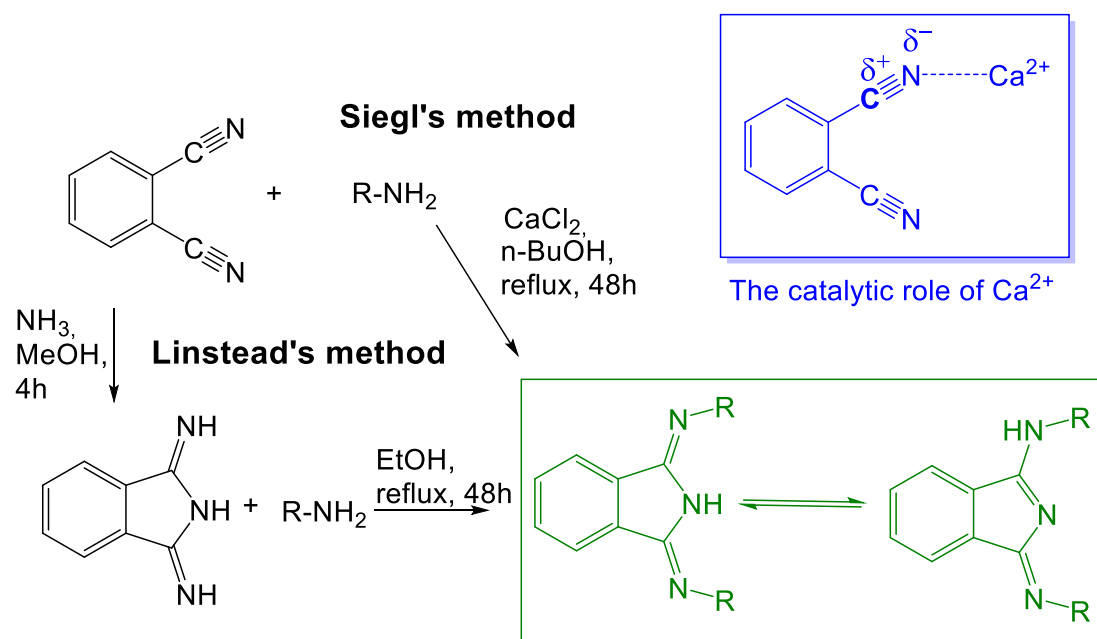
Figure 4.3 Linstead`s and Siegl`s methods for obtaining bis(pyridyl) isoindolines.

The Siegl`s method is reported to return higher yields than the Linstead`s method which is due to the catalytic role of the Ca^{2+} ion (marked in blue in

Figure 4.3). The Lewis acidity of the Ca^{2+} centre means that its low electron density centre can accept electron density from a neighbouring atom therefore causing a polarisation of the carbon-nitrogen bond and subsequent activation of the partially positive carbon (shown in bold) to a nucleophilic attack by an incoming amine.[9,10]

Characterisation of the BPI can be readily achieved using UV-Vis and FT-FTIR spectroscopy. All BPI ligands undergo tautomerism, as illustrated in green in **Figure 4.3**, where the mobile component of the structure is the H atom either placed on one of the imino arms or at the endocyclic amino group. FT-FTIR stretches of the nonspecific C=N vibrations appear as two stretches of strong intensity at 1600 cm^{-1} and 1660 cm^{-1}. Coordination of the BPI ligand via deprotonation of the endocyclic amine group results in weakening of the signal and its shift to frequencies below 1600 cm^{-1} which is consistent with a weaker nature of the C=N bond. In the case of the H atom residing on one of the imino arms, these strong vibrations remain identifiable with additional features emerging around 1550 cm^{-1}.[11,12,13] The UV-Vis analysis of BPI ligands should reveal very characteristic multiple band pattern in the region of 360-500 nm which originates from the extended π-bond system across the entFTIRe molecule. These transitions are assigned to have a π-π* character. Upon coordination of the ligand to a metal centre these transitions are reported to exhibit ~2-20 nm red or blue shifts.[8, 14, 15, 16, 17, 18] Further characterisation focuses on ^{1}H NMR analysis. Importantly, Irrespective of the location, the signal for the mobile H atom (endocyclic or imino) is observed above 12 ppm and is reported to often shift beyond the standard ^{1}H NMR ppm limits (0-14 ppm). Due to the broad nature and low intensity of the peak, it can be difficult to observe. [19] The fluxional behaviour of the H atom was investigated by Tamgho *et al.,* who discovered that aliphatic substituents (R group in **Figure 4.3**) result in the H atom residing on the imino arm which was supported with the change in multiplicity of the ^{1}H NMR shift from a singlet (endocyclic) to a triplet (imino).[20] Low temperature (-50 °C) was necessary to detect this interaction of the imino H atom and the aliphatic chain.

The heavily conjugated BPI system introduces rigidity to both the ligand and the resulting complex, and TM complexes with a 2:1 BPI to metal ratio are reported to exhibit octahedral geometry.[15,16,21,22,23,24,25,28,30] **Table 4.1** (below) shows reported BPI coordinated metal complexes and the corresponding distances reported for $M-N_{py}$ and $M-N_{ind}$ bonds and trans angles with atom nomenclature illustrated in **Figure 4.4** for reference.
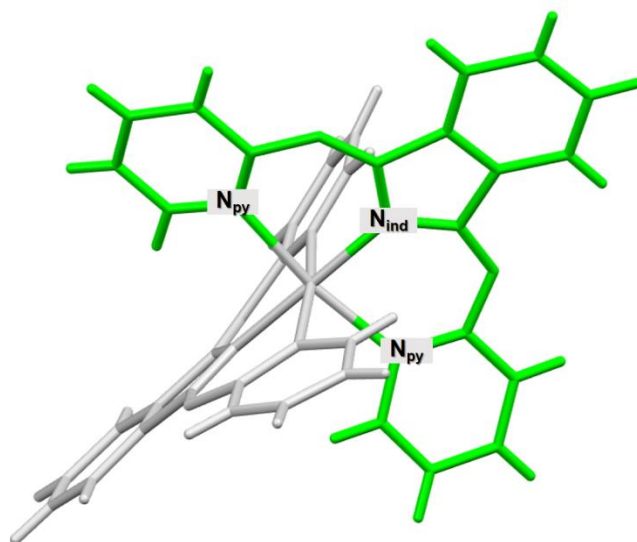
Figure 4.4 Highlighted N atoms for a crystal structure of [Ni(BPI)$_2$]; the nomenclature is universal for all complexes listed in **Table 4.1**

Table 4.1 Bond lengths (M-N$_{py}$ and M-N$_{ind}$) and trans-angles for a series of representative metal-based homoleptic [M(BPI)$_2$] complexes.

Complex	M-N$_{py}$(Å)	M-N$_{ind}$-M(Å)	N$_{ind}$-M-N$_{ind}$ (°)	N$_{py}$-M-N$_{py}$ (°)	N$_{py}$-M-N$_{py}$ (°)	Ref.
[Mn(BPI)$_2$]	2.295(4)	2.163(3), 2.143(3)	178.46(14)	162.05(13)	161.46(14)	16
[Mn(3'-Me-BPI)$_2$]	2.293 (0.005)	2.144, 2.151 (0.005)	175.15(0.1)	163.96(0.1)	159.76(0.1)	21
[Fe(BPI)$_2$]	2.243(10), 2.231(9)	2.069(10)	177.20(4)	164.87(3)	164.07(4)	15
[Fe(4'-Me-BPI)$_2$]	2.078(4), 2.092(5)	1.979(4)	175.34(3)	173.35(2)	173.35(2)	22
[Co(3'-Me-BPI)$_2$]	2.196	2.004, 2.005	179.53	170.62	171.32	23
[Ni(BPI)$_2$]	2.180(5), 2.155(5)	2.024(5)	179.62(3)	171.52(2)	171.52(2)	24
[Ni(4'-Me-BPI)$_2$]	2.180(2), 2.179(2)	2.017(2)	179.77(15)	173.54(9)	173.54(9)	28
[Cu(3'-Me-BPI)$_2$]	2.265(18)	1.952(17), 1.948(17)	178.92(7)	172.95(6)	172.78(6)	25
[Zn(4'-Me-BPI)$_2$]	2.243(2)	2.053(2), 2.038(2)	178.91(8)	169.90(7)	167.05(7)	26
[Cd(4'-Me-BPI)$_2$]	2.370(2)	2.258(2), 2.233(2)	177.91(8)	161.65(8)	159.27(8)	30

All complexes included in **Table 4.1** showed octahedral geometry, as evidenced by trans angles very close to 180°, and in all cases the M-N$_{ind}$ bonds were shorter than M- N$_{py}$.

All synthetic procedures reported in the literature, except for the synthesis of [Cu(3′-Me-BPI)₂] involved a base (LDA/TEA/NaOt-Bu) used to deprotonate the BPI ligand, nevertheless the [Cu(3′-Me-ind)₂] example suggests that deprotonation might occur spontaneously.[29] The 1,3-bis(pyridin-2-ylimino) isoindolin-2-ide are known to be utilised in the synthesis of other transition metal complexes. Considering only the unsubstituted 1,3-bis(pyridin-2-ylimino) isoindolin-2-ide ligand, a Sci-Finder® search produces 65 metal complexes. Amongst others there are Al(III), Re(I) and Ru(II) metal complexes utilising this ligand. [27]

During the course of this project, Cheng *et al.,* reported a series of 1,3-bis(pyridin-2-ylimino) isoindolin-2-ide and their chromium(III) complexes. All reported complexes are illustrated in **Figure 4.5**. [29]

A) R_1 = H, R_2 = H   D) R_1 = NMe₂, R_2 = H
B) R_1 = Me, R_2 = H   E) R_1 = H, R_2 = OMe
C) R_1 = OMe, R_2 = H
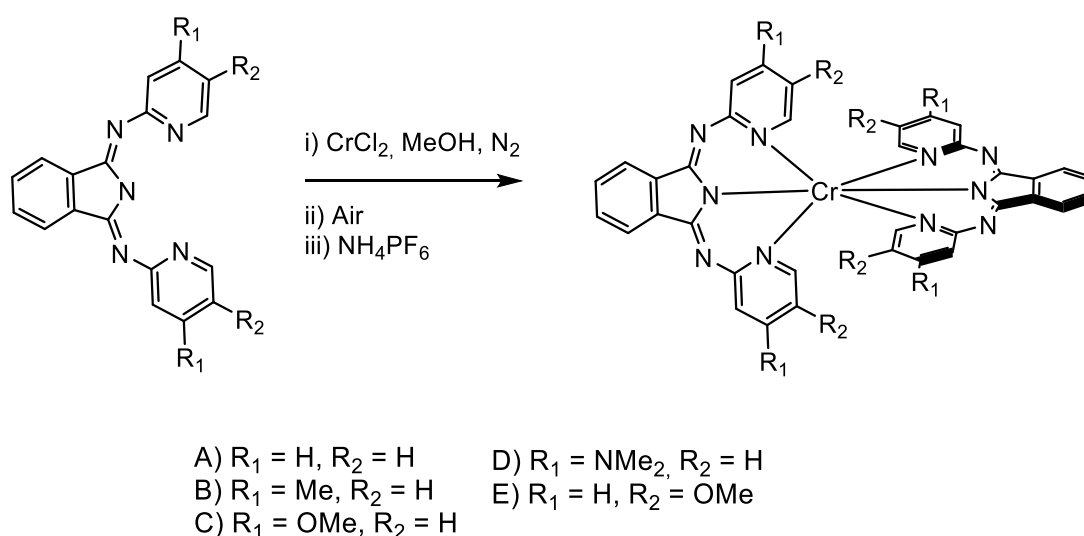
Figure 4.5 Cr(III) complexes reported by Cheng.

The 1,3-bis(pyridin-2-ylimino) isoindolin-2-ide type ligands all formed six-membered chelates upon coordination and, similarly to the reports of Wenger, utilised a Cr-N imido type coordination to the metal centre potentially increasing the covalency of the Cr-N (imido) bond. Their detailed analysis of the Cr-N stretches observed via FT-FTIR are discussed in **Section 4.3.2**, as a comparison to the values observed for the series reported in this chapter. Cheng *et al.,* reported all of the complexes to emit in the 777-970 nm range at

room temperature when excited with 480 nm in degassed MeCN. This represents an impressive achievement upon consideration of the fact that emission from $[Cr(dpc)_2]^{3+}$ could only be detected at 77 K. The lifetimes reported were in the range of 4.3-310 μs and the quantum yields were reported as 0.059 for complex D (**Figure 4.5**) and 0.0011, 0.0024, 0.0137, and 0.0003 for complexes A-C and E.[28] It is important to note that two of the complexes synthesised and discussed as part of this chapter were communicated in mid-April 2022;[29] six months prior to the communication by Cheng *et, al*..

4.1.3 Cr(III) ZFS parameters

Focusing on the EPR parameters, **Section 3.3.9** determined the *D*-value to range from 0.3 to 0.5 cm^{-1} for $[Cr(bpy)_3]^{3+}$ analogues. This places the polypyridyl system in between $[Cr(H_2O)_6]^{3+}$ with a *D*-value of 0.1 cm^{-1} and $Cr(acac)_3$ with the *D*-value of 0.59 cm^{-1} (**Figure 4.6**). Considering that the *D*-value decreases with increasing octahedral geometry, it suggests that $[Cr(bpy)_3]^{3+}$ analogues do not show perfect octahedral geometry as opposed to $[Cr(H_2O)_6]^{3+}$ (all trans angles are 180°). Nevertheless, it is crucial to consider the geometry of $[Cr(acac)_3]$; although, the *D*-value shows a large increase from that of $[Cr(H_2O)_6]^{3+}$, it does not imply that the geometry of $[Cr(acac)_3]$ is more distorted than that of $[Cr(bpy)_3]^{3+}$. To investigate this further, the nature of the coordinating atoms needs to be addressed. Whilst for $[Cr(H_2O)_6]^{3+}$ and $[Cr(bpy)_3]^{3+}$, all coordinating atoms are of neutral charge, all oxygen atoms in $[Cr(acac)_3]$ have a partial negative charge. Therefore, $Cr(acac)_3$ is an example of an octahedral complex (experimental trans angles: 179.32°, 178.37°, 177.28°) with a large influx of electron density pointed at the Cr(III) centre. Whilst the *D*-value reflects the ZFS interaction between three unpaired electrons at the Cr(III), it is understood that the negative charge on the oxygen atom results in much shorter Cr-O bond than in $[Cr(H_2O)_6]^{3+}$ which facilitates mixing of excited states into the ground state leading to a larger D value in comparison with for $[Cr(H_2O)_6]^{3+}$.

decreasing *D*-value
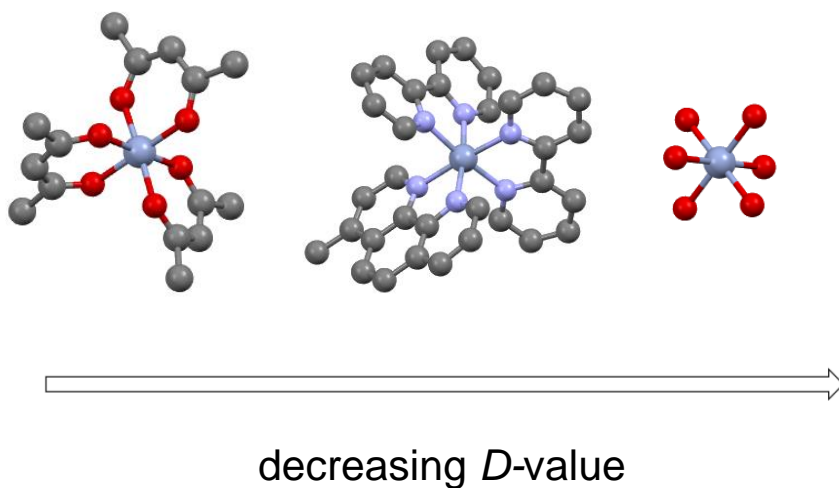
Figure 4.6 The relationship between the *D*-value and ZFS interaction represented by using the crystal structures of $[Cr(H_2O)_6]^{3+}$[30], $[Cr(bpy)_2(4\text{-Me-phen})]^{3+}$[31] and $[Cr(acac)_3]^{32}$ as known examples of Cr(III) complexes.

4.2 Aim

The aim of this chapter was to employ a six-membered chelating ligand system in order to encourage a near-perfect octahedral geometry of the synthesised Cr(III) complexes; to analyse the photophysical properties of the series and explore the response of the ZFS to the potentially increased Cr-N (imido) bond covalency and analyse its relationship to the luminescent properties. It is hypothesised that the increased covalency of the Cr-N$_{ind}$ bond can be reflected in ZFS parameters of the Cr(III) complexes, and this is investigated herein.

4.3 Results and discussion

4.3.1 Synthesis

As outlined in **Figure 4.7**, six different ligands were targeted which provided different types of substituents across the pyridyl and isoindoline components. All ligands were synthesised using n-BuOH as the solvent of choice and were obtained in yields 60-80%.[29] Phathalonitrile and 2-aminopyrdine variants were stirred under reflux for 48 h with 0.01 equivalents of the calcium salt. Since $CaCl_2$ is known for its drying properties, it was crucial that a fresh batch of n-BuOH was used to prevent deactivating the catalytic capabilities of $CaCl_2$. In cases where high water content was suspected, additional portions of $CaCl_2$ were added until the reactions had gone to completion or until minimal concentrations of starting materials remained, as monitored by TLC.

L_1, Cr-1	R_1=H	R_2=H	R_3=H
L_2, Cr-2	R_1= Et	R_2= H	R_3=H
L_3, Cr-3	R_1= H	R_2= H	R_3= OPh
L_4, Cr-4	R_1= Et	R_2= H	R_3= OPh
L_5, Cr-5	R_1=H	R_2= H	R_3= tBu
L_6, Cr-6	R_1= Et	R_2= H	R_3= tBu
L_7, Cr-7	R_1=H	R_2= Me	R_3= H
L_8, Cr-8	R_1=H	R_2= Et	R_3= H
L_9, Cr-9	R_1=Me	R_2= Me	R_3= H
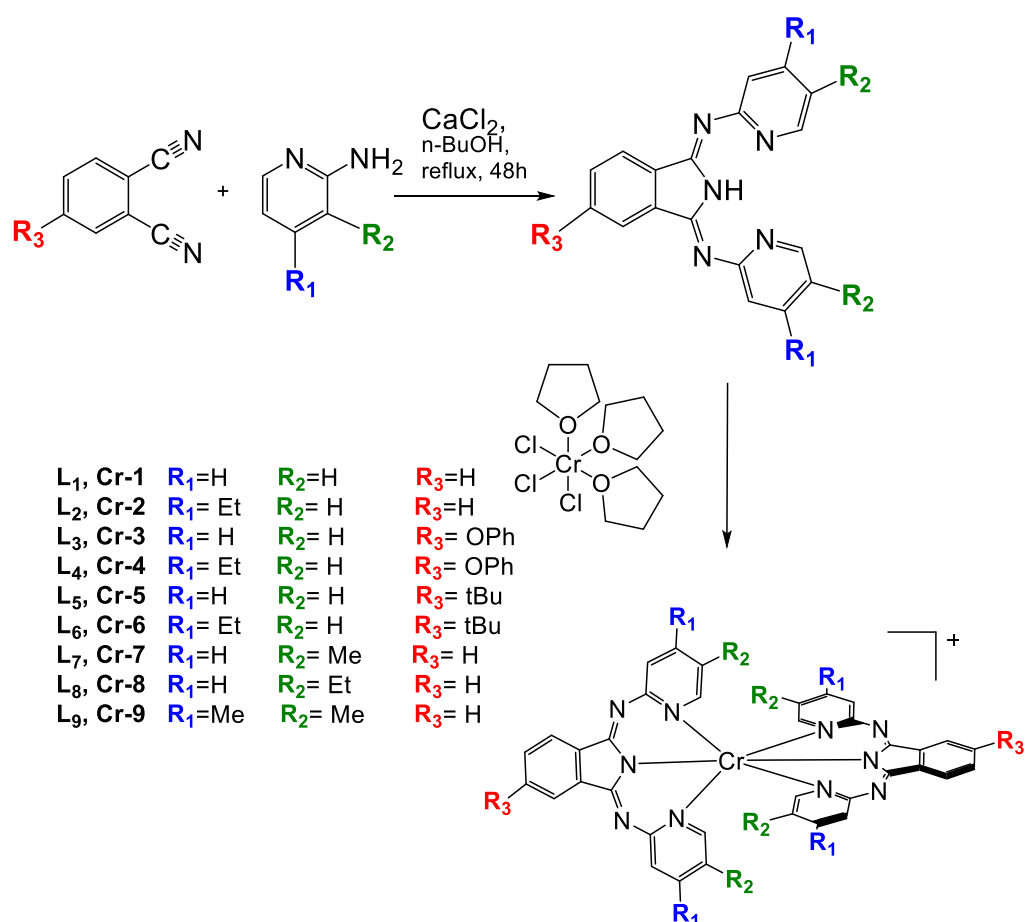
Figure 4.7 The synthetic route for isoindoline Cr(III) complexes discussed in this chapter.

174

After concentration of the solvents using a rotary evaporator, the crude product was redissolved in MeOH and equal amounts of water were added causing a precipitation of a yellow material. The desired product was observed to elute in the second fraction using a more polar 99:1 DCM/MeOH solvent system. Upon evaporation of the solvent, all ligands produced bright yellow needle-like crystals, except for the t-Bu-substituted analogues which initially produced yellow oils which crystallised over time.

As shown in **Figure 4.8**, identification of the correct ligand was observed by ^{1}H NMR spectroscopy as indicated by the appearance of a broad singlet in the 11-14 ppm range corresponding to the NH proton within the isoindoline ring moiety. The location of the amino proton is confirmed by the crystal structure obtained for **L₇** (**Figure 4.9**). The structure is further discussed in **Section 4.3.4**. The set of red crystals was grown in H_2O/MeOH mixture placed in a freezer for a week.
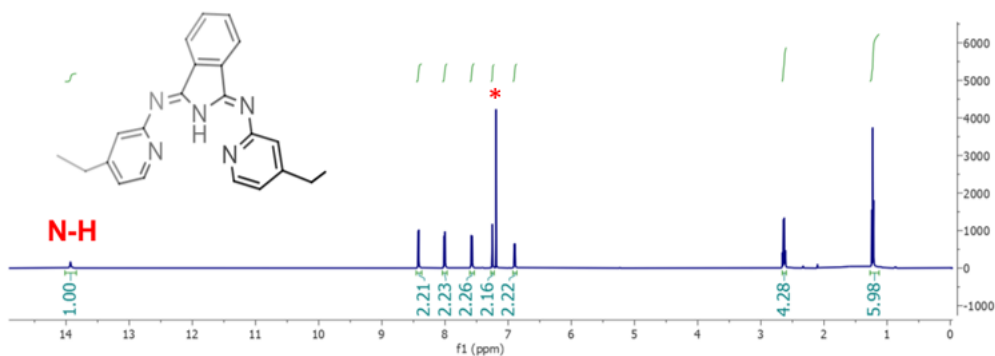
Figure 4.8 ^{1}H NMR spectrum of **L₂** recorded in CDCl₃.

Figure 4.9 Crystal structure solved for **L₇** with ellipsoids shown at 50% probability. Experimental parameters are available in **Table 4.8**.

Despite successful collection of ^{1}H NMR and ^{13}C NMR data obtained for each ligand, [M+H]$^+$ ion was observed via mass spectrometry for all ligands except for **L₂**, where it is assumed adducts and/or fragmentation is the reason for this

outcome.

The corresponding series of Cr(III) complexes was synthesised in the same manner as described in **Section 2.3.1**. *mer*-Cr(Cl)$_3$(thf)$_3$ and two equivalents of the ligand of choice were stirred under reflux in dry EtOH for 24h. Upon cooling, a gold precipitate was observed and isolated, however it was not possible to identify any potential side products such as a poorly soluble mono-Cr(BPI)Cl$_3$ complex. The remaining red coloured filtrate was concentrated and redissolved in minimum amounts of MeOH to which NH$_4$PF$_{6(aq)}$ was added and a red precipitate was obtained. Further purification employed column chromatography. The first eluent was identified as the ligand and was eluted with acetone. The complex of interest eluted as the second fraction with MeCN/H$_2$O/KNO$_3$ (14:2:1). Following concentration of the solvent a DCM/H$_2$O solvent extraction was performed with solid NH$_4$PF$_6$ added in order to carry out counterion extraction. Pure product was identified by LC-MS and HPLC. As can be observed in **Figure 4.10**, some complexes produced more than one peak in the chromatogram. However, LC-MS analysis revealed that all the peaks represented the complex of interest. It is thought that isomer formation, which is also discussed in the X-ray crystallography **Section 4.3.4**, could be the reason for this. Alternatively, it is thought that the complexes could stick to the LC-MS column and elute in fractions.
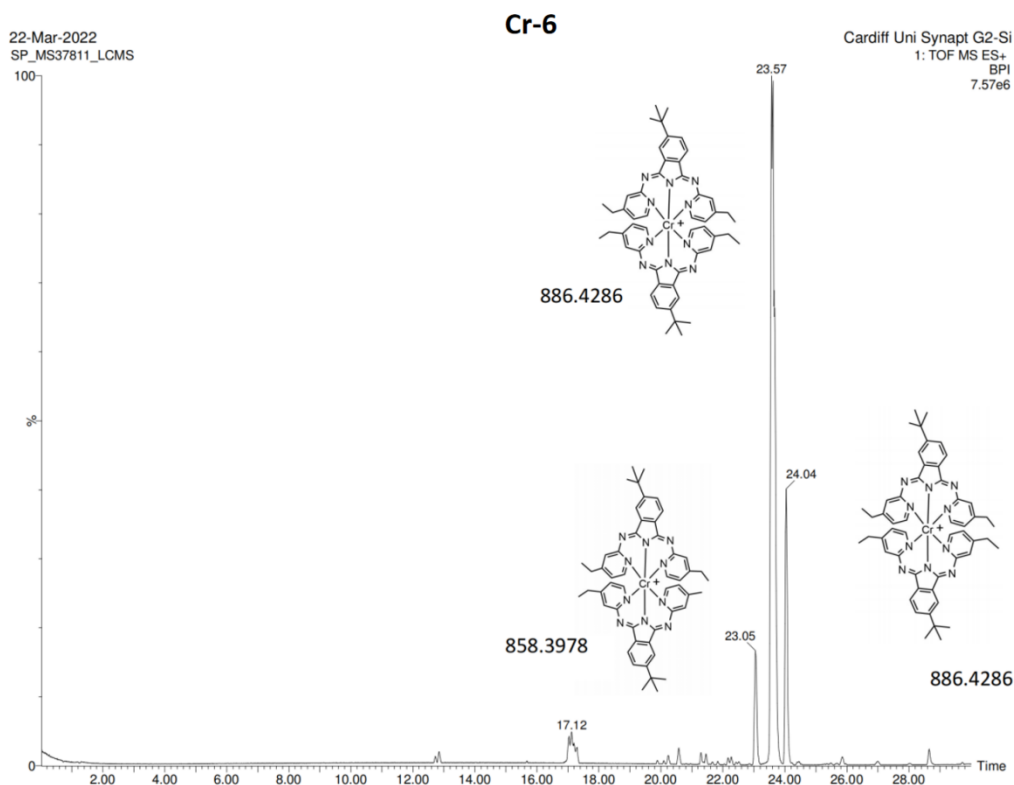
Figure 4.10 LC-MS chromatogram of **Cr-6** recorded in MeCN. Feature at 17.12 min represents a minor ligand impurity.

All attempts at utilising ^{1}H NMR spectroscopy to characterise the series of Cr(III) complexes failed, even when wide range NMR measurements were employed. It is assumed that the relaxation time for this series of complexes is too short to be detected via ^{1}H NMR spectroscopy or that the paramagnetic broadening weakens the signal when aquired.[33]

As previously discussed in **Section 2.3.4**, doping the paramagnetic Cr(III) complexes into a diamagnetic host can significantly aid spectral acquisition and interpretation of EPR spectra. Hence, a series of Co(III) complexes was synthesised for the EPR analysis of the above Cr(III) complexes using EPR and is discussed in the EPR **Section 4.3.9.** CoCl$_2$ and the ligand of choice were reacted together in MeOH at room temperature for 24 h. Brown precipitate was observed and filtered, then suspended in H$_2$O. Excess Br$_2$ was dissolved in 1 mL of H$_2$O and added dropwise to the stirring suspension of the Co(II) complex and stirred for another 24 h. A red-brown precipitate

evolved over the course of the reaction. The precipitate was filtered and redissolved in minimal amounts of MeOH, then $NH_4PF_{6(aq)}$ was added to afford red precipitate, which was subsequently filtered and, in some cases, afforded pure product. Impure samples were purified by column chromatography using CH_2Cl_2 to elute the remaining ligand and 99:1 $CH_2Cl_2/MeOH$ to elute the product.

Oxidation of Co(II) to Co(III) and final purity was monitored by ^{1}H NMR, where Co(II) samples would manifest with very weak but paramagnetically shifted signal and unidentifiable multiplicity patterns. Upon oxidation, the corresponding Co(III) complexes produced strong ^{1}H NMR (**Figure 4.11**) spectral signals and very well-defined multiplicities. Identification of the complexes was confirmed by the expected shifts in the ^{1}H NMR spectra as well as the disappearance of the broad singlet within the 11-14 ppm range suggesting the deprotonation and coordination of the isoindoline. No new broad singlets were observed suggesting no tautomerism occurred upon deprotonation/coordination of the ligand.
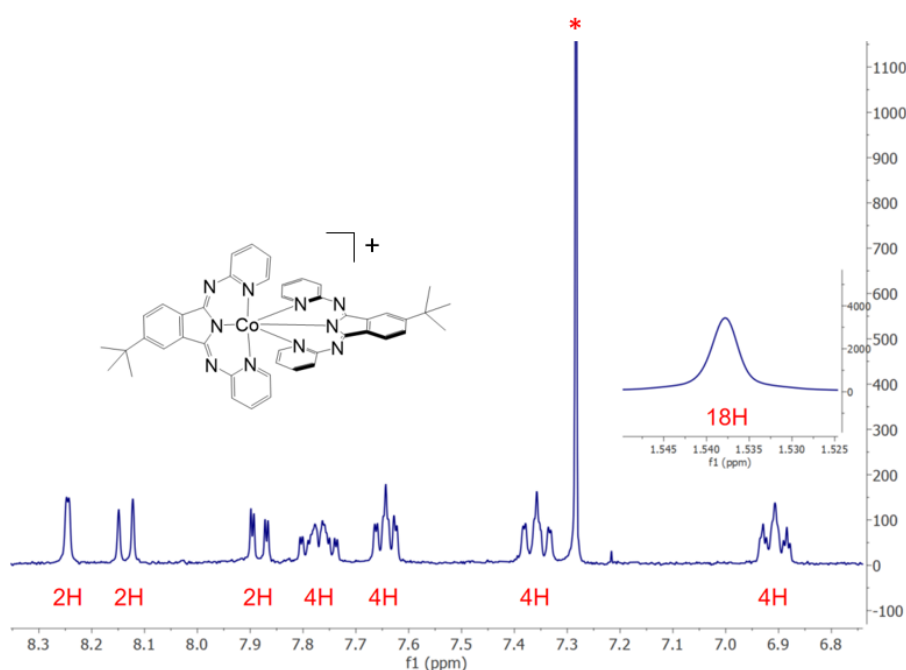
Figure 4.11 ^{1}H NMR spectrum of **Co-5** recorded in CDCl₃.

The phenoxy analogues of Co(III) proved difficult to characterise. Initially, it was thought that the reason for weak ^{1}H NMR signals for **Co-3** and **Co-4** was incomplete oxidation. However, multiple oxidation attempts were carried out and the intensity of the signal remained the same, yielding low intensity and unidentifiable shifts. Using more concentrated samples did not improve signal intensity. Attempts at identifying the complexes via mass spectrometry showed no peak to match for the expected M$^+$ at 839.20 and 951.32 *m/z*. Additionally, the FT-FTIR data matched the trend that the other two Co(III) complexes have shown. All Co(III) complexes were screened via EPR and were defined to be silent, therefore all four complexes were used as doping matrices for their respective Cr(III) complexes.

4.3.2 FTIR Spectroscopy

All ligands and complexes were analysed using FT-FTIR spectroscopy. The most significant stretch was that in the range of 1600-1604 cm^{-1} representing C=N imine stretch and therefore acting as proof of successful synthesis (stretches 1577 and 1607 cm^{-1} in **Figure 4.12**). Upon coordination of the ligand this stretch is observed to decrease in energy by about 20 cm^{-1}, as expected for π-acceptor ligands. For the phenoxy substituted ligand (**L$_3$**, in **Figure 4.12**) a stretch around 1248 cm^{-1} corresponds to an aromatic ether. All ligands and complexes show weak stretches around 3000 cm^{-1} as expected for sp^2 C-H vibrations. Moreover, the C-H bending mode is observed around 1400 cm^{-1}. For alkyl substituted ligands (all ligands except for **L$_1$** and **L$_4$**), out-of-plane bends are observed at 1450 and 1375 cm^{-1}. For instance, for **L$_2$** those bends are observed at 1455 and 1373 cm^{-1}, moreover the scissoring mode is observed at 1464 cm^{-1}. In **Figure 4.12**, the same modes are indicated for **L$_4$**. Weak stretches beyond 3000 cm^{-1} are likely to correspond to N-H stretches, albeit expected to manifest as medium intensity.
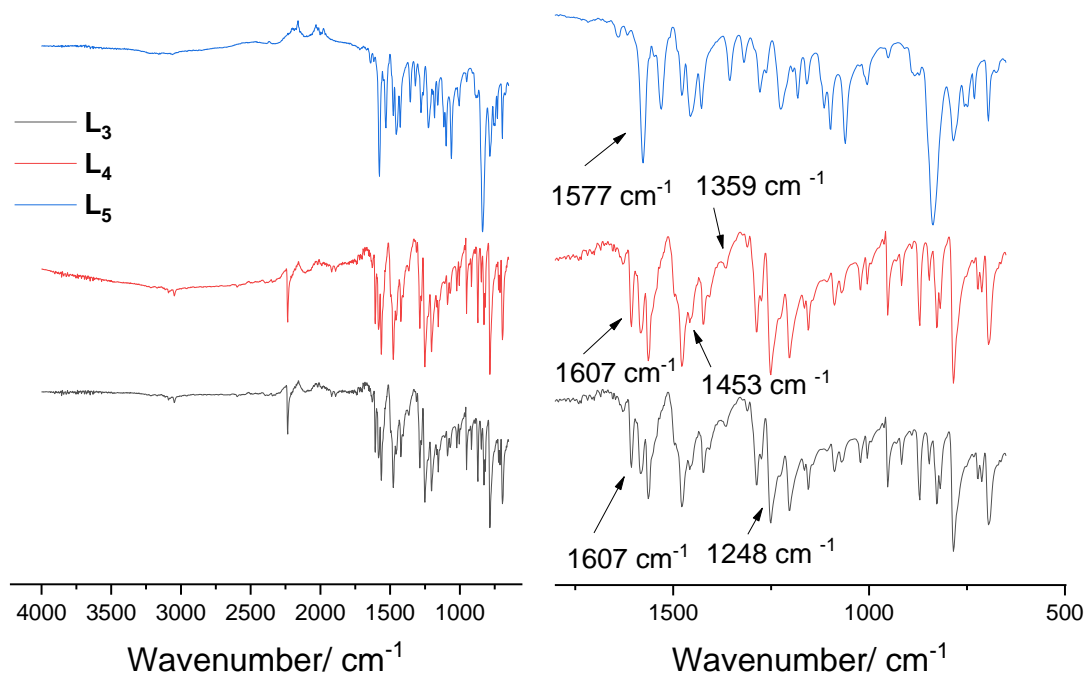
Figure 4.12 FT-FTIR spectrum of **L₃-L₅**.

Considering the stretches recorded for **Cr-3** (**Figure 4.13**), there is a stretch at 824 cm^{-1} corresponding to the PF$_6^-$ counterion. The imine stretch can be observed around 1580 cm^{-1}, whilst the aromatic ether of the 4-phenoxy group is observed around 1232 cm^{-1}. In the region around 3000-3500 cm^{-1}, there are several weak signals that could represent unresolved alkene C-H stretches and/or O-H stretches coming from potential moisture present within the sample. This could be due to unsatisfactory drying/humidity in the instrument room. Stretches around 2000 cm^{-1} most likely represent aromatic C-H stretches.
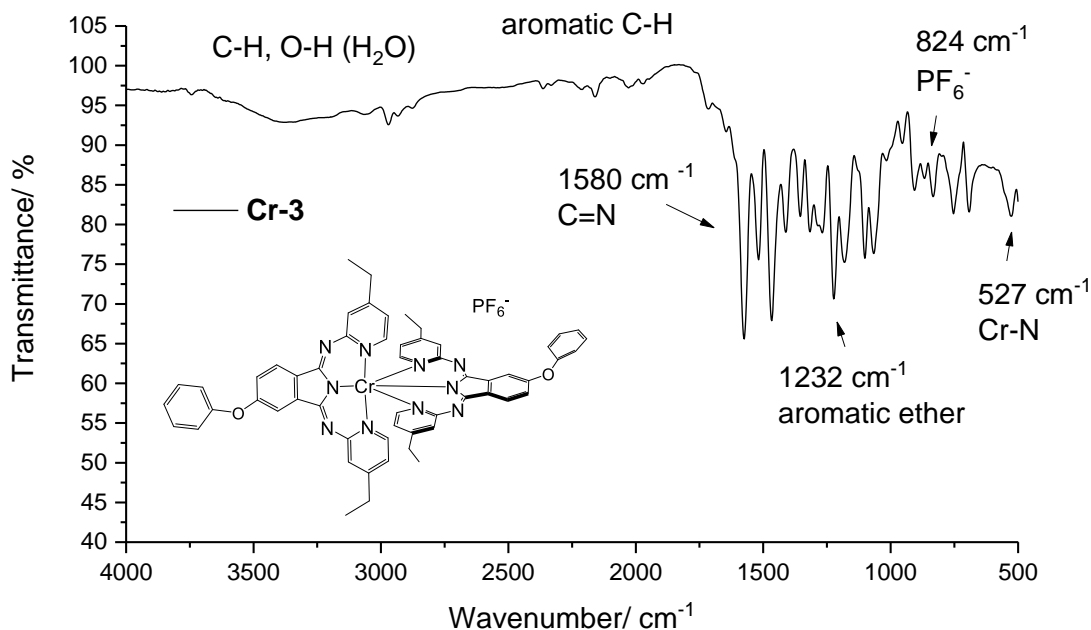
Figure 4.13 FTIR spectrum of **Cr-3**.

As previously discussed in **Section 4.1**, the value of the C=N stretch of the final [M(BPI)$_2$]$^+$ complex depends on the exact location of the H atom and where the coordination occurs via deprotonation of the indole N atom, the C=N stretch weakens and shifts to values below 1600 cm^{-1}. The analysis of the C=N stretch values for complexes **Cr-1** to **Cr-4** and **Cr-6** revealed that all values are shifted below 1600 cm^{-1} (**Table 4.2**). Moreover, all stretches observed for **L$_1$** to **L$_6$** could not be identified in any of the FTIR spectra of their corresponding complexes and therefore further supporting coordination via deprotonation of the indole N atom. This is confirmed with two crystal structures of complexes **Cr-1** and **Cr-3** which are discussed in **Section 4.3.4**.

Cheng discussed the influence of the covalency of the Cr-N$_{ind}$ bond and its appearance in the FTIR spectrum. Normally reported at 189-385 cm^{-1}, the Cr-N$_{ind}$ stretch was reported at 556 cm^{-1} by Cheng for all of their isoindoline complexes. [29] For the complexes discussed in this chapter the a stretch is observed at 557-525 cm^{-1} for complexes **Cr-1** to **Cr-7** reported in this series (**Table 4.2**) and were absent in the FTIR spectra of the corresponding ligands. Additionally, the increased covalent character of the Cr-N$_{ind}$ bond is expected to be observed at higher frequency as it is a stronger bond in comparison with Cr-N$_{py}$. This slight shift could suggestd an increase in bond strength for Cr-N$_{ind}$ when compared to Cr-N$_{py}$ and therefore an increase in the frequency of the stretch representing the Cr-N$_{ind}$ bond. This is supported by the crystal structures obtained for **Cr-1** and **Cr-3** which are discussed in **Section 4.3.4**.[29]

Table 4.2 Comparison of the C=N stretches between the ligands and their corresponding complexes which suggests coordination via the indole N atom upon deprotonation.

Complex	v(CN) ligand/cm^{-1}	v(CN) complex/cm^{-1}	Cr-N$_{ind}$
Cr-1	1628, 1581	1578	557
Cr-2	1628, 1589	1522	555
Cr-3	1606, 1582	1580	519
Cr-4	1625, 1606	1576	527
Cr-5	1620, 1597	Not observed	525
Cr-6	1620, 1605	1519	533

4.3.3 Bulky ligands in position 6

The success of the bis-pyridyl-isoindoline Cr(III) complexes encouraged further ligand improvement through bulky substitutions within close vicinity of the metal centre (**Figure 4.14**) to form complexes **Cr-7** to **Cr-9** (**Figure 4.7**). Connecting a large ligand in short-range bonding to the metal centre is thought to minimise deactivation of the doublet excited state by reducing oxygen quenching with the large ligand physically protecting the metal centre from molecular oxygen and therefore resulting in an increase of the quantum yield.

L-7   **L-8**   **L-9**
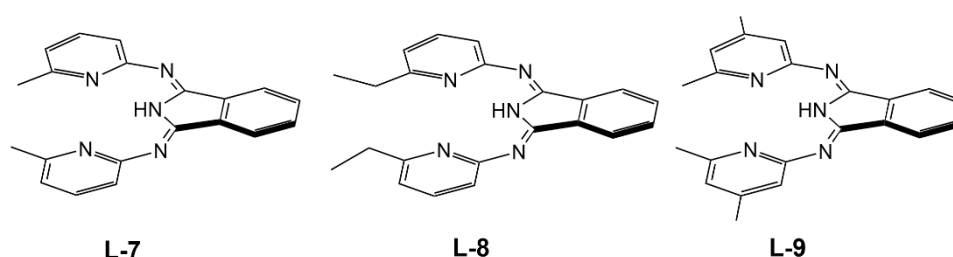
Figure 4.14 Three alkylated variants of BPI used as sterically protective ligands.

Initial attempts involved the same synthetic approach as described in **Section 4.3.1**. However, addition of *mer*-Cr(Cl)$_3$(thf)$_3$ to ligands **L7** to **L9** led to a change in the colour of the reaction solution to green, which did not change thereafter. For complexes **Cr-1** to **Cr-6**, the reaction solution changed its colour to deep red upon addition of Cr(Cl)$_3$(THF)$_3$ which signified coordination of both ligands to the metal centre (see **Experimental Section 4.6**), therefore it was believed that the reactions utilising **L7** to **L9** did not proceed as expected in this case. Furthermore, no MS evidence of the molecular ion for [Cr(**L7/8/9**)$_2$]$^+$ was found. Further attempts involved using CrCl$_2$ as the chromium source, with further oxidation carried out by stirring the reaction mixture exposed to air over 48h, however the same result was observed, namely a green solution with no clear indication of the complexes forming by MS or TLC.

Further to that, *mer*-Cr(Cl)$_3$(thf)$_3$ was again used as a starting material and once the reaction mixture changed the colour to green, a catalytic amount of Zn powder was added, to reduce the suspected mono-coordinated complex (ligand to metal ratio 1:1) to the Cr(II) oxidation state (see **Section 1.4.3**), upon which an instant colour change from green to red/orange was observed. The work up proceeded as previously, however the characterisation proved challenging. Regardless of the promising colour change of the reaction mixture, no molecular ions were observed in mass spectroscopy. Several attempts at utilising MALDI showed no results. It was suspected that the Me group substituted ligands are prone to fragmentation. Several fragments suggesting the loss of the Me group were found however too many protons were observed in each case (+ 2H). Single red block-shaped crystals were grown from a concentrated methanolic solution of a supposed [Cr(**L$_7$**)$_2$]$^+$ complex in the freezer over a week. The solved crystal structure confirmed that coordination of ligand **L$_7$** to the Cr(III) metal central was unsuccessful, and the structure obtained was of ligand only for which data is available in the following Section (See **Table 4.6**, **L-7**).

As discussed in **Section 4.1.1**, Heinze reported attempt at synthesising Cr(III) complexes, where the ligands possessed Me groups in position 6 of the pyridyl ring as unsuccessful. However, no synthetic details were disclosed.[4]

4.3.4 X-ray Crystallography

Single red needle-shaped crystals were achieved via recrystallisation from MeCN, Et_2O and toluene. The crystal used was a non-merohedral twin. A single molecule was determined to occupy the asymmetric unit.
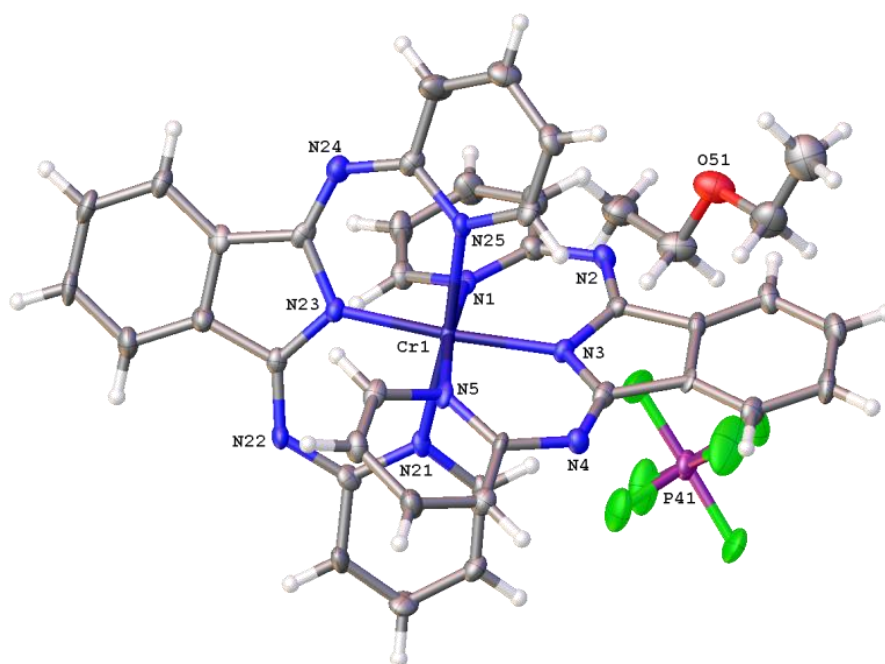
Figure 4.15 Crystal structure of **Cr-1**. Ellipsoids shown at 50% probability.
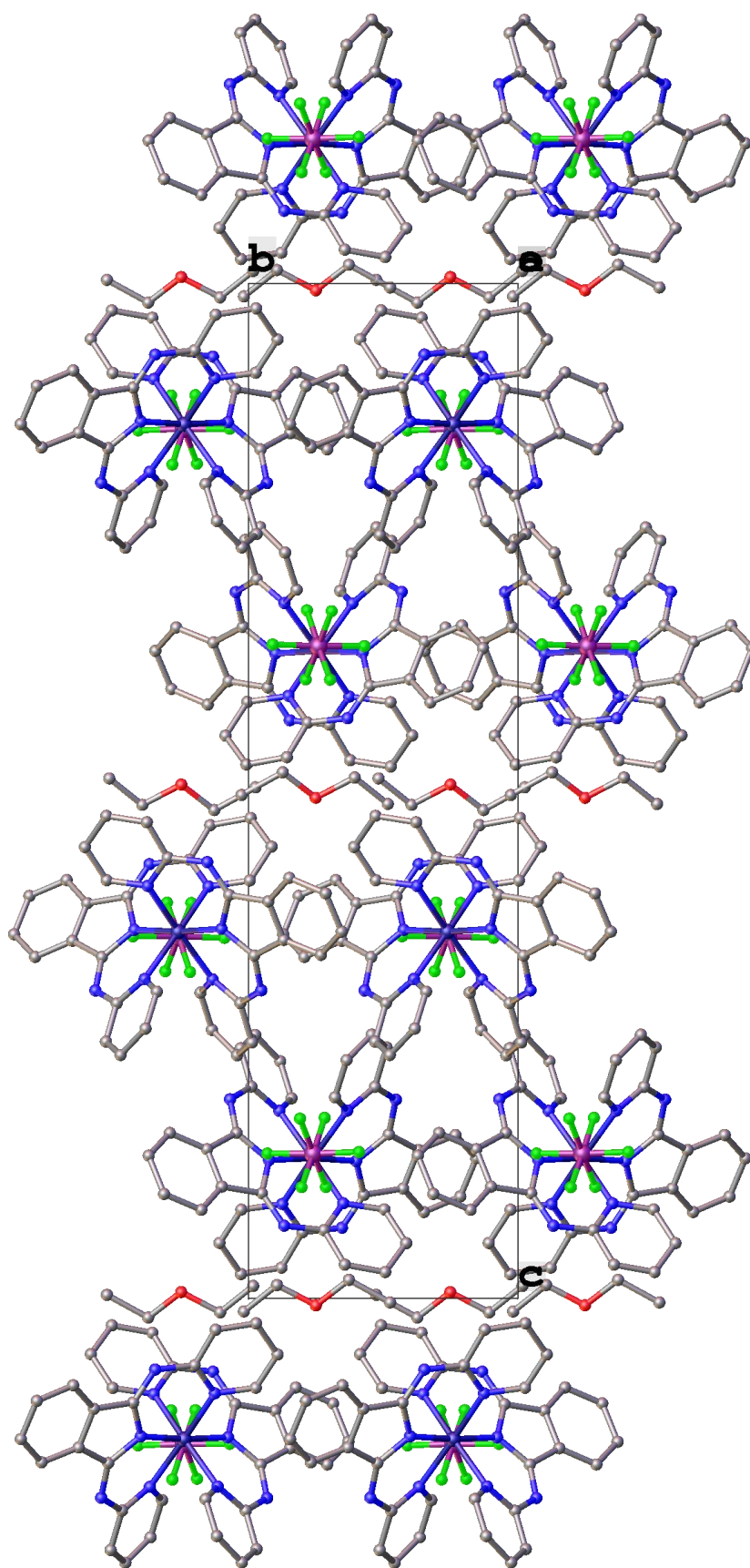
Figure 4.16 Packing diagram of **Cr-1**.

Single red plate-shaped crystals of **Cr-3** were achieved via recrystallisation from MeCN and toluene. The Flack parameter was refined to 0.492(9), which means the crystal consists of a racemic mixture of the two enantiomers as exemplified by two phenoxy groups on the same benzene ring in the solved structure (where it should be just one phenoxy group). Depending on the position of the coordinating ligand, the phenoxy groups of both ligands could either point in the same direction or opposite. The asymmetric unit was determined to consist of a single molecule.
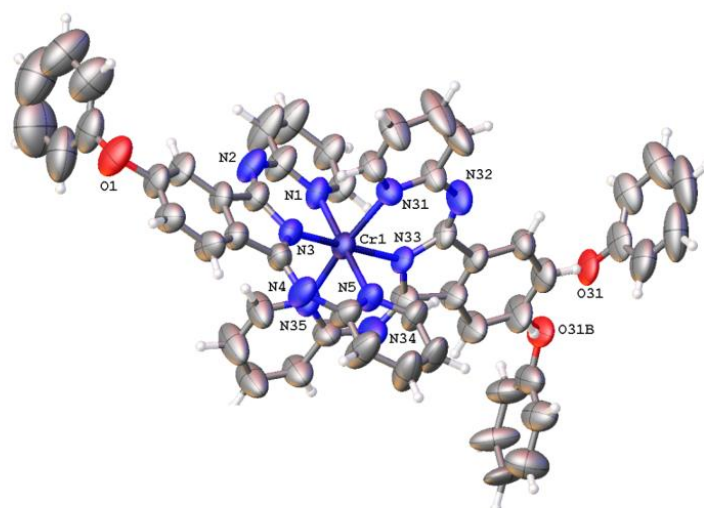
Figure 4.17 Crystal structure of **Cr-3**. Ellipsoids shown at 50% probability with solvate molecules omitted for clarity.
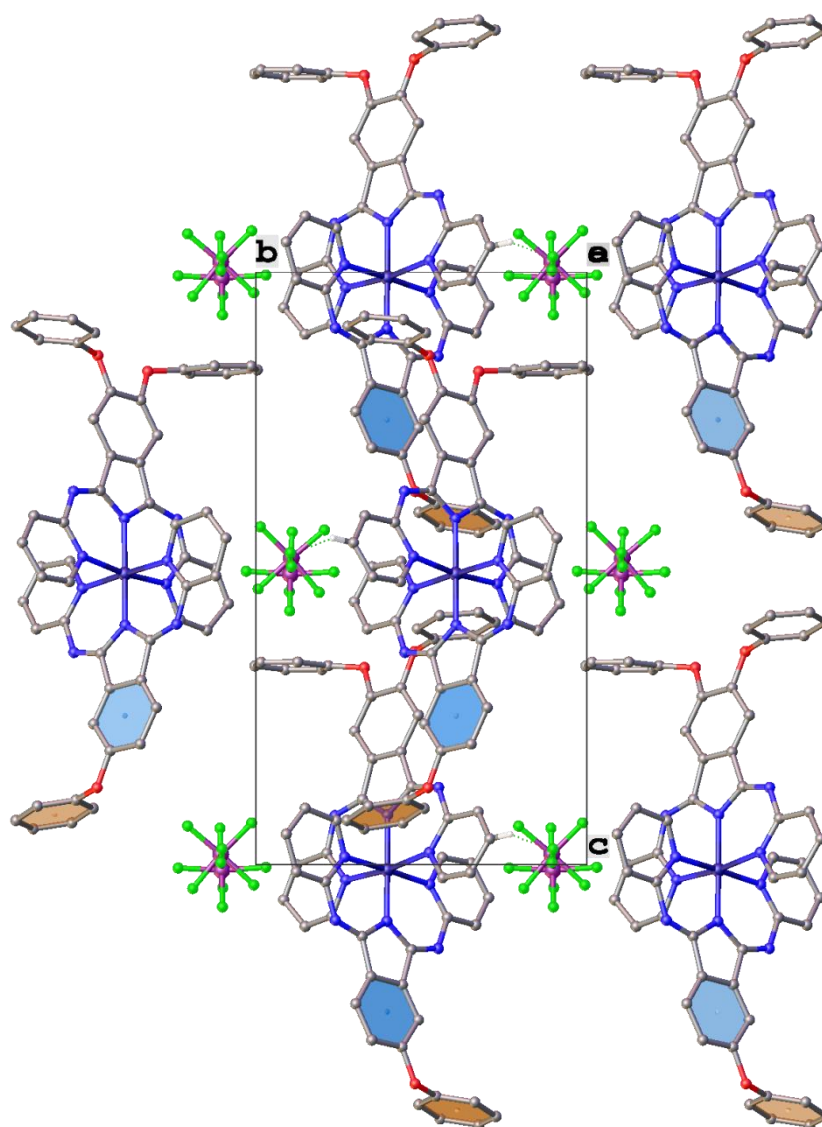
Figure 4.18 Packing diagram of **Cr-3**.

From the analysis of the two crystal structures obtained it is understood that placing bulky ligands on the isoindoline encourages a more octahedral geometry. [Cr(BPI)$_2$]PF$_6$ shows trans angles of 175.6°(2), 173.5°(2) and 176.52°(2), whereas [Cr(BPI-5-PhO)$_2$]PF$_6$ extracted trans angles are 174.69°(2), 179.27°(19), 176.52°(2). When compared with the trans angles reported by Cheng *et al.*, in the range 171.8°-179.74°(6-17), displayed in **Table 4.3**, it proves consistent. Moreover, data provided in the literature suggests that substitution in position 4 of the pyridyl moiety increases the imido trans angle and therefore encourages an increase in the octahedral geometry. [29]

Observing the trans angles extracted from the crystal structure of [Cr(bpy)$_2$(4-Me-phen)](PF$_6$)$_3$ (176.20°(7), 174.05°(6) and 174.49°(6)) reported in **Chapter 3**, bis-pyridyl-isoindoline ligands do not provide any significant changes when considering the trans angles. However, when the bond lengths are compared, for [Cr(bpy)$_2$(4-Me-phen)](PF$_6$)$_3$ the range is 2.0386-2.0546(16) Å, whereas the bis-pyridyl-isoindoline complexes show a range of 2.097 - 2.1318(6-12) Å for the Cr-N$_{py}$ and 1.963-2.018(5-12) Å for the Cr-N$_{ind}$ as indicated in **Table 4.4**.

Table 4.3 Trans angles extracted from the crystal structures of **Cr-1** and **Cr-3** and angles reported by Cheng shown as a range for complexes A-D.

Cr-1		Cr-3		Cheng *et al.*	
N$_1$-Cr-N$_{21}$	173.5(2)	N$_3$-Cr-N$_{33}$	179.27(19)	N$_{ind}$-Cr-N$_{ind}$	176.1(8)-179.74(16)
N$_3$-Cr-N$_{23}$	175.6(2)	N$_1$-Cr-N$_{31}$	174.69(2)	N$_{py}$-Cr-N$_{py}$	176.1(8)-179.74(16)
N$_5$-Cr-N$_{25}$	172.8(2)	N$_5$-Cr-N$_{35}$	176.52(2)	N$_{py}$-Cr-N$_{py}$	171.8(6)-175.05(6)

Table 4.4 Cr-N bond lengths (Å) extracted from **Cr-1** and **Cr-3** and bond lengths reported by Cheng shown as a range for complexes A-D. Numbers shown in bold represent the Cr-N$_{ind}$ bonds.

Cr-1		Cr-3		Cheng *et al.*	
Cr-N$_1$	2.097(6)	Cr-N$_1$	2.131(5)	Cr-N$_{py}$	2.068(6)-2.1158(15)
Cr-N$_3$	**1.993(6)**	**Cr-N$_3$**	**2.018(5)**	**Cr-N$_{ind}$**	**1.965(2)-1.997(15)**
Cr-N$_5$	2.088(6)	Cr-N$_5$	2.101(6)	Cr-N$_{py}$	2.068(6)-2.1158(15)
Cr-N$_{21}$	2.107(6)	Cr-N$_{31}$	2.096(5)	Cr-N$_{py}$	2.068(6)-2.1158(15)
Cr-N$_{23}$	**1.986(6)**	**Cr-N$_{33}$**	**1.963(5)**	**Cr-N$_{ind}$**	**1.965(2)-1.997(15)**
Cr-N$_{25}$	2.098(6)	Cr-N$_{35}$	2.138(5)	Cr-N$_{py}$	2.068(6)-2.1158(15)

The Cr-N$_{ind}$ bonds are shorter than Cr-N$_{py}$ with a neutral nitrogen atom coordinated. This could suggest a more covalent character of the bond and therefore shortening of it with respect to the neutral nitrogen atom coordinated to the Cr centre. Additionally, five crystal structures of the complexes reported by Cheng *et al.,* show a range of 1.965(2)-1.997(15) Å for the Cr-N$_{ind}$ bond length, therefore supporting this theory (**Figure 4.19**; **Table 4.5**).

A) R$_1$ = H, R$_2$ = H   D) R$_1$ = NMe$_2$, R$_2$ = H
B) R$_1$ = Me, R$_2$ = H   E) R$_1$ = H, R$_2$ = OMe
C) R$_1$ = OMe, R$_2$ = H
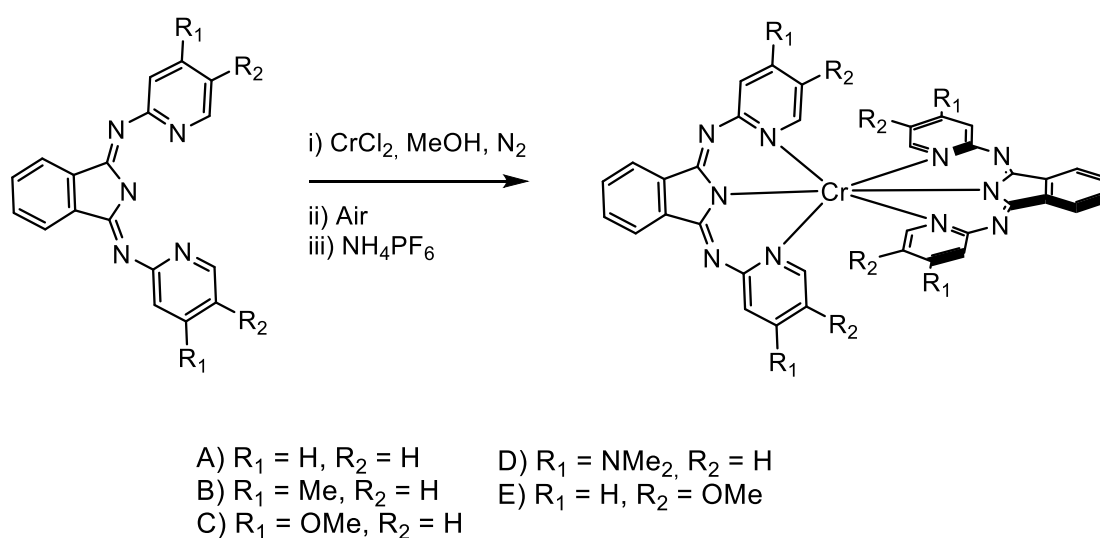
Figure 4.19 Cr(III) complexes reported by Cheng.

Table 4.6 Crystallographic data for **Cr-1**, **Cr-3** and **L$_7$**.

Complex	Cr-1	Cr-3	L-7
Formula	$C_{38}H_{29}CrF_6N_{10}O_{0.5}P$	$C_{48}H_{32}CrF_6N_{10}O_2P$	$C_{20}H_{17}N_5$
$D_{calc.}$/ g cm^{-3}	1.560	1.019	1.338
m/mm^{-1}	3.787	2.186	0.083
Formula Weight	830.68	977.80	327.392
Colour	red	red	red
Shape	needle-shaped	plate-shaped	block-shaped
Size/mm^3	0.14×0.02×0.01	0.180×0.070×0.015	0.220×0.200×0.090
T/K	100(2)	100(2)	100(2)
Crystal System	monoclinic	monoclinic	monoclinic
Flack Parameter		0.492(9)	
Hooft Parameter		-0.44(16)	
Space Group	$P2_1/n$	Pn	$P2_1/c$
a/Å	12.2896(3)	12.9887(5)	17.0043(5)
b/Å	8.7251(2)	11.7091(5)	18.0573(5)
c/Å	32.9959(10)	20.9690(6)	10.6363(3)
a/°	90	90	90
b/°	91.483(2)	91.955(3)	95.524(3)
g/°	90	90	90
V/Å^3	3536.90(16)	3187.2(2)	3250.73(16)
Z	4	2	8
$Z`$	1	1	2
Wavelength/Å	1.54178	1.54178	0.71075
Radiation type	Cu K$_\square$	Cu K$_a$	Mo K$_a$
Q_{min}/°	2.679	3.944	2.23
Q_{max}/°	70.606	68.245	28.70
Measured Refl`s.	9714	33726	42080
Indep`t Refl`s	9714	10068	8403
Refl`s I≥2 s(I)	7915	7973	6643
R_{int}	.	0.0581	0.0341
Parameters	535	706	455
Restraints	21	1616	0
Largest Peak	1.913	1.240	0.3422
Deepest Hole	-0.677	-0.314	-0.2772
GooF	1.050	1.094	1.0235
wR_2 (all data)	0.2576	0.2220	0.1149
wR_2	0.2486	0.2082	0.1081
R_1 (all data)	0.1038	0.0819	0.0612
R_1	0.0894	0.0714	0.0448

$R_1 = \Sigma ||F_o| - |F_c|| / \Sigma |F_o|$, $wR_2 = \{\Sigma [w(F_o^2 - F_c^2)^2] / \Sigma [w(F_o^2)^2] \}^{1/2}$, GooF = S = $\{ \Sigma [w(F_o^2 - F_c^2)^2] / (n-p) \}^{1/2}$ Fo – experimental model, Fc – calculated model, w -weighting scheme

4.3.5 DFT geometry optimisation

Considering that crystal structures could not be obtained for all complexes in this series, geometry optimisation using DFT was employed to further analyse the geometry trends within the series. Firstly, it was crucial to compare the values extracted from the crystal structures and those obtained via DFT.

From comparison of the experimental and DFT calculated values for complexes **Cr-1** and **Cr-3**, the N_{py}-Cr-N_{py} trans angles are predicted with good accuracy, whilst the N_{ind}-Cr-N_{ind} angles are not. The two N_{py}-Cr-N_{py} trans angles for **Cr-1** complex are calculated to be 173.97° and are within 1° error, however for N_{ind}-Cr-N_{ind}, the trans angles values determined from the crystal structures are 175.6°(2) and 179.27°(19) for the unsubstituted and phenoxy substituted complexes respectively, which compare with a calculated value of 197.97° (an identical value was calculated from DFT for the two complexes). Although the DFT calculations prediction for the phenoxy substituted complex are quite accurate ($\pm$1°), the calculations for the unsubstituted complex show poorer agreement with experiment ($\pm$4°). It is important to highlight the error value for the N_{ind}-Cr-N_{ind} trans angle of **Cr-3** is quite high.

With respect to the bond length values extracted from the crystal structures, the Cr-N_{ind} bond lengths range between 1.993(6)-2.018(5) Å, whilst the DFT calculated value is 2.010 Å for all Cr-N_{ind} bonds. All the other Cr-N_{py} bonds seem to be predicted with good accuracy and can be seen in the **Table 4.7**.

Table 4.7 Comparison of the crystal structure extracted vs DFT simulated values for trans angles and bond lengths for **Cr-1** and **Cr-3**.

	$[Cr(BPI))_2)]PF_6$ **Cr-1**					
	X-ray			**DFT**		
	N_{py}-Cr-N_{py}	N_{ind}-Cr-N_{ind}	N_{py}-Cr-N_{py}	N_{py}-Cr-N_{py}	N_{ind}-Cr-N_{ind}	N_{py}-Cr-N_{py}
Trans angles (°)	173.5(2)	175.6(2)	172.8(2)	173.97	179.97	173.97
	Cr-N_{py}	**Cr-N_{ind}**	**Cr-N_{py}**	**Cr-N_{py}**	**Cr-N_{ind}**	**Cr-N_{py}**
Bond lengths (Å)	2.097(6)	1.993(6)	2.088(6)	2.140	2.010	2.140
	2.107(6)	1.986(6)	2.098(6)	2.140	2.010	2.140
	$[Cr(BPI-5-PhO)_2]PF_6$ **Cr-3**					
	X-ray			**DFT**		
	N_{py}-Cr-N_{py}	N_{ind}-Cr-N_{ind}	N_{py}-Cr-N_{py}	N_{py}-Cr-N_{py}	N_{ind}-Cr-N_{ind}	N_{py}-Cr-N_{py}
Trans angles (°)	174.69(2)	179.27(19)	176.52(2)	174.02	179.97	174.02
Bond lengths (Å)	**Cr-N_{py}**	**Cr-N_{ind}**	**Cr-N_{py}**	**Cr-N_{py}**	**Cr-N_{ind}**	**Cr-N_{py}**
	2.131(5)	2.018(5)	2.101(6)	2.142	2.010	2.138
	2.096(5)	1.963(5)	2.138(5)	2.138	2.010	2.142

It has been reported before that the DFT methods which describe complexes with more than one unpaired electron might lead to some limitations when computing interelectronic interactions. [34] In 2005, Atanasov suggested that utilising LFDFT (Ligand Field Density Functional Theory) can offer some advance when computing the interelectronic repulsion phenomenon with an atomic-like Racah parameter B utilised in the method.[35,36] This suggests that predicting d-d transitions for Cr(III) systems is challenging.

Moreover, Stepanovic reported that currently employed DFTB3 (Density Functional Tight Binding, third order variant, 2020) method presents large errors for metal-ligand bonding interactions, especially when charged ligands are considered such as the BPI ligands utilised in this chapter. [37]

Considering that the N_{ind}-Cr-N_{ind} trans angle for **Cr-1** and **Cr-3** were estimated to be the same, whilst the crystal structure data showed those angles to be different from each other, it suggests a similar case to that reported by Stepanovic.

Importantly, the errors between the experimental and optimized values for $[Cr(bpy)_2(4\text{-Me-phen})]^{3+}$ reported in **Section 3.3.7** were low enough ($\pm1°$) suggesting good accuracy of DFT calculations therefore suggesting that it is the ligand system utilised in this chapter that poses a challenge. As discussed in **Section 4.3.2**, and earlier on in this section, the Cr-N_{ind} bonds present increased covalency character which leads to decreased interelectronic repulsion facilitated via the π-accepting character of the BPI ligands. Considering that it is only the trans angles and bond lengths involving the Cr-N_{ind} bonds which are directly involved in the increased covalency character and lowered interelectronic repulsion phenomena that are incorrectly calculated herein, it is reasonable to assume that in this case, the chosen DFT method could not simulate the interelectronic interactions accurately.

4.3.6 Photophysical properties

The UV-Vis spectra for all ligands were recorded in aerated MeCN at room temperature using concentrations of 10^{-5} M. The bands in the 270-300 nm region are ascribed as $\pi\text{-}\pi^*$ transitions of the different aromatic rings as previously discussed in **Section 4.1.2**. The transitions observed between 300

and 415 nm are likely to be of charge transfer origin considering the large molar extinction coefficient values. It is possible that $n\text{-}\pi^*$ transitions are buried within the region. The highest energy bands around 200 nm are likely to be of $\pi\text{-}\pi^*$ origin. The strong vibronic structure of the bands within 300-415 nm are expected to be due to the extended conjugation of these rigid ligands (**Figure 4.20**).
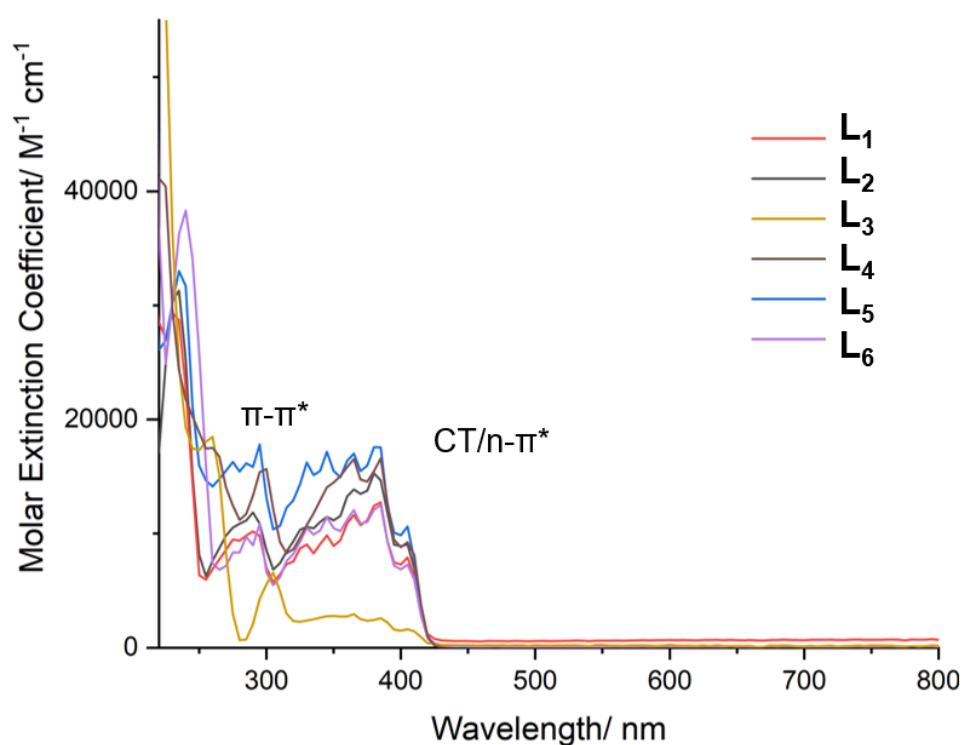
Figure 4.20 UV-Vis spectra of **L₁-L₆** recorded in MeCN at 10^{-5} M concentration.

As illustrated in **Figure 4.21**, a clear red-shift of the ligand-based absorption bands (270-300 nm bands in **Figure 4.20**) were observed in the UV-Vis spectra of the corresponding Cr(III) complexes (300-400 nm region in **Figure 4.21**). This suggests successful coordination of the isoindoline ligand as the electron density of the ligand is directed towards the Cr(III) centre therefore decreasing the energy of the transition.
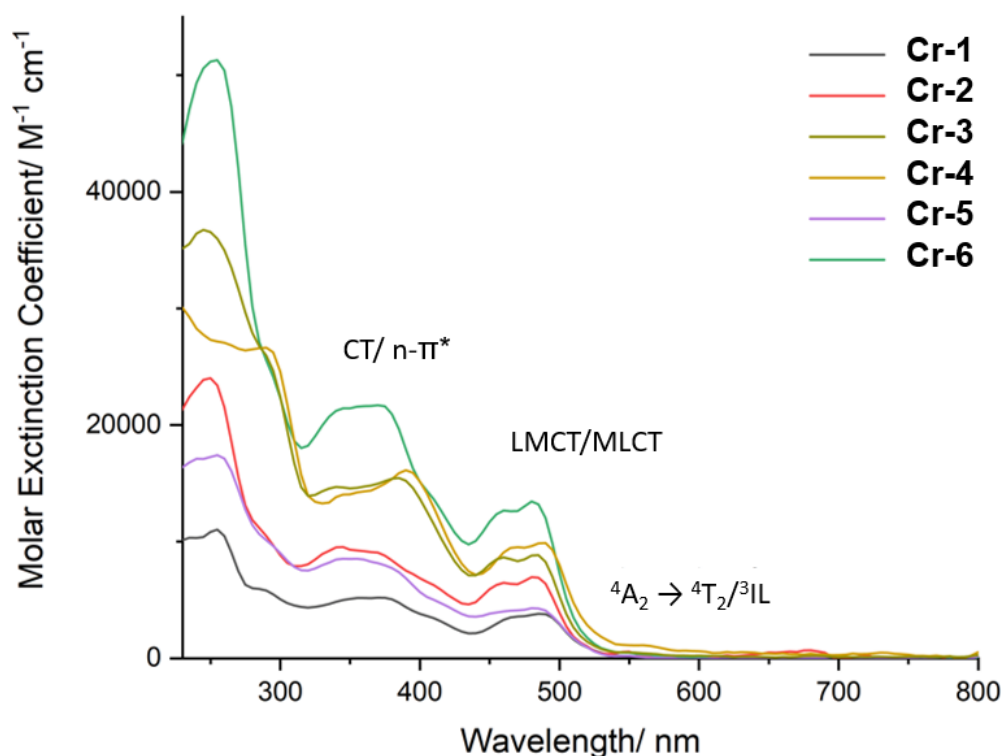
Figure 4.21 UV-Vis spectra of Cr(III) complexes **Cr-1** to **Cr-6** recorded at room temperature in deaerated MeCN at 10^{-5} M.

The bands observed between 450 and 550 nm are not present in the spectra recorded for the ligands and those transitions likely consist of ligand to metal (LMCT) or metal to ligand nature (MLCT). This is supported by Wenger and co-workers, wherein the $[Cr(dpc)_2]^+$ complex presents admixture of ^{2}LMCT and MLCT character bands around 450 nm.[5] The weak bands observed around 500-600 nm for complexes **Cr-1** to **Cr-6** are most likely red-shifted $^4A_2 \rightarrow {}^4T_2$, as previously demonstrated by Wenger for $[Cr(dpc)_2]^+$ (521 nm, $\mathcal{E}$=3000 M^{-1} cm^{-1}) or ^{3}IL transitions as discussed in **Section 3.3.6**. [5]

Given the spin forbidden nature of d-d transitions for $^4A_2$ to $^2T_1/^2T_2/^2E$, the UV-Vis bands are expected to be of very low intensity ($\varepsilon < 100$ M^{-1} cm^{-1}) and therefore concentrations around 10^{-3} M were used to investigate these bands (**Figure 4.22**).
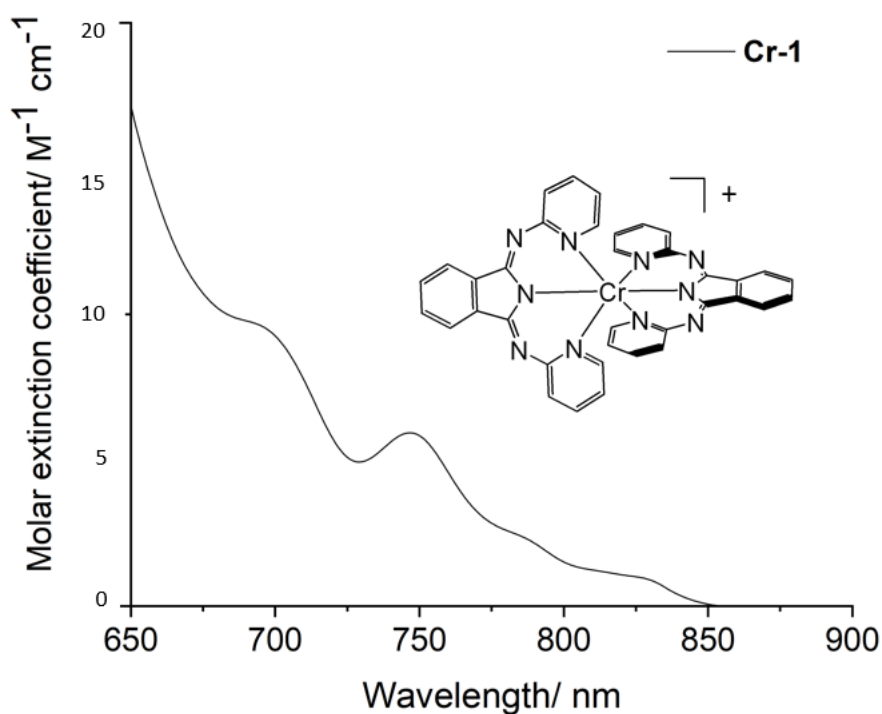
Figure 4.22 UV-Vis spectrum of concentrated **Cr-1** showing spin-forbidden d-d bands recorded in aerated MeCN.

When compared with the literature values reported for complexes of $[Cr(bpy)_3]^{3+}$ type (**Section 2.3.2**), it is clear that all d-d bands observed for this series are red-shifted (**Figure 4.22**). The same phenomenon was observed by Wenger and co-workers, for which they reported values of 690 (ε = 84 M^{-1} cm^{-1}) and 970 nm (ε = 6 M^{-1} cm^{-1}), for their $[Cr(dpc)_2]^+$, where the first band was assigned to have ^{2}LMCT character according to their TD-DFT calculations. The second band was suggested to represent a transition of spin-forbidden character of d-d origin. Due to the broad appearance, Wenger suggested the possibility of LMCT admixture to the spin-forbidden transition according to their computational analysis. Therefore, excited state admixture of doublet excited states (^{2}E/^{2}T$_1$) and doublet ligand-to-metal charge transfer (^{2}LMCT) cannot be ruled out for the isoindoline series reported herein. Especially considering the broad appearance of the bands observed.

Table 4.8 lists three transitions for **Cr-1** to **Cr-6** of very low intensity (ε < 20 M^{-1} cm^{-1}) which are ascribed to ^{2}E, ^{2}T$_1$ and ^{2}T$_2$ respectively, based on the literature

data on these type of transitions for $[Cr(bpy)_3]^{3+}$.[38] What is more, some spectra show additional bands observed above 800 nm with even lower molar extinction coefficient values. The identity of these bands is not known but their existence seems to be consistent with the excited state admixture theory. These additional bands are listed in the experimental section.

Table 4.8 Spin-forbidden d-d bands observed for complexes **Cr-1 to Cr-6** in aerated MeCN at 10^{-3} M. Values shown in brackets are the molar extinction coefficient values (in units of M^{-1} cm^{-1}).

Complexes	$^2E^a$ cm^{-1}	$^2T_1$ cm^{-1}	$^2T_2^b$ cm^{-1}
Cr-1	13 333 (4)	14 306 (8)	14 836 (9)
Cr-2	13 297 (2)	14 184 (5)	14 705 (8)
Cr-3	12 755 (6)	14 285 (8)	14 792 (11)
Cr-4	12 870 (10)	14 492 (12)	14 814 (15)
Cr-5	12 658 (4)	13 869 (5)	14 858 (8)
Cr-6	12 706 (8)	14 224 (9)	14 771 (14)

[a] 14,300 cm^{-1} for $[Cr(bpy)_3]^{3+}$; [b] 15,500 cm^{-1} for $[Cr(bpy)_3]^{3+}$

Table 4.9 Racah parameter (B) and nephelauxetic effect parameter (ζ) calculation and the calculated values for each step of the process.

Racah parameter calculations: ${}^4A_2 \rightarrow {}^2T_2$ is E_2, ${}^4A_2 \rightarrow {}^2E$ is E_1. Ratios of energies:

$$\frac{\frac{E_2}{B}}{\frac{E_1}{B}} = \frac{E_2}{E_1} = \frac{\Delta_{oct}}{B}$$

Complex	E_2/E_1	Δ_{oct}	B	ζ^a
Cr-1	1.11	3.00	689	0.75
Cr-2	1.11	3.00	683	0.74
Cr-3	1.16	4.20	654	0.71
Cr-4	1.15	4.05	659	0.71
Cr-5	1.17	4.45	647	0.70
Cr-6	1.16	4.20	653	0.71
$[Cr(phen)_3]^{3+}$			780[40]	0.85[40]
$[Cr(dpc)_2]^{3+}$			470[5]	0.52[5]

[a] $B(Cr(III)_{\text{free ion}}) = 918$ cm^{-1}.

The red-shifted values for the ${}^4A_2 \rightarrow {}^4T_2$ and d-d transitions are indicative of a lower energy regime for the series reported in this chapter in comparison with the $[Cr(bpy)_3]^{3+}$ type complexes (including the series reported in **Chapter 3**). Considering the π-accepting character of BPI ligands, the more covalent character of the Cr-N$_{ind}$ bond should result in some electron density of the Cr(III) centre being accepted into the non-bonding π orbitals of the coordinated BPI ligand and therefore decreasing the interelectronic repulsion between the d-electrons at the metal centre. As explicitly discussed in **Section 1.3.1**, interelectronic repulsion is measured by means of the nephelauxetic effect parameter (ζ), which is determined by the ratio of the Racah B parameters of the complex the free ion (**Section 3.1.3**) .[39]

All complexes listed in **Table 4.9** show an increased level of covalency across the Cr-N_{ind} bonds. When compared with the literature, for [Cr(phen)$_3$]$^{3+}$ the Racah parameter is 780 cm^{-1} and the nephelauxetic effect parameter is 0.85.[40] For [Cr(dpc)$_2$]$^{3+}$, the Racah parameter is defined to be approximately 470 cm^{-1} and the nephelauxetic effect parameter is 0.52.[5] The clearly shows the increased covalency of the Cr-N_{ind} bond for the complexes reported in this chapter. Although, it is not as pronounced as it is for [Cr(dpc)$_2$]$^{3+}$ which resulted in a stronger red-shift of the emission maxima (1067 nm at 77 K) than for the complexes reported in this chapter.

4.3.7 Luminescent properties

All luminescence measurements were performed in aerated MeCN at room temperature and all complexes were excited using 430 nm irradiation (**Figure 4.23**). All of the complexes show a main broad emission band in the 929-953 nm range with a tail extending to longer wavelengths (**Table 4.10**) as the first ever emission to be observed for Cr(III) complexes in this nm range at room temperature. This unusual, red-shifted emission was previously explained on the basis of [Cr(dpc)$_2$]$^+$. The emission signal around 1270 nm is due to photo-generated singlet oxygen and therefore in line with expectations for luminescence measurements in aerated solvents.[41] The broad appearance of the emission bands contrasts with previously reported sharp emission bands for [Cr(bpy)$_3$]$^{3+}$ complexes and those reported in **Section 3.3.6**. This could be due to excited state distortions likely to come from the ^{2}LMCT excited state admixtures reported previously by Wenger and Barbour.[5, 42]

Table 4.10 Photophysical properties of the complexes determined in this chapter. All measurements were recorded at room temperature in aerated MeCN.

Complex	Emission/ nm	τ/µs
Cr-1	948	4.5
Cr-2	929	8.1
Cr-3	953	4.1
Cr-4	929	5.1
Cr-5	860	5.9
Cr-6	925	7.0
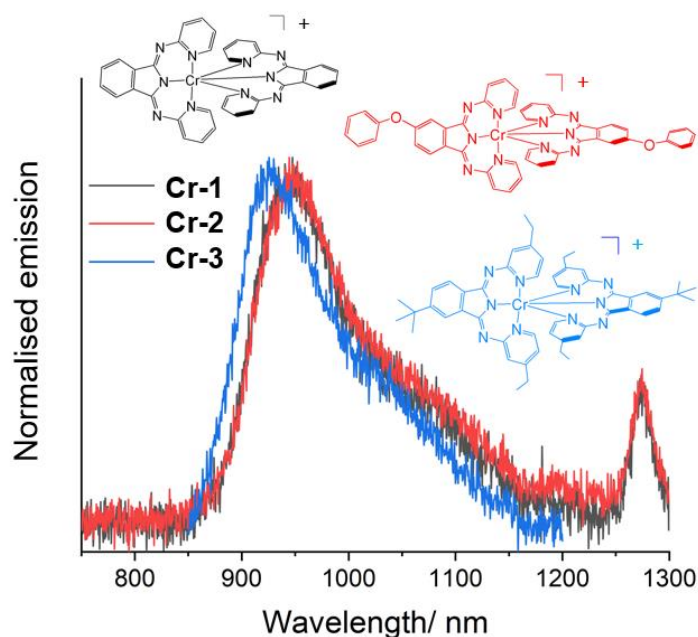
Figure 4.23 Emission spectra of complexes **Cr-1**, **Cr-4** and **Cr-6**.

The kinetic traces of the lifetimes were each fitted to a single exponential decay and values of 4.1-8.1 µs were obtained in aerated solvent at room temperature (**Table 4.10**). This is significantly lower than other six-membered Cr(III) chelates reported previously such as [Cr(ddpd)$_2$]^3 with the lifetime of 177 µs in aerated H$_2$O emit around 750 nm. More importantly, the lifetime values of

all complexes in this chapter are significantly higher than $[Cr(tpy)_2]^{3+}$ (0.14 μs, deaerated MeCN) and $[Cr(dpc)_2]^+$ (non-emissive at room temperature) which emit respectively in NIR-I (700-900 nm) and NIR-II region (> 900 nm).

4.3.8 EPR Spectroscopy results

In order to probe a transition, it is necessary to provide it with a frequency that matches its energy gap as outlined in **Section 1.6**. Therefore, it should be noted that for any high-spin system for which the *D*-value exceeds the operating frequency of the spectrometer, additional measurements at higher frequencies are required for all possible transitions to be probed.

As exemplified for complexes **Cr-1** to **Cr-4**, the X-band data of the neat solid appears very broad and featureless (**Figure 4.24**). Therefore, extraction of the ZFS parameters was not possible at this frequency and all complexes were measured at higher frequencies. Having learnt the complexity of spectra at X-band microwave frequency, complexes **Cr-5** and **Cr-6** were only measured at higher frequencies and are discussed later on in this section.
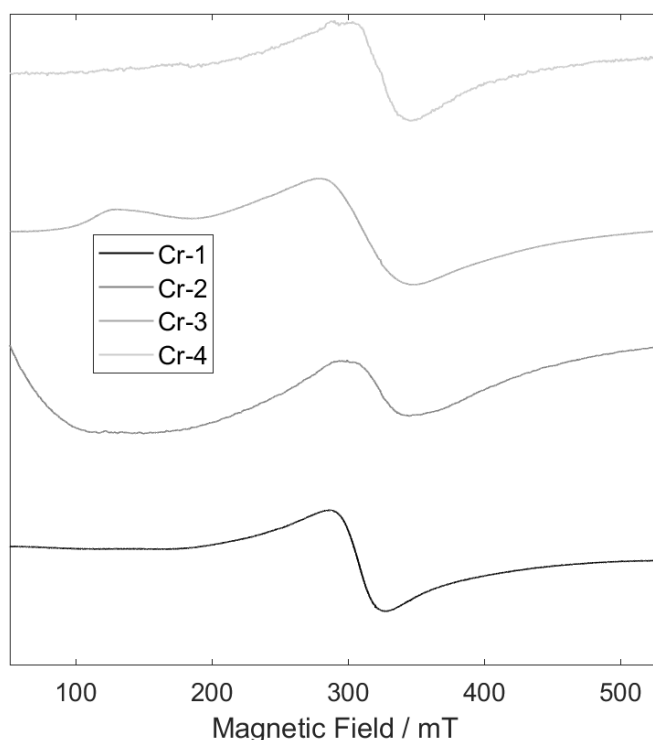

Figure 4.24 X-band EPR spectra stack **Cr-1** to **Cr-4** as neat solids recorded at 298 K.

As discussed in **Section 1.6.6**, for paramagnetic solids for which the ZFS character leads to complex and featureless spectra, doped solids are preferred and therefore complexes **Cr-1** to **Cr-6** were doped at 1% into their respective EPR silent Co(III) analogues (for structures refer to the Experimental **Section 4.6**) and were characterised using Q-band microwave frequency. As can be seen in **Figure 4.25**, although of better quality, the experimental spectra show significant level of broadening in the 1000-1200 mT region. Additionally, a satisfactory simulation of the three signals recorded between 1200-1300 mT could not be obtained. Further experiments at higher frequency (W-band) were therefore required to validate the ZFS parameters chosen to simulate the Q-band spectra. It is also worth noting that solids doped at 1% provided very weak signal intensities leading to signal artefacts of the empty cavity emerging of which the full extent is also presented in **Appendix 4**.
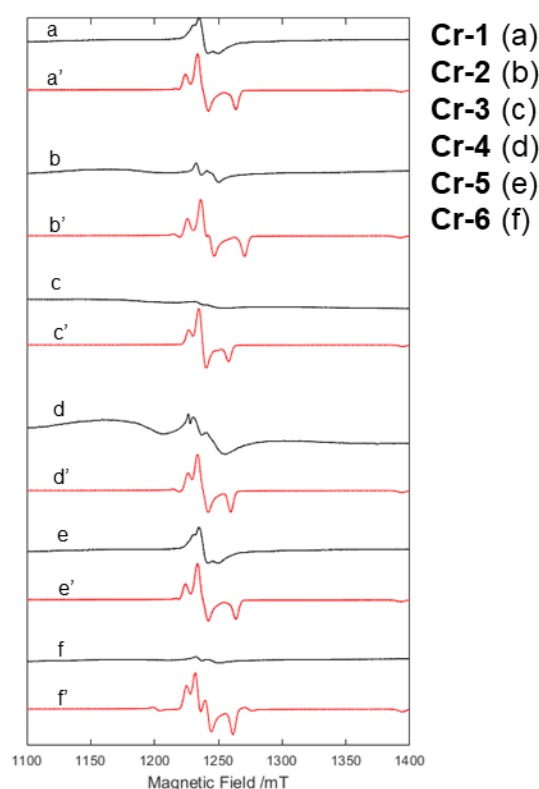

Figure 4.25 Experimental (a-f) and simulated (a`-f`) Q-band EPR spectra of **Cr-1** to **Cr-6** doped at 1% into their respective EPR silent **Co-1** to **Co-6** analogues.

As exemplified in **Figure 4.26** of W-band frequency spectrum recorded for **Cr-1** to **Cr-6** doped at 1% shows no broadening with the lines recorded in 3360-3400 mT region.
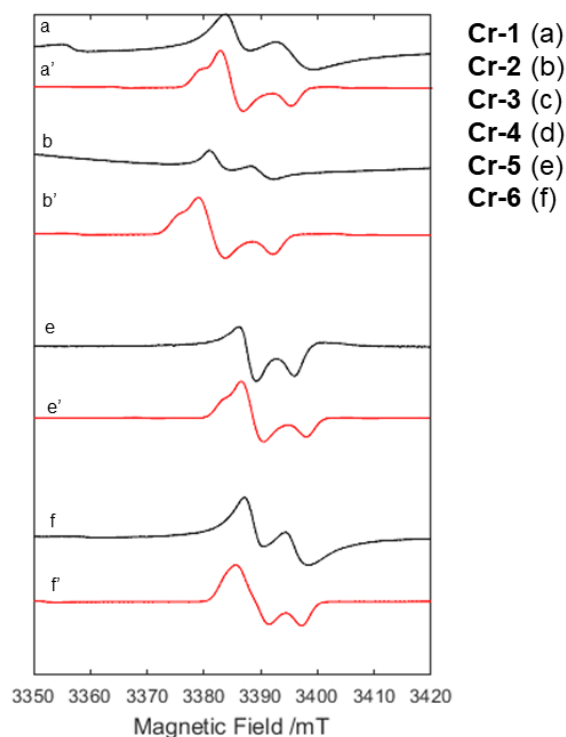

Figure 4.26 Experimental (a-b and e-f) and simulated (a`-b` and e`-f`) W-band EPR spectra (298 K) of **Cr-1**, **Cr-2** and **Cr-5**, **Cr-6** doped at 1% into their respective EPR silent **Co-1**, **Co-2** and **Co-5**, **Co-6** analogues.

The *D*-values are listed in this chapter for **Cr-1** to **Cr-6** complexes (0.1-0.116 cm^{-1}), show to be considerably lower than those of the polypyridyl series reported in **Chapter 3** 0.54-0.4 cm^{-1}; **Table 3.** This can be understood upon consideration of the structural geometry of the two series: the complexes in this chapter presented trans angles in the range of 173-176(2)° for **Cr-1** and 174-180(2)° for **Cr-3**. While no significant difference in trans angles was observed between **Cr-1** and the experimentally obtained trans angles of the [Cr(bpy)$_2$(4-Me-phen)]$^{3+}$ were in the range of 174(6)-176(7)°. While no significant difference in trans angles was observed between **Cr-1** and [Cr(bpy)$_2$(4-Me-phen)]$^{3+}$, comparison of the bond lengths provides some clarity. The bond lengths identified for [Cr(bpy)$_2$(4-Me-phen)]$^{3+}$ are in the range of 2.04-2.05 (16) Å, whilst **Cr-1** and **Cr-3** both showed bond lengths to be around 2.1 (5-6) Å for Cr-N$_{py}$

and around 2 (5-6) Å for Cr-N_{ind}. This suggests that the direct interaction of the N atoms and Cr metal centre are very different for complexes presented in this Chapter as opposed to the polypyridyl series. It is therefore expected that the D values are to be lower than those for the polypyridyl series due to the aforementioned covalent character of the Cr-N_{ind} bond and the resulting nephelauxetic effect. Interestingly, all complexes with 4-Et group incorporated within their pyridyl ring of the ligand core which is directly opposite to the coordination site seem the exhibit higher E/D values with respect to their matched pairs (unsubstituted pyridyl ring). For instance the E/D values for complexes **Cr-1** and **Cr-2** are 0.23 and 0.28 respectively. Similarly, **Cr-3** and **Cr-4** exhibit E/D values of 0.27 and 0.28 and the latter pair **Cr-5** and **Cr-6** present E/D values of 0.27 and 0.28. Naturally, this calls for correlation between the electron donating character of 4-Et group and an increase in the E value within this series.

All experimental D-values are listed in **Table 4.11** and are in the range 0.094-0.116 cm^{-1}; notably these are all slightly higher than the corresponding values predicted by DFT calculations in the range 0.082-0.136 cm^{-1}, with the notable exception of the crystal structure-based prediction for complex **Cr-1** (D = 0.136 cm^{-1}). Due to the higher D-value, the E/D values are in the range of 0.23-0.30 and somewhat lower than ORCA calculated values in the range of 0.29-0.33, again with the exception of the crystal structure-based calculation for complex **Cr-1** for which the calculated E/D value is 0.11. The D-value discrepancy of 500-700 MHz suggests that ORCA predicted ZFS parameters are overestimated by around 20 % further supporting the challenge of simulating interelectronic repulsion as discussed in **Section 4.3.8**.

Resolution of the fine structure in the experimental EPR spectra is required to obtain accurate values of the ZFS parameters. The fine structure originates from the splitting of a given multiplet in the absence of the magnetic field and is directly dependent on the magnitude of spin-orbit coupling. Unfortunately, even for the experimental measurements recorded at W-band frequency, resolution of the fine structure components for the solid samples was poor. Therefore, the discussion of the ZFS parameters should focus on the magnitude of the ZFS interaction rather than detailed comparison between

each of the complexes. Full sweep width measurements at helium temperature were attempted for **Cr-1** (**Figure 4.27**) and **Cr-2** and no complete `fine` structure was observed, therefore sweeping coils were used in the following experiments for the remaining complexes. The spectrum of **Cr-2** is available for the reader in **Appendix 4**.

Comparison of the experimental and calculated ZFS parameters show some discrepancy as discussed later in **Section 4.3.9**, furthermore the simulated traces for **Cr-1** and **Cr-2** show fine structure in regions of 3100-3350 mT and 3550-3650 mT which were not observed in the experimental spectrum. Evaluation of the accuracy of these simulations are therefore not possible as the full fine structure was not resolved. This potentially could be addressed by further measurements at lower temperatures (ca. 5 K) and/or using higher doping % of the EPR active Cr dopant.
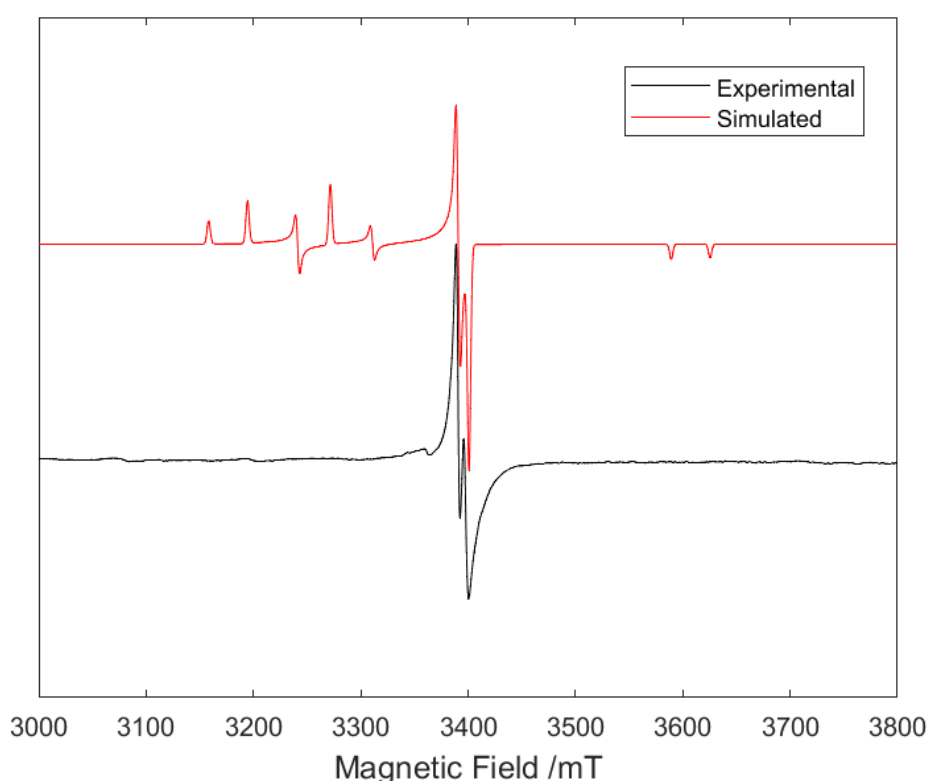

Figure 4.27 EPR spectrum of **Cr-1** doped at 1 % in **Co-1** recorded at W-band frequency at 20 K. $D = 0.108$ cm^{-1}, $E/D = 0.23$.

Comparison of the *D*-values between the polypyridyl series reported in **Chapter 3** and the series discussed in this chapter suggest a significant difference in the electronic behaviour. As discussed earlier, the *D*-values show a significant decrease in comparison with the series reported in **Chapter 3**. This is likely to be as a result of the increased covalent bonding between the Cr-N_{ind} atoms and a decreased interelectronic repulsion between the three unpaired electrons at the Cr(III) metal centre. Collectively, this shows a lower ZFS interaction between the unpaired electrons of Cr(III) centre for the isoindoline series.

As exemplified with experimentally obtained structures for **Cr-1** and **Cr-3**, it is likely that the nephelauxetic effect resulting from the increased covalency of the Cr-N_{ind} bond is responsible for lower ground state energy which correlates with decreased interelectronic repulsion of the three unpaired electrons at chromium centre which is likely to be observed via EPR in the form of lowered *D*-values. Therefore, it is reasonable to conclude that the increased covalency of the isoindoline Cr(III) complexes can be observed via EPR.

4.3.9 ORCA calculated spin Hamiltonian parameters

As discussed in the **Section 1.6.6**, multiple unpaired electrons can interact with each other and therefore transition metal complexes with $S > {}^1/_2$ will exhibit a zero-field interaction. In addition to this intrinsic character of an individual TM centre, when paramagnetic materials are measured in the solid state, it is crucial to recognise any additional spin-spin interactions that may be present within the bulk material and how these will impact on resulting experimental measurements and manifest spectral signatures.

All geometry optimisation calculations were carried out with Gaussian 09 package prior to running ORCA calculations in order to obtain ZFS parameters for this series of complexes. For ORCA calculations, the BLYP functional was used with the EPR-II basis set for all atoms, except for Cr for which QZVP was used. For the calculations of the spin-orbital coupling contributions (DSOC) the QRO (quasi-restricted orbital) method of was used in place of the standard cp method as previous literature reports had determined this to be the most accurate for Cr(III) ZFS parameters calculations.[43,44]

The ORCA calculations of the spin-Hamiltonian parameters are listed in **Table 4.11** for all complexes and indicate similar values across the series. It is noted that there is some discrepancy between the values for the unsubstituted (**Cr-1**) complex based on the crystal structure and geometry optimised coordinates, however there is much closer agreement for the substituted (i.e. **Cr-3**) substituted complex. The D-value for **Cr-1** complex appears slightly higher for the experimentally determined coordination of the solid-state crystal structure and the E/D value appears around three times smaller than the calculated values for geometry optimized DFT results used to obtain the ZFS parameters. While the D-values describe the ZFS interaction in the axial plane, the E-value represents the ZFS interaction within the equatorial plane (as the E-value represents the rhombicity of the zero-field parameter). The ZFS parameters derived from the experimental structure for the unsubstituted complex indicate that there is less delocalisation of the electron density across the equatorial plane than the substituted complexes. This could be supported by the electron donating nature of the substituents and increased π-accepting character of the substituted ligands leading to a decrease in interelectronic repulsion at the metal centre. This is further exemplified by the spin density models created from atomic coordinates obtained from the crystal structures **Cr-1** and **Cr-3** (**Figure 4.24**). It is noted that the spin density expands over the phenyl moiety of the isoindoline framework for **Cr-3** much more efficiently than for **Cr-1** (**Figure 4.24b** and **4.24a**, respectively; indicated with an asterisk). For comparison, electron density models for both complexes are shown in **Figure 4.24** (**4.24c** and **4.24d**, respectively), however it is obvious that no significant changes in electron density between the models can be noted. This leads to a conclusion that the general D-value decrease observed for the substituted complexes in comparison with the unsubstituted **Cr-1** complex is a result of a more prominent decrease in interelectronic repulsion at Cr(III) centre which correlates with electron-donating character of the substituents present.

Table 4.11 Spin-Hamiltonian ZFS parameters **Cr-1** to **Cr-6**.

Complex	*g*-value			*D* (cm^{-1})	*E/D*	*g*-value			*D* (cm^{-1})	*E/D*
	Calculated					**Experimental**				
Cr-1	1.98	1.99	1.99	0.0846	0.29					
Cr-1[a]	1.98	1.99	1.99	0.136	0.11	1.98	1.98	1.98	0.108	0.23
Cr-2	1.98	1.99	1.99	0.092	0.29	1.98	1.98	1.98	0.108	0.28
Cr-3	1.98	1.99	1.99	0.082	0.33					
Cr-3[a]	1.98	1.99	1.99	0.089	0.32	1.98	1.98	1.98	0.11	0.27
Cr-4	1.98	1.99	1.99	0.094	0.30	1.98	1.98	1.98	0.094	0.30
Cr-5	1.98	1.99	1.99	0.90	0.31	1.98	1.98	1.98	0.116	0.27
Cr-6	1.98	1.99	1.99	0.097	0.31	1.98	1.98	1.98	0.113	0.28

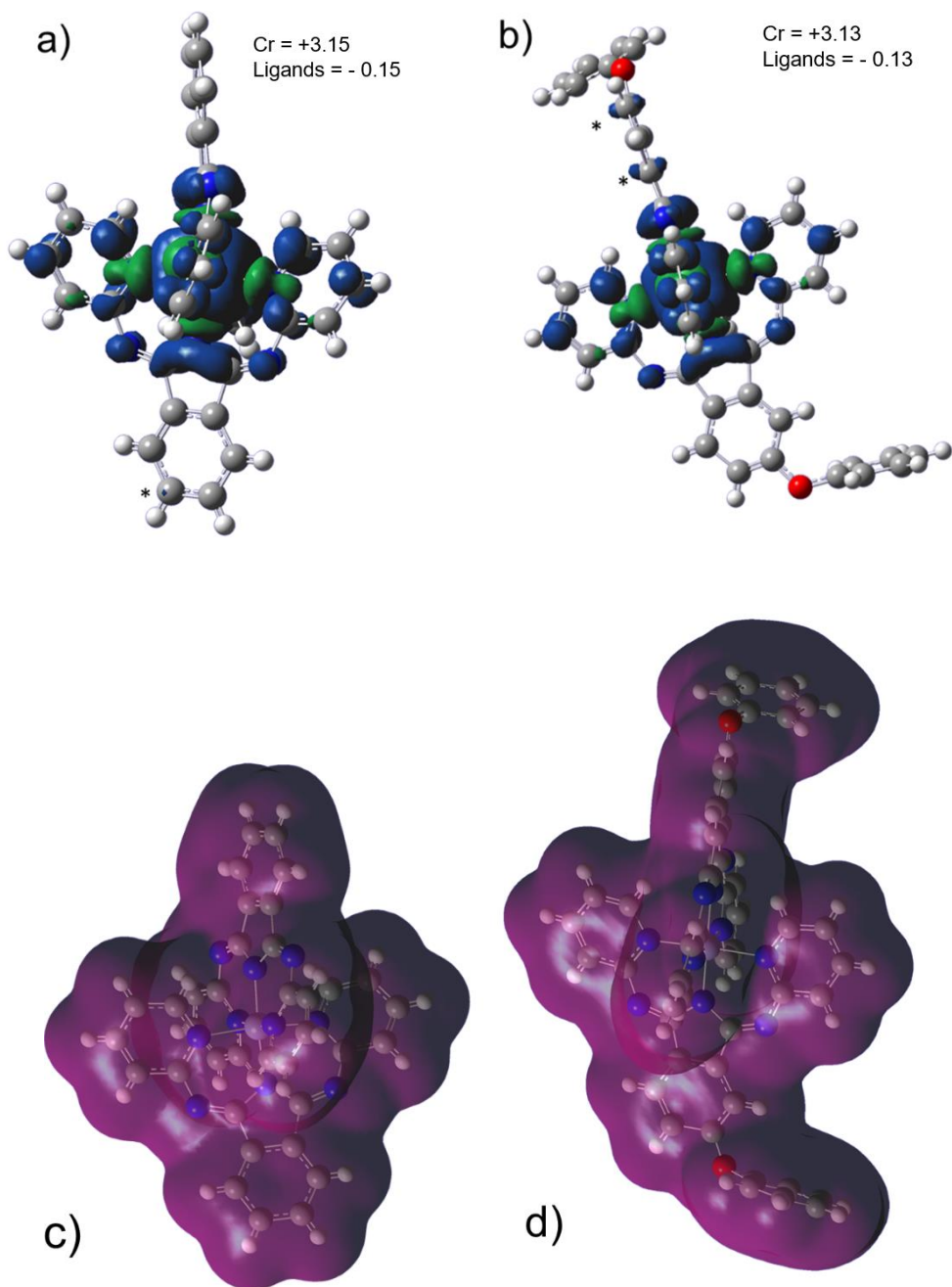[a] calculated using the crystal structure atomic coordinates; [b] 1 cm^{-1} = 29979 MHz

Figure 4.28 Top: spin density models for **Cr-1** (a) and **Cr-3** (b). Bottom: electron density models for **Cr-1** (a) and **Cr-3** (b). All models were obtained using *GaussView* software from the experimentally obtained structures. Blue = positive lobes, green = negative lobes.

4.4 Conclusion

To summarise, all ligands were synthesised from 2-aminopyridine and phthalonitrile derivatives in n-BuOH using catalytic amounts of $CaCl_2$ and were successfully characterised by NMR spectroscopy and mass spectroscopy. The yields obtained were 60-80%. A corresponding series of BPI Cr(III) complexes were synthesised using *mer*-Cr(Cr)$_3$(thf)$_3$ as the Cr(III) metal source and were obtained in satisfactory yields of 20-50%. The complexes were characterized utilising FT-FTIR, mass spectroscopy, EPR and luminescence spectroscopy. All complexes show emission in the NIR-II region with long lifetimes in the μs regime resulting from the nephelauxetic effect. This is supported with a nephelauxetic effect parameter of 0.75 placing the complexes in between the $[Cr(dpc)_2]^+$ reported by Wenger with a nephelauxetic effect parameter of 0.5-0.6 and $[Cr(phen)_3]^{3+}$ type complexes with the nephelauxetic effect parameter of around 0.85. and therefore, lowering of the ground state of Cr(III), where $[Cr(dpc)_2]^+$ shows unusual Cr-N bond covalency and $[Cr(phen)_3]^{3+}$ does not. This was also confirmed via EPR, where all complexes exhibited ZFS parameters significantly lower than those of the polypyridyl series reported in **Chapter 3** suggesting that the ZFS interaction at the paramagnetic Cr(III) metal centre is significantly reduced. This is in line with the work published by Wenger and co-workers on their $[Cr(dpc)_2]^+$ complex, however complexes **Cr-1** to **Cr-6** all show emission signals at room temperature in comparison with signal obtained only at 77 K by the Wenger group. Furthermore these results match the results obtained by the Cheng group, particularly for $[Cr(BPI)_2]^+$ which was also published by that group. Further to these results and the latest discovery by the Heinze group, where the bulky substituents increased the quantum yield values of the resulting complexes, it would be interesting to explore this idea with respect to the BPI complexes reported herein.

4.5 Experimental

All reactions were performed with the use of vacuum line and Schlenk techniques. Reagents were commercial grade and were used without further purification. ^{1}H and ^{13}C{H} NMR spectra were recorded on a Bruker Avance dpx 400, or Bruker Avance dpx 500 MHz spectrometer and were recorded in CDCl$_3$. ^{1}H and ^{13}C {^{1}H} NMR chemical shifts (δ) were determined relative to internal tetramethylsilane, Si(CH$_3$)$_4$ and are given in ppm. Low- and high-resolution mass spectra were obtained by the staff at Cardiff University. All photophysical data was obtained on a JobinYvon-Horiba Fluorolog-3 spectrometer fitted with a Hamamatsu R5509-73 detector. FTIR spectra were recorded using ATR equipped Shimadzu IRAffinity-1 spectrophotometer. UV-Vis data were recorded as solutions on a Perkin Elmer Lamda20 spectrophotometer. LC-MS analysis was conducted using a Waters Synapt G2 SI using a water/MeCN solvent gradient.

4.5.1 EPR Spectroscopy

Samples for EPR measurements were prepared in solvents, as listed in the discussion Section, under atmospheric conditions. The X-band EPR measurements were performed on a Bruker EMX spectrometer utilising an ER4119HS resonator, 100 kHz field modulation and 0.4 mT modulation depth at 140 K. EPR simulations were performed using the *Easyspin* toolbox within *Matlab*. [45]

4.5.2 DFT studies

Non-relativistic calculations of the fully relaxed geometries in the ground state and optimized excited state were performed on the Gaussian 09 program, and calculations of the spin Hamiltonian parameters were performed using ORCA (version 4.0.0.1).[46,47] Geometry optimisation calculations were computed using B3LYP functional and 6-311G(d, p) basis set for all atoms except Cr which was computed using LANL2DZ.[48] The chosen solvent was MeCN for all complexes.[49] TD-DFT calculations were computed using B3LYP functional and def2-SVP basis set with diffuse function and (d,p) accounting for polarisation

function.[50,51] ORCA calulations were computed using BLYP functional and QZVP basis sets produce results of ZFS parameters estimation using quasi-restricted orbitals (qro) method for calculating the spin-orbit coupling contributions.[74,52,53]

4.5.3 Synthesis

L-1

Phthalonitrile (0.334 g, 2.61 mmol), 2-aminopyridine (0.492 g, 5.23 mmol) and $CaCl_2$ (0.065 g, 0.582 mmol) were stirred in n-butanol for 48 at reflux. Upon cooling, yellow needle-like crystals were observed and subsequently filtered followed by washing with H_2O to afford pure product. (0.453 g, 58.1%). ^{1}H NMR (500 MHz, $CDCl_3$) δ_H 13.99 (s, 1H), 8.61 (ddd, $^3J_{HH}$ = 4.9, $^4J_{HH}$ = 2.0, $^5J_{HH}$ = 0.9 Hz, 2H), 8.11 – 8.04 (m, 2H), 7.76 (ddd, $^3J_{HH}$ = 8.1, $^4J_{HH}$ = 7.4, 2.0 Hz, 2H), 7.68 – 7.61 (m, 2H), 7.46 (dt, $^{3,}J_{HH}$ = 8.0, $^4J_{HH}$ = 1.0 Hz, 2H), 7.11 (ddd, $^{3,}J_{HH}$ = = 7.4, $^4J_{HH}$ = 4.9, $^5J_{HH}$ = 1.1 Hz, 2H); ^{13}C NMR (126 MHz, $CDCl_3$) δ_C 160.59, 153.87, 147.91, 138.19, 135.89, 131.79, 123.33, 122.71, 120.34; FTIR (solid, V_{max})/ cm^{-1}: w, 2980, 1628, 1581, 1570, 1456, 1458, 1377, 1259, 1221, 1144, 1097, 1036, 966, 767, 698 s, 524 s, 401; UV/Vis (MeCN): λ_{max} / nm (ε / M^{-1}cm^{-1}): 206 (138500), 209 sh (120500), 234 (333300), 285 (11100), 367 (6600) nm; LRMS (ESI+, CH_2Cl_2) [M+H]$^+$ m/z found 300.13, m/z calculated 300.1249 for $C_{18}H_{14}N_5$.

L-2

4-tert-butylphthalonitrile (0.463 g, 2.51 mmol), 2-aminopyridine (0.507 g, 5.39 mmol) and $CaCl_2$ (0.028 g, 0.248 mmol) were stirred in n-butanol under reflux for 48h. Upon cooling, n-butanol was removed *in vacuo* and the resulting oil was extracted with DCM/H_2O. Once combined, the organic layer was dried with $MgSO_4$ and reduced *in vacuo* to afford a bright yellow oil. (0.614 g, 68.8%). ^{1}H NMR (500 MHz, $CDCl_3$) δ_H 13.93 (s, 1H), 8.06 (ddd, $^3J_{HH}$ = 5.1, $^4J_{HH}$ = 2.0, $^5J_{HH}$ = 0.9 Hz, 2H), 7.80 (t, $^3J_{HH}$ = 1.3 Hz, $^4J_{HH}$ = 1H), 7.73 (d, $^3J_{HH}$ = 1.2 Hz, 2H), 7.41 (ddd, $^3J_{HH}$ = 8.2, $^4J_{HH}$ = 7.2, $^5J_{HH}$ = 1.9 Hz, 2H), 6.63 (ddd, $^3J_{HH}$ = = 7.2, $^4J_{HH}$ = 5.1, $^5J_{HH}$ = 1.0 Hz, 2H), 6.49 (dt, $^3J_{HH}$ = 8.3, $^4J_{HH}$ = 1.0 Hz, 2H), 1.35 (s, 9H). ^{13}C{^{1}H} NMR (126 MHz, $CDCl_3$) δ_C 158.49, 157.82, 148.25, 137.87, 133.49,

131.01, 130.51, 115.94, 115.85, 115.71, 114.16, 108.72, 77.41, 77.16, 76.91, 35.73, 30.82; FTIR (solid, V_{max})/ cm^{-1}: 3495 w, 3397 (N-H) w, 3217 w, 1620, 1597, 1568, 1487, 1441, 1319, 1261, 1221, 1151, 995, 879, 761, 682, 520 cm; UV/Vis (MeCN): λ_{max} / nm (ε / M^{-1}cm^{-1}): 211 (13200), 216 (73100), 240 (29400), 290 (10100), 380 (3900) nm; HRMS (ESI+, CH$_2$Cl$_2$) [M+H]$^+$ m/z found 356.1876, m/z calculated 356.1875 for C$_{22}$H$_{23}$N$_5$.

L-3

Phthalonitrile (0.323 g, 2.52 mmol), 4-ethylpyridin-2-amine (0.649 g, 5.31 mmol) and CaCl$_2$ (0.050 g, 0.450 mmol) were stirred in n-butanol under reflux for 48h.was added to n-butanol (5 mL). Upon cooling, yellow needle-like crystals were observed and subsequently filtered followed by washing with H$_2$O to afford pure product. (0.539 g, 60.8%).^{1}H NMR (500 MHz, CDCl$_3$) δ_H 13.99 (s, 1H), 8.49 (dd, $^3J_{HH}$ = 5.1, $^4J_{HH}$ = 0.7 Hz, 2H), 8.07 (dd, $^3J_{HH}$ = 5.6, $^4J_{HH}$ = 3.1 Hz, 2H), 7.64 (dd, $^3J_{HH}$ = 5.6, $^4J_{HH}$ = 3.1 Hz, 2H), 7.35 – 7.29 (m, 2H), 7.00 – 6.94 (m, 2H), 2.70 (q, $^3J_{HH}$ = 7.6 Hz, 4H), 1.30 (t, $^3J_{HH}$ = 7.6 Hz, 6H). ^{13}C{1H} NMR (126 MHz, CDCl$_3$) δ_C 160.66, 155.43, 153.87, 147.74, 135.92, 133.72, 133.25, 131.73, 122.65, 122.49, 120.42, 28.37, 14.47; FTIR (solid, V_{max})/ cm^{-1}: 3240 (N-H) w, 1647, 1628, 1589, 1582, 1466, 1452,1406, 1302, 1244, 1101, 1042, 893, 841, 777, 691, 457, 419 cm; UV/Vis (MeCN): λ_{max}/nm (ε / M^{-1}cm^{-1}) : 210 sh (37400), 234 (39600), 285 (22700), 364 (23600) nm; HRMS (ESI+, CH$_2$Cl$_2$) [M+H]$^+$ m/z found 356.1874, m/z calculated 356.1875 for C$_{22}$H$_{23}$N$_5$.

L-4

4-phenoxyphthalonitrile (0.367 g, 1.66 mmol), 2-aminopyridine (0.313 g, 3.32 mmol) and CaCl$_2$ (0.020 mg, 0.18 mmol) were stirred in n-butanol for 48 h at reflux. Upon cooling, yellow needle-like crystals were observed and subsequently filtered followed by washing with H$_2$O to afford pure product. (0.426 g, 66 %). ^{1}H NMR (500 MHz, CDCl$_3$) δ_H 13.86 (s, 1H), 8.59 – 8.46 (m, 2H), 7.95 (dd, $^3J_{HH}$ = 8.3, $^4J_{HH}$ = 0.5 Hz, 1H), 7.77 – 7.60 (m, 1H), 7.53 (dd, $^3J_{HH}$ = 2.3, $^4J_{HH}$ = 0.5 Hz, 1H), 7.43 – 7.27 (m, 3H), 7.21 (dd, 3H), 7.18 – 7.11 (m, 1H), 7.09 – 7.01 (m, 4H). ^{13}C NMR (126 MHz, CDCl$_3$) δ_C 161.83, 160.22, 156.60, 156.03, 147.77, 137.20, 126.86, 124.46, 121.92, 120.66, 120.02,

117.68, 115.40, 114.59, 112.27, 108.30. FTIR (solid, V_{max})/ cm^{-1} : 3202 (N-H), 3107, 3080, 3063, 3040, 2231, 1625, 1606, 1578, 1559, 1552, 1534, 1507, 1484, 1456, 1447, 1429, 1399, 1375, 1367, 1305, 1259, 1248, 1219, 1205, 1191, 1181, 1165, 1165, 1142, 1099, 1081, 1043, 993, 853, 793, 739, 669. UV/Vis (MeCN): λ_{max} / nm (ε / M^{-1}cm^{-1}): 259 (17400), 298 (15500), 345 (14000), 364 (16800), 385 (16500), 405 (9200). HRMS (ESI+, MeOH) [M+H]$^+$ m/z found 391.1433, m/z calculated 391.1511 for $C_{24}H_{18}N_5O$.

L-5

4-phenoxyphthalonitrile (0.367 g, 1.66 mmol), 4-ethylpyridin-2-amine (0.407 g, 3.33 mmol) and $CaCl_2$ (0.020 mg, 0.18 mmol) were stirred in n-butanol for 48 h at reflux. Upon cooling, yellow needle-like crystals were observed and subsequently filtered followed by washing with H_2O to afford pure product. (0.289 g, 39.4 %). ^{1}H NMR (500 MHz, CDCl$_3$) δ_H 13.86 (s, 1H), 8.56 – 8.51 (m, 2H), 7.96 (dd, $^{3,4}J_{HH}$ = 8.3 Hz, 1H), 7.68 (dddd, $^3J_{HH}$ = 9.4, $^3J_{HH}$ = 8.0, $^4J_{HH}$ = 7.3, $^5J_{HH}$ = 2.0 Hz, 2H), 7.54 (ddd, $^3J_{HH}$ = 2.3, $^4J_{HH}$ = 0.5 Hz, 1H), 7.40 – 7.30 (m, 5H), 7.22 (dd, $^3J_{HH}$ = 8.1, $^4J_{HH}$ = 2.25, 1H), 7.16 – 7.12 (m, 1H), 7.09 – 7.01 (m, 4H), 3.42 (s, 4H), 1.18 (s, 6H). ^{13}C NMR (126 MHz, CDCl$_3$) δ_C 161.25, 156.07, 147.82, 147.77, 138.03, 137.99, 130.11, 124.49, 123.11, 122.96, 121.86, 120.28, 119.86, 111.32, 93.92, 51.46, 50.75, 30.87. FTIR (solid, V_{max})/ cm^{-1} : 2233, 1606, 1582, 1561, 1496, 1490, 1475, 1457, 1452, 1421, 1406, 1285, 1274, 1249, 1201, 1165, 1153, 1085, 1069, 1021, 1003, 950, 916, 870, 846, 826, 818, 784, 722, 712, 694. UV/Vis (MeCN): λ_{max} / nm (ε / M^{-1}cm^{-1}): 259 (18600), 306 (6500), 342 (2900), 364 (3100), 385 (3000), 408 (1500).

L-6

5-tert-butyl-phthalonitrile (0.305 g, 1.66 mmol), 4-ethylpyridin-2-amine (0.407 g, 3.33 mmol) and $CaCl_2$ (0.020 g, 0.18 mmol) were stirred in n-butanol for 48 h at reflux. The solvent was then concentrated upon cooling and the product was purified with DCM column chromatography being the second eluent (0.253 g, 37 %). ^{1}H NMR (300 MHz, (CD$_3$)$_2$CO) δ_H 13.81 (s, 1H), 8.41 (s, 2H), 8.15 (d, $^3J_{HH}$ = 8.0 Hz, 2H), 7.92 (dd, $^{3,4}J_{HHH}$ = 8.1, 1.7 Hz, 4H), 7.77 (dd, $^3J_{HH}$ = 6.5, $^4J_{HH}$ = 4.5 Hz, 4H), 7.27 (d, $^3J_{HH}$ = 5.9 Hz, 4H), 6.17 (dt, $^3J_{HH}$ = 6.6, $^4J_{HH}$ = 1.8

Hz, 2H), 1.92 (qd, $^3J_{HH}$ = 7.5, $^4J_{HH}$ = 1.4 Hz, 4H), 1.33 (s, 18H), 1.15 (td, $^3J_{HH}$ = 7.6, $^3J_{HH}$ = 1.6 Hz, 6H). ^{13}C NMR (126 MHz, (CD$_3$)$_2$CO) δ_C 160.14, 157.84, 155.70, 155.42, 149.22, 128.82, 122.31, 122.13, 118.89, 115.85, 115.70, 115.27, 112.47, 35.39, 30.74, 27.78, 13.92. FTIR (solid, V$_{max}$)/ cm^{-1}: 1641, 1620, 1605, 1576, 1561, 1550, 1508, 1464, 1455, 1426, 1399, 1388, 1373, 1362, 1303, 1258, 1247, 1216, 1199, 1179, 1164, 1140, 1096, 1090, 1041, 1031, 1007, 998, 991. UV/Vis (MeCN): λ$_{max}$ / nm (ε / M^{-1}cm^{-1}): 240 (38300), 275 (8400), 285 (9700), 294 (11100), 314 (7600), 330 (10700), 344 (11500), 365 (12000), 384 (12300), 405 (7400). HRMS (ESI+, MeOH) [M]$^+$ m/z found 412.2506, m/z calculated 412.5610 for C$_{26}$H$_{30}$N$_5$.

L-7

Phthalonitrile (0.323 g, 2.52 mmol), 6-Mepyridin-2-amine (0.544 g, 5.04 mmol) and CaCl$_2$ (0.027 g, 0.18 mmol) were stirred in n-butanol for 48 h at reflux. The solvent was then concentrated upon cooling and the product was purified with DCM column chromatography being the second eluent delivering yellow needle like crystals upon evaporation (0.388 g, 48 %). ^{1}H NMR (500 MHz, CDCl$_3$) δ_H 12.56 (s, 1H), 8.04 (dd, $^3J_{HH}$ = 5.6, $^4J_{HH}$ = 3.1 Hz, 2H), 7.88 – 7.67 (m, 2H), 7.63 (dd, $^3J_{HH}$ = 5.6, $^4J_{HH}$ = 3.0 Hz, 2H), 7.06 – 6.90 (m, 2H), 6.86 – 6.70 (m, 2H), 2.33 (t, 6H). ^{13}C NMR (126 MHz, CDCl$_3$) δ_C 159.81, 157.04, 153.03, 138.43, 135.35, 132.16, 131.83, 122.73, 120.72, 119.71, 118.44, 24.70. FTIR (solid, V$_{max}$)/ cm^{-1} : 3332 (N-H), 2965, 2928, 1627, 1581, 1551, 1466, 1440, 1414, 1375, 1292, 1265, 1243, 1210, 1153, 1090, 1035, 983, 950, 918, 813, 767, 702, 650. UV/Vis (MeCN): λ$_{max}$ / nm (ε / M^{-1}cm^{-1}): 233 (32000), 275 (16200), 300 (12200), 329 (15200), 348 (17000), 364 (16500), 386 (138900), 414 (5400) sh.

L-8

Phthalonitrile (0.323 g, 2.52 mmol), 4,6-Mepyridine-2-amine (0.614 g, 5.04 mmol) and CaCl$_2$ (0.027 g, 0.18 mmol) were stirred in n-butanol for 48 h at reflux. The solvent was then concentrated upon cooling and the product was purified with DCM column chromatography being the second eluent (0.578 g, 64.4 %). ^{1}H NMR (500 MHz, CDCl$_3$) δ_H 12.50 (s, 1H), 8.01 – 7.94 (m, 1H), 7.81 – 7.65 (m, 1H), 7.61 – 7.53 (m, 1H), 6.94 (dt, $^3J_{HH}$ = = 1.5, $^4J_{HH}$ = 0.7 Hz, 1H),

6.73 – 6.70 (m, 1H), 2.40 (s, 3H), 2.29 – 2.25 (m, 4H). ^{13}C NMR (75 MHz, CDCl$_3$) δ$_C$ 156.82, 138.49, 131.73, 122.58, 120.02, 116.04, 115.31, 114.83, 28.89, 14.76. FTIR (solid, V$_{max}$)/ cm^{-1} : 3322 (N-H), 2953, 2916, 1640, 1541, 1466, 1438, 1401, 1369, 1293, 1264, 1245, 1210, 1147, 1097, 1033, 994, 949, 838, 705, 661. UV/Vis (MeCN): λ$_{max}$ / nm (ε / M^{-1}cm^{-1}): 233 (26500), 278 (10000), 303 (9400), 328 (13400), 347 (14700), 363 (15100), 387 (14000), 412 (6900) sh.

L-9

(0.323 g, 2.52 mmol), 6-ethylpyridin-2-amine (0.614 g, 5.04 mmol) and CaCl$_2$ (0.027 g, 0.18 mmol) were stirred in n-butanol for 48 at reflux. The solvent was then concentrated upon cooling and the product was purified with DCM column chromatography being the second eluent (0.500 g, 56 %). ^{1}H NMR (500 MHz, CDCl$_3$) δ$_H$ 7.99 (dd, $^3J_{HH}$ = 5.7, $^4J_{HH}$ = 3.0 Hz, 1H), 7.63 – 7.55 (m, 2H), 7.07 (dd, $^3J_{HH}$ = 7.9, $^4J_{HH}$ = 1.0 Hz, 1H), 6.91 – 6.86 (m, 1H), 2.66 (q, $^3J_{HH}$ = 7.6 Hz, 2H), 1.09 (td, $^3J_{HH}$ = 7.6, $^4J_{HH}$ = 0.6 Hz, 3H). ^{13}C NMR (126 MHz, CDCl$_3$) δ$_C$ 157.05, 153.05, 138.44, 135.36, 131.84, 122.73, 119.71, 118.43, 30.94, 24.70. FTIR (solid, V$_{max}$)/ cm^{-1} : 3342 (N-H), 2952, 2918, 1639, 1559, 1466, 1444, 1405, 1372, 1290, 1253, 1237, 1209, 1147, 1095, 1047, 991, 951, 841, 718, 633. UV/Vis (MeCN): λ$_{max}$ / nm (ε / M^{-1}cm^{-1}): 236 (44500), 275 (28900), 303 (21900), 332 (22500), 346 (23900), 366 (25600), 385 (24000), 413 (10900). HRMS (ESI+, MeOH) [M+H]$^+$ m/z found 356.1885, m/z calculated 356.1875 for C$_{22}$H$_{22}$N$_5$.

Cr-1

Di(pyridin-2-yl)isoindoline-1,3-diimine (0.295 g, 0.988 mmol) and CrCl$_3$(THF)$_3$ (0.185 g, 0.494 mmol) were stirred under reflux in dry ethanol for 24h. Upon cooling, the dark brown solution was filtered to obtain a brown precipitate and red-brown filtrate. NH$_4$PF$_6$ was added in excess to the red-brown ethanol solution resulting in red-brown precipitate which was subsequently filtered and washed with diethyl ether. (0.432 g, 19%). FTIR (solid, V$_{max}$)/ cm^{-1} : 3344 w, 1645, 1578, 1533, 1468, 1433, 1285, 1196, 1089, 835 (PF$_6$), 773, 718, 557 (PF$_6$), 518 cm^{-1}; UV/Vis (MeCN): λ$_{max}$ / nm (ε / M^{-1}cm^{-1}): 234 (18700), 256

(13800), 293 sh (4400), 320 sh (7000), 354 sh (8300), 380 (8300), 412 sh (5500), 464 (5700), 490 (6200), 607 (90), 699 (10), 750 (6), 825 (1) nm. ; HRMS (ESI+, MeOH) [M]$^+$ m/z found 648.1610, m/z calculated 648.1590 for $C_{36}H_{24}N_{10}{}^{52}Cr^+$.

Cr-2

Di(pyridin-2-yl)-5-tBu-isoindoline-1,3-diimine) (0.614 g, 1.728 mmol) and CrCl$_3$(THF)$_3$ (0.278 g, 0.743 mmol) were stirred under reflux in dry ethanol for 24h. Upon cooling, white precipitate and green filtrate were obtained. Subsequently NH$_4$PF$_6$ was added to the green solution resulting in precipitation of a green solid which was filtered to obtain the pure product. (0.153 g, 27%). FTIR (solid, V$_{max}$)/ cm^{-1} : 3339 w, 3084 w, 1672, 1638, 1429, 822 (PF$_6$), 555 (PF6) cm^{-1}; UV/Vis (MeCN): λ_{max} / nm (ε / M^{-1}cm^{-1}): 235 (15700), 290 (8800), 364 (00, 458 (4400), 670 (8), 721 (5),790 (4). ; HRMS (ESI+, C$_2$H$_5$OH) [M]$^+$ m/z found 760.2842, m/z calculated 760.2842 for $C_{44}H_{40}N_{10}{}^{52}Cr^+$.

Cr-3

Di(4-ethyl-pyridin-2-yl)-5-tBu-isoindoline-1,3-diimine) (0.2 g, 0.49 mmol) and CrCl$_3$(THF)$_3$ (0.090 g, 0.24 mmol) were stirred under reflux in dry ethanol for 24h. Upon cooling, white precipitate and green filtrate were obtained. Subsequently NH$_4$PF$_6$ was added to the green solution resulting in precipitation of a red solid which was filtered to obtain the pure product (0.06 g, 28 %). FTIR (solid, V$_{max}$)/ cm^{-1} : 3336, 2990, 2916, 1649, 1606, 1519, 1448, 1425, 1329, 1240, 1159, 1079, 1030, 829, 725, 688, 533. UV/Vis (MeCN): λ_{max} / nm (ε / M^{-1}cm^{-1}): 253 (51300), 296 (24300), 343 (21500), 376 (21700), 415 (13000), 458 (12700), 483 (13500), 551 (300), 677 (14), 700 (9), 800 (8) nm. HRMS (ESI+, MeOH) [M+CH$_3$]$^+$ m/z found 886.4286, m/z calculated 886.4251 for $C_{52}H_{56}N_{10}{}^{52}Cr^+$.

Cr-4

Di(4-ethylpyridin-2-yl)isoindoline-1,3-diimine (0.501 g, 1.410 mmol) and CrCl$_3$(THF)$_3$ (0.254 g, 0.678 mmol) were stirred in dry ethanol for 24h under reflux. The red-brown solution was filtered under vacuum upon cooling.

Subsequently, NH$_4$PF$_6$ was added to the filtrate resulting in a precipitation of a red-brown solid which was filtered and washed with diethyl ether to obtain a pure product (0.612 g, 59%). FTIR (solid, V$_{max}$)/ cm^{-1}: 3395 w, 2986 s, 1724, 1630, 1582, 1522, 1474, 1416, 1381, 1298, 1190, 1084, 833 s (PF$_6$), 718, 555 s (PF$_6$) cm^{-1}; UV/Vis (MeCN): λ$_{max}$ / nm (ε / M^{-1}cm^{-1}): 242 (28300), 282 (17400), 335 (10200), 353 (9400), 377 (8300), 411 (6800), 459 (6200), 483 (6100), 752 (9), 840 (9) nm. HRMS (ESI+, MeOH) [M]$^+$ m/z found 760.2845, m/z calculated 760.2842 for C$_{44}$H$_{40}$N$_{10}$^{52}Cr$^+$.

Cr-5

4-phenoxy-di(pyridin-2-yl)isoindoline-1,3-diimine (0.070 g, 0.179 mmol) and CrCl$_3$(THF)$_3$ (0.033 g, 0.088 mmol) were stirred in dry ethanol at reflux for 24h. Upon cooling, the dark brown solution was filtered to obtain a brown precipitate and red-brown filtrate. NH$_4$PF$_6$ was added in excess to the red-brown ethanol solution resulting in red-brown precipitate which was subsequently filtered and washed with diethyl ether (0.042 g, 59%). FTIR (solid, V$_{max}$)/ cm^{-1}: 3338, 2991, 2912, 1658, 1607, 1576, 1530, 1477, 1455, 1427, 1278, 1225, 1181, 1158, 1114,1098, 1060, 1004, 836, 784, 756, 749, 731, 695, 519. UV-Vis (MeCN) λmax (ε, M^{-1}cm^{-1}): 232 (29500), 262 (26900), 292 (26800), 342 (14100) sh, 391 (16100), 464 (9500), 489 (10200), 564 (1200), 632 (530), 676 (10), 700 (8), 784 (6) nm. HRMS (ES+, MeOH) [M]$^+$ m/z found 832.2130, m/z calculated 832.2115 for C$_{48}$H$_{32}$N$_{10}$^{52}Cr$^+$.

Cr-6

4-phenoxy-di(4-ethylpyridin-2-yl)isoindoline-1,3-diimine (0.2 g, 0.447 mmol) and CrCl$_3$(THF)$_3$ (0.090 g, 0.24 mmol) were stirred in dry ethanol at reflux for 24h. Upon cooling, the dark brown solution was filtered to obtain a brown precipitate and red-brown filtrate. No precipitate was observed upon addition of NH$_4$PF$_6$, therefore the solvent was removed followed by DCM/H$_2$O extraction to obtain a dark brown oil that crystallized over time (0.070 g 34%). FTIR (solid, V$_{max}$)/ cm^{-1}: 1576, 1548, 1530, 1477, 1455, 1427, 1355, 1319, 1278, 1262, 1225, 1194, 1181, 1114, 1098, 1060, 1023, 1004, 950, 883, 872, 836, 784, 756, 749, 731, 695, 675, 652, 527 UV-Vis (MeCN) λmax (ε, M^{-1}cm^{-1}): 247 (36600),293 (25600) sh, 339 (14800), 385 (15300), 457 (8600), 485 (8700),

552 (500), 700 (4), 700 (15), 710 (12) nm. HRMS (ESI+, C_2H_5OH) [M+H]$^+$ m/z found 945.3438, m/z calculated 945.3445 for $C_{56}H_{49}N_{10}{}^{52}Cr$.

Co-1

$CoCl_2$ (0.018 g, 0.15 mmol) was dissolved in MeOH and bis(di(pyridin-2-yl)isoindoline-1,3-diimine (0.1 g, 0.33 mmol) was subsequently added. The solution was stirred for 24h at room temperature resulting in dark red-brown coloured precipitate. Once filtered, the precipitate was suspended in H_2O (5 mL) and 5 drops of Br_2 previously diluted in 1 mL of H_2O were added dropwise to the solution which was left to stir for 24 h. Subtle darkening of the precipitate was observed upon complete evaporation/reaction of Br_2. Followed by filtering of the precipitate, it was then dissolved in minimal amounts of MeOH and $NH_4PF_{6\ (aq)}$ was added in excess to afford a brown precipitate (lighter in colour than its precessor). Upon filtration, the solid was dried in the oven for 24h. (0.2 g, 20 %) ^{1}H NMR (300 MHz, CDCl$_3$) δ$_H$ 8.12 (dd, $^3J_{HH}$ = 5.5, $^4J_{HH}$ = 3.0 Hz, 2H), 7.75 (dd, $^3J_{HH}$ = 5.6, $^4J_{HH}$ = 3.1 Hz, 2H), 7.70 – 7.62 (m, 2H), 7.55 (dd, $^3J_{HH}$ = 6.3, $^4J_{HH}$ = 1.6 Hz, 2H), 7.25 (dd, $^3J_{HH}$ = 8.0, $^4J_{HH}$ = 1.7 Hz, 2H), 6.85 – 6.74 (m, 2H). ^{13}C{1H} NMR* could not be obtained across 75-125 MHz range of frequencies available within the facility. FTIR (solid, V$_{max}$)/ cm^{-1}: 3326, 2956, 2924, 1633, 1571, 1445, 1426, 1377, 1292, 1274, 1224, 1182, 1157, 1092, 1012, 819, 740, 691. HRMS (ESI+, MeOH) [M+H]$^+$ m/z found 655.1371, m/z calculated 655.1517 for $C_{36}H_{24}CoN_{10}{}^+$.

Co-2

$CoCl_2$ (0.018 g, 0.15 mmol) was dissolved in MeOH and Di(pyridin-2-yl)-5-tBu-isoindoline-1,3-diimine) (0.117 g, 0.33 mmol) was subsequently added. The solution was stirred for 24h at room temperature resulting in dark red-brown coloured precipitate. Once filtered, the precipitate was suspended in H_2O (5 mL) and 5 drops of Br_2 previously diluted in 1 mL of H_2O were added dropwise to the solution which was left to stir for 24 h. Subtle darkening of the precipitate was observed upon complete evaporation/reaction of Br_2. Followed by filtering of the precipitate, it was then dissolved in minimal amounts of MeOH and $NH_4PF_{6\ (aq)}$ was added in excess to afford a brown precipitate (lighter in colour than its precessor). Upon filtration, the solid was dried in the oven for 24h. (0.25

g, 25 %). FTIR (solid, V_{max})/ cm^{-1} : 3337, 2971, 2931, 1635, 1569, 1458, 1417, 1381, 1251, 1152, 1072, 1008, 821, 736, 685.

Co-3

$CoCl_2$ (0.018 g, 0.15 mmol) was dissolved in MeOH and Di(4-ethyl-pyridin-2-yl)-5-tBu-isoindoline-1,3-diimine) (0.136 g, 0.33 mmol) was subsequently added. The solution was stirred for 24h at room temperature resulting in dark red-brown coloured precipitate. Once filtered, the precipitate was suspended in H_2O (5 mL) and 5 drops of Br_2 previously diluted in 1 mL of H_2O were added dropwise to the solution which was left to stir for 24 h. Subtle darkening of the precipitate was observed upon complete evaporation/reaction of Br_2. Followed by filtering of the precipitate, it was then dissolved in minimal amounts of MeOH and $NH_4PF_{6\ (aq)}$ was added in excess to afford a brown precipitate (lighter in colour than its precessor). Upon filtration, the solid was dried in the oven for 24h. (0.27 g, 24.3 %). FTIR (solid, V_{max})/ cm^{-1} : 3337, 2972, 2932, 1635, 1569, 1458, 1417, 1382, 1251, 1152, 1072, 1003, 816, 736, 687.

Co-4

$CoCl_2$ (0.014 g, 0.11 mmol) was dissolved in MeOH and 5-(tert-butyl)-di(pyridin-2-yl)isoindoline-1,3-diimine (0.077 g, 0.22 mmol) was subsequently added. The solution was stirred for 24h at room temperature resulting in dark red-brown coloured precipitate. Once filtered, the precipitate was suspended in H_2O (5 mL) and 5 drops of Br_2 previously diluted in 1 mL of H_2O were added dropwise to the solution which was left to stir for 24 h. Subtle darkening of the precipitate was observed upon complete evaporation/reaction of Br_2. Followed by filtering of the precipitate, it was then dissolved in minimal amounts of MeOH and $NH_4PF_{6\ (aq)}$ was added in excess to afford a brown precipitate (lighter in colour than its precessor). Upon filtration, the solid was dried in the oven for 24h (0.054 g, 67 %). ^{1}H NMR (300 MHz, CDCl$_3$) δ_H 8.24 (d, 2H), 8.14 (d, $^3J_{HH}$ = 8.0 Hz, $^4J_{HH}$ = 2H), 7.88 (dd, $^3J_{HH}$ = 8.0, $^4J_{HH}$ = 1.7 Hz, 2H), 7.84 – 7.70 (m, 4H), 7.64 (ddd, $^3J_{HH}$ = 6.4, $^4J_{HH}$ = 4.7, $^5J_{HH}$ = 1.6 Hz, 4H), 7.36 (ddd, $^3J_{HH}$ = 7.83, $^4J_{HH}$ = 6.45, $^5J_{HH}$ = 1.68 Hz, 4H), 6.91 (ttt, 4H), $^3J_{HH}$ = 8.67, $^4J_{HH}$ = 4.35, $^5J_{HH}$ = 1.65 Hz, 1.54 (s, 18H). ^{13}C{1H} NMR* could not be obtained across the range of

frequencies available within the facility. FTIR (solid, V_{max})/ cm^{-1} : 3342, 2963, 2928, 1629, 1566, 1445, 1427, 1366, 1288, 1253, 1224, 1207, 1157, 1098, 1066, 1012, 950, 829, 727, 665. HRMS (ESI+, MeOH), [M$^+$] m/z found 767.2769, m/z calculated 767.2769 for $C_{44} H_{40} N_{10}$ $^{59}Co^+$.

Co-5

CoCl$_2$ (0.006 g, 0.048 mmol) was dissolved in MeOH and 5-(tert-butyl)-di-4-ethyl-(pyridin-2-yl)isoindoline-1,3-diimine (0.037 g, 0.094 mmol) was subsequently added. The solution was stirred for 24h at room temperature resulting in dark red-brown coloured precipitate. Once filtered, the precipitate was suspended in H$_2$O (5 mL) and 5 drops of Br$_2$ previously diluted in 1 mL of H$_2$O were added dropwise to the solution which was left to stirr for 24 h. Subtle darkening of the precipitate was observed upon complete evaporation/reaction of Br$_2$. Followed by filtering of the precipitate, it was then dissolved in minimal amounts of MeOH and NH$_4$PF$_6$ $_{(aq)}$ was added in excess to afford a brown precipitate (lighter in colour than its precessor). Pure product was afforded with column chromatography. Ligand impurity eluted with diethyl ether, followed by a dark brown band (product) which eluted with MeOH. (0.007 g, 19 %). ^{1}H NMR (300 MHz, CDCl$_3$) δ_H 8.22 (s, 2H), 8.11 (d, $^3J_{HH}$ = 8.0 Hz, 2H), 7.86 (dd, $^3J_{HH}$ = 8.1, $^4J_{HH}$ = 1.7 Hz, 4H), 7.47 (dd, $^3J_{HH}$ = 6.5, $^4J_{HH}$ = 4.5 Hz, 4H), 7.19 (d, $^3J_{HH}$ = 5.9 Hz, 4H), 6.70 (dt, $^3J_{HH}$ = 6.6, $^4J_{HH}$ = 1.8 Hz, 2H), 2.65 (qd, $^3J_{HH}$ = 7.5, $^4J_{HH}$ = 1.4 Hz, 4H), 1.52 (s, 18H), 1.20 (td, $^3J_{HH}$ = 7.6, $^4J_{HH}$ = 1.6 Hz, 6H). ^{13}C{^{1}H} NMR* could not be obtained across 75-125 MHz range of frequencies available within the facility. FTIR (solid, V_{max})/ cm^{-1} : 3341, 2964, 2937, 1637, 1570, 1446, 1429, 1362, 1286, 1254, 1222, 1195, 1153, 1099, 1074, 1014, 944, 833, 726, 663. HRMS (ESI+, MeOH), [M]$^+$ m/z found 879.4020, m/z calculated 879.4021 for $C_{52} H_{57} N_{10}$ $^{59}Co^+$.

Co-6

CoCl$_2$ (0.017 g, 0.14 mmol) was dissolved in MeOH and bis-4-ethyl-(pyridin-2-yl)isoindoline-1,3-diimine (0.100 g, 0.28 mmol) was subsequently added. The solution was stirred for 24h at room temperature resulting in dark red-brown coloured precipitate. Once filtered, the precipitate was suspended in H$_2$O (5

mL) and 5 drops of Br_2 previously diluted in 1 mL of H_2O were added dropwise to the solution which was left to stir for 24 h. Subtle darkening of the precipitate was observed upon complete evaporation/reaction of Br_2. Followed by filtering of the precipitate, it was then dissolved in minimal amounts of MeOH and $NH_4PF_{6\,(aq)}$ was added in excess to afford a brown precipitate (lighter in colour than its precessor). Pure product was afforded with column chromatography. Ligand impurity eluted with diethyl ether, followed by a dark brown band (product) which eluted with MeOH (0.010 g, 9 %). ^{1}H NMR (300 MHz, $CDCl_3$) δ_H 8.16 (q, $^3J_{HH}$ = 5.0 Hz, 2H), 7.78 (dd, $^3J_{HH}$ = 2.7 Hz, 2H), 7.41 (d, $^3J_{HH}$ = 6.5 Hz, 2H), 7.17 (s, 2H), 6.70 (d, $^3J_{HH}$ = 6.8 Hz, 2H), 2.60 (q, $^3J_{HH}$ = 7.7 Hz, 4H), 1.13 (t, $^3J_{HH}$ = 7.5 Hz, 6H). FTIR (solid, V_{max})/ cm^{-1} : 3342, 2954, 2917, 1635, 1570, 1458, 1411, 1372, 1298, 1258, 1225, 1186, 1155, 1099, 1015, 993, 824, 729, 670. HRMS(ESI+, MeOH), [M[+]] m/z found 767.2769, m/z calculated 767.2769 for $C_{44}H_{40}N_{10}{}^{59}Co^+$.

4.7 References

[1] C. Wang, S. Otto, M. Dorn, E. Kreidt, J. Lebon, L. Sršan, P. Di Martino-Fumo, M. Gerhards, U. Resch-Genger, M. Seitz, K. Heinze, *Angew Chem Int Ed,* 2018, Chem. 57, 4, 1112-1116.

[2] S. Otto, C. Förster, C. Wang, U. Resch-Genger, K. Heinze, 2018, *Chem. A Eur. J.*, 24, 48, 12555-12563.

[3] F. Reichenauer, C. Wang, C. Förster, P. Boden, N. Ugur, R. Báez-Cruz, J. Kalmbach, L. M. Carrella, E. Rentschler, C. Ramanan, G. Niedner-Schatteburg, M. Gerhards, M. Seitz, U. Resch-Genger, K. Heinze., *J. Am. Chem. Soc.,* 2021, 143*,* 30, 11843-11855.

[4] L. Stein, C. Wang, C. Förster, U. Resch-Genger, K. Heinze**,** *Dalton Trans.***,** 2022, 51, 17664-17670

[5] N. Sinha, J.-R. Jiménez, B. Pfund, A. Prescimone, C. Piguet, O. S. Wenger, *Angew. Chem., Int. Ed.* 2021, 60, 23722-23728.

[6] I. Sović, V. Stilinović, B. Kaitner, S. Kraljević-Pavelić, M. Bujak, K. Čuljak, P. Novak and G. Karminski-Zamola, *J. Mol. Struct.,* 2011, 1006, 259-265.

[7] R. R. Gagné, R. S. Gall, G. S. Lisensky, R. E. Marsh and L. M. Speltz, *Inorg. Chem.,* 1979, 18, 771-789.

[8] J. A. Elvidge and R. P. Linstead, *J. Chem. Soc.,* 1954, 442-448.

[9] W. O. Siegl, *Inorg. Chim. Acta,* 1977, 25, 65-69.

[10] D. Pinnell, C. B. Wright, R. B. Jordon, *J. Am. Chem. Soc.,*1972, 94, 6104-6106.

[11] J. S. Pap, M. A. Cranswick, É. Balogh-Hergovich, G. Baráth, M. Giorgi, G. T. Rohde, J. Kaizer, G. Speier and L. Que Jr., *Eur. J. Inorg. Chem.,* 2013, 3858-3866.

[12] J. S. Pap, B. Kripli, V. Bányai, M. Giorgi, L. Korecz, T. Gajda, D. Árus, J. Kaizer and G. Speier, *Inorg. Chim. Acta*, 2011, 376, 158-169.

[13] R. R. Gagné and D. N. Marks, *Inorg. Chem.,* 1984, 23, 65-74.

[14] B. Kripli, G. Baráth, É. Balogh-Hergovich, M. Giorgi, A. J. Simaan, L. Párkányi, J. S. Pap, J. Kaizer and G. Speier, *Inorg. Chem. Comm.,* 2011, 14, 205-209.

[15] É. Balogh-Hergovich, G. Speier, M. Réglier, M. Giorgi, E. Kuzmann and A. Vértes, *Inorg. Chem. Comm.,* 2005, 8, 5, 457-459.

[16] J. Kaizer, G. Baráth, G. Speier, M. Réglier and M. Giorgi, *Inorg. Chem. Comm.,* 2007, 10, 292-294.

[17] J. Kaizer, B. Kripli, G. Speier and L. Párkányi, *Polyh.,* 2009, 28, 933-936.

[18] J. S. Pap, M. Giorgi, J. Kaizer and G. Speier, *Inorg. Chem. Comm.,* 2013, 27, 152-155.

[19] K. Hanson, N. Patel, M. T. Whited, P. I. Djurovich and M. E. Thompson, *Org. Lett.,* 2011, 13, 7, 1598-1609.

[20] I-S. Tamgho, J. T. Engle and C. J. Ziegler, *Tet. Lett.,* 2013, 54, 45, 6114-6117.

[21] P. J. Domaille, R. L. Harlow, S. D. Ittel and W. G. Peet, *Inorg. Chem.,* 1983, 22, 3940-3944.

[22] M. B. Meder, B. A. Siggelkow and L. H. Gade, Z. *Anorg. Allg. Chem.,* 2004, 630, 1962-1968.

[23] C. A. Tolman, J. D. Druliner, P. J. Krusic, M. J. Nappa, W. C. Seidel, I. D. Williams and S. D. Ittel, *J .Mol. Catal.,* 1988, 48, 129-148.

[24] J. S. Pap, B. Kripli, T. Váradi, M. Giorgi, J. Kaizer and G. Speier, J. *Inorg. Biochem.,* 2011, 105, 5, 911-918.

[25] J. S. Pap, B. Kripli, V. Bányai, M. Giorgi, L. Korecz, T. Gajda, D. Árus, J. Kaizer and G. Speier, *Inorg. Chim. Acta,* 2011, 376, 1, 158-169.

[26] M. Wicholas, A. D. Garrett, M. Gleaves, A. M. Morris, M. Rehm, O. P. Anderson and A. la Cour, *Inorg. Chem.,* 2006, 45,15,5804-5811.

[27] SciFinder; Chemical Abstracts Service: Columbus, OH; https://scifinder.cas.org (accessed 01/02/2023)

[28] Y. Cheng, Q. Yang, J. He, W. Zou, K. Liao, X. Chang, C. Zou, W. Lu, *Dalt. Trans.,* 2023, 52, 2561-2565.

[29] N. Sawicka, C. J. Craze, P. N. Horton, S. J. Coles, E. Richards, S. J. A. Pope, *Chem. Comm.,* 2022, 58, 5733-5736.

[30] E. Spundflasche, H. Fink, H. J. Seifert, Z. *Anorg. Allg. Chem.,* 1989, 579, 143-150.

[31] N. Sawicka, PhD thesis, 2023, Chapter 3, Cardiff University.

[32] B.Morosin, *Acta. Crystallogr.,* 1965, 19, 131.

33 M. Lehr, T. Paschelke, E. Trumpf, A. M. Vogt, C. Näther, F. D. Sönnichsen, A. J. McConnell, *Angew. Chem., Int. Ed.* 2020, *59*, 19344– 19351.

34 A. Zunger, *Nat. Comp. Sci.,* 2022, 2, 529–532.

35 F. Vlahović, M. Perić, M. Gruden-Pavlović, M. Zlatar,. *J Chem Phys.,* 2015, 7, 142, 21, 214111-214114.

36 M. Atanasov, C. A. Daul, *C. R. Chim.*, 2005, 8, 1421–1433.

37 S. Stepanovic, R. Lai, M. Elstner, M. Gruden, P. Garcia-Fernandez, Q. Cui, *2020, Phys. Chem. Chem. Phys.,*22, 27084-27095.

38 S. J. Milder, J. S. Gold and D. S. Kliger, *Inorg. Chem.,* 1990, 29, 2506-2511.

39 S. K. Singh, J. Eng, M. Atanasov, F. Neese, *Coord. Chem. Rev.,* 2017, 344, 2-25.

40 B. Doistau, G. Collet, E. A. Bolomey, V. Sadat-Noorbakhsh, C. Besnard, C. Piguet, *Inorg. Chem.,* 2018, 57*, 22, 14362-14373.

41C . Zhang, H. Lin, Y. Hu, J. Sui, L. Lin, B. Li, *J. Innov. Opt. Health Sci.,* 2022, 15, 6, 22400-11.

42 J. C. Barbour, A. J. I. Kim, E. deVries, S. E. Shaner, B. M. Lovaasen, *Inorg. Chem.,* 2017, 56*, 14, 8212-8222.

43 K. Sugisaki, K. Toyota, K. Sato, D. Shiomi, T. Takui., *J. Phys. Chem. A* 2016, 120, 49, 9857–9866.

44 Simon Bennie, Thesis, 2013, Manchester University

45 S. Stoll, A. Schweiger, *J. Magn. Reson.* 2006, 178, 1, 42-55.

46 Gaussian 16, Revision C.01, Frisch, M. J.; Trucks, G. W.; Schlegel, H. B.; Scuseria, G. E.; Robb, M. A.; Cheeseman, J. R.; Scalmani, G.; Barone, V.; Petersson, G. A.; Nakatsuji, H.; Li, X.; Caricato, M.; Marenich, A. V.; Bloino, J.; Janesko, B. G.; Gomperts, R.; Mennucci, B.; Hratchian, H. P.; Ortiz, J. V.; Izmaylov, A. F.; Sonnenberg, J. L.; Williams-Young, D.; Ding, F.; Lipparini, F.; Egidi, F.; Goings, J.; Peng, B.; Petrone, A.; Henderson, T.; Ranasinghe, D.; Zakrzewski, V. G.; Gao, J.; Rega, N.; Zheng, G.; Liang, W.; Hada, M.; Ehara, M.; Toyota, K.; Fukuda, R.; Hasegawa, J.; Ishida, M.; Nakajima, T.; Honda, Y.; Kitao, O.; Nakai, H.; Vreven, T.; Throssell, K.; Montgomery, J. A., Jr.; Peralta, J. E.; Ogliaro, F.; Bearpark, M. J.; Heyd, J. J.; Brothers, E. N.; Kudin,

K. N.; Staroverov, V. N.; Keith, T. A.; Kobayashi, R.; Normand, J.; Raghavachari, K.; Rendell, A. P.; Burant, J. C.; Iyengar, S. S.; Tomasi, J.; Cossi, M.; Millam, J. M.; Klene, M.; Adamo, C.; Cammi, R.; Ochterski, J. W.; Martin, R. L.; Morokuma, K.; Farkas, O.; Foresman, J. B.; Fox, D. J. Gaussian, Inc., Wallingford CT, 2016.

[47] F. Neese, Software Update: The ORCA Program System—Version 5.0. Wiley Interdiscip. *Rev. Comput. Mol. Sci.* 2022, 12, e1606.

[48] P. J. Hay and W. R. Wadt, *J. Chem. Phys.,* 1985, 82, 299-310.

[49] J. Tomasi, B. Mennucci, and R. Cammi, *Chem. Rev.*, 2005, 105, 2999-3093.

[50] A.D. Becke, , *Phys. Rev.,* 1988, 38, 3098.

[51] F. Weigend, R. Ahlrichs, *Phys. Chem. Chem. Phys.,* 2005, 7, 3297.

[52] F. Weigend and R. Ahlrichs, *Phys. Chem. Chem. Phys.*, 2005, 7, 3297-305.

[53] F. Neese*, J. Am. Chem. Soc.*, 2006, 128, 10213-10222.

Appendix 2 to Chapter 2

LC-MS chromatograms of **Cr-1 to Cr-4**
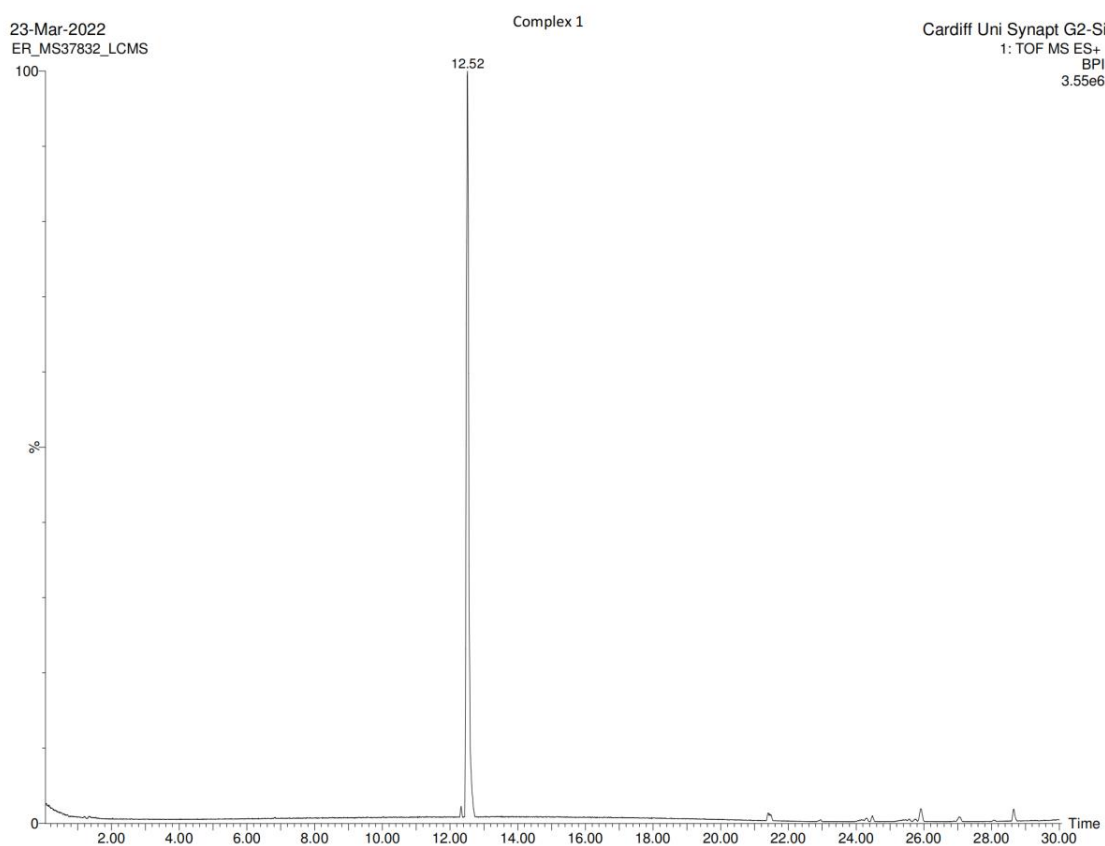
Figure A2.1 Chromatogram for **Cr-1**; LC-MS run with H_2O/MeCN gradient.

23-Mar-2022
ER_MS37832_LCMS 1424 (12.510) Cm (1417:1430-1451:1463)

Complex 1

Cardiff Uni Synapt G2-Si
1: TOF MS ES+
2.83e7
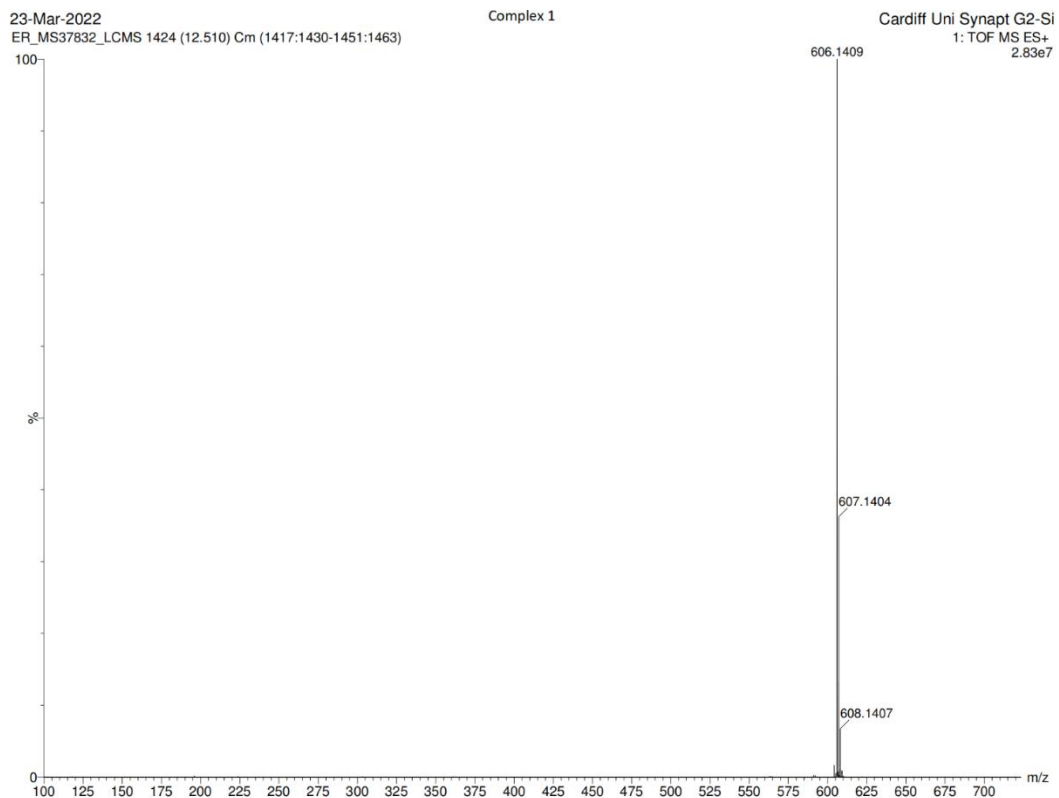
Figure A2.2 MS spectra from LC-MS for **Cr-1**; ionisation method chosen was ESI$^+$.
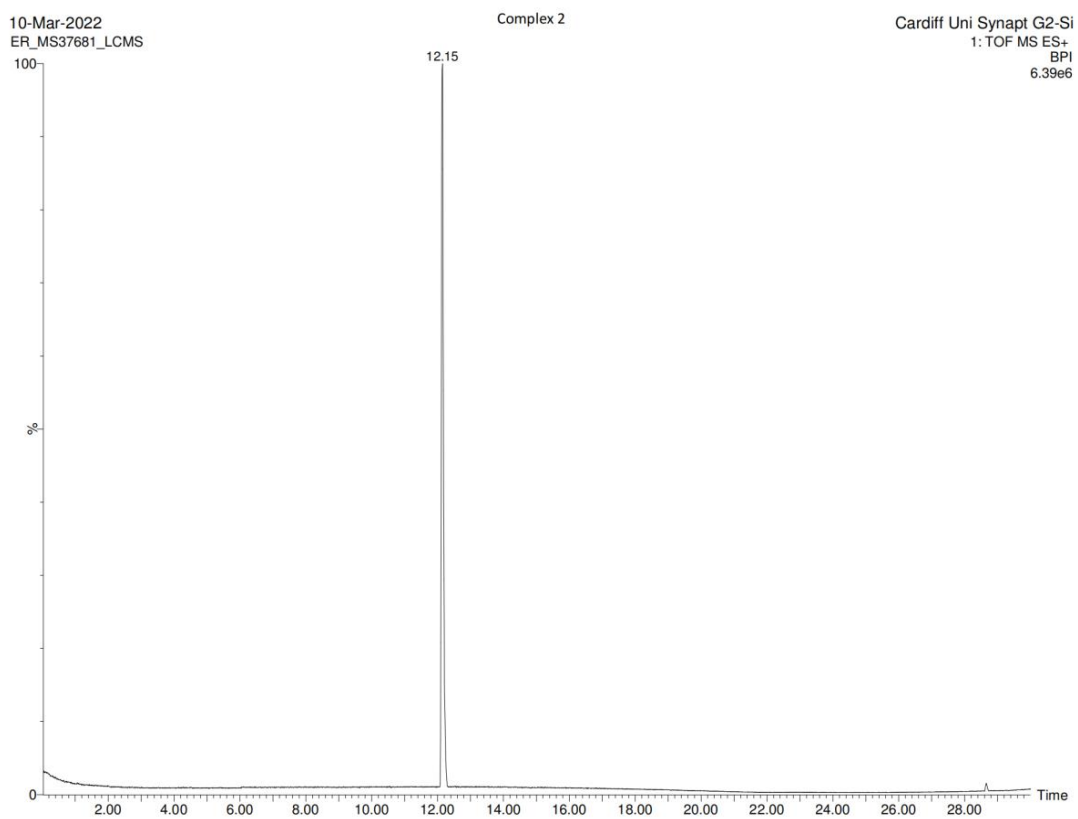
Figure A2.3 Chromatogram for Complex **Cr-2;** LC-MS run with H_2O/MeCN gradient.

10-Mar-2022
ER_MS37681_LCMS 1382 (12.149) Cm (1378:1384-(1369:1372+1406:1411))

Complex 2

Cardiff Uni Synapt G2-Si
1: TOF MS ES+
3.85e7
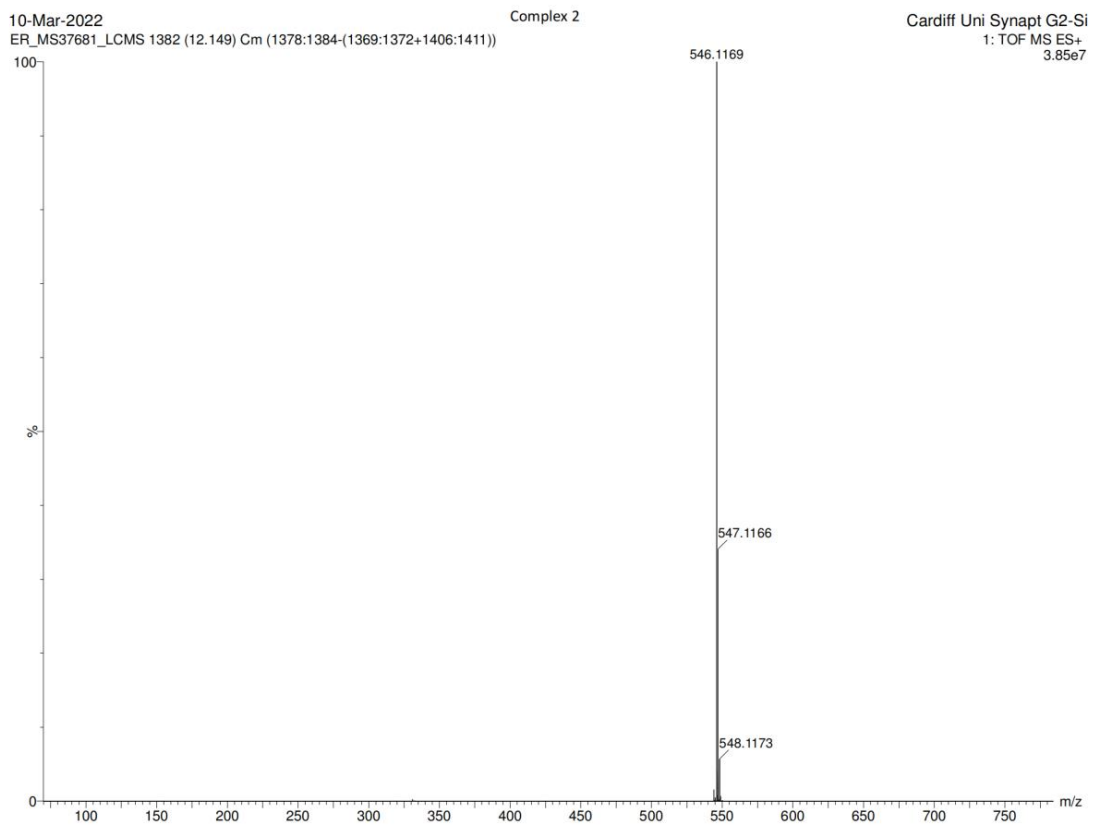
Figure A2.4 MS spectra from LC-MS for complex **Cr-2**; Ionisation method chosen was ES.
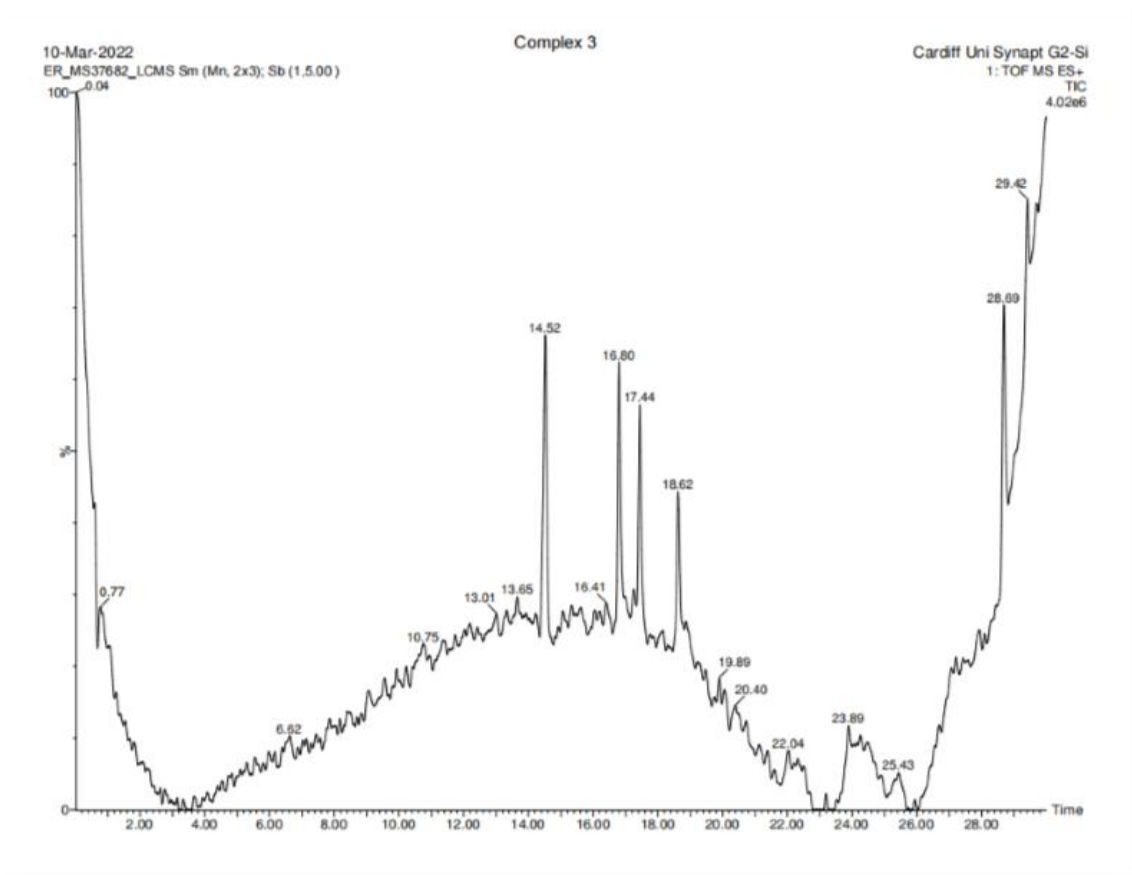
Figure A2.5 Chromatogram for **Cr-3**; LC-MS run with H$_2$O/MeCN gradient.
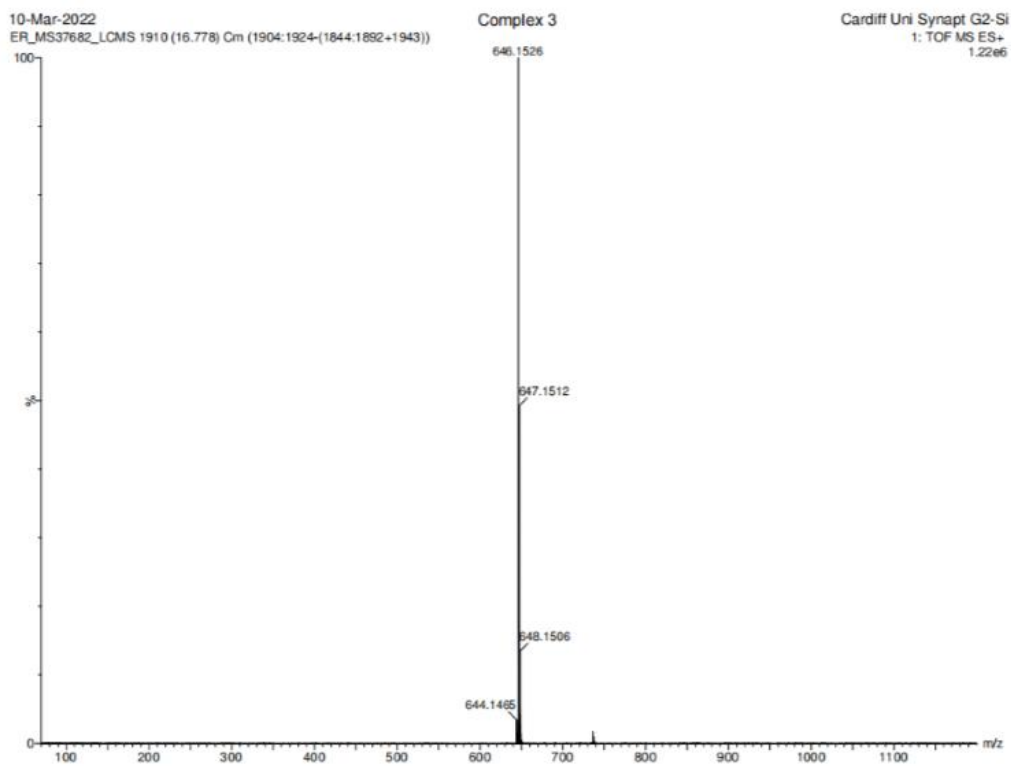
Figure A2.6 MS spectra from LC-MS for complex **Cr-3**; Ionisation method chosen was ES.
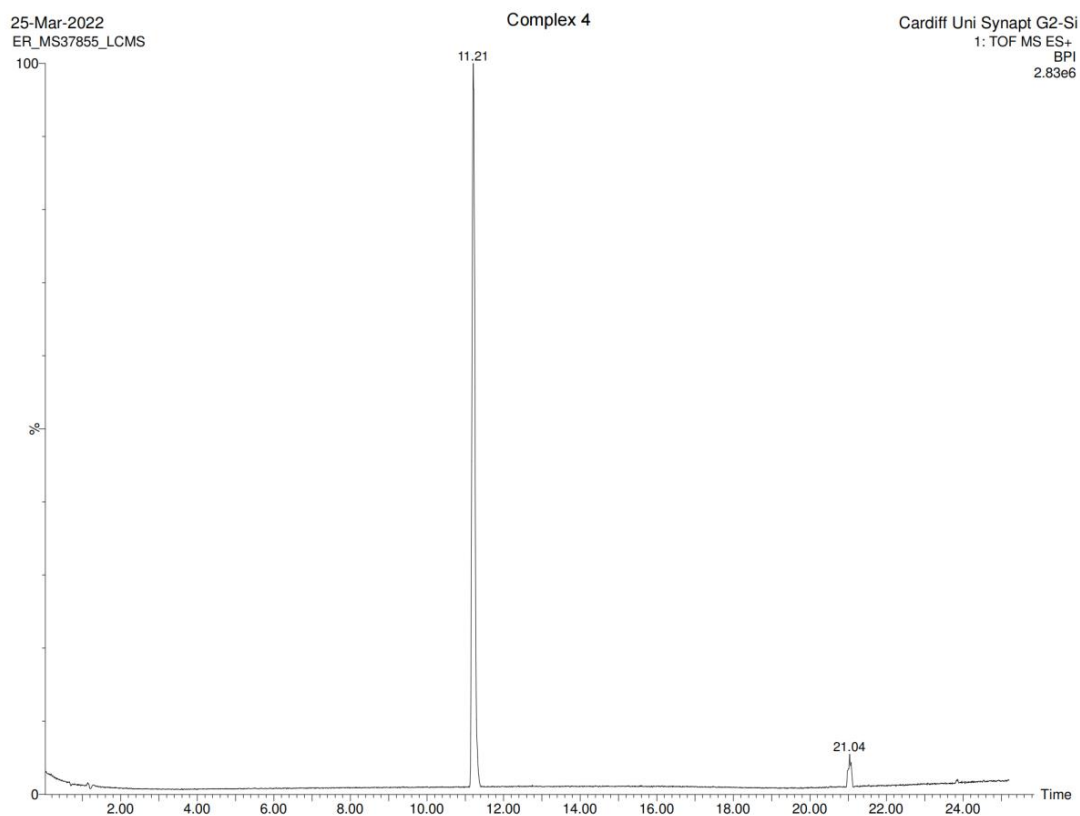
Figure A2.7 Chromatogram for Complex **Cr-4**. LC-MS run with H_2O/MeCN gradient. Note that the peak at Time = 21.04 min was reported as column contamination by the Cardiff University Analytical Services.
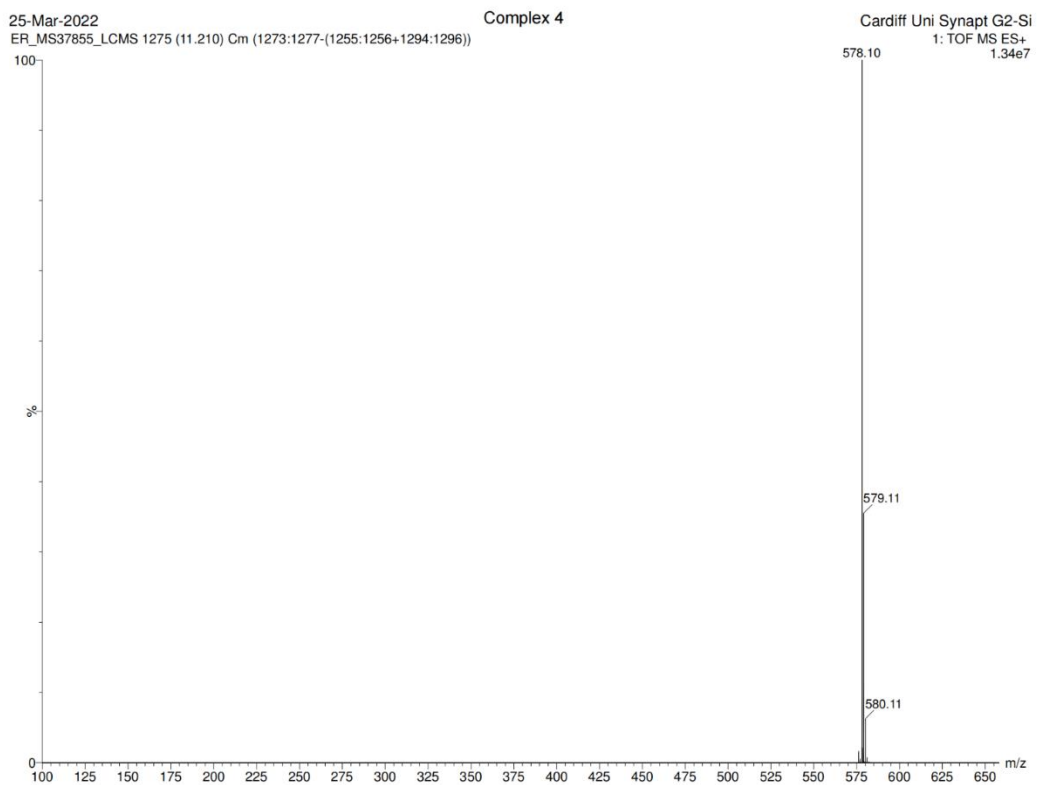
Figure A2.8 MS spectra from LC-MS for complex **Cr-4**; ionisation method chosen was ESI⁺.
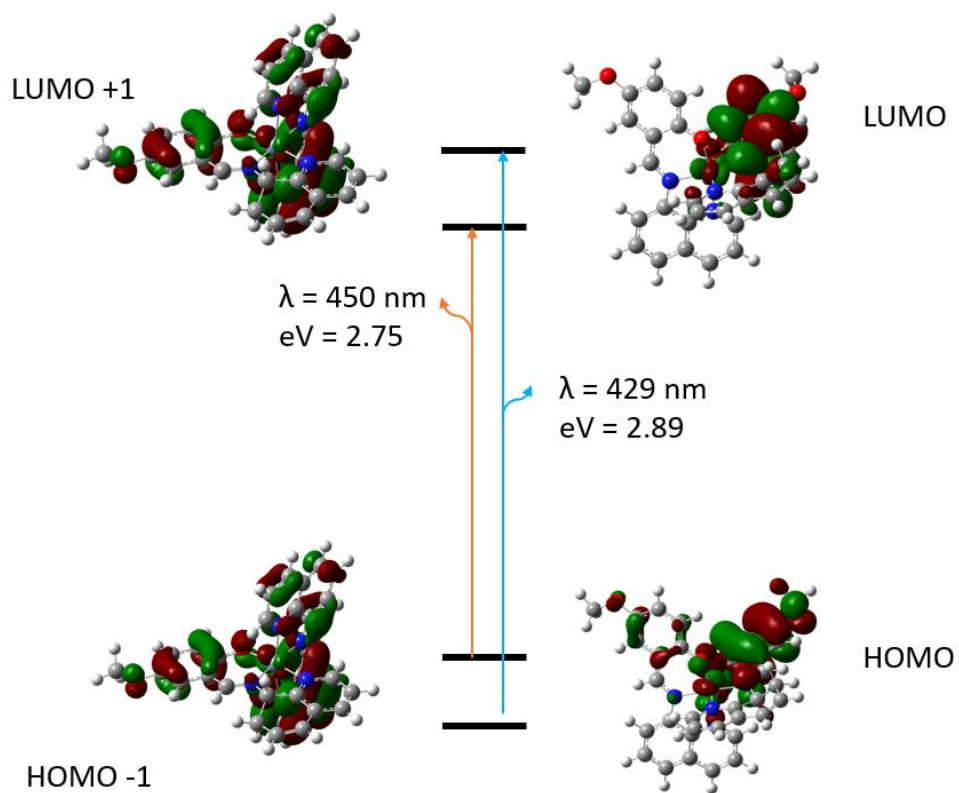
Figure A2.9 DFT calculated HOMO-LUMO orbitals for **Cr-1**. Calculated using previously geometry optimized structures (B3LYP/6-311G(d,p)). TD-DFT calculations were computed using B3LYP functional and def2-SVP basis set with "+" accounting for diffuse function and (d,p) accounting for polarisation function.
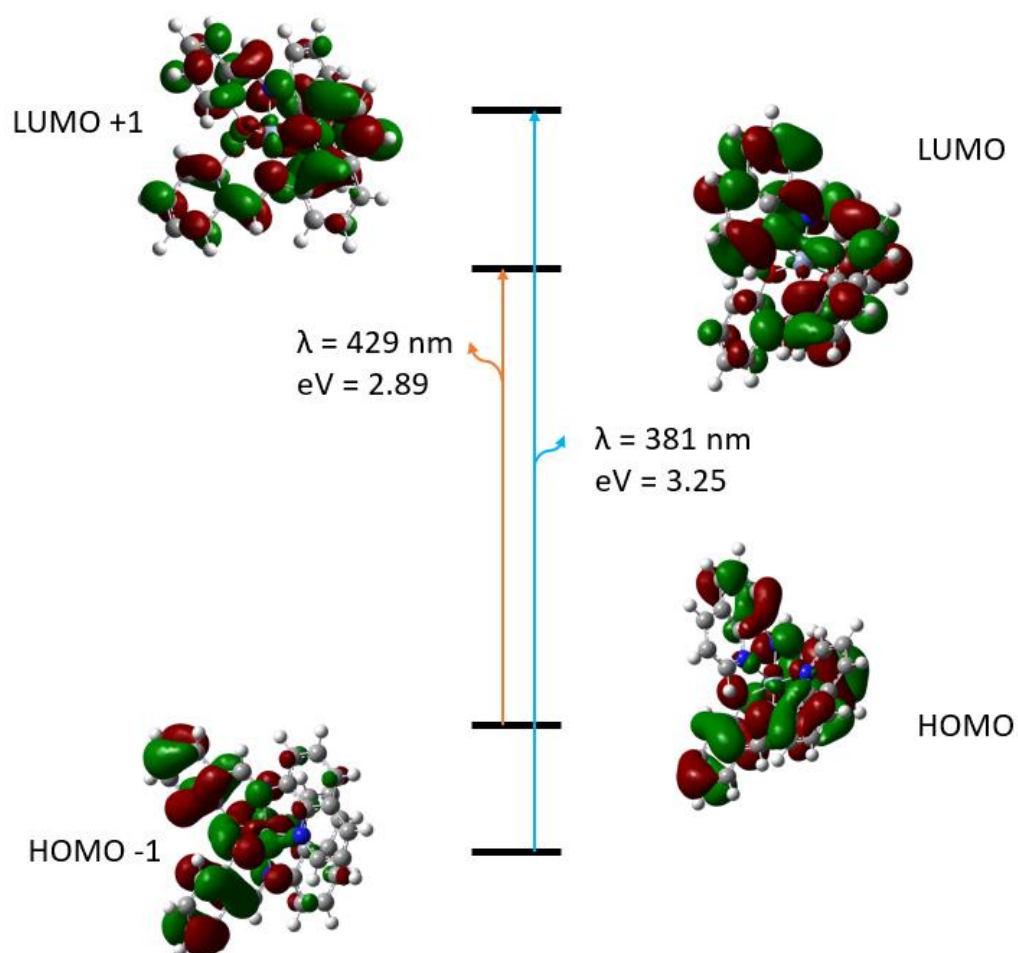
Figure A2.10 DFT calculated HOMO-LUMO orbitals for **Cr-2**. Calculated using previously geometry optimized structures (B3LYP/6-311G(d,p)). TD-DFT calculations were computed using B3LYP functional and def2-SVP basis set with "+" accounting for diffuse function and (d,p) accounting for polarisation function.
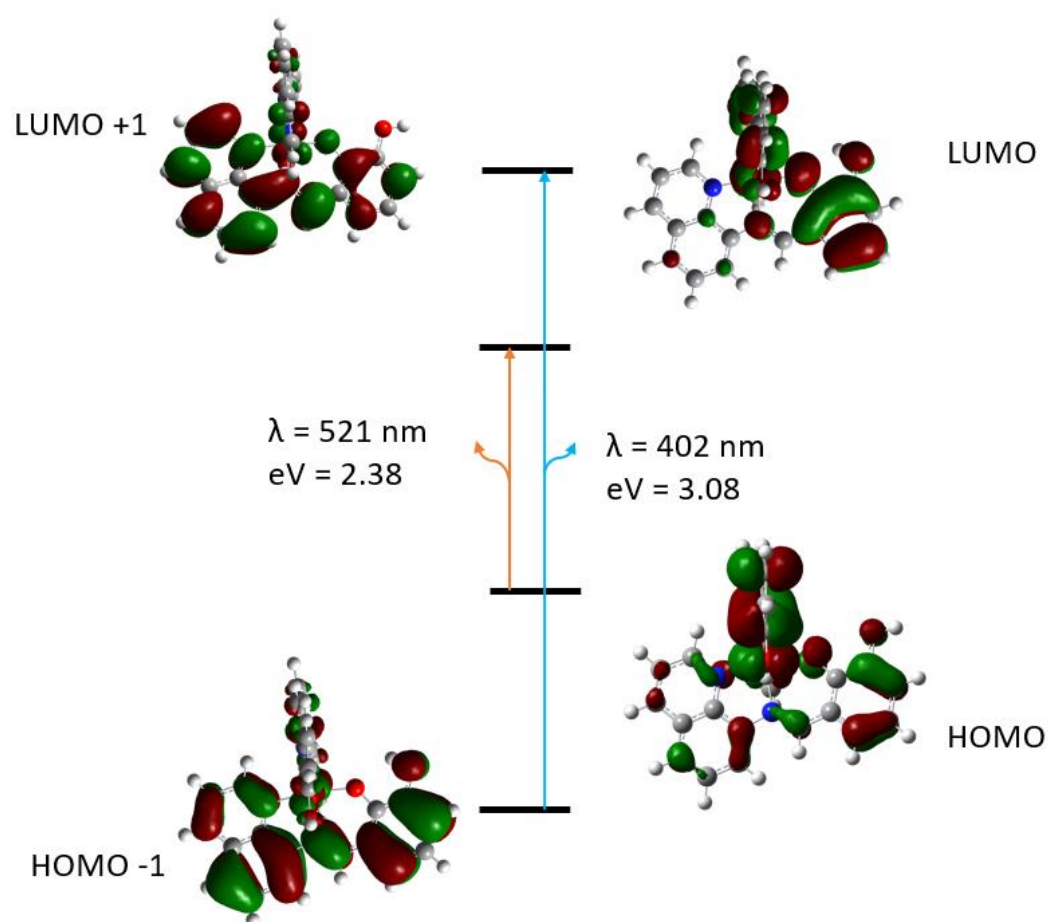
Figure A2.11 DFT calculated HOMO-LUMO orbitals for **Cr-4**. Calculated using previously geometry optimized structures (B3LYP/6-311G(d,p)). TD-DFT calculations were computed using B3LYP functional and def2-SVP basis set with "+" accounting for diffuse function and (d,p) accounting for polarisation function.
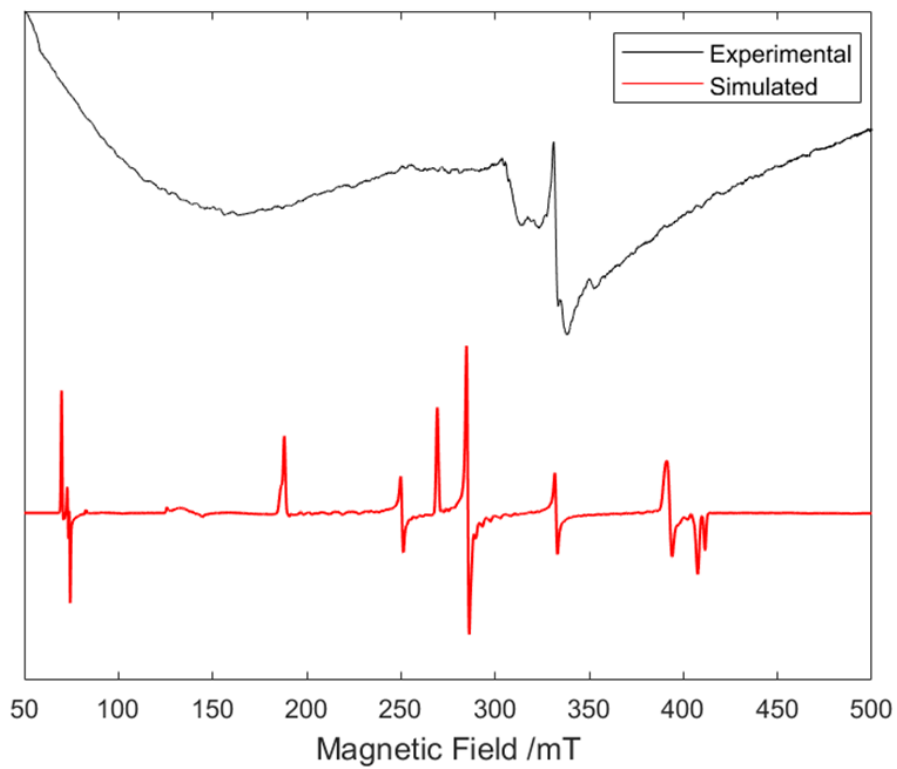
Figure A2.12 X-band EPR spectrum (T = 298 K) of solid **Cr-1** doped at 1% into corresponding Co(III).
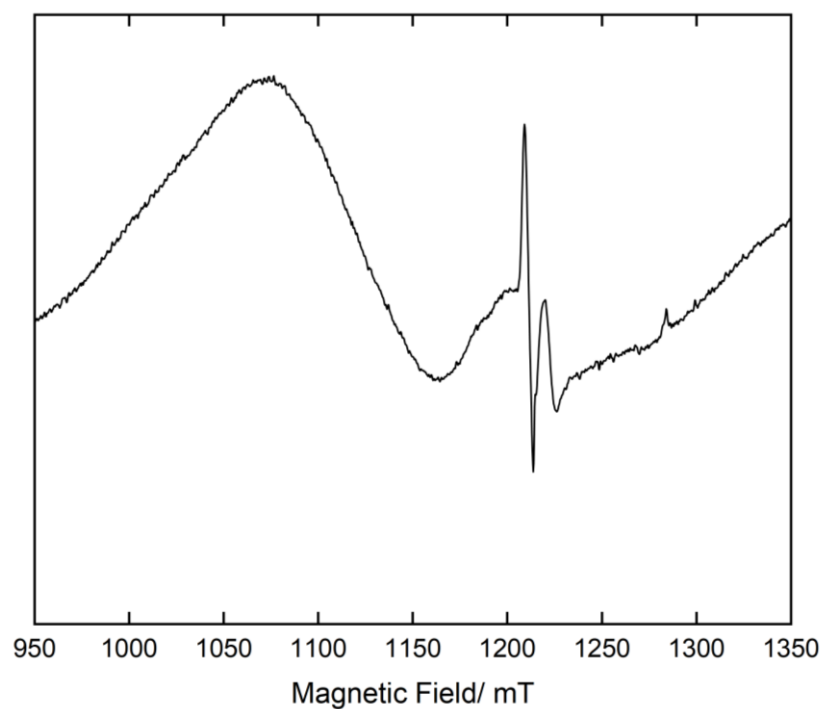
Figure A2.13 Baseline corrected Q-band EPR spectrum of neat solid **Cr-1** recorded at 298 K.
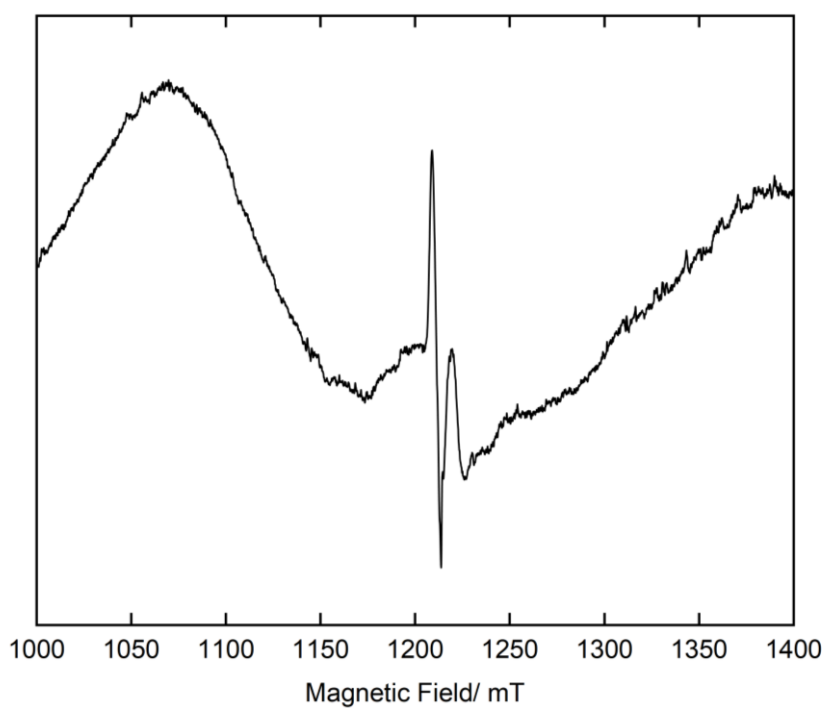
Figure A2.14 Baseline corrected Q-band EPR spectrum of neat solid **Cr-1** recorded at 298 K.

Appendix to Chapter 3
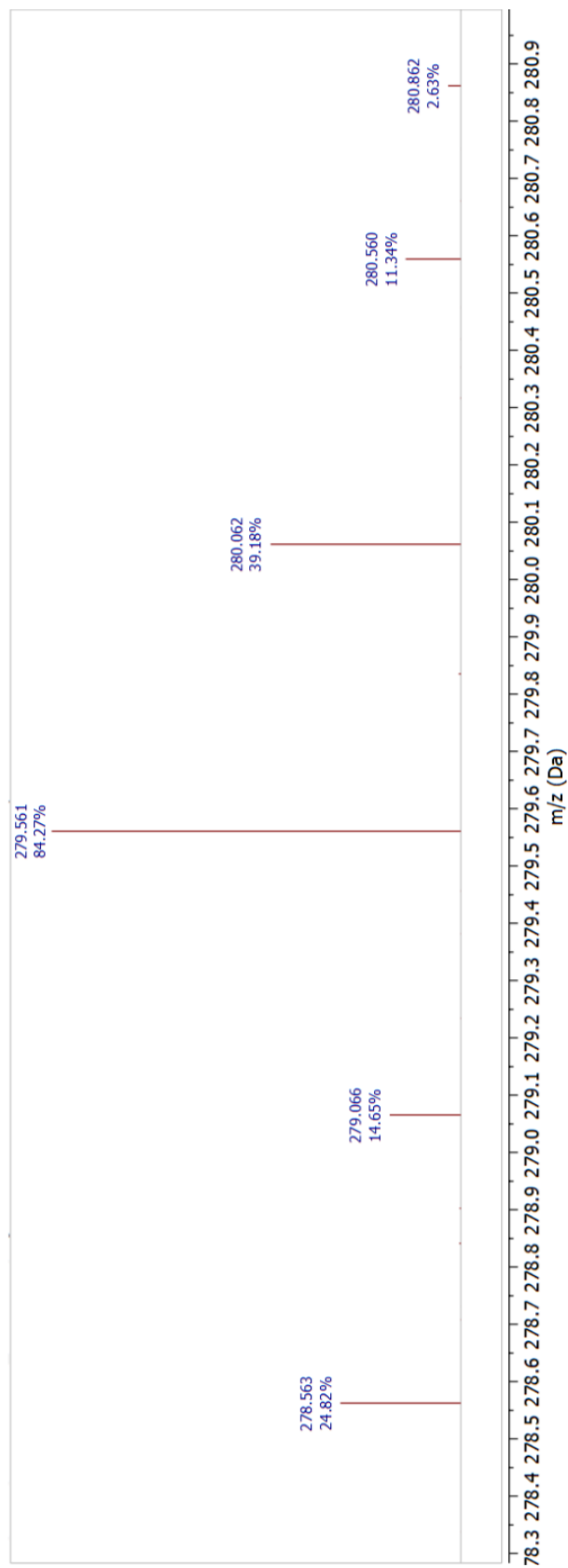
A3.1 Isotope pattern of the peak at 279.561 m/z from **Cr-1** LC-MS.
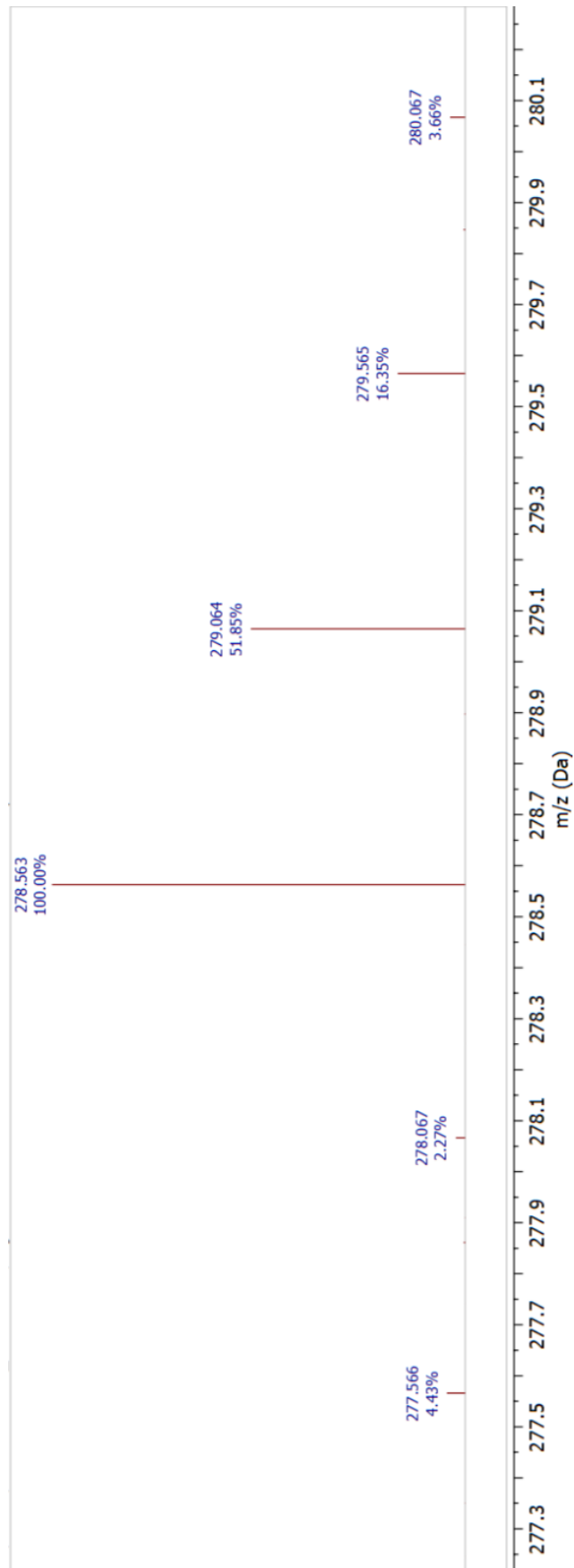
A3.2 Isotope pattern of the peak at 278.563 m/z from **Cr-1** LC-MS.
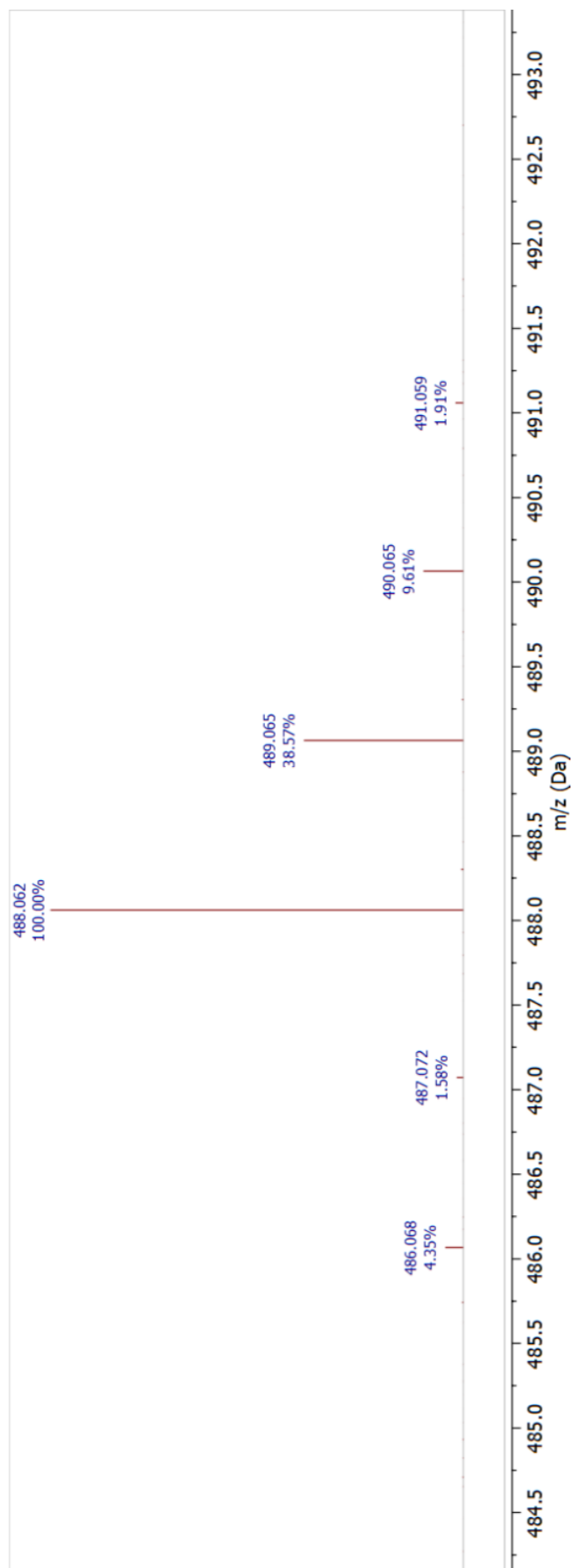
A3.3 Isotope pattern of the peak at 488.062 m/z from **Cr-1** LC-MS.
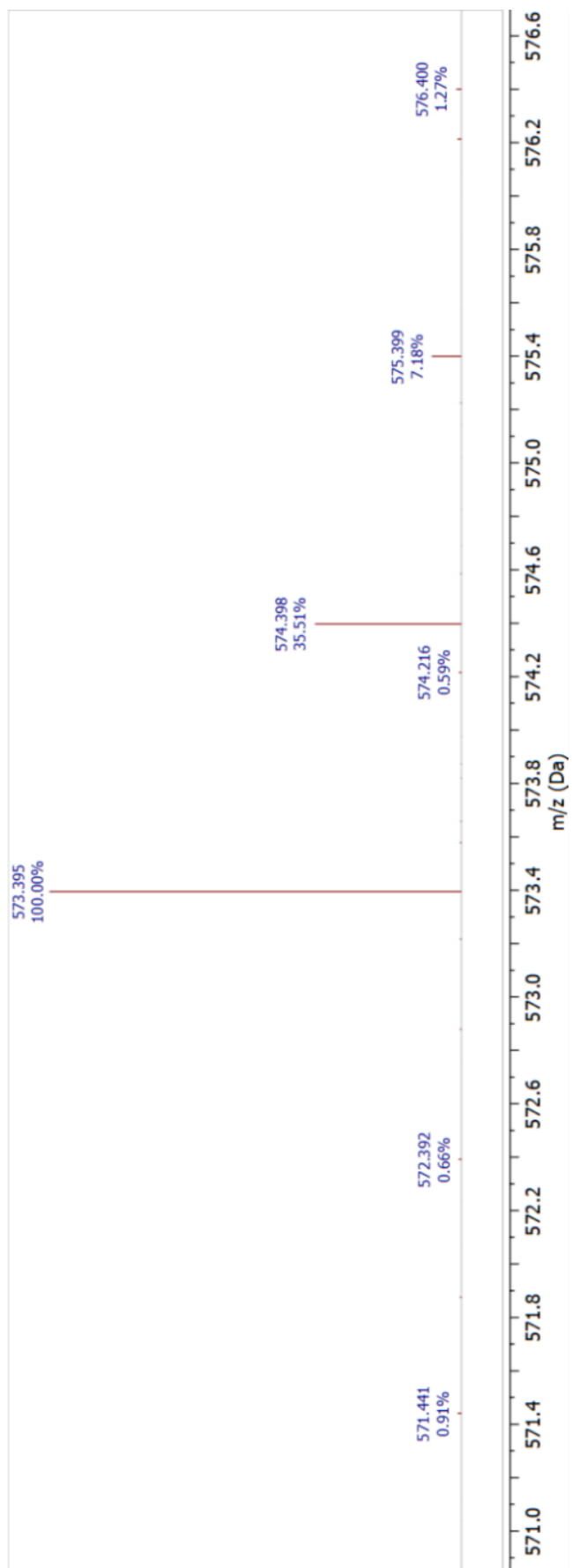
A3.4 Isotope pattern of the peak at 573.395 m/z from **Cr-1** LC-MS.
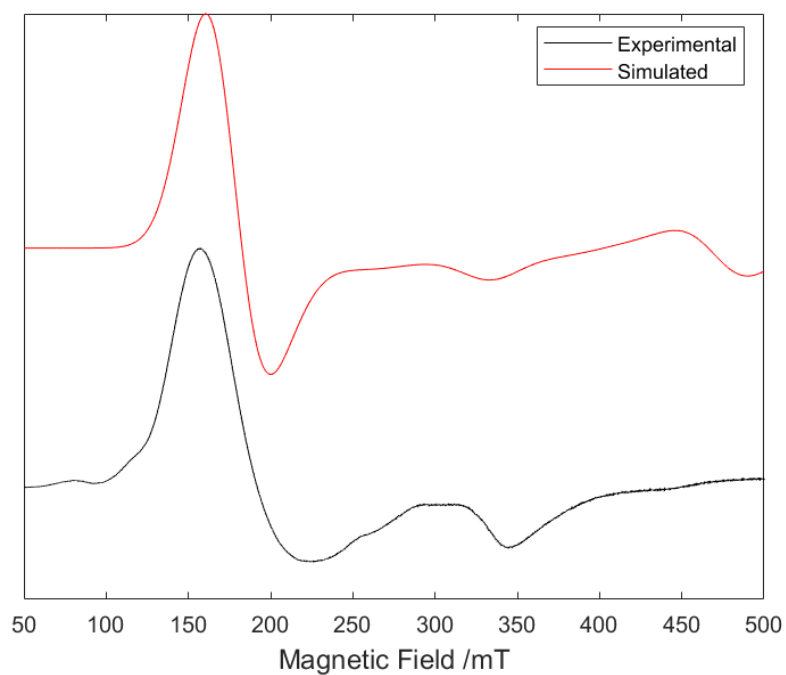
A3.5 X-band EPR spectrum and its simulated trace in solid state at T=298 K for **Cr-1**. D = 0.37 cm^{-1} (11092 MHz) and E/D = 0.013
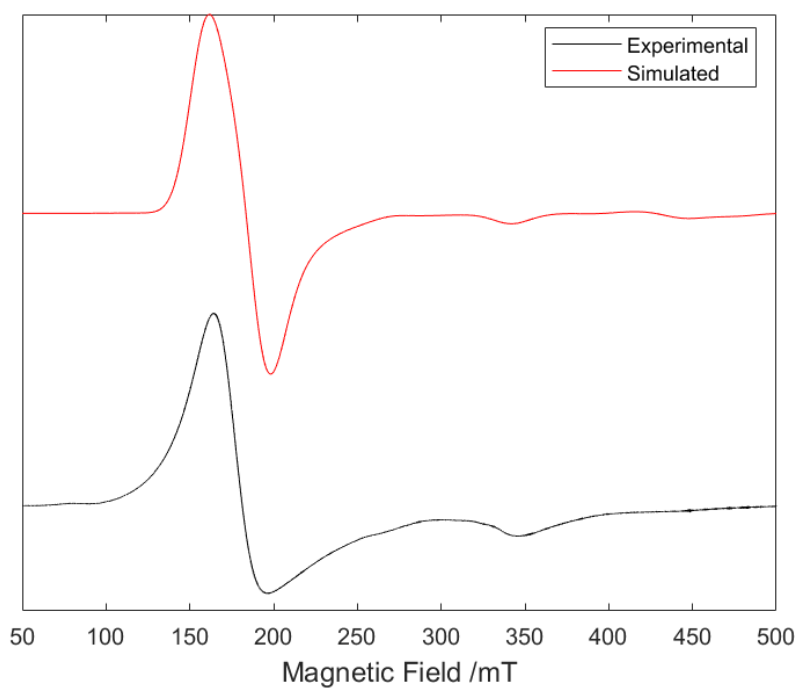
A3.6 X-band EPR spectrum and its simulated trace in solid state at T=298 K for **Cr-2**. D = 0.42 cm^{-1} (12591 MHz) and E/D = 0.096.
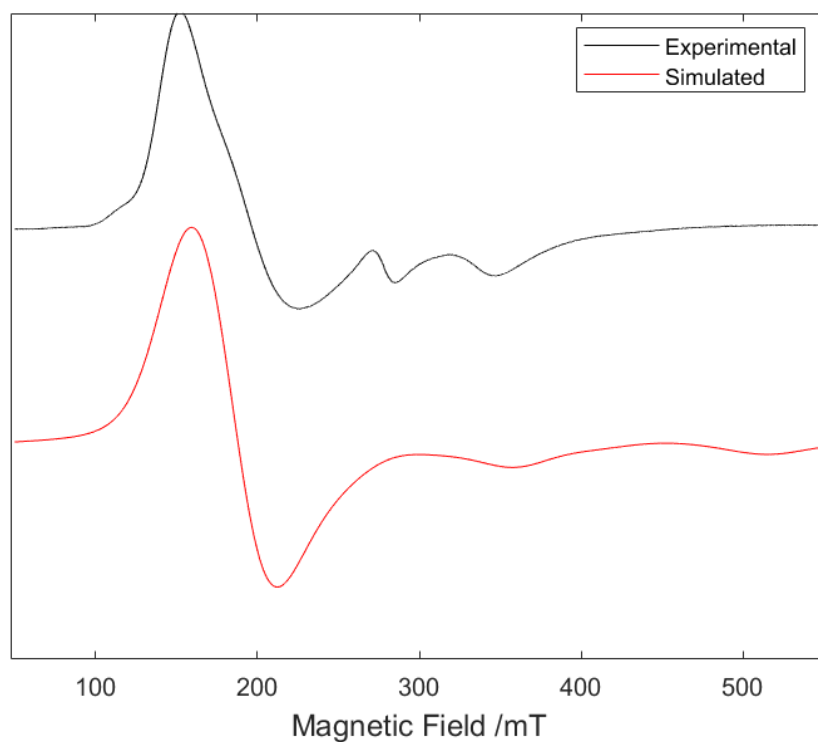
A3. X-band EPR spectrum and its simulated trace in solid state at T=298 K for **Cr-3**. . D = 0.4 cm^{-1} (11992 MHz) and E/D = 0.058
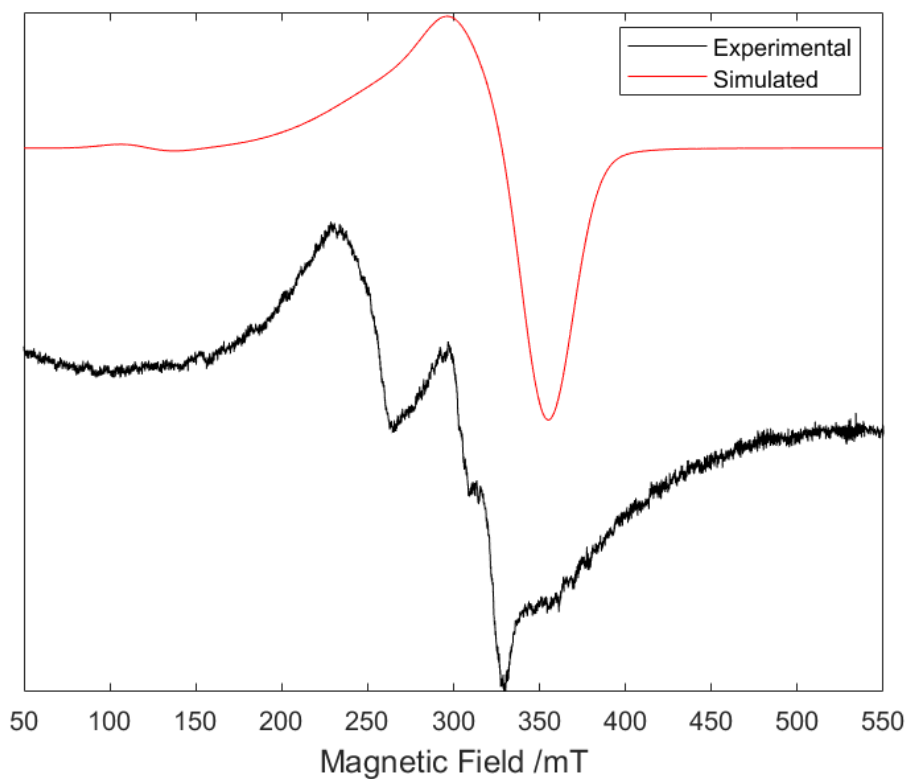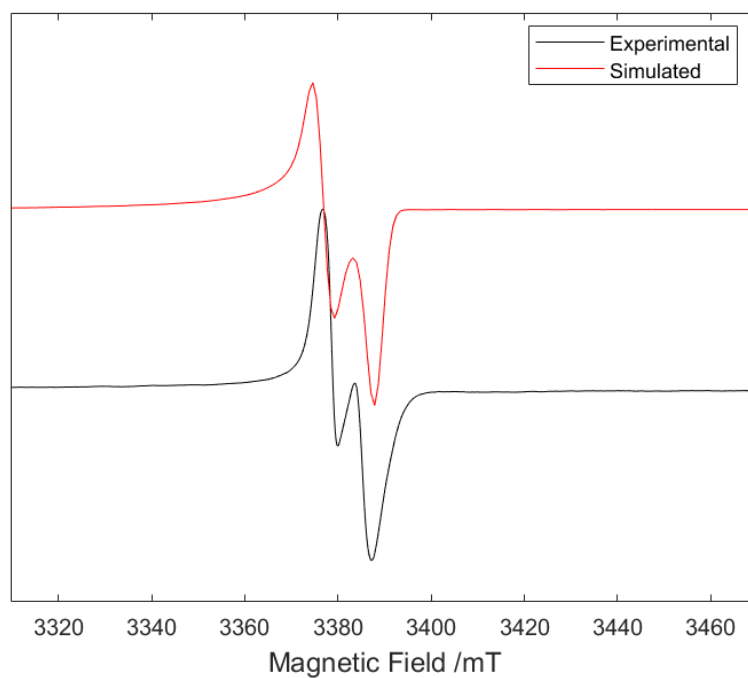

A3.8 X-band EPR spectrum and its simulated trace in solid state at T=298 K for **Cr-4**. D = 0.42 cm^{-1} (12591 MHz) and E/D = 0.071.
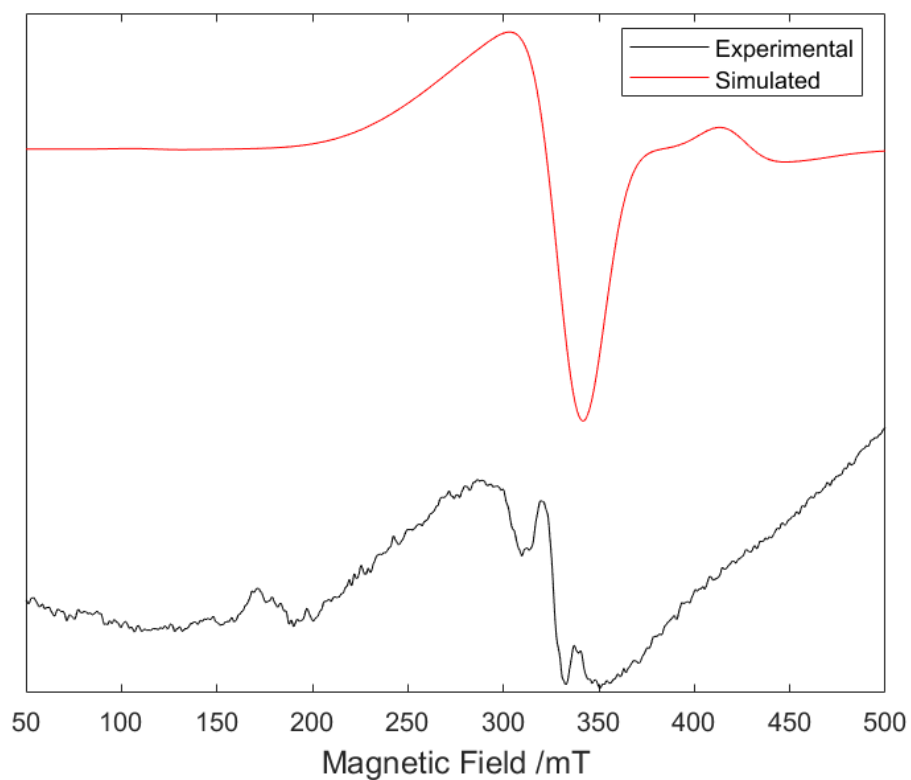
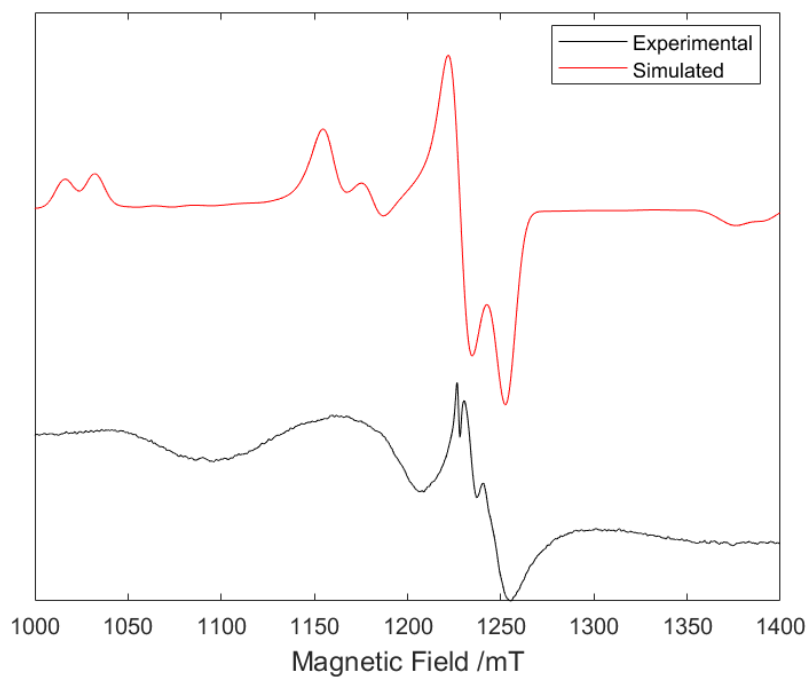A3.9 X-band EPR spectrum and its simulated trace in solid state at T=298 K
for **Cr-5**. D = 0.54 cm^{-1} (16189 MHz) and E/D = 0.016.
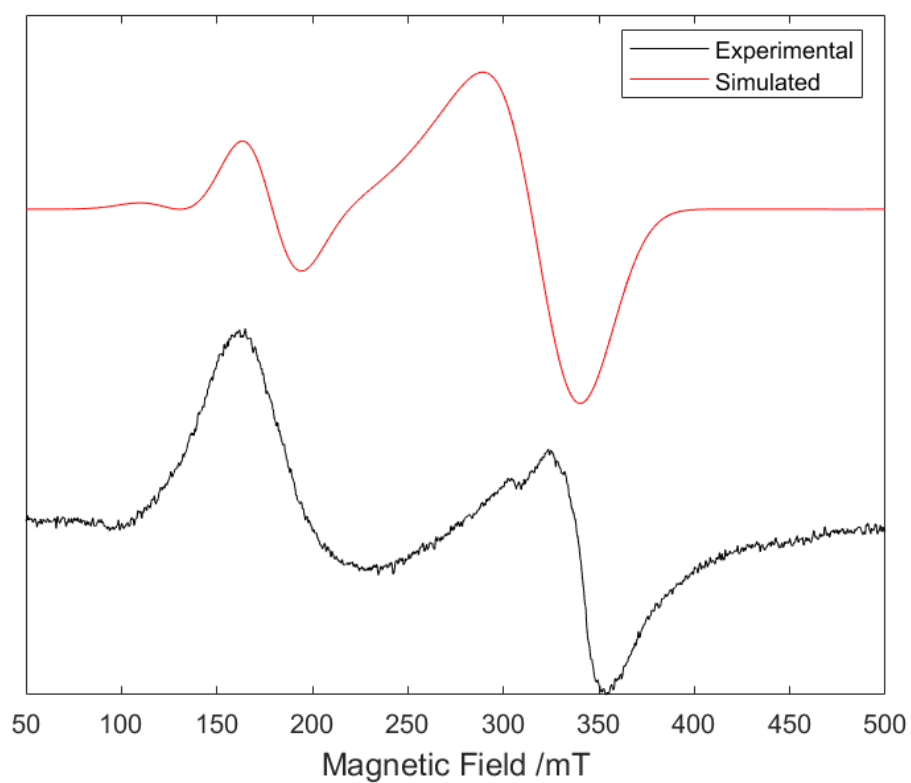
A3.10 X-band EPR spectrum and its simulated trace in solid state at T=298 K for **Cr-6.** D = 0.31 cm^{-1} (9294 MHz) and E/D = 0.071.
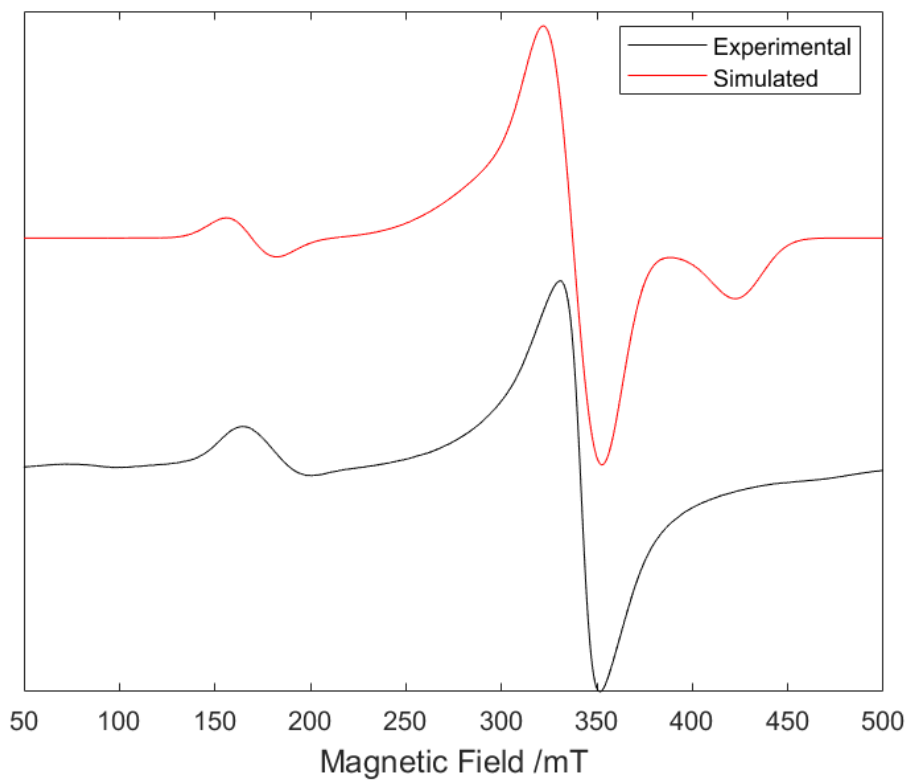
A3.11 X-band EPR spectrum and its simulated trace in solid state at T=298 K for **Cr-7**. D = 0.3 cm^{-1} (8994 MHz) and E/D = 0.007.

Appendix to Chapter 4
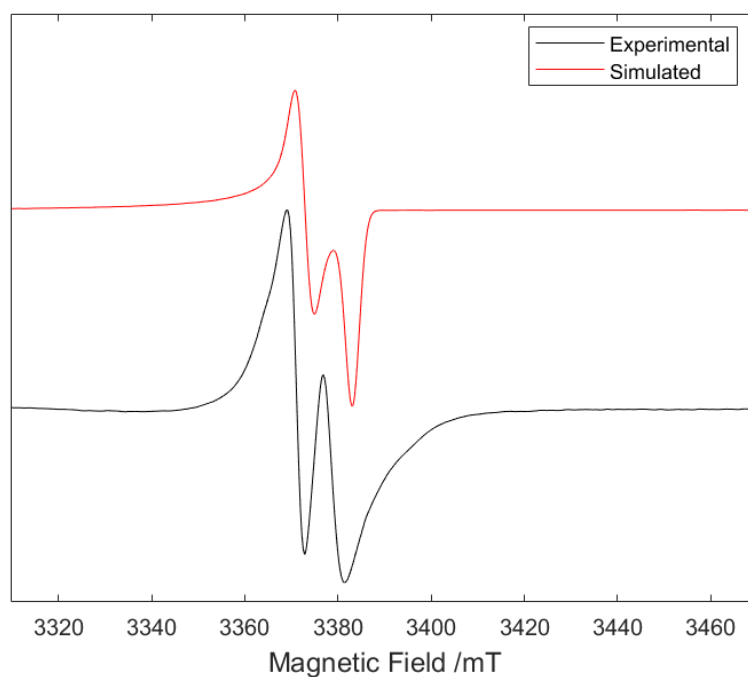
Figure A4.1 W-band EPR spectrum and its simulated trace in solid state at T=298 K for **Cr-1** (doped, 1%). D = 0.108 cm^{-1} (3237 MHz) and E/D = 0.23.

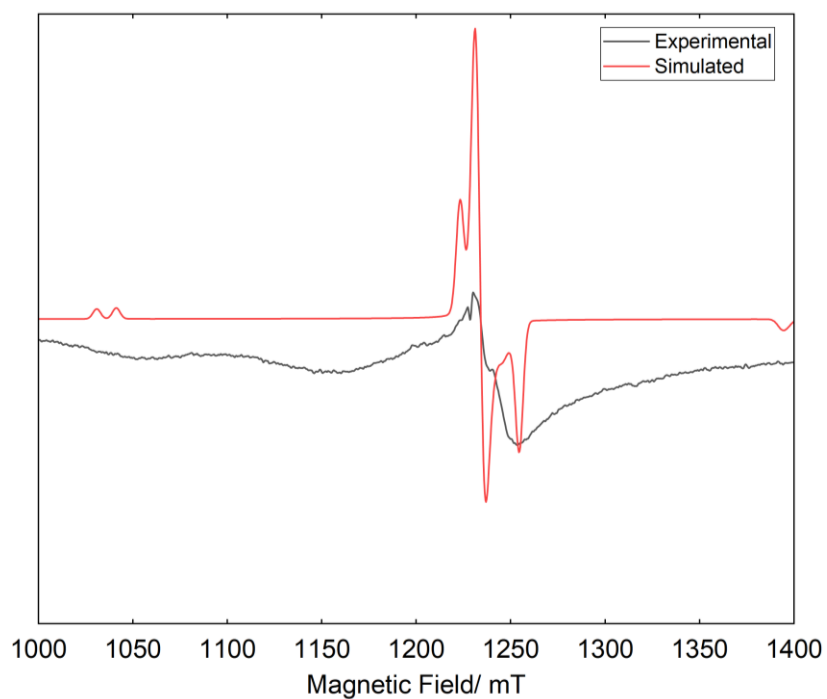**Figure A4.2** W-band EPR spectrum and its simulated trace in solid state at T=298 K for **Cr-2** (doped, 1%). D = 0.108 cm^{-1} (3237 MHz) and E/D = 0.28.

Figure A4.3 Q-band EPR spectrum and its simulated trace in solid state at T=298 K for EPR spectrum for **Cr-3** (doped, 1%). D = 0.1 cm^{-1} (2997 MHz) and E/D = 0.27.

Figure A4.4 Q-band EPR spectrum and its simulated trace in solid state at T=298 K for EPR spectrum for **Cr-4** (doped, 1%). D = 0.094 cm^{-1} (2818 MHz) and E/D = 0.3.

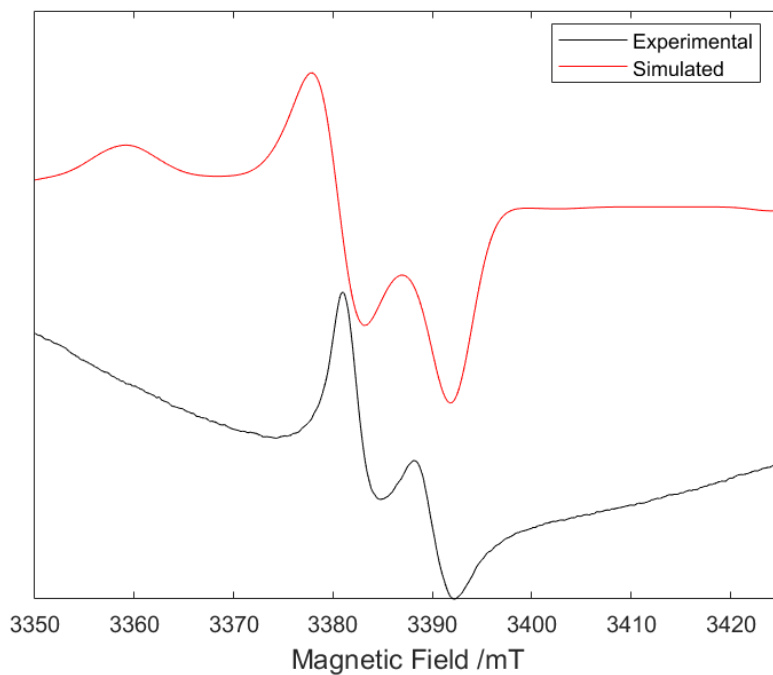**Figure A4.5** Q-band EPR spectrum and its simulated trace in solid state at T=298 K for EPR spectrum for **Cr-5** (doped, 1%). D = 0.116 cm^{-1} (3477 MHz) and E/D = 0.27.
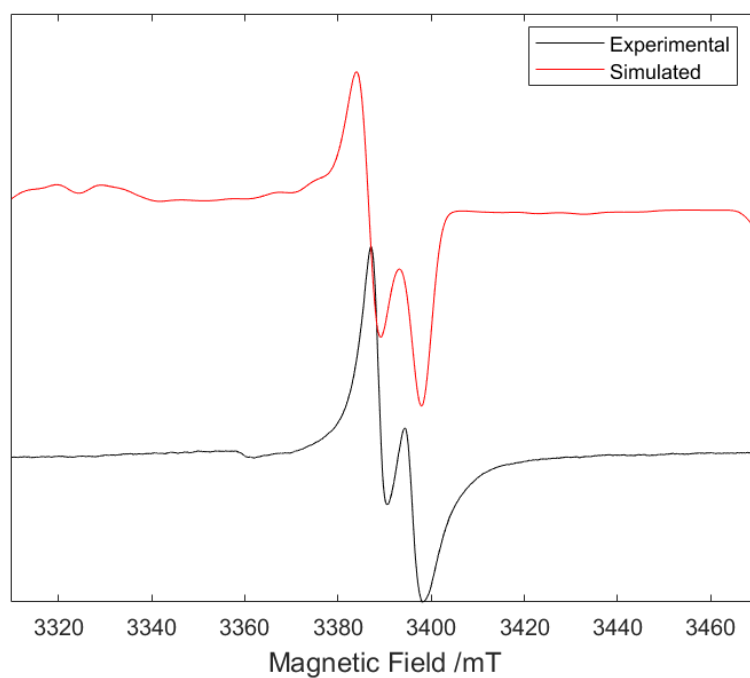
Figure A4.6 Q-band EPR spectrum and its simulated trace in solid state at T=298 K for EPR spectrum for **Cr-6** (doped, 1%). D = 0.113 cm^{-1} (3387 MHz) and E/D = 0.28.
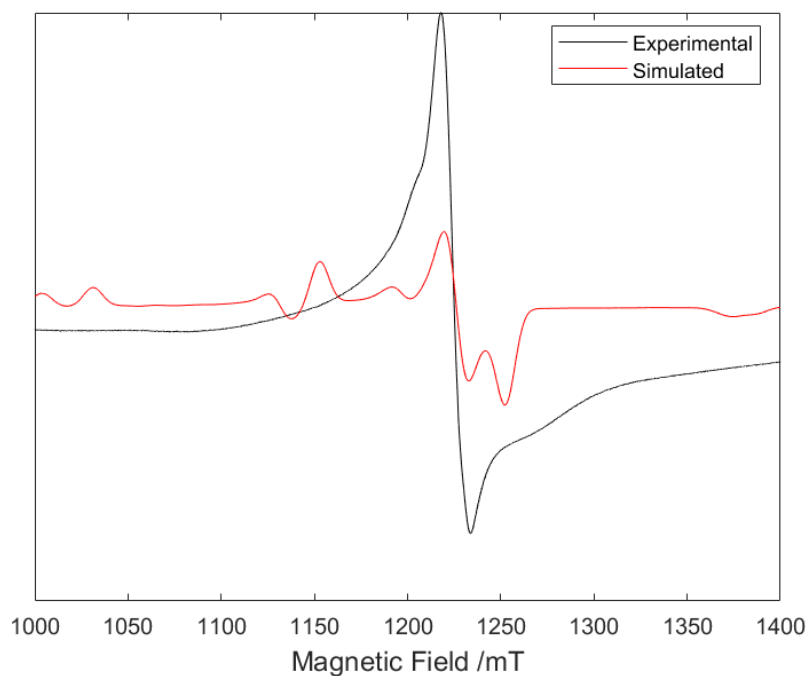

Figure A4.7 Q-band EPR spectrum and its simulated trace in solid state at T=298 K for EPR spectrum for Cr-1 (neat solid). D = 0.108 cm^{-1} (3237 MHz) and E/D = 0.23.
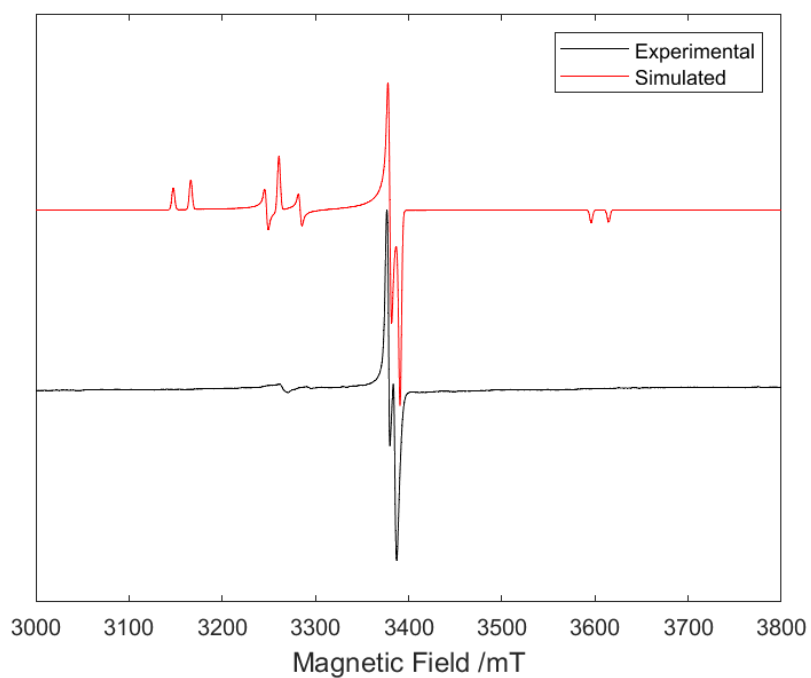
Figure A4.8 W-band EPR spectrum and its simulated trace in solid state at T=20 K for **Cr-2** (doped, 1%). D = 0.108 cm^{-1} (3237 MHz) and E/D = 0.28.